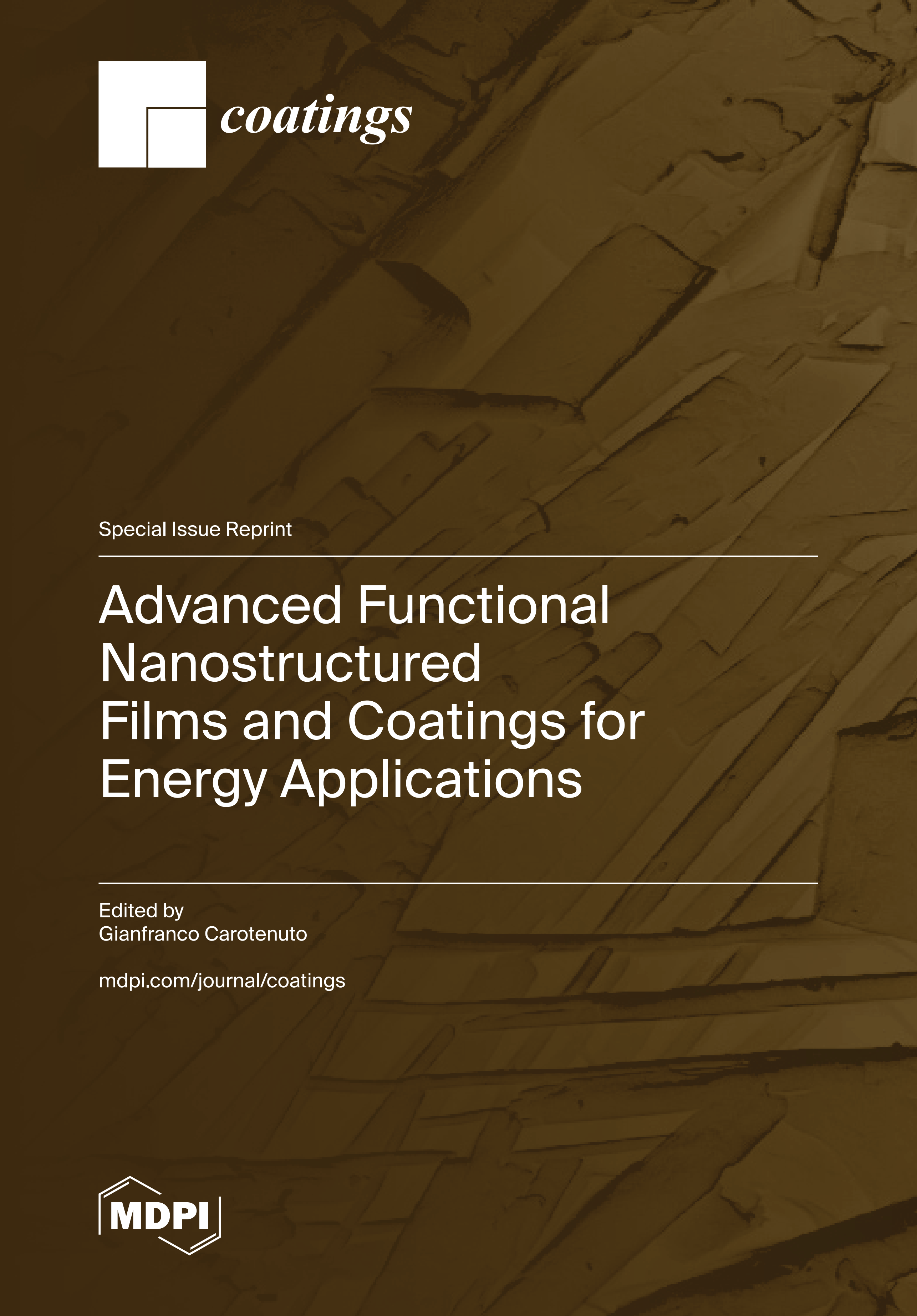

coatings

Special Issue Reprint

Advanced Functional Nanostructured Films and Coatings for Energy Applications

Edited by
Gianfranco Carotenuto

mdpi.com/journal/coatings

MDPI

Advanced Functional Nanostructured Films and Coatings for Energy Applications

Advanced Functional Nanostructured Films and Coatings for Energy Applications

Editor

Gianfranco Carotenuto

MDPI

Basel • Beijing • Wuhan • Barcelona • Belgrade • Novi Sad • Cluj • Manchester

Editor
Gianfranco Carotenuto
Institute of Polymers, Composites and
Biomaterials — National Research Council
(IPCB-CNR)
Portici
Italy

Editorial Office
MDPI
St. Alban-Anlage 66
4052 Basel, Switzerland

This is a reprint of articles from the Special Issue published online in the open access journal *Coatings* (ISSN 2079-6412) (available at: https://www.mdpi.com/journal/coatings/special_issues/Adv_Funct_Nanostructured_Film_Coat_Energy_Appl).

For citation purposes, cite each article independently as indicated on the article page online and as indicated below:

Lastname, A.A.; Lastname, B.B. Article Title. *Journal Name* **Year**, *Volume Number*, Page Range.

ISBN 978-3-7258-0995-0 (Hbk)
ISBN 978-3-7258-0996-7 (PDF)
doi.org/10.3390/books978-3-7258-0996-7

Cover image courtesy of Gianfranco Carotenuto

Contents

About the Editor

Gianfranco Carotenuto

Gianfranco Carotenuto is Research Director at the Institute of Polymers, Composites, and Biomaterials (IPCB) of the Italian National Research Council of Naples. He received his degree in Chemistry (1991) and Ph.D. in Materials Technology and Industrial Plants (1994) at the University 'Federico II' of Naples, Italy. He was a postdoc (1995) at The Center for Advanced Materials Processing (CAMP), Clarkson University, Potsdam (New York State, U.S.A.); visiting scientist (1996) at INM (Leibniz-Institute für Neue Materialen) in Saarbrücken (Germany); postdoc (1997–1998) at the Department of Material Science and Engineering, University 'Federico II' of Naples; Contract Researcher (1999–2000) at the Institute for the Technology of Composite Materials (ITMC-CNR) in Naples; and then Researcher (2001) at the Institute for Composites and Biomedical Materials (IMCB-CNR) in Naples. Dr. Carotenuto was also a Contract Professor (2000–2010) at the Engineering Faculty and Letters and Philosophy Faculty at University 'Federico II' of Naples. He is the author or co-author of more than 300 publications in international journals in material science and engineering and the Editor of two books on 'Metal-Polymer Nanocomposites' (Wiley). He has 10 international patents and has given many presentations at national and international conferences. He is on the Editorial Board of the journals: *Coatings* (MDPI), *Advances in Materials Science and Engineering* (Wiley) and the *Journal of Advanced Biotechnology and Bioengineering* (Synergy Publishers). His present research interests are the followings: functional microcomposites materials, metal–polymer nanocomposites, solid-state ionic conductors, polymer-supported graphite nano-coatings, polymer-embedded nanostructures, new electrical conductors, and chemical sensors.

Preface

At the beginning of human history, mankind found all necessary energy sources in the living environment. Energy sources in this primitive earth were limited to solar radiation (visible and infrared light), heat produced by volcanic activity, caloric energy from food people consumed to perform their basic tasks for survival, and biomass burning (wood, animal dung, charcoal). However, food, fire, and the sun provided more than sufficient chemical, thermal, and light energy to meet the needs of the human race at that time. The energy demand of a society depends on its degree of advancement: advanced societies are characterized by a proportionally higher energy demand compared to some poorly developed societies. In particular, a high technological development requires highly specialized and diversified energy sources. Indeed, there should be a specific energy source for each technological requirement (let us consider how many electric batteries are available nowadays). We could say that the human energetic requirements did not change, but the thermal energy of the fire and sun is very difficult to manage (it degrades, scarcely accumulates, etc.), and therefore new solutions to store and convert them to heat, light, kinetic/potential energy, etc. are strictly required. According to this statement, no novel energy sources are needed since the available types are just enough, but our attention should be focused on finding ways to interconvert all the existing energy forms. Increasing the possible approaches for effectively transducting the available energy forms must be a priority. Niche methods for energy transduction are welcome in a world counting an extremely large number of sophisticated civil/military technologies. Natural substances are not excluded from this task; for example, zeolites can store energy based on their latent heat of hydration. Owing to their anomalous physical properties, advanced materials based on nanostructures (e.g., graphene, carbon nanotubes, metal nanoparticles, etc.) have a key role in this special technology area. Similarly, niche materials such as intercalated compounds (graphite bisulfate), multicomposites, and hybrid solids can be exploited in energy transduction for different purposes. All these materials have been treated in papers collected in the Special Issue. Advanced materials frequently have a multiphasic nature and include some functional interfaces because most physical phenomena occur in regions extending along two different solid phases. The interface extension represents a key factor for amplifying the transduction phenomena. In such a context, the science of advanced functional materials perfectly intersects with the knowledge of film, surface, and interface potentialities. This is why this paper collection has been organized as part of the *Coatings* journal. This Special Issue aims to inform scholars of the materials science community of various unusual approaches, expedients, and practical solutions of material chemistry that are useful for energy transduction by collecting topical papers. It is specially addressed to scientists interested in the scope of functional interfaces, surfaces, and special materials potentially useful in scavenging all different energy forms.

Gianfranco Carotenuto
Editor

coatings

Editorial

Composite Films for Time Measurement—A Case Study

Gianfranco Carotenuto

Institute for Polymers, Composites and Biomaterials (IPCB-CNR), National Research Council, Piazzale E. Fermi, 1, 80055 Portici, Italy; gianfr.carotenuto@virgilio.it

Citation: Carotenuto, G. Composite Films for Time Measurement—A Case Study. *Coatings* **2022**, *12*, 1118. https://doi.org/10.3390/coatings12081118

Received: 21 July 2022
Accepted: 23 July 2022
Published: 4 August 2022

Each event starts in the past and proceeds towards the future, going through the present. Time measurement consists in the determination of the length of an event. Over the centuries many types of devices have been developed for time measurement [1]. Examples of primitive technological solutions used for time measurement include hourglass, water clock, candle clock, oil lamp clock, and incense clock, as the most relevant. Today, common types of time measurement tools are mechanical watches/clocks, digital watches/clocks, stopwatches, calendars, etc. Clearly, the measurement of time has always been delegated to mechanical or electrical devices and never to a material capable of slowly but progressively modifying over time its own physical properties, from whose modifications a way to determine the flowing of time follows. However, such a technological solution would not be very difficult to develop by combining knowledge on advanced composite materials and thin-film science. A material capable of self-changing over time and therefore able to act as a clock could be, for example, a resistor with a time-dependent resistance value or an optical filter with a transparency able to change slowly but continuously over a certain time period.

Occasionally pitch has suggested to humans the possibility of being used for time measurement. The 'pitch drop experiment', developed by Thomas Parnell of the University of Queensland in Brisbane (Austalia) in 1927 [2] to demonstrate the liquid nature of bitumen, represents the most famous case of device for time measurement based on pitch (the pitch drips every 7 years); however, further designs for a time related device based on pitch have been proposed too (e.g., the Kelvin's artificial glacier experiment with pitch on a plan, and the pitch flow glacier) [3]. The concept that pitch may be useful for developing a timepiece can be conveniently extended by preparing a pitch-based material capable of gradually and linearly changing its physical characteristics over the time. If, for example, this material changes its electrical conductivity, then an ohmmeter connected to it makes it embody a clock completely different from those fabricated so far. Yet why does pitch suggest this application? The reason is the possibility of inner movement that pitch can offer. In fact, a clock needs movement to work. All non-electric clocks are based on some type of movement: a flowing liquid or a fine powder (sand) is present in a hourglass, oil, wax, and water were present in the primitive clock systems, while an unfolding spring is contained in a more traditional mechanical clock. Therefore, movement is the basic requirement for a material intended for time measurement. Flow is a well-known characteristic of liquids, but it should not be allowed to solid materials. However, there are amorphous solid substances capable of flowing just like liquids do, but they do it very slowly during the time. These substances, modified by fillers, can be used to fabricate composite materials adequate for time measurement, and the resulting devices can be defined as 'molecular clocks', since the flowing of single molecular layers located at pitch-filler interface is the reason for their operation.

Movement happens under the effect of an applied force and this force represents a further requirement for a material devoted to time measurement. The applied force can be simply the gravitational field, or an external force field (e.g., magnetic or electric fields). Materials for time measurement are extremely useful since they can be integrated in the packaging of drugs, food, and electronic items, for example, but at the moment they represent a potential that is largely untapped. These materials consist of solids with some physical properties that slowly and progressively (better if also linearly) change over time. Physical properties such as the color, the electrical conductivity, the opacity, the polarizability, etc., can change in an irreversible way over time, and such a behavior can be advantageously exploited for the fabrication of devices for industrial applications such as, for example, the measurement of the shelf life for degradable and rapidly expiring products.

Pitch-metal composites (PMC) represents a new class of functional materials that can be used to develop compact solid-state clocks. Such solid devices, based on a simple self-changing mechanism, can have many technological applications such as chronometers, shelf-life indicators, timers, etc. and be used in a very compact way. The working principle of this novel functional material is the sedimentation phenomenon involving the composite filler in the viscoelastic pitch matrix. In principle, the filler may consist of a metallic powder stable to oxidation like stainless steel or a noble metal (e.g., silver, gold, etc.), but also a semiconductor powder (e.g., germanium, tellurium, etc.), or an electrically conductive ceramic powder (e.g., indium tin oxide, ITO) can be equivalently used. However, metals are the densest materials, and therefore yield the best results for this type of application. Non-toxic noble metals with high density values constitute the ideal composite filler, since these very expensive metals are characterized by extremely high density values (Au: 19.3 g/cm^3, Rh: 20.8 g/cm^3, Pt: 21.4 g/cm^3, Ir: 22.56 g/cm^3). Due to their special shape factor and low density (comparable to that of pitches like colophony), both graphene and carbon nanotubes (CNTs) are not really adequate for the present application. In addition, a segregation process based on floating is less convenient than a segregation based on settling, because forces of lower intensity are involved (the difference between the density of matrix and filler is quite small). With regard to the type of amorphous material to be preferentially used as a matrix, a pitch based on a low-molecular-weight substance, like for example colophony (density: 1.06 g/cm^3) or other tree resins, represents the best technological solution because the viscosity value of these substances is not extremely high like in the case of bitumen, asphalt, and other hydrocarbon-based pitches.

With regard to the preparation of these materials, the blending of the two components can be easily done by increasing the temperature (solution casting is not adequate as fabrication process because amorphous substances hardly release volatile solvents, due to the absence of a segregation phenomenon for these volatile components, since crystallization does not take place). However, a limitation for such a type of device is represented by the strict dependence of viscosity on temperature [4]; consequently, clocks based on this principle require a thermostatic system. On the other hand, these materials can be also used as integral temperature sensor [5] due to the dependence of the measurement time speed (i.e., sedimentation kinetics) on the pitch viscosity, which in turn is related to temperature.

The working mechanism of these devices is very simple: the sedimentation of the dispersed metallic phase (composite filler) by the effect of gravitational force slowly reduces the extension of the region of pitch where particles are embedded. The filler is segregated in a smaller and smaller portion of the sample, thus causing the simultaneous formation in the sample of: (i) an electrically insulating region (with high dielectric strength), completely free from particles, and (ii) a complementary region where the particle concentration progressively increases. In particular, in the last region, the formation of percolation paths can be observed with the flowing of time. However, particles are not uniformly dispersed in this region, but they tend to accumulate near the bottom (i.e., the sample basal plane). In this region, the sample electrical conductivity quickly increases because a network of percolation paths is progressively generated. When the percolation threshold is reached at sample bottom, the electrical properties of this basal surface change from dielectric (insulator) to conductive, and the electrical conductivity value on this face progressively improves to reach a value approximately coincident with the electrical conductivity of the pure metal used as filler. Therefore, the measurement of the sample resistance in the region of the bottom by two interdigitated electrodes does not provide a constant value, but a value linearly growing during the time, and this time-dependent resistance value is useful to fabricate some special type of electric device that can be used as an innovative clock for time flow measurement.

It is possible to develop a very simplified model for the temporal evolution of the composite filling factor. This model does not consider the accumulation of the filler particles at the sample bottom, but it is able to predict the composite filling and electrical conductivity increase. If we consider a uniform dispersion of N identical metal particles, with a spherical shape of radius: R, in a certain volume V° of pitch, having for example the shape of a rectangular prism, then the volume fraction, φ_2, of metal is given by the following equation:

$$\varphi_2 = 4/3\pi R^3 N/(4/3\pi R^3 N + V^\circ) \tag{1}$$

As the metallic filler settles at sample bottom, the pitch volume containing the particles reduces and the particles accumulate on the prism basal plane of this reduced volume $V < V^\circ$. If we indicate with v the sedimentation velocity of the identical spherical particles, then the volume, V, where particles are dispersed, is given by: $V = V^\circ - (S \cdot v \cdot t)$, where S is the surface area of the prism base and t the elapsed time; thus φ_2 becomes:

$$\varphi_2 = 4/3\pi R^3 N/[(4/3\pi R^3 N + V^\circ) - (S \cdot v) \cdot t] \tag{2}$$

As visible, the volumetric fraction of metallic phase increases during the time, and therefore the dispersion of electrically conductive particles in the dielectric matrix, initially below the percolation threshold, will gradually concentrate, as time progresses, first up to the percolation threshold and then above it. As a consequence, the electrical behavior of the material in the basal region of the prism changes from dielectric to conductive. This model allows to qualitatively predict the behavior of the material electrical conductivity, which is proportional to φ_2.

The present type of devices is a great example of how a force field (gravitational, magnetic or electric force field) can be conveniently engineered. A timepiece based on the gravitational field could be made by a thin pitch-metal micro-composite layer placed on two interdigitated electrodes. The material must have a percolation composition in order to readily change its electrical conductivity with time flowing. If the device is based on a magnetic field, a neodymium magnet must be placed below the pitch-iron, or pitch-cobalt, or pitch-nickel film.

Thin film and coating technology has a very important role in the area of materials for time measurement. In particular, an ultra-thin layer of percolation composition is strictly necessary for the device fabrication. In fact, if the filling factor, θ, of the pitch-metal composite is taken next to the percolation threshold, then even extremely small variations of θ can cause significant changes in the material electrical conductivity, and this variation typically corresponds to several magnitude orders [6]. Since metal particle sedimentation in pitches is a very slow process, the presence in the composite of a percolation structure could represent a trick to have perceptible variations of the electrical conductivity in short time intervals. A further important consideration is that the percolation structure is first generated in the basal plane of the sample and, with time progress, further percolation structures result in the above planes. As a consequence, an ultra-thin layer can perform the same function as a thicker layer, and consequently this type of device can be conveniently made by an ultra-thin layer deposited on two planar interdigitated electrodes. At beginning the composite composition is uniform inside the layer and it corresponds exactly to the percolation threshold concentration, then with time flowing the above part of the sample will become a better and better electrical insulator, while the remaining part will become more and more electrically conductive. The best place where the sample electrical conductivity can be measured is at the bottom (i.e., the prism basal plane). In addition, a pitch-metal micro-composite is more convenient than a nano-composite for this type of application. In fact, since pitches have an apparently solid nature, it is possible to develop a mathematical model for particle sedimentation, which is based on the kinetic friction force acting at filler-matrix interface. In particular, the acceleration, a, undergone by a spherical particle embedded in the very viscous pitch matrix as a result of the forces acting on it (i.e., weight force, hydrostatic force, and interfacial kinetic friction force) is given by the following approximate Equation (3) (More detail information could be found in the Supplementary Materials).

$$a = g - (3\mu_D \cdot P/d_M) \cdot (1/R) \tag{3}$$

where, g is the gravitational acceleration, P is the atmospheric pressure, μ_D is the coefficient of kinetic friction at interface, R is the particle radius, and d_M is the metal particle density. This equation is quite different from the classical expression for the particle speed, v, derived by comparing the Stokes' law to the resultant of the applied forces. However, this mathematical treatment takes correctly in account of the extremely slow particle movement in pitch. As visible, the sedimentation acceleration approaches the acceleration due to gravity with increasing of the metal density and the particle size, and therefore, a raw powder of a noble metal is the most convenient choice for an electrically conductive filler.

A further important possibility is to control the pitch viscosity by mixing it with polyols [7]. These special formulations may look apparently solid, but have lower viscosity values than the pure resin and such physical characteristics is useful for increasing the rate of sedimentation.

An example of molecular-clock can be a simple time-dependent resistor (TDR), that is a passive electrical device made by a pitch-metal mixture with time-dependent electrical conductivity. This device unendingly increases its conductivity at the bottom surface because of the slow segregation of the electrically conductive filler with high specific weight, dispersed in the pitch (e.g., colophony). Segregation is related to the different density values characterizing the inorganic filler and the organic matrix, and it consists in the slow but progressive settling of the metallic powder at the bottom of the pitch matrix. Consequently, time causes a continuous change in the material electrical conductivity, and consequently it can be used as time flow indicator (i.e., clock). However, due to the optical grade of colophony, the clock can be also based on some optical measurements, for example transparency at the sample bottom should decrease as the effect of the filler segregation.

In conclusion, the process of sedimentation of an electrically conductive micrometric powder in a highly viscous (apparently solid) dielectric matrix can be used to fabricate a composite material capable to spontaneously modify its electrical properties (e.g., electrical conductivity, polarizability, dielectric strength, etc.) over time. Optical properties (e.g., transparency, refractive index, etc.) also change and this variation can be used for the same purpose. Sedimentation may take place by the effect of the gravitational force field or by the effect of an electrical or magnetic field placed near the sample. In this case, the device operation is not dependent on its orientation. Different materials can be used as matrices (e.g., greases, gels, resins, etc.); however, vegetal resins, such as colophony, are the most adequate to achieve an apparently solid material able to self-modify over a large time period. The use of a noble metal powder as electrically conductive filler is very convenient, principally because of the high-density value that characterizes this type of solid. The optimal composition for the composite is that corresponding to the percolation threshold because it allows significant conductivity changes in short time periods. The development of materials for time measurements will launch a completely new research topic in material science, that will require knowledge in the area of films and coatings as the main investigation tool.

Supplementary Materials: The following supporting information can be downloaded at: https://www.mdpi.com/article/10.3390/coatings12081118/s1.

Conflicts of Interest: The authors declare no conflict of interest.

References

1. Lombardi, M.A. First in a series on the evolution of time measurement: Celestial, flow, and mechanical clocks [Recalibration]. *IEEE Instrum. Meas. Mag.* **2011**, *14*, 45–51. [CrossRef]
2. Edgeworth, R.; Dalton, B.J.; Parnell, T. The pitch drop experiment. *Eur. J. Phys.* **1984**, *5*, 198–200. [CrossRef]

3. Johnston, S.F. The physical tourist–Glasgow: A heritage tour. *Phys. Perspect.* **2006**, *8*, 451–465. [CrossRef]
4. Daucik, P.; Visnovsky, J.; Ambro, J.; Hajekova, E. Temperature dependence of the viscosity of hydrocarbon fractions. *Acta Chim. Slovaca* **2008**, *1*, 43–57.
5. Garramiola, F.; del Olmo, J.; Poza, J.; Madina, P.; Almandoz, G. Integral sensor fault detection and isolation for railway traction drive. *Sensors* **2018**, *18*, 1543. [CrossRef] [PubMed]
6. Misiura, A.I.; Maruzhenko, O.V.; Mamunya, Y.P.; Kulish, M.P.; Pylypenko, A.M. Influence of the type of filler distribuition on the electrical and thermal conductivity of metal-filled polymer composite. *Funct. Mater.* **2020**, *27*, 500–507.
7. Kiser, M.D. Viscosity Modification of Heavy Hydrocarbons Using Dihydric Alcohols. U.S. Patent 2005/0092652A1, 5 May 2005.

coatings

Editorial

Looking for New Materials: The Molecular Clocks

Gianfranco Carotenuto

Institute for Polymers, Composites and Biomaterials (IPCB-CNR), National Research Council, Piazzale E. Fermi, 1, 80055 Portici, Italy; gianfr.carotenuto@virgilio.it

Frequently, new materials have been discovered by looking at the interface among some of the already existing material classes. This creative approach has been used, for instance, in the development of nano-sized materials, which are merely an intermediate matter form, located between the molecules and the bulk solids. Similarly, hydrogels are a type of solid phase intermediate between water and polymers, while aerogels are intermediate between gas and ceramics; composites, depending on their filling factors, range from metals to ceramics (metal matrix composites, MMC) or from polymers to ceramics (polymer matrix composites, PMC), etc. Now, between liquids and solids there is the class of the 'amorphous solids', which can also be considered as the class of the 'extremely viscous liquids'. These 'frontier materials' can be modified by embedding an adequate functional filler, in order to achieve some technologically useful hybrid, which is adequate for applications based on its time-depending properties.

The 'flat shape' of solid matter, commonly referred as film or coating, depending on the presence or less of a substrate, has played a fundamental role in materials science and technology both in the past and in the present. Recently, graphene and other 2D materials (e.g., molybdenum sulfide, MoS_2) have had a huge success because of the large number of physical anomalies that this special shape is able to offer (e.g., optically transparent electrical conductor, zero band-gap semiconductor, high specific surface area adsorber, etc.). Films and coatings are not equivalent solid matter forms. Indeed, coatings is the only organization of matter able to maximize the interactions with the substrate, and such an unique property may offer a variety of applications for coatings, never developed before. This flat shape of matter in the form of thin film or coating is also the only form of matter organization capable of maximizing the interactions with a force field such as, for example, the gravitational field, the electrical field, or the magnetic field. Therefore, the possibility of developing some type of composite material, capable of undergoing the effects of a force field (electrical, magnetic or gravitational) by spontaneously acquiring this kind of shape if placed in it, can be very important. Matter with low cohesion like fluids very commonly show such a behavior (e.g., ferrofluids), but solids, because of their usually high cohesion, do not typically reshape in a force field. However, solids capable of reshaping for the effect of a force field can be developed on the basis of the low-molecular-weight amorphous substances. Such a time-related behavior of this hybrid solid matter can be advantageously exploited for technological applications in different industrial areas.

Depending on the intensity of the cohesion forces (i.e., covalent, ionic, dipole-dipole, or Van der Waals interactions), solids may group in 'stationary' and 'dynamic' molecular structures. A crystalline solid phase can be considered as a stationary molecular structure (that is, a covalent or ionic or dipole-dipole based framework, which remains structurally unchanged over the time). A completely different situation is that experienced by those amorphous solids (glassy materials), made of small organic/inorganic molecules. Indeed, low-molecular-weight amorphous solids are dynamically evolving molecular structures in a continuously changing structural status. On the other hand, amorphous solids can be alternatively described as very viscous liquids, and their ability to modify the own molecular structure over the time is related to the molecular mobility, which depends on

Citation: Carotenuto, G. Looking for New Materials: The Molecular Clocks. *Coatings* **2022**, *12*, 933. https://doi.org/10.3390/coatings12070933

Received: 21 June 2022
Accepted: 26 June 2022
Published: 1 July 2022

the particular viscosity value characterizing these systems. These substances structurally change more slowly with increasing of viscosity, i.e., they are less molecularly active.

This special state of the matter can offer great technological potentialities because it is a kind of 'living matter' capable of self-modifying over the time, and therefore they are able to show something like a 'vitality' that can be conveniently exploited for practical applications, such as, for example, measuring the flow of time. The lifespan of these materials is represented by the time they require to reach the own thermodynamic equilibrium state, where the energy content of the substance has reached its minimum value. An extremely viscous liquid or equivalently a solid that takes the shape of the container is a structurally evolving material, and such slow but continuous change of the molecular structure can be exploited to mark the time just like an hourglass may do. For example, when these solids are used to fill a pipe, they slowly flow through it, and after weeks, months, or years they can even drip away from one end of the pipe. Solid pieces placed on a flat surface tend to spread on the substrate, that is, to become a thin film coating the substrate surface since the minimum energy content corresponds to a thin layer if the interaction with the substrate are favored with respect to the internal ones. Therefore, a film or a thin coating is the ultimate goal of these 'living materials' and their lifespan and molecular activity depends on the strength of the interaction with the substrate. The solid will modify its shape and spread on the substrate, leading to a thin coating layer if the interactions with the substrate are favored (that is, hydrophobic solid on a hydrophobic substrate or hydrophilic solid on a hydrophilic substrate). Otherwise, it will not tend to evolve or to evolve only minimally if the interactions with the substrate are not favored compared to the internal ones. From a theoretical point of view, the resultant among gravity, applied external pressure, adhesion, and surface tension is the driving force for the shape evolution of the 'living' solid; however, from a practical point of view, a gradient of gravity force is not enough to cause a shape evolution for a small piece of an amorphous molecular solid; only liquids for their very low cohesion forces may change shape from the effect of gravitational force. The situation for a macroscopic sample is quite different; a photograph of the solid taken at regular time intervals may show its progressive shape evolution with transformation, for example, from the pseudospherical shape to a thin flat film. However, there are many other more convenient ways to evidence the structural evolution of this material over the time: if the solid is placed on a planar capacitor, the capacity of this electrical devices will evolve during the time. An electrically conductive (but quite resistive) phase, like the graphite powder, can be dispersed in the molten material up to achieve a percolative structure, in order to make the solid an electrical conductor. The electrical measurements performed on this composite solid shows a time dependent resistance value, uniformly and continuously evolving up to the achievement of the equilibrium state. To make a composite material having a magnetic phase (e.g., magnetite) uniformly dispersed in the solid is also an interesting possibility. A magnetic field applied to the solid is able to force the solid to change its shape, and this process can be easily detected by measuring a magnetic property of the solid body. Many other approaches can be used both to induce a change in the shape of the amorphous solid and to detect the shape evolution of the solid. Such 'flowing solids' can be used to fabricate compact clock mechanisms, based on a simple and very effective molecular gear. Different models of time markers can be easily designed by using these 'flowing solids' and be used as switches able to self-activate after a precise time period or above a certain temperature threshold, devices for measuring the material aging or the shelf life in food or drug packaging, etc.

However, such solid materials can be also used simply to visualize force fields, as common ferrofluids already do. The property change will be very sensible if the functional phase uniformly dispersed inside the flowing solid matrix is nano-sized, since very small variations of the embedding matrix can determine much more significant property changes. Therefore, a flowing nanocomposite can be preferred to a simple micro- or macro-composite material. Both amorphous polymeric solids (e.g., silica, organic polymers, etc.) and low molecular weight solids can be potentially used to fabricate these nanocomposite materials, but flow in high-molecular-weight solids always ends in negligible results for the very scarce mobility of these large molecular chains at room temperature. Differently, low-molecular-weight solids are characterized by moderate molecular mobility, even at room temperature, and consequently they are preferred substances for the present application. On the other hand, mobility in liquids is too high to be used for time flow measurements.

Circles in the tree trunks have been used to measure the time (the age of the plant) and from trees may come the base materials, useful to measure the time (that is, materials with time-related properties). Indeed, the resins of some trees (like fir, pine, etc.) are high viscous liquid phases that, after turpentine removal by distillation, give solid materials, known as colophony, that behave just like a solid with an evolving shape. This substance does not crystallize, but forms amorphous solids because it is a complex mixture of the abietic acid isomers. It is required only to make a blend of this natural substance (colophony) with a conductive or magnetic functional phase, in order to achieve an electrical/magnetic device with some dynamically-evolving physical characteristics.

In conclusion, it is well known that coatings and films are playing a crucial role in the material science field, the technological potentiality of these special solid structures are widely recognized; however, there are many others ways to exploit their potentialities that cannot be even imagined and will be inevitably discovered progressively over the time. Here, as an example, the role of nanostructured films and coatings in a completely new field of material science, that is, the molecular clocks, has been presented as an example of the incredible applicative potential of these types of solid structures. The possibility to develop solids with properties progressively changing over the time is one of the last prospective of material science, which can be exploited, for example, for time measurements. The availability of molecular clocks or also new devices capable to self-activate after a certain time period is always very useful in the industry, and a material with some property that spontaneously and linearly changes over the time represents the ideal situation. However, the property must be easy to measure; a property such as, for example, the electrical conductivity, the electrical capacity, the opacity, or the color could be adequate. However, this property must modify continuously and indefinitely, or at least over a very long period of time. Material combination represents the way to achieve easy-to-measure properties, and such a composite material with some continuously evolving physical characteristics is the basic component for the fabrication of a device for time measurement.

Conflicts of Interest: The authors declare no conflict of interest.

coatings

Article

Carbon Dot-Titanium Dioxide (CD/TiO_2) Nanocomposites: Reusable Photocatalyst for Sustainable H_2 Production via Photoreforming of Green Organic Compounds

Pinelopi P. Falara [1,2], Maria Antoniadou [1,3,*], Adamantia Zourou [2], Elias Sakellis [1] and Konstantinos V. Kordatos [2,*]

[1] Institute of Nanoscience and Nanotechnology, National Center for Scientific Research "Demokritos", Agia Paraskevi, 15341 Athens, Greece; e.sakellis@inn.demokritos.gr (E.S.)
[2] School of Chemical Engineering, National Technical University of Athens, 9 Iroon Polytechniou St., Zografou, 15780 Athens, Greece
[3] Department of Chemical Engineering, University of Western Macedonia, 50100 Kozani, Greece
* Correspondence: mantoniadou@uowm.gr (M.A.); kordatos@central.ntua.gr (K.V.K.)

Abstract: The present work focuses on TiO_2 modification with carbon dots (CDs) using a hydrothermal process, which results in the synthesis of CD/TiO_2 nanocomposite photocatalysts characterized by exceptional optoelectronic properties. The structural and physicochemical properties of the obtained nanocomposites, which contained varying amounts of CDs, were precisely assessed. HR-TEM analysis showed that the prepared nanocomposites consisted of rod-shaped TiO_2 nanoparticles and CDs well-dispersed on their surface. The optical properties of the nanocomposites were studied using UV–vis diffuse reflectance spectroscopy. All CD/TiO_2 samples presented decreased energy gap values compared with bare TiO_2 samples; the band gap was further decreased as the CD concentration rose. Electrochemical measurements revealed that the presence of CDs improved the photocurrent response of the TiO_2, presumably due to enhanced charge separation and decreased recombination. The synthesized nanomaterials were used as photocatalysts to produce hydrogen via the photoreforming of ethanol and glycerol green organic compounds, under 1-sun illumination. The photocatalytic experiments confirmed that the optimum loading of CDs corresponded to a percentage of 3% (w/w). Ethanol photoreforming led to a H_2 production rate of 1.7 $\mu mol \cdot min^{-1}$, while in the case of the glycerol sacrificial agent, the corresponding rate was determined to be 1.1 $\mu mol \cdot min^{-1}$. The recyclability study revealed that the photocatalyst exhibited consistent stability during its reuse for hydrogen production in the presence of both ethanol and glycerol.

Keywords: carbon dots; photocatalysis; H_2 production; ethanol reforming; glycerol reforming

Citation: Falara, P.P.; Antoniadou, M.; Zourou, A.; Sakellis, E.; Kordatos, K.V. Carbon Dot-Titanium Dioxide (CD/TiO_2) Nanocomposites: Reusable Photocatalyst for Sustainable H_2 Production via Photoreforming of Green Organic Compounds. *Coatings* **2024**, *14*, 131. https://doi.org/10.3390/coatings14010131

Academic Editor: Gianfranco Carotenuto

Received: 19 December 2023
Revised: 13 January 2024
Accepted: 17 January 2024
Published: 19 January 2024

1. Introduction

The modern world faces critical challenges concerning the energy crisis and environmental pollution. Due to heavy reliance on fossil fuels, serious damage has been done to air quality from greenhouse gas emissions. The solution resides in transitioning to renewable energy sources, with solar energy emerging as the most promising clean energy on the earth because of its abundance, effectiveness, and easy large-scale utilization [1].

In recent years, the utilization of hydrogen (H_2) as a green fuel has emerged as a crucial change. This transition has stimulated the investigation of novel technologies such as aqueous phase reforming (APR). For example, the APR of crude glycerol contained in the wastewater streams of industrial facilities has been proposed as an alternative low-cost process, able to convert oxygenated molecules into H_2 [2,3]. Significant advancements in H_2 production have been achieved also via innovative methods that exploit solar light like photocatalysis and photoelectrocatalysis [1,4]. These advanced photoinduced processes appear to be effective in addressing the dual crisis of energy sustainability and environmental contamination.

Titanium dioxide (TiO_2) is considered the most promising semiconductor material used in photocatalytic applications (e.g., water splitting, waste water treatment, etc.); however, it suffers from a low utilization of visible light and high recombination reaction rate between photogenerated electrons and holes [5]. As it has been demonstrated, the activity of the TiO_2 photocatalyst for water splitting is significantly enhanced by incorporating noble metals. M. Saleh et al. [6] investigated the influence of the co-catalyst deposition and postulated that scarce elements and cost limitations for efficient large scale hydrogen production could be resolved via the optimization of loading Pt and Cu nanocrystals onto TiO_2. Furthermore, by introducing a ZIF-67-derived Co_3O_4@C metal-free co-catalyst onto TiO_2, the same group achieved the significantly enhancement of H_2 evolution rates via photocatalytic water splitting [7]. Another successful approach to TiO_2 modification in order to overcome these limitations was the fabrication of composite heterostructures with carbon-based nanomaterials such as carbon nanotubes (CNTs) [5,8,9], graphene oxide (GO) [10,11], reduced graphene oxide (r-GO) [12–15], graphitic carbon nitride (g-C_3N_4) [16,17], or more recently with carbon dots (CDs) [18,19]. CDs' structure involves a carbon core consisting mostly of sp^2 carbon domains connected by sp^3 carbon atoms and a large number of functional groups (-OH, -COOH, -NH_2, etc.) on the surface. Despite the limited number of studies that have been performed on the use of CDs in photocatalytic hydrogen production, they are a great sensitizer for TiO_2 photocatalysts as they are characterized by broad visible light absorption, efficient electron transfer properties, and high photostability. Additionally, CDs are capable of accepting photo-excited electrons generated by the TiO_2 semiconductor under illumination. Consequently, the separation of charge carriers is greatly enhanced as the recombination rate is reduced, which is crucial for efficient photocatalytic H_2 generation [20,21].

The recombination reaction rate may be significantly suppressed with the use of electron donor substances as sacrificial agents, due to the fact that they react irreversibly with the photogenerated holes and/or oxygen. For water as the target substance, the process results in simultaneous oxygen and hydrogen production. Nonetheless, the process of water cleavage is commonly regarded as having low efficiency. Photocatalytic reforming is more efficient for hydrogen production when using biomass-derived substances like ethanol and glycerol. The reforming of organic substances in the presence of water leads to the production of hydrogen and CO_2. Organic compounds such as organic acids [22], alcohols [23–25], amines [24,26,27], and sugars [28,29] are often employed as sacrificial agents. Photocatalytic hydrogen generation occurs simultaneously with the degradation of the organic compounds. In aqueous solutions under anaerobic conditions, the chemical reaction follows a reforming model, which involves the decomposition and mineralization of the organic compound, but also water decomposition and hydrogen production [30,31]. This is described by the following general scheme:

$$C_xH_yO_z + (2x - z)\, H_2O \rightarrow x\, CO_2 + \left(2x - z + \frac{y}{2}\right) H_2 \quad (1)$$

All the energy required for this endothermic reaction is provided by photons that are taken in by the photocatalyst. While photogenerated electrons reduce hydrogen ions and produce molecular hydrogen, photogenerated holes interact with the organic material and oxidize it [32].

In this work, CD/TiO_2 nanocomposites were synthesized through a simple and low-temperature procedure. More specifically, CDs were prepared using citric acid and urea precursors in a molar ratio of 1:100, following a domestic microwave-assisted synthesis for 4 min. To the best of our knowledge, this was the first time that as-prepared CDs have been combined with TiO_2 for photocatalytic H_2 generation. The structural and physicochemical properties of the obtained nanocomposites, which contained varying amounts of CDs, were thoroughly characterized. The prepared materials were then used as photocatalysts for hydrogen production using organic compounds as sacrificial agents. For this purpose, ethanol and glycerol have been tested and the amount of generated hydrogen under 1-sun illumination was determined via gas chromatography. The obtained results confirmed that photocatalytic hydrogen production is strongly related to the nature and chemical structure of the organic substrate, the reaction conditions, and the CD content in the TiO_2 nanocomposite material. The aim of this work was to evaluate the potential of novel and low-cost CD/TiO_2 nanocomposites in the field of photocatalytic H_2 generation. It is important to note that for this application, green liquid organic hydrogen carrier systems (ethanol and glycerol) were utilized. Consequently, this study laid the foundation for the achievement of sustainable H_2 production using renewables (from/using biomass-derived compounds and solar light).

2. Materials and Methods

2.1. Materials

All chemicals of analytical grade were used as received. Urea was obtained from Sigma-Aldrich (St. Louis, MO, USA); citric acid was purchased from Fluka and glycerol (≥99%) from Carlo Erba (Cornaredo, Italy). The nanocrystalline TiO_2 used in the present work was commercial Degussa P25. Absolute ethanol (C_2H_6O, ≥99%) was purchased from Acros-Organics (Geel, Belgium). Perfluorinated Nafion ($C_7HF_{13}O_5S{\cdot}C_2F_4$, ≥98%) was obtained from Chem-Lab (Zedelgem, Belgium) and sodium hydroxide (NaOH) from Merck (Darmstadt, Germany). Deionized (DI) water was used throughout.

2.2. Synthesis of the CD/TiO_2 Nanocomposites

The CDs were prepared following a domestic microwave-assisted synthesis, constituting a bottom–up strategy. In this method, 0.1 g of citric acid and 3.12 g of urea were used as CD precursors. Specifically, a molar ratio of citric acid:urea of 1:100 was added to 10 mL of DI water [33]. The mixture was vigorously stirred for about 10 min and then was placed in a domestic microwave for 4 min. After natural cooling, the resulting product was dissolved in DI water and was centrifuged at 6000 rpm for 30 min and filtrated in order to separate the CD solution from by-products. Thus, the precipitate was removed, while the supernatant dispersion of the CDs was solidified with freeze-drying technology, and the resulting powder of the CDs was soft and light. The main steps of the synthesis route of the CDs are shown in Figure 1.

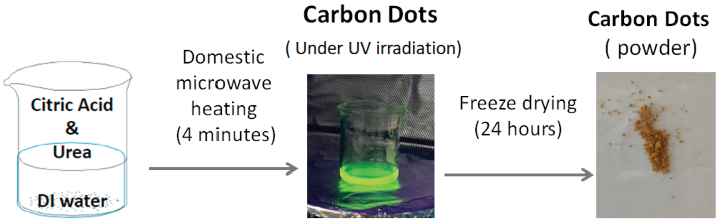

Figure 1. CD synthesis procedure diagram.

Regarding the CD/TiO_2 nanocomposites, they were obtained with a hydrothermal method. More specifically, 20 mL of distilled water and 6 mL of ethanol were mixed together, and then 400 mg of Degussa P25 and 4 mL of CDs dispersed in ethanol were added. The concentration of the CDs' dispersion varied in order to produce nanocomposites with different concentrations of CDs. To examine the influence of the content on photocatalytic H_2 production, 1, 2, 3, and 4% *w*/*w* CD/TiO_2 nanocomposites were synthesized. The reaction mixture was stirred for 30 min at room temperature in order to achieve homogeneity and then transferred into a Teflon-sealed autoclave and heated at 140 °C for 4 h [34]. The resulting photocatalysts were washed with DI water three times, collected with centrifugation, and dried at 80 °C overnight.

2.3. Photoelectrodes

The fabrication of the working electrode followed the subsequent steps: transparent FTO conductive glass electrodes (7 ohms cm^{-2}, Pilkington, Lathom, UK) underwent a thorough cleaning with a solution composed of 2% Hellmanex in water, followed by washing with ethanol and acetone. To prepare the photoelectrode, 10 mg of each photocatalyst was dispersed in a solution comprising 50 μL of Nafion perfluorinated solution, 290 μL of 3D water, and 168 μL of absolute ethanol. The resulting suspensions were ground and doctor-bladed onto the FTO electrode, forming a uniform coating. Subsequently, the samples were heated at 200 °C for 1 h.

2.4. Characterization Methods

X-ray powder diffraction (XRD) analysis was performed using a D8 Advance diffractometer, operating with Bragg–Brentano geometry with Cu $K_{\alpha1}$ (λ = 1.5406 Å) and Cu $K_{\alpha2}$ (λ = 1.5444 Å) radiation (Bruker, Billerica, MA, USA). Data were collected over the angular range of 10 to 80°, counting for 2 s at each step of 0.02° in the detector position.

Fourier transform infrared (FT-IR) spectra were obtained using a Jasco FTIR 4200 spectrometer in the range of 400–4000 cm^{-1} using KBr pellets (Jasco, Tokyo, Japan).

The nanostructure was studied with a FEI Talos F200i field-emission (scanning) transmission electron microscope (S/TEM) operating at 200 keV, equipped with a windowless energy-dispersive spectroscopy microanalyzer (6T/100 Bruker). The TEM samples were prepared by suspending the nanoparticles in ethanol and the subsequent evaporation in air using a suspension droplet on a holey carbon film supported by a copper grid.

The optical properties of the samples were analyzed with UV–vis diffuse reflectance spectroscopy, using a Hitachi 3010 spectrophotometer equipped with a 60 mm diameter integrating sphere, and $BaSO_4$ was used as a reference. The absorption data were expressed with Kubelka–Munk units using the respective equation (F(R)).

The electrochemical characterization of the samples was performed via an Autolab potentiostat (PGSTAT-302N). Photocurrent-time (I-t) characteristics were obtained at open-circuit potential, utilizing a two-electrode system and an illuminated (active) area of 3 cm^2. Platinum foil (Pt) was employed as the counter electrode. The solution used for the electrochemical measurements contained 25% v/v ethanol, 0.5 M sodium hydroxide (NaOH), and the illumination source was simulated solar light (1 sun, 1000 Wm^{-2}) from a Xenon 300 W source.

2.5. Photocatalytic Setup for Hydrogen Production and Detection

A cylindrical reactor was used, made of Pyrex glass, with carrying fittings allowing for gas inlet–outlet. The reactor was illuminated with a 300 W Xenon lamp (Oriel) and placed at a distance of 10 cm. The detection of hydrogen was realized via an SRI 8610C gas chromatograph with Ar as the carrier gas. Calibration of the gas chromatograph signal was carried out using a standard mixture of 0.25% v/v H_2 in Ar. The intensity of radiation at the position of the reactor was measured with an Oriel Radiant Power Meter. Samples were periodically collected using an automatic gas sampling valve and the exact concentration of hydrogen in the reactor effluent was measured as a function of time of illumination. For each experiment, 200 mg of the photocatalysts were dispersed in 100 mL of an aqueous solution containing a certain amount of the organic compound used as a sacrificial agent. When ethanol was used as a sacrificial agent, the concentration was 25% v/v; when glycerol was tested, the concentration was 10% v/v. The ethanol and glycerol concentrations were identified as optimal based on their performance in promoting efficient hydrogen production across various photocatalytic processes [35–43]. The reproducibility of the experiments was studied, and the results are presented in Figure S4. During all the experiments, stirring was continuous. Firstly, the solution was degassed with an Ar flow, and then the lamp was switched on.

3. Results and Discussion

3.1. Photocatalyst Characterization

The CD/TiO_2 nanocomposite photocatalysts were characterized using XRD, FT-IR, and TEM techniques. The results revealed the presence of graphitic carbon in the nanocomposite material and confirmed the uniform dispersal of the CDs on the surface of TiO_2.

The structural properties of the synthesized materials were examined through XRD analysis. The characteristic peaks of TiO_2 P25, which consists of a mixture of anatase (A) (JCPDS 21-1272) and rutile (R) (JCPDS 21-1276) nanocrystals [44], were clearly visible in both patterns, as shown in Figure 2a. More specifically, the observed diffraction peaks at 2θ: 25.24°, 27.39°, 35.90°, 36.84°, 37.72°, 38.60°, 41.10°, 48.00°, 53.91°, 55.03°, 56.66°, 62.56°, 68.87°, 70.35°, and 74.98° were assigned to the A(101), R(110), R(101), A(103), A(004), A(112), R(111), A(002), A(105), R(221), A(211), R(220), A(204), A(116), A(220), and A(215) planes, respectively [45,46]. Concerning the XRD pattern of the CD/TiO_2, the absence of the characteristic signal at 13° for the CDs [47] indicated their quantum-sized dimensions, low content, and uniform, high dispersion on the TiO_2 surface [48,49]. The results of the characterization of the synthesized materials using the FT-IR technique, used to clarify their chemical structure, are presented in Figure 2b. The broad characteristic band in the region above 3000 cm^{-1} was assigned to the water molecules absorbed on the surface and surface hydroxyl groups. FTIR spectra of the CDs and CD/TiO_2 exhibited a band around 1700 cm^{-1} indicating the presence of C=O bonds. The broad absorption band of the CD/TiO_2 nanocomposite below 1000 cm^{-1} became wider compared with that of the pure TiO_2, which was attributed to the combination of the Ti–O–Ti and Ti–O–C vibrations. It is important to note that the XRD and FT-IR results of the CD/TiO_2 presented here specifically pertain to the 3% *w*/*w* CD/TiO_2 composition. The XRD and FT-IR spectra of 1, 2, as well as 4% *w*/*w* CD/TiO_2 are presented in Figures S1 and S2, respectively.

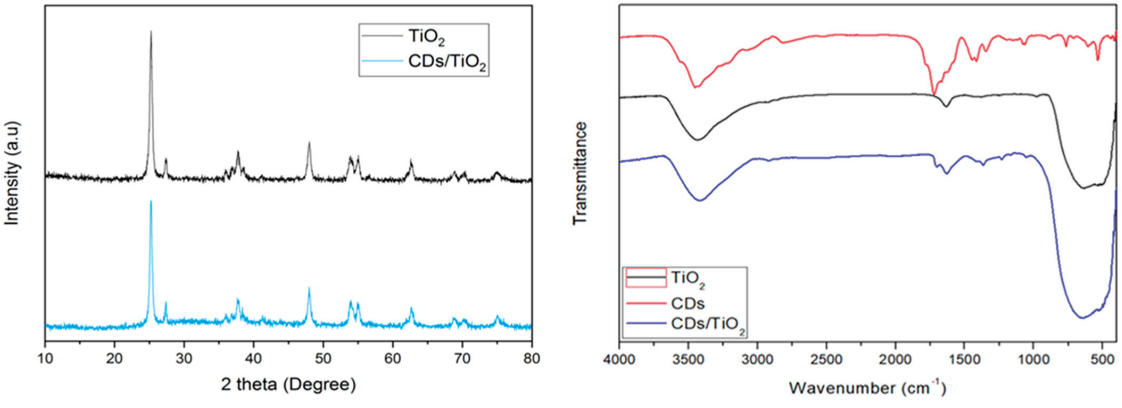

(**a**) (**b**)

Figure 2. (**a**) XRD diffraction patterns of TiO_2 and CD/TiO_2 film; (**b**) FT-IR spectra of pristine TiO_2 and the synthesized materials.

To elucidate the morphology of the CD/TiO_2 nanocomposite, HR-TEM measurement was conducted. The HR-TEM images (Figure 3) demonstrated the existence of nanoparticles with an average size less than 20 nm. Figure 3a,b demonstrate that the TiO_2 nanoparticles were rod-shaped and the CDs were well-dispersed on their surface. Lattice fringes can be clearly seen in the high-resolution image (Figure 3c,d). The spacing between the adjacent lattice fringes was measured to be 0.189 and 0.333 nm, corresponding to the interplanar distance of the (200) planes in the typical anatase phase (TiO_2) and to the (002) spacing of the graphitic carbon (CDs), respectively.

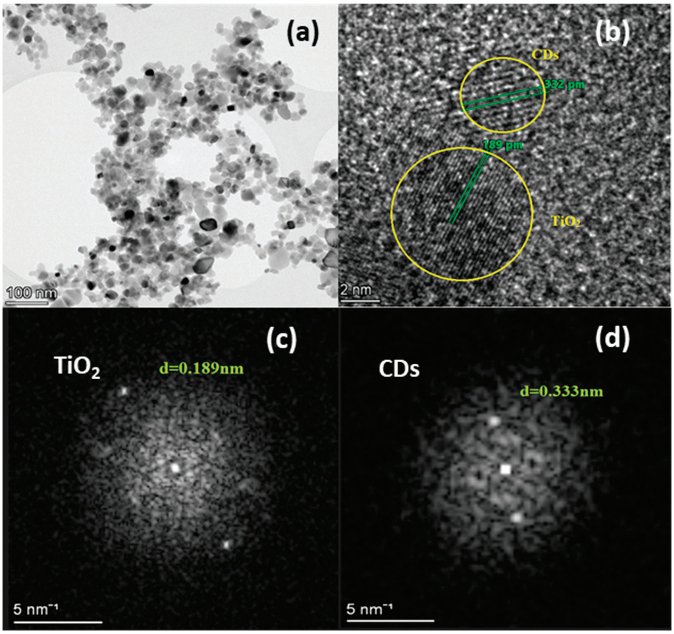

Figure 3. (**a**) TEM image of CD/TiO$_2$ nanocomposite at a magnification scale of 100 nm; (**b**) HR-TEM image of the CD/TiO$_2$ nanocomposite at a magnification scale of 10 nm, where lattice fringes of TiO$_2$ and CDs are depicted, as are fast Fourier transform (FFT) patterns of (**c**) TiO$_2$ and (**d**) CDs.

In order to study the optical properties of the nanocomposites, the DR/UV–vis spectra plotted as the Kubelka–Munk function of the reflectance F(R) versus the energy of exciting light for the samples are shown in Figure 4.

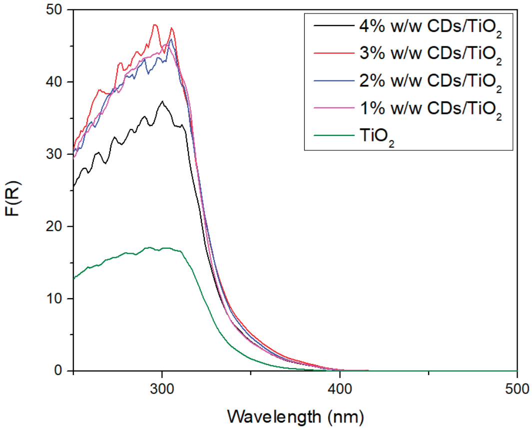

Figure 4. UV–vis/DR spectra plotted as the Kubelka–Munk function of the reflectance F(R).

The band-gap energies of the samples were estimated from the tangent lines in the plots of the modified Kubelka–Munk function [50,51]. A remarkable change in the DR/UV-vis spectra for the containing CDs could be observed, which suggested that they reflected significantly less light than the bare TiO$_2$-P25. This outcome showed great potential as it indicated an enhanced scattering of photons due the presence of CDs, leading to an improved light-harvesting efficiency. More specifically, the calculated band gaps of the samples with TiO_2, 1% *w*/*w* CD/TiO_2, 2% *w*/*w* CD/TiO_2, 3% *w*/*w* CD/TiO_2, and 4% *w*/*w* CD/TiO_2 were 3.39, 3.26, 3.24, 3.18, and 3.13 eV, respectively.

The photo-electrochemical properties of the nanocomposites deposited on the FTO electrodes were examined in 0.5 M NaOH under 1-sun illumination conditions.

To evaluate the photoelectric response of the catalysts, the transient photocurrent responses, in order to study the photocatalytic effect, were used (I-t). Figure 5 shows the photocurrent response of the CD/TiO_2 thin films of various concentrations under 1-sun illumination conditions. As expected, each of the CD/TiO_2 nanocomposites produced photocurrents upon illumination, which decreased to zero when the illumination was off. Even though the presence of CDs could improve the photocurrent response of the TiO_2, presumably due to enhancing charge separation and decreasing recombination, as shown in Figure 5, a stable but low photocurrent response, due to the quick recombination of photo-generated electrons and holes and the weak response of visible light, was presented for the samples with 1% *w*/*w* CD/TiO_2 and 2% *w*/*w* CD/TiO_2. The sample with 3% *w*/*w* CD/TiO_2 demonstrated a heightened anodic photocurrent response. This could be attributed to the increased absorption of visible light and improved charge separation, both enhanced by the higher concentration of CDs. However, a further increase in CD concentration, beyond 3% *w*/*w*, did not improve the photocurrent values (4% *w*/*w* CD/TiO_2); instead, the photocurrent density decreased. This observation suggested that an excessive CD content may block the active surface area. This was probably due to the opacity and light scattering of the CDs decreasing the absorption of the incident light. As a consequence, the photocurrent response was reduced [34].

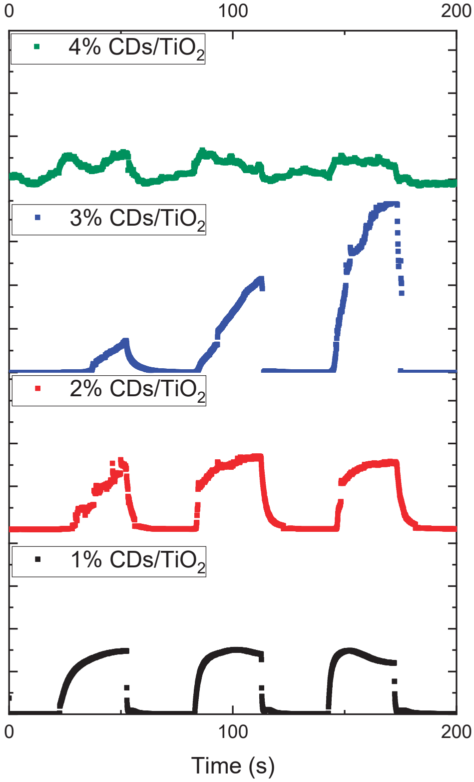

Figure 5. On–off photocurrent density–time curves of the CD/TiO_2 nanocomposites obtained at Voc in 0.5 M NaOH and 25% *v*/*v* ethanol.

3.2. Photocatalytic Hydrogen Production with Ethanol and Glycerol Reforming

Photocatalytic hydrogen generation consistently occurred in all the CD/TiO_2 photocatalysts with varying CD contents. Conversely, in the case of bare TiO_2, no hydrogen production was observed.

The temporal evolution of H_2 in the presence of CD/TiO_2 photocatalysts is shown in Figure 6. In each experiment, 200 mg of the corresponding photocatalyst was added in a 100 mL aqueous solution containing the organic substrate. In the presence of 25% *v*/*v* ethanol, the obtained data are shown in Figure 6a as a function of the CDs' percentage and reaction time. The results revealed that there was no H_2 production in the case of pure Degussa P25; however, all of the prepared nanocomposite photocatalysts exhibited satisfying hydrogen production rates. Four different loadings of CDs were tested in order to clarify which was optimal. The sample containing 3% *w*/*w* CDs demonstrated the highest H_2 production rate, reaching the value of 1.7 µmol H_2/min. In every curve, there was a section of the initial incline, representing the period required for hydrogen accumulation within the reaction mixture and its transport through the tubing to the detection area, and the peak rate, which served as an indicator of the maximum possible hydrogen production rate under the present conditions. The presence or absence of a plateau depended on the balance between the amount of photocatalysts and fuel, as well as the intensity of incident radiation.

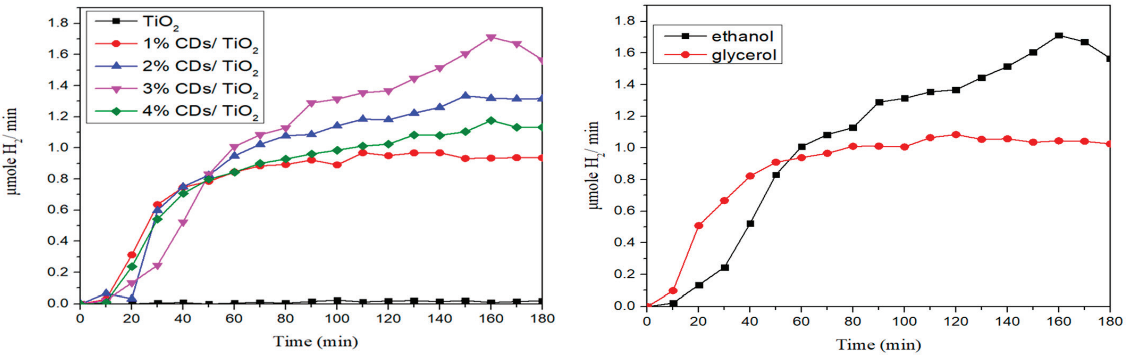

(**a**) (**b**)

Figure 6. Photocatalytic evolution of hydrogen with (**a**) ethanol reforming in the presence of CD/TiO_2 nanocomposites under 1-sun illumination and (**b**) ethanol and glycerol reforming in the presence of 3% *w*/*w* CD/TiO_2 nanocomposites under 1-sun illumination.

The nanocomposite that exhibited superior behavior in photocatalytic hydrogen production via ethanol reforming (i.e., 3% *w*/*w* CD/TiO_2) was studied using another organic substance as a sacrificial agent. The data of Figure 6b were obtained with a 10% *v*/*v* glycerol in a 100 mL aqueous solution. Following a similar experimental procedure, it was proven that the use of ethanol as a sacrificial agent exhibited better H_2 production rates than the use of glycerol. To be more precise, the maximum hydrogen production rate observed with glycerol was approximately 1.1 µmol $H_2 \cdot min^{-1}$, which was lower when compared to ethanol's rate of 1.7 µmol $H_2 \cdot min^{-1}$.

The stability and recyclability of the CD/TiO_2 photocatalysts were also investigated through the cycling experiments that are exhibited in Figure 7. More specifically, a 3% *w*/*w* CD/TiO_2 photocatalyst was used for three consecutive cycles in the presence of each sacrificial agent (ethanol and glycerol). Each cycle was carried out under the exact same conditions mentioned in Section 2.5. After each test, the photocatalyst was thoroughly washed with DI water. The recyclability study revealed that the photocatalyst exhibited consistent stability during its reuse for hydrogen production from both ethanol and glycerol. However, in both cases, there was an increment in the second cycle. This may have been due to the formation of intermediates during the process, which possibly enhanced the nanocomposite's photocatalytic activity [52]. It is worth mentioning that the XRD spectra of the CD/TiO_2 nanocomposites after the utilization of three consecutive cycles are presented in Figure S3. Based on the XRD results, there were no alterations in the crystal structure of the sample, proving the photocatalyst's high stability.

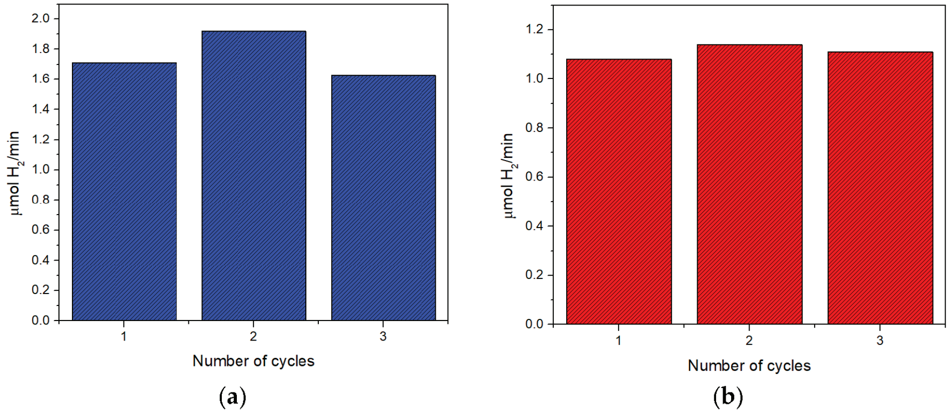

Figure 7. Recyclability tests of 3% *w*/*w* CD/TiO_2 in the presence of (**a**) 25% *v*/*v* ethanol and (**b**) 10% *v*/*v* glycerol.

Furthermore, in order to highlight the novelty and advancements of this study regarding photocatalytic hydrogen production, a survey of TiO_2-based photocatalysts within the recent literature was conducted. The comparisons between them, which is presented in Table 1, intended to clarify the contribution made within this field and distinguish the results from the existing literature.

Table 1. Comparison of TiO_2-based photocatalysts for hydrogen production in the recent literature.

Catalyst	Cocatalyst	Sacrificial Agent	Maximum Hydrogen Production Rate	Ref.
CD/TiO_2	-	25% *v*/*v* ethanol	1.7 μmol/min 102 μmol/h or 510 μmol/(h·g)	This work
	-	25% *v*/*v* methanol	9.8 μmol/h	[53]
	- Pt	0.3 M triethanolamine	472 μmol/(h·g) 1458 μmol/(h·g)	[54]
CD/g-C_3N_4/TiO_2	Pt	10% *v*/*v* triethanolamine	580 μmol/(h·g)	[55]
g-C_3N_4/TiO_2	-	20% *v*/*v* methanol	110 μmol/(h·g)	[56]
Black phosphorus quantum dot/TiO_2	-	20% *v*/*v* methanol	112 μmol/(h·g)	[57]
$MoSe_2$/TiO_2	-	30% *v*/*v* methanol	401 μmol/(h·g)	[58]
Red phosphorus/TiO_2	Pt	-	215.5 μmol/(h·g)	[59]

4. Conclusions

In summary, this work was focused on the synthesis and characterization of CD/TiO_2 nanocomposite material, as well as the evaluation of its performance in photocatalytic hydrogen production. As it is known, TiO_2 semiconductors suffer from the low utilization of visible light and a high recombination reaction rate between photogenerated electrons and holes. In order to overcome these drawbacks, its combination with CDs has been suggested. CDs, characterized by broad visible light absorption, efficient electron transfer properties, and high photostability, are among the most promising candidates for the sensitization of TiO_2 photocatalysts. Herein, a facile and novel synthetic route is presented for the first time. More specifically, a three-step process was followed for the preparation of CD/TiO_2, where CDs were first prepared with a rapid domestic microwave-assisted synthesis, followed by freeze drying. Then, a facile hydrothermal process using the as-prepared CDs and TiO_2 as precursors was conducted. The obtained CD/TiO_2 sample could be easily coated onto conductive substrates to form thin films, which could be applied in various applications. The aim of this study was the investigation of the CD concentration effect on the photocatalytic performance for hydrogen production. Therefore, four different concentrations of CDs (1% *w*/*w*, 2% *w*/*w*, 3% *w*/*w*, and 4% *w*/*w*) were evaluated. The physicochemical properties of the samples were studied via XRD, FT-IR, HR-TEM/FFT, UV–Vis, as well as photo-electrochemical measurements (I-t). More specifically, based on the XRD results, the absence of diffraction peaks in the CDs was attributed to their extremely small size and their uniform distribution onto the TiO_2 surface. Additionally, the absorption peak of 1700 cm^{-1} in the FT-IR spectra, which was attributed to the C=O stretching vibrations due to the presence of CDs in the nanocomposite material, increased when the CD concentration also increased. Regarding the morphology study of the nanocomposite, the TiO_2 nanoparticles were rod-shaped while the CDs were well-dispersed onto their surface. Moreover, it is important to note that all CD/TiO_2 samples presented decreased energy gap values compared to TiO_2; the band gap further decreased as the CD concentration rose. Similarly, the photocurrent response was enhanced as the CD concentration increased to a specific limit, where CDs could block the active surface area; this may have been due to opacity and light scattering, resulting in the decrease in incident light absorption. Finally, the performance of the as-prepared CD/TiO_2 photocatalysts containing varying amounts of CDs was evaluated in their capability to produce H_2, using green organic solvents (e.g., ethanol and glycerol) as sacrificial agents. All of the as-prepared nanocomposite photocatalysts exhibited satisfying hydrogen production rates, as opposed to the bare TiO_2. Among all the samples, the one containing 3% *w*/*w* CDs demonstrated the highest H_2 production rate reaching the value of 1.7 μmol H_2/min and 1.1 μmol H_2/min in the presence of ethanol and glycerol, respectively. The fact that the 3% *w*/*w* CD/TiO_2 exhibited the best photocatalytic performance corresponded with the photo-electrochemical measurements, as mentioned above. The high recyclability and stability of the 3% *w*/*w* CD/TiO_2 were confirmed after its utilization for three cycles reaching the value of 1.63 μmole H_2/min and 1.11 μmole H_2/min after the last cycle for ethanol and glycerol, respectively, while its crystal structure presented no alterations.

Supplementary Materials: The following supporting information can be downloaded at: https://www.mdpi.com/article/10.3390/coatings14010131/s1, Figure S1. XRD spectra of the 1% *w*/*w* CD/TiO_2, 2% *w*/*w* CD/TiO_2, and 4% *w*/*w* CD/TiO_2; Figure S2. FT-IR spectra of the 1% *w*/*w* CD/TiO_2, 2% *w*/*w* CD/TiO_2, and 4% *w*/*w* CD/TiO_2; Figure S3. XRD spectra of the 3% *w*/*w* CD/TiO_2 before and after utilization; Figure S4. Results of the 3% *w*/*w* CD/TiO_2 reproducibility in the presence of 25% *v*/*v* ethanol.

Author Contributions: Conceptualization, M.A.; methodology P.P.F., M.A. and K.V.K.; validation, P.P.F. and M.A.; formal analysis, P.P.F. and M.A.; investigation, P.P.F., M.A., A.Z., E.S. and K.V.K.; resources, P.P.F., M.A. and K.V.K.; data curation, M.A.; writing—original draft preparation, P.P.F. and A.Z.; writing—review and editing, P.P.F., M.A. and K.V.K.; visualization, P.P.F., A.Z. and M.A.; supervision, M.A. and K.V.K.; project administration, M.A.; funding acquisition, P.P.F. and M.A. All authors have read and agreed to the published version of the manuscript.

Funding: This research was funded by the Hellenic Foundation for Research and Innovation (HFRI) and the General Secretariat for Research and Technology (GSRT), under grant agreement number 2490 and the European Union's H2020 Programme iWAYS, under grant agreement number 958274.

Institutional Review Board Statement: Not applicable.

Informed Consent Statement: Not applicable.

Data Availability Statement: Data are contained within the article and supplementary materials.

Conflicts of Interest: The authors declare no conflicts of interest. The funders had no role in the design of the study; in the collection, analyses, or interpretation of data; in the writing of the manuscript; or in the decision to publish the results.

References

1. Li, Z.; Fang, S.; Sun, H.; Chung, R.J.; Fang, X.; He, J.H. Solar Hydrogen. *Adv. Energy Mater.* **2023**, *13*, 2203019. [CrossRef]
2. Zoppi, G.; Pipitone, G.; Pirone, R.; Bensaid, S. Aqueous Phase Reforming Process for the Valorization of Wastewater Streams: Application to Different Industrial Scenarios. *Catal. Today* **2022**, *387*, 224–236. [CrossRef]
3. Coronado, I.; Stekrova, M.; Reinikainen, M.; Simell, P.; Lefferts, L.; Lehtonen, J. A Review of Catalytic Aqueous-Phase Reforming of Oxygenated Hydrocarbons Derived from Biorefinery Water Fractions. *Int. J. Hydrogen Energy* **2016**, *41*, 11003–11032. [CrossRef]
4. Pitchaimuthu, S.; Sridharan, K.; Nagarajan, S.; Ananthraj, S.; Robertson, P.; Kuehnel, M.F.; Irabien, Á.; Maroto-Valer, M. Solar Hydrogen Fuel Generation from Wastewater—Beyond Photoelectrochemical Water Splitting: A Perspective. *Energies* **2022**, *15*, 7399. [CrossRef]
5. Nguyen, H.A.; Pham, T.N.; Le, N.T.T.; Huynh, L.T.N.; Nguyen, T.T.T.; Vo, Q.K.; Nguyen, T.H.; Le, V.H.; Nguyen, T.T.T.; Nguyen, T.T.; et al. Nanocomposite TiO_2@CNTs for High-Voltage Symmetrical Supercapacitor in Neutral Aqueous Media. *J. Solid State Electrochem.* **2023**, *27*, 2811–2820. [CrossRef]
6. Saleh, M.; Abdelhamid, H.N.; Fouad, D.M.; El-Bery, H.M. Enhancing Photocatalytic Water Splitting: Comparative Study of TiO_2 Decorated Nanocrystals (Pt and Cu) Using Different Synthesis Methods. *Fuel* **2023**, *354*, 129248. [CrossRef]
7. El-Bery, H.M.; Abdelhamid, H.N. Photocatalytic Hydrogen Generation via Water Splitting Using ZIF-67 Derived Co_3O_4@C/TiO_2. *J. Environ. Chem. Eng.* **2021**, *9*, 105702. [CrossRef]
8. Ren, Y.; Chen, Y.; Li, Q.; Li, H.; Bian, Z. Microwave-Assisted Photocatalytic Degradation of Organic Pollutants via CNTs/TiO_2. *Catalysts* **2022**, *12*, 940. [CrossRef]
9. Nguyen, H.P.; Cao, T.M.; Nguyen, T.T.; Van Pham, V. Improving Photocatalytic Oxidation of Semiconductor (TiO_2, SnO_2, ZnO)/CNTs for NO_x Removal. *J. Ind. Eng. Chem.* **2023**, *127*, 321–330. [CrossRef]
10. Kumaran, V.; Sudhagar, P.; Konga, A.K.; Ponniah, G. Photocatalytic Degradation of Synthetic Organic Reactive Dye Wastewater Using GO-TiO_2 Nanocomposite. *Polish J. Environ. Stud.* **2020**, *29*, 1683–1690. [CrossRef]
11. Rajoria, S.; Vashishtha, M.; Sangal, V.K. Electrochemical Treatment of Electroplating Wastewater Using Synthesized GO/TiO_2 Nanotube Electrode. *Environ. Sci. Pollut. Res.* **2023**, *30*, 71226–71251. [CrossRef]
12. Jagadeesh, B.S.; Muniyappa, M.; Navakoteswara Rao, V.; Mudike, R.; Shastri, M.; Tathagata, S.; Shivaramu, P.D.; Shankar, M.V.; Ananda Kumar, C.S.; Rangappa, D. Enhanced Photocatalytic Hydrogen Evolution from Reduced Graphene Oxide-Defect Rich TiO_{2-x} Nanocomposites. *Int. J. Hydrogen Energy* **2022**, *47*, 40242–40253. [CrossRef]
13. Liu, S.; Jiang, T.; Fan, M.; Tan, G.; Cui, S.; Shen, X. Nanostructure Rod-like TiO_2-Reduced Graphene Oxide Composite Aerogels for Highly-Efficient Visible-Light Photocatalytic CO_2 Reduction. *J. Alloys Compd.* **2021**, *861*, 158598. [CrossRef]
14. Fei, Y.; Ye, X.; Al-Baldawy, A.S.; Wan, J.; Lan, J.; Zhao, J.; Wang, Z.; Qu, S.; Hong, R.; Guo, S.; et al. Enhanced Photocatalytic Performance of TiO_2 Nanowires by Substituting Noble Metal Particles with Reduced Graphene Oxide. *Curr. Appl. Phys.* **2022**, *44*, 33–39. [CrossRef]
15. John, D.; Jose, J.; Bhat, S.G.; Achari, V.S. Integration of Heterogeneous Photocatalysis and Persulfate Based Oxidation Using TiO_2-Reduced Graphene Oxide for Water Decontamination and Disinfection. *Heliyon* **2021**, *7*, e07451. [CrossRef]
16. Ibrahim, I.; Belessiotis, G.V.; Antoniadou, M.; Kaltzoglou, A.; Sakellis, E.; Katsaros, F.; Sygellou, L.; Arfanis, M.K.; Salama, T.M.; Falaras, P. Silver Decorated TiO_2/g-C_3N_4 Bifunctional Nanocomposites for Photocatalytic Elimination of Water Pollutants under UV and Artificial Solar Light. *Results Eng.* **2022**, *14*, 100470. [CrossRef]
17. Ratshiedana, R.; Kuvarega, A.T.; Mishra, A.K. Titanium Dioxide and Graphitic Carbon Nitride–Based Nanocomposites and Nanofibres for the Degradation of Organic Pollutants in Water: A Review. *Environ. Sci. Pollut. Res.* **2021**, *28*, 10357–10374. [CrossRef]
18. Falara, P.P.; Ibrahim, I.; Zourou, A.; Sygellou, L.; Sanchez, D.E.; Romanos, G.E.; Givalou, L.; Antoniadou, M.; Arfanis, M.K.; Han, C.; et al. Bi-Functional Photocatalytic Heterostructures Combining Titania Thin Films with Carbon Quantum Dots (C-QDs/TiO_2) for Effective Elimination of Water Pollutants. *Environ. Sci. Pollut. Res.* **2023**, *30*, 124976–124991. [CrossRef]
19. Huang, X.; Sun, L.; Liu, X.; Ge, M.; Zhao, B.; Bai, Y.; Wang, Y.; Han, S.; Li, Y.; Han, Y.; et al. Increase and Enrichment of Active Electrons by Carbon Dots Induced to Improve TiO_2 Photocatalytic Hydrogen Production Activity. *Appl. Surf. Sci.* **2023**, *630*, 157494. [CrossRef]
20. Sendão, R.M.S.; Esteves da Silva, J.C.G.; Pinto da Silva, L. Photocatalytic Removal of Pharmaceutical Water Pollutants by TiO_2—Carbon Dots Nanocomposites: A Review. *Chemosphere* **2022**, *301*, 134731. [CrossRef]
21. Vyas, Y.; Chundawat, P.; Dharmendra, D.; Punjabi, P.B.; Ameta, C. Review on Hydrogen Production Photocatalytically Using Carbon Quantum Dots: Future Fuel. *Int. J. Hydrogen Energy* **2021**, *46*, 37208–37241. [CrossRef]

22. Alsalka, Y.; Al-Madanat, O.; Curti, M.; Hakki, A.; Bahnemann, D.W. Photocatalytic H_2 Evolution from Oxalic Acid: Effect of Cocatalysts and Carbon Dioxide Radical Anion on the Surface Charge Transfer Mechanisms. *ACS Appl. Energy Mater.* **2020**, *3*, 6678–6691. [CrossRef]
23. Vitiello, G.; Clarizia, L.; Abdelraheem, W.; Esposito, S.; Bonelli, B.; Ditaranto, N.; Vergara, A.; Nadagouda, M.; Dionysiou, D.D.; Andreozzi, R.; et al. Near UV-Irradiation of CuO_x-Impregnated TiO_2 Providing Active Species for H_2 Production Through Methanol Photoreforming. *ChemCatChem* **2019**, *11*, 4314–4326. [CrossRef]
24. Tang, J.H.; Sun, Y. Visible-Light-Driven Organic Transformations Integrated with H_2production on Semiconductors. *Mater. Adv.* **2020**, *1*, 2155–2162. [CrossRef]
25. Wang, L.; Geng, X.; Zhang, L.; Liu, Z.; Wang, H.; Bian, Z. Effects of Various Alcohol Sacrificial Agents on Hydrogen Evolution Based on CoS_2@SCN Nanomaterials and Its Mechanism. *Chemosphere* **2022**, *286*, 131558. [CrossRef]
26. Pantoja-Espinoza, J.C.; Domínguez-Arvizu, J.L.; Jiménez-Miramontes, J.A.; Hernández-Majalca, B.C.; Meléndez-Zaragoza, M.J.; Salinas-Gutiérrez, J.M.; Herrera-Pérez, G.M.; Collins-Martínez, V.H.; López-Ortiz, A. Comparative Study of Zn_2 Ti_3 O_8 and $ZnTio_3$ Photocatalytic Properties for Hydrogen Production. *Catalysts* **2020**, *10*, 1372. [CrossRef]
27. Muscetta, M.; Clarizia, L.; Garlisi, C.; Palmisano, G.; Marotta, R.; Andreozzi, R.; Di Somma, I. Hydrogen Production upon UV-Light Irradiation of Cu/TiO_2 Photocatalyst in the Presence of Alkanol-Amines. *Int. J. Hydrogen Energy* **2020**, *45*, 26701–26715. [CrossRef]
28. Toledo-Camacho, S.Y.; Rey, A.; Maldonado, M.I.; Llorca, J.; Contreras, S.; Medina, F. Photocatalytic Hydrogen Production from Water-Methanol and -Glycerol Mixtures Using Pd/TiO_2(-WO_3) Catalysts and Validation in a Solar Pilot Plant. *Int. J. Hydrogen Energy* **2021**, *46*, 36152–36166. [CrossRef]
29. Alvarado-Ávila, M.I.; De Luca, S.; Edlund, U.; Ye, F.; Dutta, J. Cellulose as Sacrificial Agents for Enhanced Photoactivated Hydrogen Production. *Sustain. Energy Fuels* **2023**, *7*, 1981–1991. [CrossRef]
30. Yao, Y.; Gao, X.; Li, Z.; Meng, X. Photocatalytic Reforming for Hydrogen Evolution: A Review. *Catalysts* **2020**, *10*, 335. [CrossRef]
31. Yan, Z.; Yin, K.; Xu, M.; Fang, N.; Yu, W.; Chu, Y.; Shu, S. Photocatalysis for Synergistic Water Remediation and H_2 Production: A Review. *Chem. Eng. J.* **2023**, *472*, 145066. [CrossRef]
32. Lianos, P.; Strataki, N.; Antoniadou, M. Photocatalytic and Photoelectrochemical Hydrogen Production by Photodegradation Of organic Substances. *Pure Appl. Chem.* **2009**, *81*, 1441–1448. [CrossRef]
33. Stachowska, J.D.; Murphy, A.; Mellor, C.; Fernandes, D.; Gibbons, E.N.; Krysmann, M.J.; Kelarakis, A.; Burgaz, E.; Moore, J.; Yeates, S.G. A Rich Gallery of Carbon Dots Based Photoluminescent Suspensions and Powders Derived by Citric Acid/Urea. *Sci. Rep.* **2021**, *11*, 10554. [CrossRef]
34. Yu, H.; Zhao, Y.; Zhou, C.; Shang, L.; Peng, Y.; Cao, Y.; Wu, L.Z.; Tung, C.H.; Zhang, T. Carbon Quantum Dots/TiO_2 Composites for Efficient Photocatalytic Hydrogen Evolution. *J. Mater. Chem. A* **2014**, *2*, 3344–3351. [CrossRef]
35. Antoniadou, M.; Lianos, P. Near Ultraviolet and Visible Light Photoelectrochemical Degradation of Organic Substances Producing Electricity and Hydrogen. *J. Photochem. Photobiol. A Chem.* **2009**, *204*, 69–74. [CrossRef]
36. Daskalaki, V.M.; Antoniadou, M.; Li Puma, G.; Kondarides, D.I.; Lianos, P. Solar Light-Responsive Pt/CdS/TiO_2 Photocatalysts for Hydrogen Production and Simultaneous Degradation of Inorganic or Organic Sacrificial Agents in Wastewater. *Environ. Sci. Technol.* **2010**, *44*, 7200–7205. [CrossRef]
37. Strataki, N.; Antoniadou, M.; Dracopoulos, V.; Lianos, P. Visible-Light Photocatalytic Hydrogen Production from Ethanol-Water Mixtures Using a Pt-CdS-TiO_2 Photocatalyst. *Catal. Today* **2010**, *151*, 53–57. [CrossRef]
38. Chen, W.T.; Chan, A.; Sun-Waterhouse, D.; Moriga, T.; Idriss, H.; Waterhouse, G.I.N. Ni/TiO_2: A Promising Low-Cost Photocatalytic System for Solar H_2 Production from Ethanol-Water Mixtures. *J. Catal.* **2015**, *326*, 43–53. [CrossRef]
39. Strataki, N.; Bekiari, V.; Kondarides, D.I.; Lianos, P. Hydrogen Production by Photocatalytic Alcohol Reforming Employing Highly Efficient Nanocrystalline Titania Films. *Appl. Catal. B Environ.* **2007**, *77*, 184–189. [CrossRef]
40. López-Tenllado, F.J.; Hidalgo-Carrillo, J.; Montes, V.; Marinas, A.; Urbano, F.J.; Marinas, J.M.; Ilieva, L.; Tabakova, T.; Reid, F. A Comparative Study of Hydrogen Photocatalytic Production from Glycerol and Propan-2-Ol on M/TiO_2 Systems (M = Au, Pt, Pd). *Catal. Today* **2017**, *280*, 58–64. [CrossRef]
41. Dosado, A.G.; Chen, W.T.; Chan, A.; Sun-Waterhouse, D.; Waterhouse, G.I.N. Novel Au/TiO_2 Photocatalysts for Hydrogen Production in Alcohol-Water Mixtures Based on Hydrogen Titanate Nanotube Precursors. *J. Catal.* **2015**, *330*, 238–254. [CrossRef]
42. Pajares, A.; Wang, Y.; Kronenberg, M.J.; Ramírez de la Piscina, P.; Homs, N. Photocatalytic H_2 Production from Ethanol Aqueous Solution Using TiO_2 with Tungsten Carbide Nanoparticles as Co-Catalyst. *Int. J. Hydrogen Energy* **2020**, *45*, 20558–20567. [CrossRef]
43. Romero Ocaña, I.; Beltram, A.; Delgado Jaén, J.J.; Adami, G.; Montini, T.; Fornasiero, P. Photocatalytic H_2 Production by Ethanol Photodehydrogenation: Effect of Anatase/Brookite Nanocomposites Composition. *Inorganica Chim. Acta* **2015**, *431*, 197–205. [CrossRef]
44. Kontos, A.I.; Arabatzis, I.M.; Tsoukleris, D.S.; Kontos, A.G.; Bernard, M.C.; Petrakis, D.E.; Falaras, P. Efficient Photocatalysts by Hydrothermal Treatment of TiO_2. *Catal. Today* **2005**, *101*, 275–281. [CrossRef]
45. An, X.; Liu, H.; Qu, J.; Moniz, S.J.A.; Tang, J. Photocatalytic Mineralisation of Herbicide 2,4,5-Trichlorophenoxyacetic Acid: Enhanced Performance by Triple Junction Cu-TiO_2-Cu_2O and the Underlying Reaction Mechanism. *New J. Chem.* **2015**, *39*, 314–320. [CrossRef]

46. Shaban, M.; Poostforooshan, J.; Weber, A.P. Surface-Initiated Polymerization on Unmodified Inorganic Semiconductor Nanoparticles: Via Surfactant-Free Aerosol-Based Synthesis toward Core-Shell Nanohybrids with a Tunable Shell Thickness. *J. Mater. Chem. A* **2017**, *5*, 18651–18663. [CrossRef]
47. Cheng, J.; Wang, Y.; Xing, Y.; Shahid, M.; Pan, W. A Stable and Highly Efficient Visible-Light Photocatalyst of TiO_2 and Heterogeneous Carbon Core-Shell Nanofibers. *RSC Adv.* **2017**, *7*, 15330–15336. [CrossRef]
48. Guo, Y.; Zhang, L.; Liu, X.; Li, B.; Tang, D.; Liu, W.; Qin, W. Synthesis of Magnetic Core-Shell Carbon Dot@MFe_2O_4 (M = Mn, Zn and Cu) Hybrid Materials and Their Catalytic Properties. *J. Mater. Chem. A* **2016**, *4*, 4044–4055. [CrossRef]
49. Zeng, X.; Wang, Z.; Meng, N.; McCarthy, D.T.; Deletic, A.; Pan, J.H.; Zhang, X. Highly Dispersed TiO_2 Nanocrystals and Carbon Dots on Reduced Graphene Oxide: Ternary Nanocomposites for Accelerated Photocatalytic Water Disinfection. *Appl. Catal. B Environ.* **2017**, *202*, 33–41. [CrossRef]
50. Rangel-Mendez, J.R.; Matos, J.; Cházaro-Ruiz, L.F.; González-Castillo, A.C.; Barrios-Yáñez, G. Microwave-Assisted Synthesis of C-Doped TiO_2 and ZnO Hybrid Nanostructured Materials as Quantum-Dots Sensitized Solar Cells. *Appl. Surf. Sci.* **2018**, *434*, 744–755. [CrossRef]
51. Shathy, R.A.; Fahim, S.A.; Sarker, M.; Quddus, M.S.; Moniruzzaman, M.; Masum, S.M.; Molla, M.A.I. Natural Sunlight Driven Photocatalytic Removal of Toxic Textile Dyes in Water Using B-Doped ZnO/TiO_2 Nanocomposites. *Catalysts* **2022**, *12*, 308. [CrossRef]
52. Divyasri, Y.V.; Lakshmana Reddy, N.; Lee, K.; Sakar, M.; Navakoteswara Rao, V.; Venkatramu, V.; Shankar, M.V.; Gangi Reddy, N.C. Optimization of N Doping in TiO_2 Nanotubes for the Enhanced Solar Light Mediated Photocatalytic H_2 Production and Dye Degradation. *Environ. Pollut.* **2021**, *269*, 116170. [CrossRef]
53. Shi, R.; Li, Z.; Yu, H.; Shang, L.; Zhou, C.; Waterhouse, G.I.N.; Wu, L.Z.; Zhang, T. Effect of Nitrogen Doping Level on the Performance of N-Doped Carbon Quantum Dot/TiO_2 Composites for Photocatalytic Hydrogen Evolution. *ChemSusChem* **2017**, *10*, 4650–4656. [CrossRef]
54. Sargin, I.; Yanalak, G.; Arslan, G.; Patir, I.H. Green Synthesized Carbon Quantum Dots as TiO_2 Sensitizers for Photocatalytic Hydrogen Evolution. *Int. J. Hydrogen Energy* **2019**, *44*, 21781–21789. [CrossRef]
55. Hu, Z.; Shi, D.; Wang, G.; Gao, T.; Wang, J.; Lu, L.; Li, J. Carbon Dots Incorporated in Hierarchical Macro/Mesoporous g-C_3N_4/TiO_2 as an All-Solid-State Z-Scheme Heterojunction for Enhancement of Photocatalytic H_2 Evolution under Visible Light. *Appl. Surf. Sci.* **2022**, *601*, 154167. [CrossRef]
56. Girish, Y.R.; Udayabhanu; Alnaggar, G.; Hezam, A.; Nayan, M.B.; Nagaraju, G.; Byrappa, K. Facile and Rapid Synthesis of Solar-Driven TiO_2/g-C_3N_4 Heterostructure Photocatalysts for Enhanced Photocatalytic Activity. *J. Sci. Adv. Mater. Devices* **2022**, *7*, 100419. [CrossRef]
57. Guan, R.; Wang, L.; Wang, D.; Li, K.; Tan, H.; Chen, Y.; Cheng, X.; Zhao, Z.; Shang, Q.; Sun, Z. Boosting Photocatalytic Hydrogen Production via Enhanced Exciton Dissociation in Black Phosphorus Quantum Dots/TiO_2 Heterojunction. *Chem. Eng. J.* **2022**, *435*, 135138. [CrossRef]
58. Shi, F.; Xing, C.; Wang, X. Preparation of TiO_2/$MoSe_2$ Heterostructure Composites by a Solvothermal Method and Their Photocatalytic Hydrogen Production Performance. *Int. J. Hydrogen Energy* **2021**, *46*, 38636–38644. [CrossRef]
59. Huang, G.; Ye, W.; Lv, C.; Butenko, D.S.; Yang, C.; Zhang, G.; Lu, P.; Xu, Y.; Zhang, S.; Wang, H.; et al. Hierarchical Red Phosphorus Incorporated TiO_2 Hollow Sphere Heterojunctions toward Superior Photocatalytic Hydrogen Production. *J. Mater. Sci. Technol.* **2022**, *108*, 18–25. [CrossRef]

coatings

MDPI

Article

Monitoring Aging Effects in Graphite Bisulfates by Means of Raman Spectroscopy

Carlo Camerlingo [1,*,†], Marcella Salvatore [2,3] and Gianfranco Carotenuto [4]

[1] CNR-SPIN, Institute for Superconductors, Innovative Materials and Devices, S.S. Napoli, Via Campi Flegrei 34, 80078 Pozzuoli, Italy
[2] Dipartimento di Fisica "Ettore Pancini", Università degli Studi di Napoli Federico II, Complesso Universitario Monte S. Angelo, Via Cinthia, 80126 Napoli, Italy; marcella.salvatore@unina.it
[3] Centro Servizi Metrologici e Tecnologici Avanzati (CeSMA), University of Naples "Federico II", Complesso Universitario San Giovanni, Corso Nicolangelo Protopisani, 80146 Naples, Italy
[4] CNR-IPCB, Institute for Polymers, Composites and Biomaterials, P.le E. Fermi, 1, 80055 Portici, Italy; gianfranco.carotenuto@cnr.it
[*] Correspondence: carlo.camerlingo@cnr.it
[†] Retired since 1 August 2023.

Abstract: Graphite bisulfate (GBS) compounds consist of graphite layers intercalated by HSO_4^- ions and H_2SO_4 molecules. Owing to electrostatic interactions with the graphene plane, HSO_4^- ions cause point defects in the graphite's crystalline structure, while H_2SO_4 molecules are free to move via diffusion in the spaces between the adjacent graphite sheets and segregate to form linear defects. In the present work, we report the results of our investigation using Raman spectroscopy on the temporal evolution of such defects on selected GBS samples over 84 months. Two characteristic lengths correlated with the average distance between defects have been estimated and their evolution with aging was investigated. The results show a decrease in the density of point-like defects after aging, regardless of the pristine structural configuration of the GBS samples, revealing a structural instability. This study can provide significant information for the technological development of industrial processes aimed to produce expanded graphite based on GBS precursors, where the aging of GBS is known to influence the efficiency and quality.

Keywords: graphite bisulfate; graphite intercalation; aging effects

Citation: Camerlingo, C.; Salvatore, M.; Carotenuto, G. Monitoring Aging Effects in Graphite Bisulfates by Means of Raman Spectroscopy. *Coatings* **2024**, *14*, 101. https://doi.org/10.3390/coatings14010101

Academic Editor: Dimitrios Tasis

Received: 7 December 2023
Revised: 5 January 2024
Accepted: 11 January 2024
Published: 12 January 2024

1. Introduction

Sealing components (e.g., gaskets, o-rings), resistant to high temperatures, chemically inert and thermally conductive, are mostly made of pure graphite. Frequently, these mechanical components have a very complex shape (e.g., engine gasket units) and consequently their manufacturing is difficult. The method typically used to fabricate these pure-graphite components with a complex geometry is based on compacting by pressing a special type of highly porous and disordered graphite filament known as 'expanded graphite', which is prepared from the graphite bisulfate compound ($C_{48}H_{206}O_{28}S_7$). Graphite bisulfate represents the most important of the available graphite intercalation compounds (GICs). It was prepared for the first time by Brodie in the 1855 by oxidizing graphite flakes with concentrated nitric acid (HNO_3, 65% in water) in the presence of sulfuric acid (H_2SO_4) [1]. The chemical process developed by Brodie included both an oxidating reaction of the graphite crystal by HNO_3 and the insertion of sulfuric acid molecules (H_2SO_4) uniformly among the graphite crystal sheets. However, since nitric acid oxidizes graphite to graphite cations (graphonium ions), HSO_4^- ions are also as a result inserted into the crystal in order to balance the positive charges generated in the graphite crystal. Therefore, graphite bisulfate has both an ionic nature and a covalent nature, which are the two possible classes of intercalation compounds. The presence of a strong oxidizer

(HNO_3) has a key role in this chemical process, because the oxidized edges of the graphite crystals, rich in large oxygen-containing species like carboxyl (-COOH), formyl (-CHO), and hydroxyl (-OH) groups, allow the molecular/ionic molecules (H_2SO_4 and HSO_4^-) to permeate in the crystal, with formation of graphite/H_2SO_4/HSO_4^- solid solutions. Nitric acid can be replaced by other types of strong oxidizers like potassium permanganate ($KMnO_4$), potassium dichromate (KCr_2O_7), oxygen peroxide (H_2O_2), sodium perchloride ($NaClO_3$), sodium periodate ($NaIO_4$), etc.; however, the expanding capability and the stability of the achieved graphite bisulfate products are generally much lower than the product obtained by HNO_3 oxidation. Expanded graphite, processable by compacting with pressing, is obtained via thermal treatment (thermal shock) of graphite bisulfate. During this thermal treatment, H_2SO_4 molecules present in the graphite crystal react with the nearest carbon atoms of graphite sheets, producing a gaseous mixture of carbon dioxide, sulfur dioxide, and moisture that, when violently released from the layered structure of the graphite crystal, causes significant expansion. In particular, the intercalating agent and graphite react according to the following scheme: $C + 2H_2SO_4 = CO_2 + 2SO_2 + 2H_2O$. Obviously, a low percentage of lattice defects (vacancies) randomly distributed in the graphite sheets is simultaneously generated by this chemical reaction. Expanded graphite is very useful as a precursor of many other industrial products derived from graphite like graphite nanoplatelets, graphene oxide (GO), few-layer graphene (semi-graphene), single-layer graphene, graphene aerogels, thermally reduced graphene (TRG), chemically reduced graphene (CRG), etc. Most of these materials are prepared by exfoliation of the expanded graphite filaments by using sono-acoustic energy (ultrasound). In particular, a high-intensity sonication treatment is applied to expanded graphite dispersed in a liquid medium (e.g., acetone). The resulting graphite nanocrystal thickness depends on the degree of intercalation, which is usually expressed by a ‘staging’ index (i.e., number of graphite layers contained between two intercalated layers; for example, in a stage I compound, a single layer of graphene regularly alternates with intercalated species). The staging index depends on the quality of the graphite bisulfate and therefore on the sulfuric acid concentration and the type of oxidizing agent involved in the reactive system; however, it also depends on the aging time. Indeed, freshly prepared stage I graphite bisulfate has a very strong ability to expand by the effect of a thermal shock, but such a phenomenon reduces in intensity with the aging of this chemical product. An investigation of the graphite bisulfate aging process could provide significant information for the technological development of industrial processes based on this type of compound, since its ability to expand is strongly influenced by the time elapsed since its preparation. Indeed, GBS compounds and most GICs are not stable in air, water, or organic media [2,3]. The configuration assumed by intercalation substances and the defects induced in the graphene layers influence the free energies of formation of the lamellar structure [4] and, consequently, the process of expansion.

The aging effects on HNO_3 intercalation graphite have been investigated before by E. J. Samuelsen et al. [5]. They observed a change in staging, the disappearance of the intermediate crystalline phase, and the growth of a new ordered phase over a period of 5 months. These changes are related to the thermal settling of the graphite crystals and defect configuration changes. A study of aging effects over a longer time could give interesting information from a basic and applicative point of view. As far as we know, no similar works are present in the literature. This lack of information motivates us to monitor the aging effects in GBS for considerably longer times. In the present paper, we report the results of our investigation on aging effects in GBS for a time period of 84 months. For this purpose, we fabricated GBS by reacting graphite flakes with an oxidizing agent/sulfuric acid mixture, as described in detail in ref. [6]. Seven different oxidizing agent/sulfuric acid mixtures have been used. The graphite bisulfate samples were periodically monitored by micro-Raman spectroscopy over a period of 84 months. Raman spectroscopy provides an efficient method to characterize graphene and graphite-based materials [6–11]. Indeed, information on defect configurations can be inferred from a Raman spectral analysis [12,13]. In GBS compounds, HSO_4^- ions cause point defects in the graphite crystalline structure.

These defects are localized; indeed, they cannot move from the lattice positions where they originate. Differently, H_2SO_4 molecules are free to move by diffusion in the space between the adjacent graphite crystallographic planes and segregate mostly at the crystal edges to maximize all physical interactions, allowing the formation of a network of linear defects in the graphite matrix structure [4,14].

2. Materials and Methods

Graphite bisulfates were synthesized from graphite flakes by using seven different oxidizing agent/sulfuric acid mixtures: nitric acid, potassium nitrate, potassium dichromate, potassium permanganate, sodium periodate, sodium chlorate, and hydrogen peroxide (see the list in Table 1). The reactions were performed under thermostatic conditions, using a 9:1 parts by volume H_2SO_4/oxidizing agent ratio with a reaction time of 1 h. Constant quantities of graphite flakes (2 g, Aldrich, >100 mesh) and sulfuric acid (40 mL) and molar amounts of oxidizing agent were used. Preparation details are reported in ref. [6]. The samples were periodically characterized by micro-Raman spectroscopy over a time period of 84 months. Visible Raman spectroscopy was used employing a 17 mW He-Ne laser source (wavelength 632.8 nm). The apparatus was a Jobin-Yvon system from Horiba ISA, with a Triax 180 monochromator equipped with a liquid-nitrogen-cooled charge-coupled detector. The grating of 1800 grooves/mm allows for a final spectral resolution of 4 cm^{-1}. The spectra were recorded in air at room temperature with an acquisition time of 120 s. A 100× optical objective was used to collect the signal in an area size of ca. 2 μm. Spectral data were analyzed numerically using the best-fitting routine in GRAMS/AI (2001, Thermo Electron, Waltham, MA, USA) to model the spectra by an overlap of Lorentzian functions. This allowed us to determine the main vibrational modes occurring in the Raman signal and to estimate their parameters, namely the centers, widths, and intensities of the spectral peaks.

Table 1. Raman spectroscopy data of GBS compounds measured before aging (0 months).

Sample	Oxidizing Agent	E_g Band (cm^{-1})		2D Band (cm^{-1})	
		G Mode	G_b Mode	$2D_1$	$2D_2$
A	HNO_3	1581	1602	2646	2681
B	$NaClO_3$	1580	1603	2637	2681
C	$NaIO_4$	1585	1608	2659	2681
D	$KMnO_4$	1580	–	2634	2680
E	$K_2Cr_2O_7$	1580	1599	2644	2681
F	H_2O_2	1580	–	2642	2681
G	KNO_3	1579	1596	2644	2681
graphite flakes	–	1582	–	2641	2681

3. Results

The Raman spectrum of GBS sample A (HNO_3) is reported in Figure 1 and is compared with the Raman spectrum of pristine graphite. The spectrum of graphite is dominated by a strong peak at 1582 cm^{-1}, which is related to the E_g degenerated vibrational modes of carbon atoms (G mode). The occurrence of intercalation layers in the graphite modifies this peak and splits it into two modes, which are assigned to displacements of carbon atoms belonging to internal layers of stacking regions and to stacking boundary layers, respectively. The G mode related to interior layer phonons is centered at ca. 1580 cm^{-1}, similar to graphite, while the position of the G_b mode due to boundary layer phonons is at a higher wavenumber, depending on the stacking order [10,11]. The split of the G peak is clearly shown in Figure 1a. Two modes occur at 1602 cm^{-1} and 1581 cm^{-1} in the spectrum of A (HNO_3) (i), while a single peak centered at 1582 cm^{-1} is observed in the spectrum of graphite flakes (ii). A list of the position of these modes is reported in Table 1 for GBS compounds that were produced with different oxidizing agents. In the case of samples D ($KMnO_4$), F (H_2O_2), and G (KNO_3), the split of the E_g mode is negligible, and the signal can be modeled by a single peak centered at about 1581 cm^{-1}. The thermogravimetric analysis (TGA) reported in ref. [6] has confirmed a relatively low intercalation degree for these GBS compounds as the weight loss percentages during TGA are lower than 10% while values were estimated in the 17%–52% range for the weight loss percentages of the remaining GBS compounds. In the case of sample A (HNO_3), the measured weight loss was 17%. The D mode located at about 1334 cm^{-1} originates from edge or discontinuities in the carbon lattice, where translational symmetry is broken, and it is usually associated with structural defects occurring in the graphite [8,15]. This mode is relatively weak in the flakes of pure graphite (spectrum (ii) in Figure 1a) but becomes more intense in the GBS spectrum (spectrum (i) in Figure 1a) because of the bounding surface increase and an expected larger number of defects. The second order of this mode (2D band) is observable in the high wavenumber region of the Raman spectrum at about 2640 cm^{-1}. The D and 2D modes are dispersive bands, and hence, their actual position and intensity depend on the laser excitation energy [8]. In Figure 1b, the broad bands assigned to 2D modes of the sample A (KNO_3) (i) and graphite flakes (ii) are shown. The spectrum of graphite flakes (ii) is characterized by two main peaks ($2D_1$ and $2D_2$) centered at 2641 cm^{-1} and 2681 cm^{-1}, respectively. Two further weaker components occur at 2611 cm^{-1} and 2710 cm^{-1}. These features are consistent with the Raman response of graphite, where a double resonance process involving a link between phonons and the electronic band structure is expected. Indeed, the four components of the 2D band are related to a splitting of the graphite electron bands [8]. The position of the $2D_1$ mode in the GBS spectrum (spectrum (i) in Figure 1b) is 2646 cm^{-1}, slightly higher than in the graphite flake spectrum, and its relative intensity concerning the $2D_2$ mode increases, thus indicating a change in the electronic structure related to a modified stacking configuration, in agreement with the behavior exhibited by multilayer graphene [8]. A list of the $2D_1$ and $2D_2$ mode positions in GBS compounds produced with different oxidizing agents is reported in Table 1. The position of the $2D_2$ modes does not change, while the centers of the $2D_1$ mode vary in the range of 2637–2659 cm^{-1} depending on the fabrication process. Aging of the samples implies some changes in the Raman spectroscopy response due to structural readjustments of intercalation components inside the stacked layered structure of GBS compounds. The Raman spectra of sample A (KNO_3) over time are reported in Figure 2 for the spectral ranges of 1200–1800 cm^{-1} (Figure 2a) and 2500–2775 cm^{-1} (Figure 2b). Raman acquisitions were performed on a pristine sample after 3, 12, 14, 20, 30, 61, and 84 months, as indicated in Figure 2. The split of the G band is clearly visible in almost all spectra, with component modes centered at 1602 cm^{-1} and 1581 cm^{-1} (Figure 2a). Their relative intensity changes with aging. Indeed, the intensity of the mode assigned to the vibration of bounding layer atoms (at 1602 cm^{-1}) initially increases with respect to the peak at 1581 cm^{-1}, reaching a maximum in the spectrum measured after 20 months of aging, gradually decreasing afterwards. A less regular dependence on the intensity of the D mode is observed, but a clear decrease in the intensity is visible in the last two spectra, for aging times longer than 61 months. In the higher region of the spectrum (Figure 2b), the spectra are characterized by two main peaks, which are centered at 2641 cm^{-1} and 2681 cm^{-1}. Starting from the spectrum collected after 30 months of aging, a gradually broadening of the modes occurs and their energy is lowered, particularly relevant for the $2D_1$ peak initially centered at 2641 cm^{-1}, which moves to 2636 cm^{-1}. In general, the effects of aging on the Raman responses are qualitatively similar in all the GBS compounds considered. However, in the case of sample B ($NaClO_3$), the intensity of the D mode is higher and the peaks are broader than in the other samples (see Figure S1). The dependence of the area ratio of the G and G_b peaks and of the area ratio of the D and G modes is reported in Figure S2a and S2b, respectively. The G_b mode component increases in the first aging period and reaches a maximum after about 14–20 months, after which it decreases in intensity. The behavior shown by different samples can be ascribed to a relocation of the defects inside the graphene layers with aging, which affects the Raman response of the material. As inferred in Figures 2 and S2, the D and 2D mode intensities have a non-monotonic dependence on the aging time, indicating a reduction in the punctual defects in graphene layers after an initial increase in their density during the first 30 months. This process also influences the strain of the graphene layers inside and, more significantly, at the boundary of the stacking regions of the GBS, as inferred from the time dependence of the relative intensity of the G and Gb modes. A relaxation of the graphene lattice is inferred after aging, which can be ascribed to a segregation of moving intercalating components at the graphite grain boundaries.

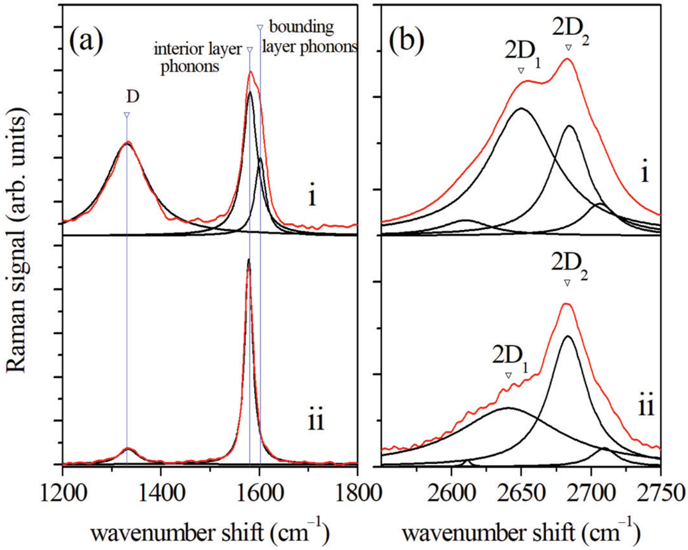

Figure 1. Raman spectrum of GBS A (HNO_3) (i) and of graphite flakes (ii) in the wavenumber range of 1100–1800 cm^{-1} (**a**) and 2450–2750 cm^{-1} (**b**), respectively. Red lines represent the experimental data and the black lines represents the modes which have been determined by the fit of the signal with an overlap of Lorentzian peaks. The spectroscopy data refer to pristine samples.

The influence of aging on the Raman spectroscopy response of GBS compounds can be related to the configuration of defects in the samples and their modification occurring over time due to thermal relaxation mechanisms. Similarly to graphene, two kinds of lattice defects can occur in the graphite intercalation layers: point-like defects generated by lattice vacancies or chemical effects and extended defects, which are related to edge effects, appearing as strain, dislocations, or discontinuities at crystal grain borders [16].

Instead, the neutral molecules of the intercalant H_2SO_4 can indeed move by thermal diffusion in the spaces between the adjacent graphite stacks and segregate to maximize all physical interactions. This allows the formation of aggregates that electrostatically interact with external layers of the graphite stacking structures, locally deforming them and inducing linear-like defects. The observed splitting of the E_g band in the two G and G_b modes depends on the extent of the influence of these defects on the Raman response.

The defects induce disorder in the system that can be accounted for by two characteristic lengths, L_D and L_a, which are correlated with the average distance between defects. The parameter L_D is related to point-like defects, while L_a takes into account the extended defects at the grain borders. L. G. Cançado et al. proposed a method to distinguish the contributions of the two kinds of defects in graphene via Raman spectroscopy and estimate L_D and L_a from the A_D/A_G ratio of the peak areas of the D and G modes and the Γ_G

peak width of the E_G mode [13]. The A_D/A_G ratio gives an indication of the relevance of point-like defects in the graphene layers because the Raman D mode is related to light scattering events enabled by defects and is not allowed in defect-free graphene.

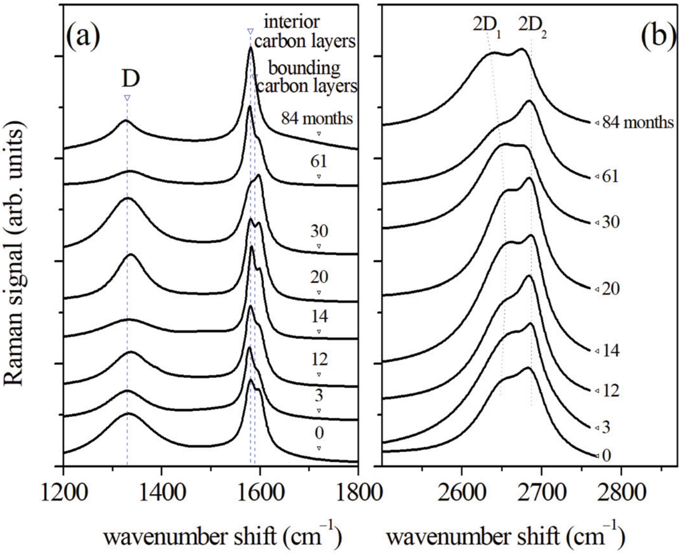

Figure 2. Sample A (HNO_3): dependence of the Raman spectrum on the aging time in the spectral ranges of 1200–1800 cm^{-1} (**a**) and 2500–2800 cm^{-1} (**b**), respectively.

Depending on the light excitation energy E_L, the A_D/A_G ratio and Γ_G values are correlated, because both are a function of L_D and L_a.

Indeed, Γ_G is given by:

$$\Gamma_G(L_D, L_a) = \Gamma_G(\infty) + C_\Gamma e^{-\frac{\xi}{l_{ph}}} \tag{1}$$

where ξ is the phonon localization length, l_{ph} is the phonon coherence length, $\Gamma_G(\infty)$ is the peak width of the material without defects, and C_Γ is a constant. The A_D/A_G ratio is calculated as:

$$\begin{aligned} \frac{A_D}{A_G} E_L^4 = C_S^{0D} \left(1 - e^{-\frac{\pi r_S^2}{L_D^2}}\right) + 4C_S^{1D} l_S \frac{(L_a - l_S)}{L_a^2} e^{-\frac{\pi r_S^2}{L_D^2}} + \\ 2\pi C_A^{0D} l_c \frac{(L_a + r_S)}{L_D^2} \left[1 + 4 l_S \frac{(L_a - l_S)}{L_a^2}\right] e^{-\frac{\pi r_S^2}{L_D^2}} + 2C_A^{1D} l_c \frac{(L_a - 2l_S)}{L_a^2} \left(1 - e^{\frac{(L_a - 2l_S)}{l_c}}\right) e^{-\pi \frac{r_S^2}{L_D^2}} \end{aligned} \tag{2}$$

where C_S^{0D}, C_S^{1D}, C_A^{0D}, and C_S^{1D} are constants, l_c is the electron coherence length, and r_S and l_s are the sizes of point and extended defects, respectively. We extended this approach to the intercalated graphite samples, considering the G mode of the Raman response (1581 cm^{-1} peak) in the analysis, which is related to carbon interlayers. We used the parameter values adopted in ref. [13] to model the A_D/A_G ratio's dependence on Γ_G ($\Gamma_G(\infty)$ = cm^{-1} l_{ph} = 16 nm; l_c = 4.1 nm; l_S = 2 nm; l_e = 3.7 nm; and r_S = 2.2 nm). Similarly, a small value of between $\xi = L_a$ and $\xi = 10\ L_D$ was assumed for the phonon localization length, depending on the kind of defect which is dominant out of point-like and extended defects. The experimental values of the $A_D/A_G(E_L)^4$ ratio vs. Γ_G are reported in Figure 3, where E_L = 1.96 eV is the photon energy of the laser excitation beam. The data refer to sample A (HNO_3) which was characterized by Raman spectroscopy before aging (black circles in Figure 3) and after 84 months of aging (red circles in Figure 3). The Raman acquisitions were performed at different positions of the GBS surface. In Figure 3, the spread of $A_D/A_G(E_L)^4$ ratio values is relatively large, and no significant variation between the initial and aged state is noticed. In fact, the average values are $A_D/A_G(E_L)^4 = 34.5 \pm 12.7$ eV^4 for the pristine sample and $A_D/A_G(E_L)^4 = 27.9 \pm 12.8$ eV^4 for the aged one. These data were compared with the $A_D/A_G(E_L)^4$ dependence on Γ_G calculated via Equations (1) and (2). A good match with the experimental data can be obtained by setting $L_a = 28$ nm and $L_D = 13.3$ nm for the pristine state and $L_a = 43$ nm and L_D=14.8 nm after aging. The curves in Figure 3 refer to the model-predicted dependence for values of $L_D = 13.3$ nm (black curve) and $L_D = 14.8$ nm (red curve) and variable L_a values. This suggests an increase in the Raman scattering homogeneity due to larger sizes and more relaxed grains. This feature is compatible with a segregation of mobile intercalating components to the grain boundaries and an increase in the regularity of the stacked boundary layers. A similar behavior was observed in the remaining samples. In Figure 4, the average values of $A_D/A_G(E_L)^4$ and Γ_G data are reported, referring to GBS compounds produced with $NaClO_3$ (sample B, black dots), $NaIO_3$ (sample C, red dots), $KMnO_4$ (sample D, blue dots), and H_2O_2 (sample F, green dots). Full dots refer to pristine samples, while data collected after the aging are plotted with empty circles. As a reference, the trend predicted by the model for the dependence of $A_D/A_G(E_L)^4$ on Γ_G (Equation (2)) is reported in Figure 4 for fixed L_D values of 11.4 nm (black line), 18 nm (red line), and 30 nm (blue line) and a variable L_a. In Figure 4, a larger variation with aging is observed in sample B. Both the $A_D/A_G(E_L)^4$ ratios and Γ_G decrease with aging as in the case of sample A (Figure 3). These spectroscopy data are compatible with a relatively high density of point defects because they can be modeled by relatively low L_D parameters. The values of L_D and L_a were estimated by a numerical fit of the data with Equation (2). A moderate increase in L_D from 11 ± 1 nm to 13 ± 1 nm is demonstrated with aging. The change in Γ_G values, and consequently in L_a, is more relevant, reflecting a relaxation of the graphite grains. In such a case, both point-like and linear defects weakly evolve towards a clean configuration. The defect density in sample C is lower than in sample B and a larger L_D of 17 ± 1 nm was estimated in the initial state. In this case, aging weakly influences the defect configuration, even if a trend towards a decrease in the defect density is inferred, mainly concerning L_D and point-like defects. Samples D and F are characterized by a low density of defects, but a significant increase in L_D is exhibited after aging also in these cases.

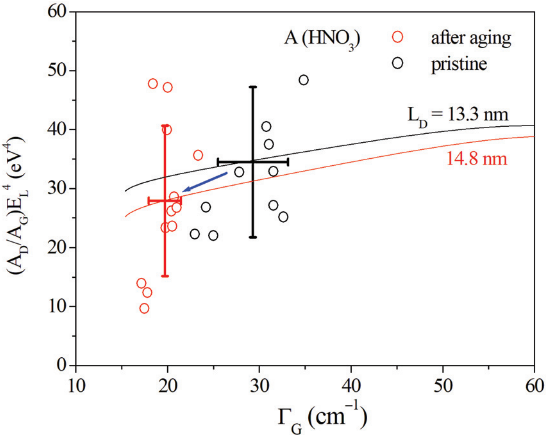

Figure 3. Effects of the aging on the area ratio of D and G modes ($A_D/A_G(E_L)^4$) (E_L = 1.96 eV) and the width of G peak (Γ_G) of sample A (HNO_3). Red circles refer to data collected at 84 months after the data reported with black circles. The curves were calculated using the model of L. G. Cançado et al. [13] for L_D = 13.3 nm (black curve) and L_D = 14.8 nm (red curve), and a variable L_a.

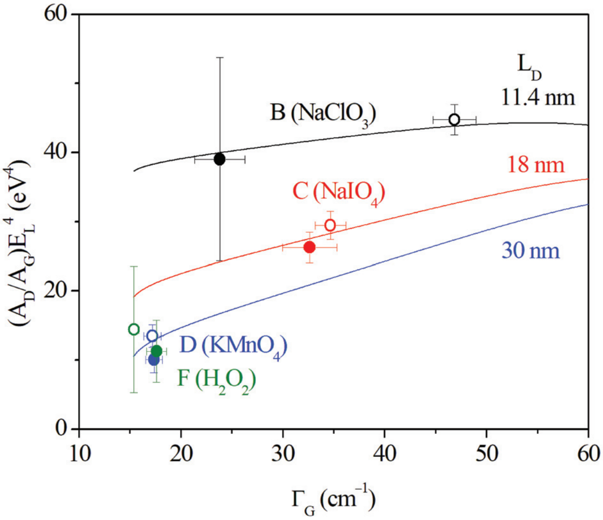

Figure 4. Effects of aging on the area ratio of D and G modes (A_D/A_GE_L) and the width of G peak (Γ_G). The data refer to GBS compounds produced with different oxidation agents, namely $NaClO_3$ (sample B, black dots), $NaIO_4$ (sample C, red dots), $KMnO_4$ (sample D, blue dots), and H_2O_2 (sample F, green dots). Full dots refer to data collected at 84 months after the data reported with empty circles. As a reference, the trend predicted by the model for the dependence of $A_D/A_G(E_L)^4$ on Γ_G (Equation (2)) is reported in the figure for a fixed L_D of 11.4 nm (black line), 18 nm (red line), and 30 nm (blue line) and a variable L_a.

Samples E ($K_2Cr_2O_7$) and G (KNO_3) are not shown in Figure 4, but their behavior is similar to that of samples D and F, with a relatively high L_D value correlated with a relatively low density of point defects. A list of the estimated L_a and L_D parameters before and after aging is reported in Table 2. A list of experimental $A_D/A_G(E_L)^4$ and Γ_G values far all the GBS compounds investigated is reported in Table S1 in the Supplementary Materials. In general, L_a does not change significantly or slightly increases with aging but, in the case of sample F, L_a decreases from 78.0 nm to 57.3 nm, indicating a relocation of extended defects.

Table 2. Aging and defect characterization.

Sample	Oxidizing Agent	L_D (nm)		L_a (nm)	
		Pristine	After Aging	Pristine	After Aging
A	HNO_3	14 ± 1	15 ± 1	28 ± 2	43 ± 1
B	$NaClO_3$	11 ± 1	13 ± 1	16± 1	37 ± 1
C	$NaIO_4$	17 ± 1	19 ± 1	24 ± 1	26 ± 1
D	$KMnO_4$	26 ± 1	52 ± 4	63 ± 1	58 ± 2
E	$K_2Cr_2O_7$	22 ± 2	33 ± 4	>80	>80
F	H_2O_2	22 ± 7	53 ± 8	78 ± 1	57 ± 2
G	KNO_3	59 ± 13	>80	46 ± 2	>80

4. Discussion

In GBS compounds, localized point-like defects in the graphite crystalline structure can be generated by HSO_4^- ions which interact electrostatically with graphene layers, while H_2SO_4 molecules form a network of linear defects in the graphite matrix structure. Neutral molecules can indeed move via diffusion in the spaces between the adjacent graphite crystallographic planes and segregate to maximize all physical interactions. As the oxidized and intercalated graphite crystals are separated from the liquid reaction medium where they were generated (i.e., H_2SO_4+HNO_3 65%), they become unstable systems. Such crystal instability causes a progressive segregation of the mobile intercalating molecules (H_2SO_4) at the boundaries of the crystal and therefore on the external crystal surface. The intercalated graphite crystal has a polycrystalline nature; indeed, the structure of an intercalated crystal can be described as a system of small crystallites separated by defective regions that are centered on the intercalating molecules. However, this polycrystal is not a static but a dynamic system. As a result of the strong $\pi - \pi$ interactions acting between adjacent graphite sheets, these crystalline regions tend to grow slowly over time by squeezing out the mobile intercalating molecules that, as a consequence, accumulate and/or segregate. Over time, most of these mobile intercalating molecules migrate inside the crystal up to the crystal boundary, where they accumulate and then are released outside the crystal. However, only neutral molecules like H_2SO_4 can move inside the crystal; indeed, ionic intercalating molecules ($H_2SO_4^-$) are stably positioned close to the positive charges in the sheets. During the sulfuric acid segregation process, a small percentage of mobile intercalating molecules does not reach the crystal boundary to escape, and is trapped in the crystal between two adjacent crystallites, producing linear defects because all sheet deformations produced by the intercalating molecule propagate to the full graphene sheet and defects in the crystal always are linear. In this work, we have estimated the defect configuration of graphene layers of GBS by applying the model proposed by L. G. Cançado et al. [13] for graphene. This model allowed us to distinguish between point-like and linear defect changes occurring with aging in GBS. As far as we know, this is the first time that this model has been applied to the analysis of GBS, even if Raman spectroscopy is widely used for characterizing graphene and graphene oxides. Previously, aging effects have been investigated in GBS by X-ray diffractometry [5]. Changes in the GBS crystallographic phases have been reported with aging, indicating a relocation of the intercalant molecules that interact with graphene layers. In general, we found a decrease in the density of localized point-like defects with aging, regardless of the pristine structural configuration of the samples. Indeed, GBS compounds fabricated using different oxidizing agents have been considered in this study. Larger relative increases in the L_D characteristic length for point-like defects have been observed in samples D ($KMnO_4$), E ($K_2Cr_2O_7$), F (H_2O_2), and G (KNO_3), which exhibit L_D values larger than 20 nm in the pristine state. Aging did not affect the extended defect configuration, and the L_a characteristic length did not change significantly over time, except in the case of sample F (H_2O_2), which exhibits a small decrease in L_a with aging.

5. Conclusions

Knowledge of the effects of aging on the structural properties of graphite intercalation compounds is an important requirement for industrial processes of expanded graphite production and in general for GBS applications. In this work, we have investigated the effect of aging on graphite bisulfate compounds over 84 months, a period considerably longer than the ones considered in similar works. In particular, Raman spectroscopy allowed us to monitor the changes occurring in the defect configuration of the graphene layers and the stacking regions of the GBS due to the interaction between graphene layers and intercalant ions and molecules. To achieve this, we have extended the approach used for graphene characterization to the analysis of the spectroscopic data of GBS. To the best of our knowledge, this is the first time that an investigation of this type has been performed. This study allowed us to distinguish between point-like and linear defect changes occurring with aging. In general, we found a decrease in the density of localized point-like defects with aging, regardless of the pristine structural configuration of the samples. In the case of samples with a relatively high density of point-defects, a slight decrease in the density of linear defects was inferred, concurrent with a segregation of mobile intercalating components to the grain boundaries and an increase in the regularity of the stacked boundary layers. In general, the proposed approach provides a convenient method for GBS and GIC characterization, not only for aging effect estimations, but also for controlling the processes of GBS, GIC, and expanded graphite fabrication.

Supplementary Materials: The following supporting information can be downloaded at https://www.mdpi.com/article/10.3390/coatings14010101/s1: Figure S1: Effect of aging on the Raman response of the graphite bisulphate prepared with $NaClO_3$ as oxidizing component (sample B ($NaClO_3$)). The Raman spectra have been collected on a fresh prepared sample (0) and after 3, 12, 14, 29, 30, 61, and 84 months of aging, respectively. Figure S2: Effect of aging on the Raman response of the graphite bisulphates prepared with HNO_3 (sample A, black dots and line) and $NaClO_3$ (sample B, red dots and line) as oxidizing component. The time dependence of the A_{Gb}/A_G area ratio of the G_b and G mode peaks (a) and of the ratio of the D and G mode peaks (b) are reported. Table S1: Effects of the aging on the A_D/A_G area ratio of D and G Raman modes and the width of G peak (Γ_G). Data refer to GBS produced with different oxidation agents and have been used to estimate L_a and L_D parameters reported in Table 2. E_L = 1.96 eV is photon energy of the excitation laser.

Author Contributions: Conceptualization and methodology, C.C., M.S. and G.C.; investigation, C.C. and M.S.; writing—review and editing, C.C., M.S. and G.C. All authors have read and agreed to the published version of the manuscript.

Funding: This research received no external funding.

Data Availability Statement: Data are contained within the article.

Conflicts of Interest: The authors declare no conflicts of interest.

References

1. Brodie, B. Note sur un nouveau procédé pour la purification et la désagrégation du graphite. *Ann. Chem. Phys.* **1855**, *45*, 351–352.
2. Inagaki, M. Application of graphite intercalation compounds. *J. Mater. Res.* **1989**, *4*, 1560–1568. [CrossRef]
3. Chang, J.-K.; Hsu, C.-C.; Liu, S.-Y.; Wu, C.-I.; Gharib, M.; Yeh, N.-C. Spectroscopic studies of the physical origin of environmental aging effects on doped graphene. *J. Appl. Phys.* **2016**, *119*, 235301. [CrossRef]
4. Aronson, S.; Frishberg, C.; Frankl, G. Thermodynamic properties of the graphite-bisulphate lamellar compounds. *Carbon* **1971**, *9*, 715–723. [CrossRef]
5. Samuelsen, E.J.; Moret, R.; Fuzellier, H.; Klatt, M.; Lelaurain, M.; Herold, A. Phase transitions and aging effects of the graphite intercalation compound α-C5n-HNO_3. *Phys. Rev. B* **1985**, *32*, 417–427. [CrossRef] [PubMed]
6. Salvatore, M.; Carotenuto, G.; De Nicola, S.; Camerlingo, C.; Ambrogi, V.; Carfagna, C. Synthesis and characterization of highly intercalated graphite bisulfate. *Nano Res. Lett.* **2017**, *12*, 167. [CrossRef] [PubMed]
7. Pimenta, M.A.; Dresselhaus, G.; Dresselhaus, M.S.; Cançado, L.G.; Jorio, A.; Saito, R. Studying disorder in graphite-based systems by Raman spectroscopy. *Phys. Chem. Chem. Phys.* **2007**, *9*, 1276–1291. [CrossRef] [PubMed]
8. Ferrari, A.C.; Meyer, J.C.; Scardaci, V.; Casiraghi, C.; Lazzeri, M.; Mauri, F.; Piscanec, S.; Jiang, D.; Novoselov, K.S.; Roth, S.; et al. Raman Spectrum of Graphene and Graphene Layers. *Phys. Rev. Lett.* **2006**, *97*, 187401. [CrossRef] [PubMed]
9. Carotenuto, G.; Longo, A.; De Nicola, S.; Camerlingo, C.; Nicolais, L. A simple mechanical technique to obtain carbon nanoscrolls from graphite nanoplatelets. *Nano Res. Lett.* **2013**, *8*, 403. [CrossRef] [PubMed]
10. Doll, G.L.; Eklund, P.C. Raman scattering study of the high-frequency intralayer modes in Li-graphite and the stage dependence of the mode frequency in donor graphite intercalation compounds. *Phys. Rev. B* **1987**, *36*, 4940–4945. [CrossRef] [PubMed]
11. Chacón-Torres, J.C.; Wirtz, L.; Pichler, T. Manifestation of charged and strained graphene layers in the Raman response of graphite intercalation compounds. *ACS Nano* **2013**, *7*, 9249–9259. [CrossRef] [PubMed]
12. Cançado, L.G.; Jorio, A.; Martins Ferreira, E.H.; Stavale, F.; Achete, C.A.; Capaz, R.B.; Moutinho, M.V.O.; Lombardo, A.; Kulmala, T.S.; Ferrari, A.C. Quantifying defects in Graphene via Raman spectroscopy at different excitation energies. *Nano Lett.* **2011**, *11*, 3190–3196. [CrossRef] [PubMed]
13. Cançado, L.G.; Gomes da Silva, M.; Ferreira, E.H.M.; Hof, F.; Kampioti, K.; Huang, K.; Pénicaud, A.; Achete, C.A.; Capaz, R.B.; Jorio, A. Disentangling contributions of point and line defects in the Raman spectra of graphene-related materials. *2D Mater.* **2017**, *4*, 025039. [CrossRef]
14. Tormin, U.; Beck, F. Transport of intercalated anions in graphite according to Walden's rule. *Electrochim. Acta* **1995**, *40*, 1955–1962. [CrossRef]

15. Sasaki, K.-I.; Tokura, Y.; Sogawa, T. The origin of D-band: Bonding and antibonding orbitals in graphene. *Crystals* **2013**, *3*, 120–140. [CrossRef]
16. Bhatt, M.D.; Kim, H.; Kim, G. Various defects in graphene. *RSC Adv.* **2022**, *12*, 21520. [CrossRef] [PubMed]

coatings

MDPI

Article

$CoNi_2O_4$ Coated on Activated Carbon Wheat Husk (ACWH) as a Novel Nano-Electrocatalyst for Methanol and Ethanol Electro-Oxidation

Fatemeh Jamali [1], Majid Seifi [1,*] and Mohammad Bagher Askari [2,*]

[1] Department of Physics, Faculty of Science, University of Guilan, Rasht P.O. Box 41335-1914, Iran
[2] Department of Semiconductor, Institute of Science and High Technology and Environmental Sciences, Graduate University of Advanced Technology, Kerman P.O. Box 7631818356, Iran
* Correspondence: seifi@guilan.ac.ir (M.S.); mbaskari@phd.guilan.ac.ir (M.B.A.)

Abstract: In this paper, for the first time, a $CoNi_2O_4$ nanocatalyst coated on the surface of activated carbon wheat husk (ACWH) was synthesized in the form of $CoNi_2O_4$/ACWH through a hydrothermal process. The electrocatalytic activity of this catalyst was evaluated using methanol oxidation reaction (MOR) and ethanol oxidation reaction (EOR) processes for use in anodes of alcohol fuel cells. Adding ACWH, as a cheap carbon biomass with an excellent active surface area, improves the performance of the catalyst in the oxidation of alcohols. The current density of $CoNi_2O_4$/ACWH in the MOR process is 160 mA/cm^2 at an optimal methanol concentration of 2 M; this oxidation current density in the EOR process and at a concentration of 1.5 M ethanol is 150 mA/cm^2. The stability of $CoNi_2O_4$/ACWH in MOR and EOR processes, after 1000 consecutive CV cycles, is 98.6% and 94.6%, respectively.

Keywords: $CoNi_2O_4$; activated carbon wheat husk; methanol oxidation; ethanol oxidation

Citation: Jamali, F.; Seifi, M.; Askari, M.B. $CoNi_2O_4$ Coated on Activated Carbon Wheat Husk (ACWH) as a Novel Nano-Electrocatalyst for Methanol and Ethanol Electro-Oxidation. *Coatings* **2023**, *13*, 1124. https://doi.org/10.3390/coatings13061124

Academic Editor: Gianfranco Carotenuto

Received: 19 February 2023
Revised: 19 March 2023
Accepted: 14 June 2023
Published: 19 June 2023

1. Introduction

Today, energy demand is increasing continuously in the advanced and developing world [1]. Limited sources of fossil fuels not only lead to global energy and fuel shortages, but also endanger human lives due to the enhanced amounts of greenhouse gases and consequences of environmental change [2,3]. A low-cost and environmentally friendly fuel could be used as a suitable alternative to fossil fuels to overcome this problem. There is no doubt that using sustainable and renewable fuel sources, such as sunlight, wind power, geothermal power, etc., is a wise solution for overcoming the energy crisis across the world [4,5].

Reviewing the yearly statistics and data of developed countries on their use of renewable fuel sources indicates that countries allocate enormous budgets for this purpose yearly [6,7]. Although almost all countries have access to renewable and clean energy sources, the production and industrialization of energy transformation to be used in this field need special technical and technological knowledge [8,9]. As an example, a specific photovoltaic cell should be designed and constructed in each location to exploit electric energy from sunlight with the minimum cost and maximum efficiency; the same is true for other cases like wind turbines, devices, and equipment for using sea waves and geothermal energy.

In recent years, with the considerable advancements in nanoscience in energy storage and production, we have witnessed the industrialization of some equipment in this field, such as supercapacitors, various electrochemical batteries, and fuel cells, which are very appealing to customers due to being portable and having small sizes [10,11]. Furthermore, extensive equipment applications in different fields, including pharmaceutical, military, etc., have made developed countries allocate a suitable budget to this field.

Among the mentioned equipment, supercapacitors and electrochemical batteries are used for energy storage [12,13], and fuel cells directly produce energy by transforming chemical energy into electrical power [14]. One of the advantages of fuel cells is the production of water as a side product [15]. Nowadays, fuel cells have found a special place in energy production. In addition to being clean and efficient, they can be used in any application that needs energy since they can produce 1 W to 10 MW power [16]. Fuel cells are divided into high- and low-temperature cells; alcoholic fuel cells comprise low-temperature cells [17]. Among the different alcohols, methanol and ethanol are significant sources of energy production due to their high energy density, availability, and easy storage and transportation [18–20].

Alcoholic fuel cells consist of three main parts: the anode, cathode, and membrane [21,22]. Fuel electrochemical oxidation occurs on the anode and oxygen reduction occurs on the cathode [23]. One of the parameters that determines the effectiveness of cell efficiency is the structure of the anode electrode, which is responsible for the alcohol oxidation process. Although platinum-based electrocatalysts [24,25], composites, and composite-based hybrids [26–30] have the maximum catalytic activity in alcohol oxidation, their high cost and limited availability are among the challenges of the practical utilization of fuel cells [31]. Other metals, except platinum, with electrocatalytic properties, are ruthenium, palladium, rubidium, and gold [32–34].

Examples of catalyst applications, especially metal oxide-based catalysts, include the use of catalysts based on nickel and cobalt in oxygen evolution reaction (OER) and hydrogen evolution reaction (HER) processes. This broad application of catalysts has attracted much attention recently and has been highly welcomed by researchers [35–37]. The electrode material is a crucial factor in methanol fuel cells due to their slow reaction kinetics. The structure of the electrode material plays an essential role in its electrocatalytic activity. This material should be electrically conductive, with a suitable effective surface area and adequate electrocatalytic activity [38,39].

Metal oxides were studied as electrodes and catalyst materials that can be theoretically applied to electrochemical processes. However, these materials have low electric conductivity and effective surface area. Various methods are reported to improve the performance of metal oxides. Doping or compositing these materials with efficient and precious catalysts like platinum and palladium, or hybridizing metal oxides with surface-active and conductive materials such as MOF, conductive polymers, etc., are among the proposed methods [40–43].

One of the most attractive, cost-effective, and efficient methods of improving the electrocatalytic activity of metal oxides is using carbon in their structures. Various types of carbonaceous material, such as graphene oxide nanotubes and hollow carbon nanospheres (HCNs), facilitate electrochemical processes by increasing the their conductivity and improving their catalytic activity [44]. Among the metal oxides, due to the synergistic effect of two metal oxides in one structure in the form of AB_2O_4, it seems that binary intermediate metal oxides (BTMOs) might be excellent candidates to be used as catalysts in fuel cell structures like $NiCo_2O_4/CuO\text{-}C$ [45], $MnNi_2O_4$-MWCNTs [8], and $MnCo_2O_4/NiCo_2O_4/rGO$ [11].

Among the carbonaceous materials, using the carbon obtained from industrial and agricultural wastes, such as active and conductive carbon, in catalyst structures can be very interesting for scientists. The production processes of these carbons are almost environmentally friendly processes. These carbonaceous materials have attracted much attention due to their availability and low-cost synthesis. Banana fiber [46], rice husk [47], and natural wood [48] are some of these carbons. In this study, wheat husk wastes are used as the source of biomass carbon production, and their combination with $CoNi_2O_4$, as a low-cost and efficient binary metal oxide nanocatalyst, is used in methanol and ethanol oxidation in alcoholic fuel cell anodes. One of the reasons for using wheat husk for carbon production is its abundance and availability, as well as the ease and low cost of preparing biomass carbon from wheat husk waste compared to other materials. According to studies, this type of catalyst, which includes binary metal oxide and biomass carbon, is not used in fuel cell anodes. EIS, LSV, CV, and chronoamperometry analyses of the catalysts have revealed that $CoNi_2O_4$/ACWH and $CoNi_2O_4$ have the ability to oxidize methanol and ethanol. Although both of these catalysts are suitable candidates to be used in alcoholic fuel cell anodes, the presence of ACWH in the CoNi2O4 structure improves its electrocatalytic properties due to the active surface and electric conductivity of this carbon.

2. Materials and Methods

All the materials used were Merck Company products with 99% purity. X-ray diffraction (XRD) analysis was performed using an XRD Xpert Pro Panalytical device (Almelo, The Netherlands). FE-SEM ZEISS equipment (GeminiSEM 300, Carl Zeiss, Oberkochen, Germany) was used for FESEM imaging. Raman spectroscopy was performed using Confocal Microscopy (LabRAM ARAMIS, Horiba Jobin Yvon, Longjumeau, France). All the electrochemical analyses were carried out using Potentiostat/Galvanostat Autolab 302 N (Metrohm, Herisau, Switzerland) with a three-electrode system.

2.1. Synthesis of Carbon Biomass

A total of 50 g of pure wheat husk was poured into 450 mL of 1 M nitric acid (HNO_3) and left for one day under stirring; then, it was dried at 60 °C. The product was poured into 500 mL of 1 M NaOH and stirred for 24 h; then, it was dried at 65 °C. The dried product was put in a 400 °C furnace for 3 h. The obtained black material was mixed with 300 mL of 1 M NaOH and stirred for 30 min. The product was dried at 70 °C. The obtained material was mixed with KOH in a 1:4 ratio (WHC/KOH) and put in a CVD at 800 °C. After an acid wash, the powder reached pH 7, and the activated carbon prepared from the wheat husk (ACWH) was ready.

2.2. Synthesis of $CoNi_2O_4$ and $CoNi_2O_4$/ACWH

The hydrothermal method was used to synthesize $CoNi_2O_4$ and $CoNi_2O_4$/ACWH. For this purpose, 0.581 g nickel nitrate hexahydrate and 0.291 g cobalt hexahydrate molecules were poured into 15 mL of deionized water and stirred. Then, 3.60 g urea was added to the solution and stirred for 45 min. The resultant homogeneous solutions were placed in a 40 mL autoclave for 12 h at 90 °C. Then, the dilute product was washed with water and ethanol and dried at 80 °C. The obtained powder was annealed at 400 °C.

The $CoNi_2O_4$/ACWH was prepared using a similar method, with the difference that nickel and cobalt nitrate hexahydrates were added to 10 mL deionized water and mixed with urea. Then, 0.001 g of ACWH that was sonicated in 10 mL water was added to the solution and placed in an autoclave with a similar temperature and conditions to those of the synthesis process; the preparation procedure for the powdered product was then followed. The formation mechanism of the $CoNi_2O_4$ nanocatalyst was as follows:

$$3Co(NO_3)_2 + 6Ni(NO_3)_2 + 14CH_4N_2O \rightarrow 3CoNi_2O_4 + 23N_2 + 14CO_2 + 28H_2O$$

2.3. Preparation of Electrode

A setup was prepared to investigate the catalysts' behavior in methanol and ethanol oxidation reactions to be used in alcoholic fuel cell anodes. For this purpose, some slurries containing 0.4 g each of $CoNi_2O_4$ and $CoNi_2O_4$/ACWH catalyst in 0.5 mL Naphion 5% and 0.5 mL isopropyl alcohol were separately prepared with ultrasonication for 30 min to disperse the particles completely. An amount of 0.6 µL of this slurry was poured on the surface of the GCE electrode using a micropipette. The electrochemical tests were performed after drying. The electrode system used in this study consisted of a glass carbon electrode (GCE) that was modified by the catalysts to be used as the working electrode. The auxiliary and reference electrodes were a platinum rod with a 0.5 mm diameter and a Ag/AgCl electrode, respectively.

3. Results

3.1. X-ray Diffraction (XRD)

To study the structure and confirm the successful synthesis of nanocatalysts, their crystalline structure was investigated via X-ray diffraction analysis. Figure 1 shows the X-ray diffraction of nanocatalysts and ACWH. As seen in this figure, two intensive peaks of $CoNi_2O_4$ and $CoNi_2O_4$/ACWH appeared at about 38 and 44 degrees. Also, one peak was observed at 29 degrees in the ACWH diffraction pattern. The diffraction patterns of $CoNi_2O_4$ and $CoNi_2O_4$/ACWH comply with JCPDS No. 00.040.1191. The characteristic peaks of $CoNi_2O_4$ and $CoNi_2O_4$/ACWH were occurred at 18.801, 31.005, 38.269, 44.508, 55.187, 58.930, 64.779, and 76.707 degrees, and are related to the Miller planes of (111), (220), (222), (400), (422), (511), (440), and (533), respectively. A comparison of the two diffraction patterns of $CoNi_2O_4$ and $CoNi_2O_4$/ACWH indicates that $CoNi_2O_4$/ACWH peaks have lower intensity at the (220), (222), and (400) Miller planes, which is due to the presence of ACWH in the crystal structure.

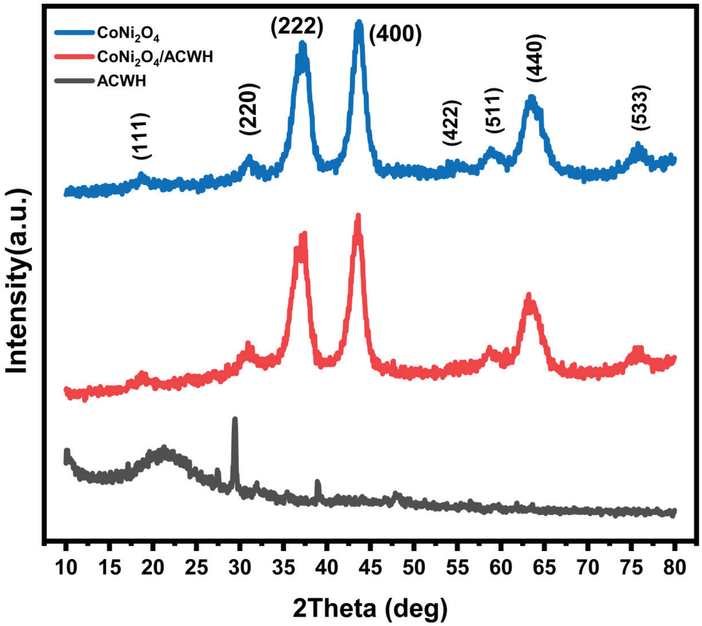

Figure 1. XRD pattern of synthesized $CoNi_2O_4$, $CoNi_2O_4$/ACWH, and ACWH.

3.2. FE-SEM

The surface morphology of the prepared nanocatalysts was investigated via Field Emission Scanning Electron Microscopy (FESEM) images. Figure 2 shows the FESEM images of $CoNi_2O_4$, $CoNi_2O_4$/ACWH, and ACWH nanoparticles. Figure 2a–c show images from the $CoNi_2O_4$ nanocatalyst which were taken at 100 nm, 200 nm, and 1 µm, respectively. A surface with contiguous spheres with relatively homogeneous sizes is observed in the picture. Figure 2d–f show images of the $CoNi_2O_4$/ACWH nanocatalyst; as seen, there is a smooth surface consisting of separate spheres that are attached to nanorods, and the surface particles are at a long distance from each other compared to the nanocatalysts. Figure 2g–i present images taken from ACWH that show a porous surface consisting of nanoparticles and nanosheets.

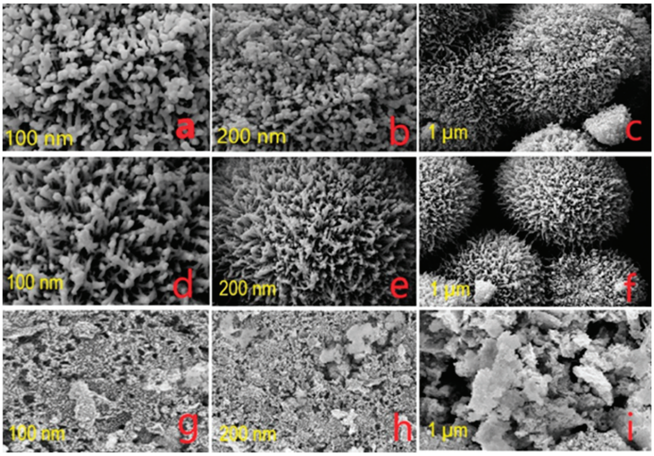

Figure 2. SEM images of $CoNi_2O_4$ (**a**–**c**), $CoNi_2O_4$/ACWH (**d**–**f**), and ACWH (**g**–**i**) at different magnifications.

3.3. EDX-Mapping

EDX-mapping elemental analysis was used to identify the composition of $CoNi_2O_4$ and $CoNi_2O_4$/ACWH nanocatalysts. As seen in Figures 3 and 4, Co, O, Ni, and C elements are present in the synthesized nanostructures. According to mapping images of $CoNi_2O_4$ nanocatalyst in Figure 3a, the presence of Co, Ni, and O elements is confirmed. Besides, the mapping images of $CoNi_2O_4$/ACWH in Figure 3b indicate the presence and uniform distribution of Co, Ni, O, and C elements.

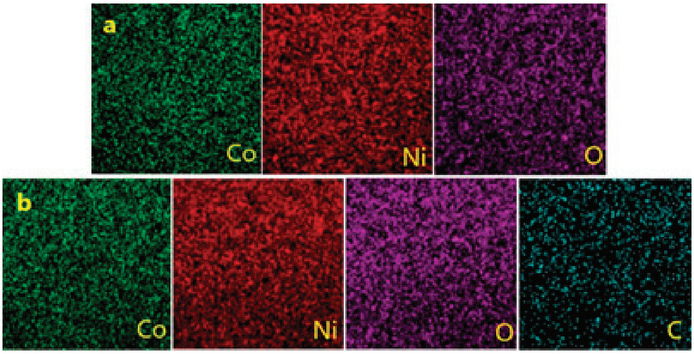

Figure 3. Mapping analysis of $CoNi_2O_4$ (**a**) and $CoNi_2O_4$/ACWH (**b**).

3.4. Raman Spectroscopy

Raman spectroscopy is used for the structural study of the nanocatalysts to confirm the presence of carbon in their structures. Figure 5 presents the Raman spectra of the nanocatalysts. Two peaks with high resolution are observed in the Raman spectra of the nanocatalyst containing ACWH that are related to the D and G bonds of carbon. Bond D in the 1300 to 1400 (cm^{-1}) range belongs to carbonaceous atoms that experienced irregularity. Bond G at about 1600 (cm^{-1}) is related to the E_2g state of the graphite structure. These two peaks confirm the carbonaceous and graphene structure of ACWH, which are evident in the Raman spectra of the $CoNi_2O_4$/ACWH nanocatalyst and indicate the presence of ACWH in this structure.

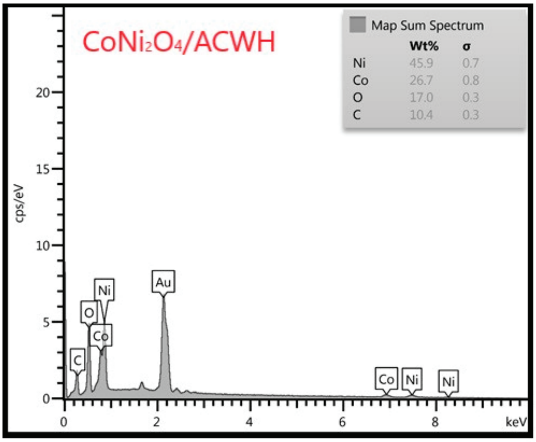

Figure 4. EDX analysis of $CoNi_2O_4$/ACWH.

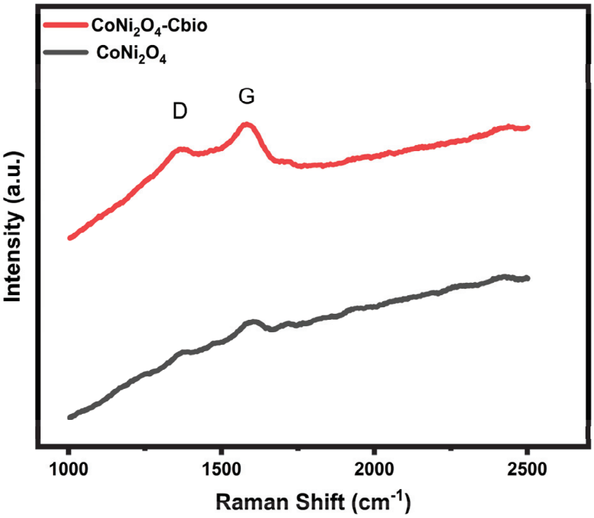

Figure 5. Raman spectra of $CoNi_2O_4$/ACWH and $CoNi_2O_4$.

3.5. BET Method

The BET method is used to check the specific surface area and porosity of samples based on nitrogen adsorption and desorption isotherms at a nitrogen boiling temperature of 77 degrees Kelvin. Figure 6 shows the adsorption–desorption isotherms of the $CoNi_2O_4$ and $CoNi_2O_4$/ACWH samples. According to the AUPAC isotherms, the $CoNi_2O_4$ and $CoNi_2O_4$/ACWH isotherms are of type IV, which shows that the samples have a mesoporous structure and the relationship between the surface of the sample and the adsorbent is relatively strong. Investigating the $CoNi_2O_4$ and $CoNi_2O_4$/ACWH isotherms indicated that adding ACWH to $CoNi_2O_4$ increases the specific surface area. Based on the results obtained from the analysis, the specific surface area of $CoNi_2O_4$ and $CoNi_2O_4$/ACWH nanocatalysts is 69.686 and 75.089 m^2/g, respectively. These results confirm the claim that by increasing the effective level of the catalyst, the performance of the catalyst improves, and these results can be attributed to the addition of ACWH to the $CoNi_2O_4$ catalyst.

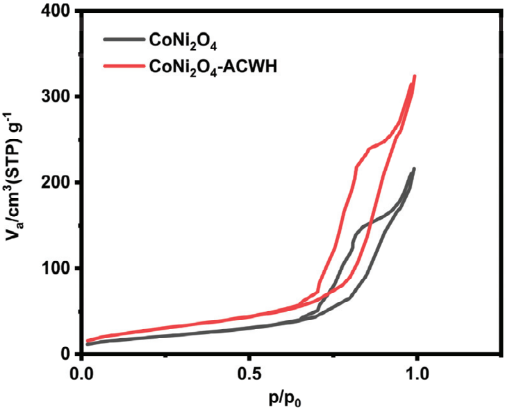

Figure 6. BET of $CoNi_2O_4$/ACWH and $CoNi_2O_4$.

3.6. Electrochemical Studies

3.6.1. Investigation of $CoNi_2O_4$ and $CoNi_2O_4$/ACWH Nanocatalysts' Abilities in Methanol Oxidation Process

As far as we know, metal oxides exhibit maximum efficiency in alcohol oxidation processes in alkaline environments. A 0.5 M KOH solution was prepared, and cyclic voltammetry (CV) analysis was carried out on the modified electrodes with $CoNi_2O_4$ and $CoNi_2O_4$/ACWH, at a scan rate of 20 mV/s. The results are presented in Figure 7a. As seen, $CoNi_2O_4$/ACWH has a higher capacitive current density due to its higher electrical conductivity and more electrochemically active surface compared to $CoNi_2O_4$. The reason for this superiority is the presence of biomass carbon from the wheat husk in the $CoNi_2O_4$/ACWH structure. The results of the Electrochemical Impedance Spectroscopy (EIS) analysis of $CoNi_2O_4$ and $CoNi_2O_4$/ACWH catalysts, in the frequency range of 1 MHz to 10 KHz, are presented in Figure 7b. The resistance against charge transfer for $CoNi_2O_4$ and $CoNi_2O_4$/ACWH is 30.5 and 18.2 Ω, respectively, which shows the positive effect of carbon biomass present in the catalysts' structure.

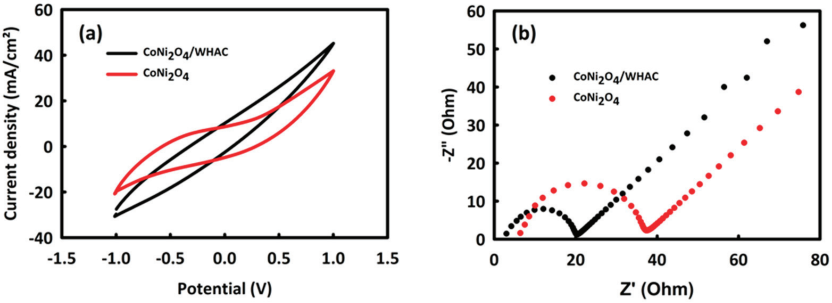

Figure 7. CV (**a**) and EIS (**b**) analysis of $CoNi_2O_4$ and $CoNi_2O_4$/WHAC in 0.5 M KOH.

To investigate the behavior of $CoNi_2O_4$ and $CoNi_2O_4$/ACWH in the methanol oxidation process, some solutions were prepared containing 0.5 M KOH and various methanol concentrations (0.5–3 M). As can be seen in the CV analysis of the two nanocatalysts, in the potential range of 0–0.8 V and at a scan rate of 20 mV/s, enhanced methanol concentration causes an increase in the current density of the electrode that was modified with $CoNi_2O_4$. This enhancement in the current density continues up to a 1.5 M concentration, a further increase in the concentration causes a reduction in current density, and the oxidation peak has a descending trend. The same trend is observed in $CoNi_2O_4$/ACWH; the current density of the methanol oxidation peak increases up to a methanol concentration of 2 M, but lower current density is observed at higher concentrations. It seems that the nanocatalyst surface becomes saturated at a concentration higher than the optimum concentration, and electrolyte/methanol cannot penetrate easily to the catalyst core; this causes a reduction in current density. The behavior of $CoNi_2O_4$ and $CoNi_2O_4$/ACWH nanocatalysts at different methanol concentrations is presented in Figure 8a,b.

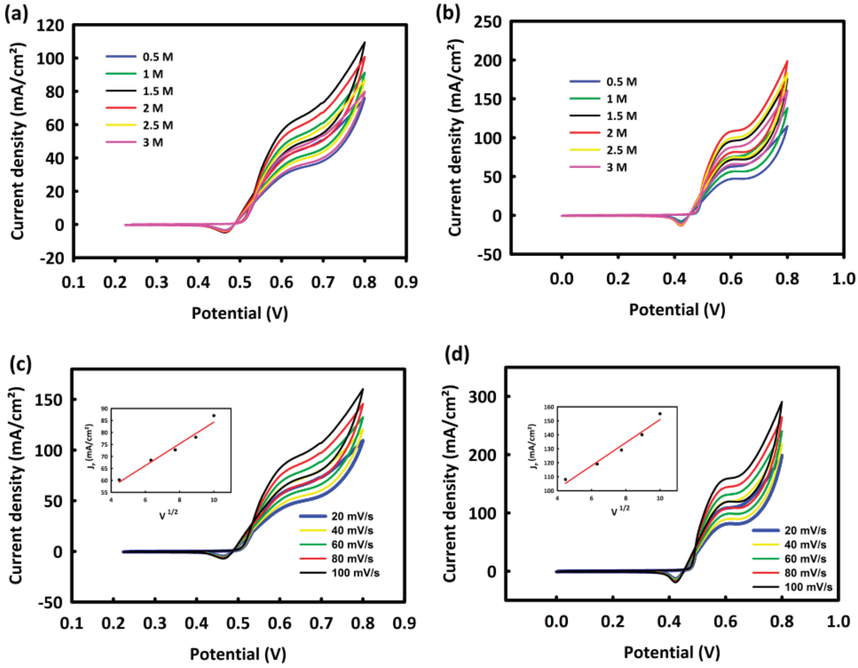

Figure 8. CV from $CoNi_2O_4$ (**a**) and $CoNi_2O_4$/ACWH (**b**) in 0.5 M KOH/different concentrations of methanol. CV from $CoNi_2O_4$ (**c**) and $CoNi_2O_4$/ACWH (**d**) in 0.5 M KOH/optimal concentration of methanol/at different scan rates. The plots of the square root of scan rate in terms of peak current density (J_P) for $CoNi_2O_4$ and $CoNi_2O_4$/ACWH are shown in insets of (**c**,**d**).

The CV analysis was carried out at different scan rates of 20 to 100 mv/s to study the methanol oxidation mechanism of $CoNi_2O_4$ and $CoNi_2O_4$/ACWH. An enhanced current density of the oxidative peak was observed for $CoNi_2O_4$ and $CoNi_2O_4$/ACWH after increasing the scan rate. This ascending trend is presented in Figure 8c,d, respectively. The square of the scan rate as a function of peak current density (Jp) is shown in the insets of these figures. The linear relationship between these two parameters, with $R^2 = 0.996$ and $R^2 = 0.991$, indicates that diffusion is the controlling mechanism of methanol oxidation by $CoNi_2O_4$ and $CoNi_2O_4$/ACWH. The proposed six-electron mechanism for these nanocatalysts is in the following form [49]:

$$\text{Catalyst} + CH_3OH \rightarrow \text{Catalyst} - CH_3OH_{ads}$$

$$\text{Catalyst} - CH_3OH_{ads} + 4OH^- \rightarrow \text{Catalyst} - (CO)_{ads} + 4H_2O + 4e^-$$

$$\text{Catalyst} + OH^- \rightarrow \text{Catalyst} - OH_{ads} + e^-$$

$$\text{Catalyst} - CO_{ads} + \text{Catalyst} - OH_{ads} + OH^- \rightarrow \text{Catalyst} + CO_2 + H_2O + e^-$$

The stability of $CoNi_2O_4$ and $CoNi_2O_4$/ACWH nanocatalysts in methanol oxidation can be assessed via CV. The $CoNi_2O_4$ nanocatalyst shows 95.8% stability after 1000 consecutive CV cycles at 0.5 KOH/1.5 methanol solution at a scanning rate of 100 mV/s (Figure 9a), while $CoNi_2O_4$/ACWH shows 98.6% stability after the same number of cycles and the same scan rate, but in 0.5 KOH/2 methanol solution (Figure 9b).

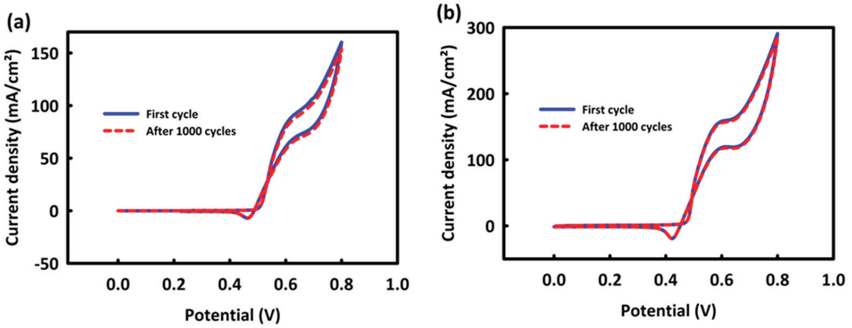

Figure 9. Cyclic stability for $CoNi_2O_4$ (**a**) and $CoNi_2O_4$/ACWH (**b**) in MOR process after 1000 consecutive CV cycles.

3.6.2. Investigation of $CoNi_2O_4$ and $CoNi_2O_4$/ACWH Nanocatalyst Capabilities in Ethanol Oxidation Process for Use in Ethanol Fuel Cells

To investigate the capability of $CoNi_2O_4$ and $CoNi_2O_4$/ACWH nanocatalysts in the oxidation of ethanol in an alkaline environment, various amounts of ethanol were added to KOH 0.5 M, and CV analysis was performed at a 20 mV/s scan rate and in the potential range of 0–0.8 V. Figure 10a shows $CoNi_2O_4$ nanocatalyst behavior and Figure 10b shows $CoNi_2O_4$/ACWH nanocatalyst behavior at different ethanol concentrations. The surfaces of $CoNi_2O_4$ and $CoNi_2O_4$/ACWH nanocatalysts become saturated at 1 and 1.5 M ethanol concentrations, and the oxidative peak of current density undergoes a descending trend at higher ethanol concentrations. Here, it also seems that the catalyst surface became saturated at concentrations higher than the critical concentration, and ethanol could not penetrate the depth of the catalyst anymore.

The methanol oxidation mechanism of $CoNi_2O_4$ and $CoNi_2O_4$/ACWH nanocatalysts was determined via a CV test at the optimum ethanol concentration and a scan rate of 10–100 mV/s. Figure 10c,d show the behavior of $CoNi_2O_4$ and $CoNi_2O_4$/ ACWH nanocatalysts at different scan rates. An increase in anodic current density is observed with increasingscan rate.

The squared scan rate as a function of the peak current density (Jp) is presented in the insets of these figures. The linear relationship of these two parameters with R^2 = 0.994 and R^2 = 0.996 for $CoNi_2O_4$ and $CoNi_2O_4$/ACWH, respectively, implies that diffusion is the controlling mechanism in the EOR process.

The proposed mechanism for ethanol oxidation can be expressed in the following form:

$$\text{Catalyst} + OH^- \rightarrow \text{Catalyst} - OH_{ads} + e^-$$

$$\text{Catalyst} + CH_3CH_2OH \rightarrow \text{Catalyst} - (CH_3CH_2OH)_{ads}$$

$$\text{Catalyst} - (CH_3CH_2OH)_{ads} + 3OH^- \rightarrow \text{Catalyst} - (CH_3CO)_{ads} + 3H_2O + 3e^-$$

$$\text{Catalyst} - (CH_3CO)_{ads} + \text{Catalyst} - OH_{ads} \rightarrow \text{Catalyst} - (CH_3COOH)_{ads} + \text{Catalyst}$$

$$\text{Catalyst} - (CH_3COOH)_{ads} + OH^- \rightarrow \text{Catalyst} + CH_3COO^- + H_2O$$

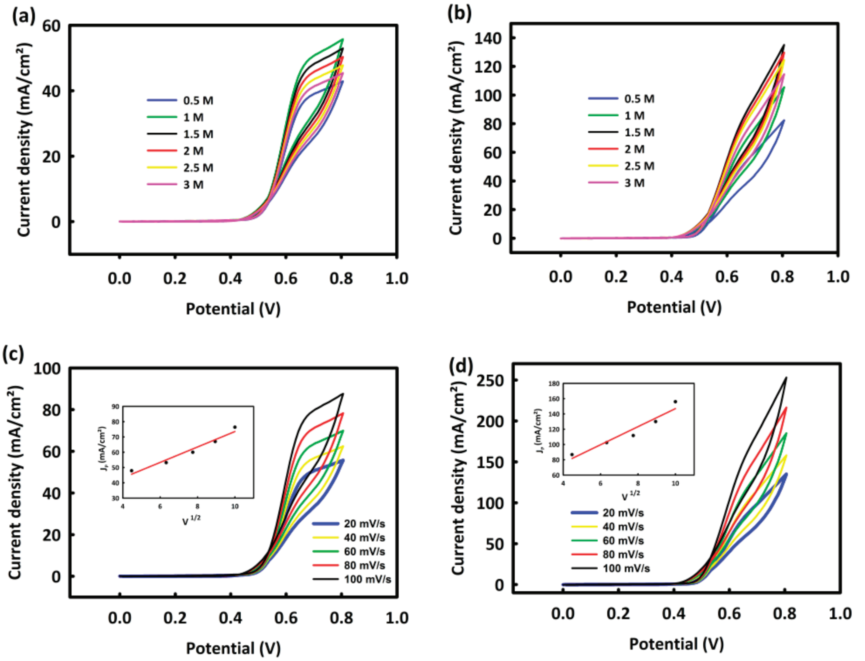

Figure 10. CV from $CoNi_2O_4$ (**a**) and $CoNi_2O_4$/ACWH (**b**) in 0.5 M KOH/different concentrations of ethanol. CV from $CoNi_2O_4$ (**c**) and $CoNi_2O_4$/ACWH (**d**) in 0.5 M KOH/optimal concentration of ethanol/at different scan rates. The plots of the square root of the scan rate in terms of maximum current density for $CoNi_2O_4$ and $CoNi_2O_4$/ACWH are shown in insets of (**c**,**d**).

The stability of $CoNi_2O_4$ and $CoNi_2O_4$/ACWH nanocatalysts in the EOR process was evaluated through 1000 consecutive CV analyses at the optimum ethanol concentration and a scan rate of 60 mV/s. Figure 11a,b present the cyclic stability of $CoNi_2O_4$ and $CoNi_2O_4$/ACWH. After these cycles, a stability of 91.5% for $CoNi_2O_4$ and 94.6% for $CoNi_2O_4$/ACWH is obtained.

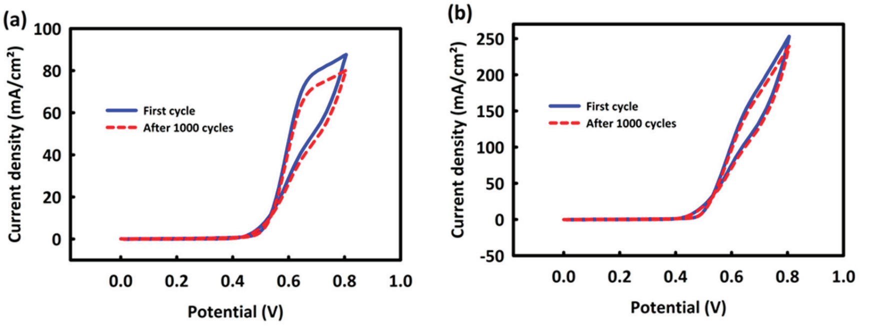

Figure 11. Cyclic stability of $CoNi_2O_4$ (**a**) and $CoNi_2O_4$/ACWH (**b**) in MOR process after 1000 consecutive CV cycles.

In Table 1, we compare the performance and efficiency of $CoNi_2O_4$/ACWH nanocatalyst in the MOR and EOR processes with other recent research.

Table 1. Comparison of MOR and EOR performance of $CoNi_2O_4$/ACWH nanocatalyst with other recent research.

Electrocatalyst	Electrolyte Composition	Peak Potential (V)	Current Density (mA cm^{-2})	Scan Rate (mV/s)	Reference
$CoNi_2O_4$/ACWH	2 M methanol/0.5 M KOH	0.58	160	60	This work
$CoNi_2O_4$/ACWH	1.5 M ethanol/0.5 M KOH	0.63	150	60	This work
ZrO_2/NiO/rGO	0.7 M methanol/0.5 M KOH	0.52	26.6	20	[10]
ZrO_2/NiO/rGO	0.5 M ethanol/0.5 M KOH	0.52	17.3	20	[10]
Mn_3O_4-CeO_2-rGO	0.8 M methanol/1 M KOH	0.51	17.7	90	[49]
Ni_3S_4–NiS-rGO	0.7 M methanol/1 M KOH	0.54	55	80	[50]
Ni_3S_4–NiS-rGO	0.5 M ethanol/1 M KOH	0.59	11	60	[50]
$NiCo_2O_4$	0.5 M methanol/1 M KOH	0.7	129	10	[51]
$NiCo_2O_4$/carbon xerogel	0.5 M methanol/0.5 M KOH	0.29	98	50	[52]
3D Ni/NiO/RG	1 M methanol/1 M KOH	About 0.6	79.21	50	[53]
NiO 2.5CeO_2–NiO	1 M methanol/1 M KOH	About 0.55	159.62	50	[54]
Cu-Ni/CuO-NiO/GNs	0.5 M methanol/1 M KOH	0.7	150	50	[55]
NiO NS@NW/NF	0.5 M methanol/1 M KOH	1.62	89	10	[56]
PEDOT:PSS/MnO_2/rGO	0.5 M methanol/1 M NaOH	0.32	56.38	50	[57]

4. Conclusions

In this research study, $CoNi_2O_4$ and $CoNi_2O_4$/ACWH nanocatalysts were synthesized and their capabilities in the oxidation of methanol and ethanol, to be used in alcohol fuel cell anodes, were investigated. The $CoNi_2O_4$/ACWH nanocatalyst was more efficient than the $CoNi_2O_4$ nanocatalyst, and its higher efficiency was due to the presence of synthesized biomass from the wheat husk in the $CoNi_2O_4$/ACWH structure. The synthesized carbon with a large active surface and acceptable electric conductivity provides a higher catalytic surface for methanol and ethanol and facilitates the oxidation of these two alcohols by the catalyst. In methanol oxidation at a scan rate of 100 mV/s, $CoNi_2O_4$/ACWH had an oxidative current density of 160 mA/cm^2 at the excessive potential of 0.58 V, and its stability was 98.6% after 1000 consecutive CV cycles. $CoNi_2O_4$/ ACWH was also a cost-effective and stable catalyst for ethanol oxidation; its stability was 94.6% after 1000 consecutive CV cycles. The oxidative current density for this nanocatalyst was 150 mA/cm^2 at ethanol oxidation with a peak voltage of 0.63 V. This is the first time that the proposed nanocatalysts have been assessed in MOR and EOR processes, and the results are promising regarding their application in alcoholic fuel cells.

Author Contributions: Conceptualization, F.J., M.S. and M.B.A.; data curation F.J.; formal analysis, F.J. and M.B.A.; funding acquisition M.S. and M.B.A.; investigation, F.J. and M.B.A.; methodology, F.J., M.B.A. and M.S.; resources, M.B.A.; software, F.J. and M.S.; supervision, M.S. and M.B.A.; validation, M.B.A.; visualization, F.J.; writing—original draft, F.J. and M.B.A.; writing—review and editing, M.S. All authors have read and agreed to the published version of the manuscript.

Funding: This research received no external funding.

Institutional Review Board Statement: Not applicable.

Informed Consent Statement: Not applicable.

Data Availability Statement: The data are available upon request from the authors.

Conflicts of Interest: The authors declare no conflict of interest.

References

1. Bahrampour, H.; Marnani, A.K.B.; Askari, M.B.; Bahrampour, M.R. Evaluation of renewable energies production potential in the Middle East: Confronting the world's energy crisis. *Front. Energy* **2017**, *14*, 42–56. [CrossRef]
2. Singh, S. *Energy Crisis and Climate Change: Global Concerns and Their Solutions, Energy: Crises, Challenges and Solutions*; John Wiley & Sons: Hoboken, NJ, USA, 2021; pp. 1–17.
3. Shen, M.; Huang, W.; Chen, M.; Song, B.; Zeng, G.; Zhang, Y. (Micro)plastic crisis: Un-ignorable contribution to global greenhouse gas emissions and climate change. *J. Clean. Prod.* **2020**, *254*, 120138. [CrossRef]

4. Shojaeifar, M.; Askari, M.B.; Hashemi, S.R.S.; Di Bartolomeo, A. MnO_2–NiO–MWCNTs nanocomposite as a catalyst for methanol and ethanol electrooxidation. *J. Phys. D Appl. Phys.* **2022**, *55*, 355502. [CrossRef]
5. Bhuiyan, M.R.A.; Mamur, H.; Begum, J. A brief review on renewable and sustainable energy resources in Bangladesh. *Clean. Eng. Technol.* **2021**, *4*, 100208. [CrossRef]
6. Shang, Y.; Razzaq, A.; Chupradit, S.; An, N.B.; Abdul-Samad, Z. The role of renewable energy consumption and health expenditures in improving load capacity factor in ASEAN countries: Exploring new paradigm using advance panel models. *Renew. Energy* **2022**, *191*, 715–722. [CrossRef]
7. Aslanturk, O.; Kıprızlı, G. The role of renewable energy in ensuring energy security of supply and reducing energy-related import. *Int. J. Energy Econ. Policy* **2020**, *10*, 354–359. [CrossRef]
8. Hosseini, S.; Askari, M.B.; Beitollahi, H. MnNi2O4-MWCNTs as a nano-electrocatalyst for methanol oxidation reaction. *Int. J. Hydrogen Energy* **2022**, *48*, 21240–21248. [CrossRef]
9. Azarpour, A.; Mohammadzadeh, O.; Rezaei, N.; Zendehboudi, S. Current status and future prospects of renewable and sustainable energy in North America: Progress and challenges. *Energy Convers. Manag.* **2022**, *269*, 115945. [CrossRef]
10. Askari, M.B.; Beitollahi, H.; Di Bartolomeo, A. Methanol and Ethanol Electrooxidation on ZrO_2/NiO/rGO. *Nanomaterials* **2023**, *13*, 679. [CrossRef]
11. Askari, M.B.; Azizi, S.; Moghadam, M.T.T.; Seifi, M.; Rozati, S.M.; Di Bartolomeo, A. $MnCo_2O_4$/$NiCo_2O_4$/rGO as a Catalyst Based on Binary Transition Metal Oxide for the Methanol Oxidation Reaction. *Nanomaterials* **2022**, *12*, 4072. [CrossRef] [PubMed]
12. Olabi, A.G.; Abbas, Q.; Al Makky, A.; Abdelkareem, M.A. Supercapacitors as next generation energy storage devices: Properties and applications. *Energy* **2022**, *248*, 123617. [CrossRef]
13. Iqbal, M.Z.; Aziz, U. Supercapattery: Merging of battery-supercapacitor electrodes for hybrid energy storage devices. *J. Energy Storage* **2022**, *46*, 103823. [CrossRef]
14. Kaur, A.; Kaur, G.; Singh, P.P.; Kaushal, S. Supported bimetallic nanoparticles as anode catalysts for direct methanol fuel cells: A review. *Int. J. Hydrogen Energy* **2021**, *46*, 15820–15849. [CrossRef]
15. Okonkwo, P.C.; Otor, C. A review of gas diffusion layer properties and water management in proton exchange membrane fuel cell system. *Int. J. Energy Res.* **2020**, *45*, 3780–3800. [CrossRef]
16. Lasseter, R. Dynamic models for micro-turbines and fuel cells. In Proceedings of the 2001 Power Engineering Society Summer Meeting. Conference Proceedings (Cat. No. 01CH37262), IEEE, Vancouver, BC, Canada, 15–19 July 2001.
17. Yang, B.C.; Koo, J.; Shin, J.W.; Go, D.; Shim, J.H.; An, J. Direct Alcohol-Fueled Low-Temperature Solid Oxide Fuel Cells: A Review. *Energy Technol.* **2018**, *7*, 5–19. [CrossRef]
18. Salarizadeh, P.; Moghadam, M.T.T.; Askari, M.B. Comparison of methanol oxidation reaction process for $NiCo_2O_4$/X (X= rGO, MWCNTs, HCNs) nanocatalyst. *Diam. Relat. Mater.* **2023**, *131*, 109534. [CrossRef]
19. Salarizadeh, P.; Askari, M.B.; Di Bartolomeo, A. MoS_2/Ni_3S_2/Reduced graphene oxide nanostructure as an electrocatalyst for alcohol fuel cells. *ACS Appl. Nano Mater.* **2022**, *5*, 3361–3373. [CrossRef]
20. Jinxi, W.; Aimin, W.; Ghasemi, A.K.; Lashkenari, M.S.; Pashai, E.; Karaman, C.; Niculina, D.E.; Karimi-Maleh, H. Tailoring of $ZnFe_2O_4$-ZrO_2-based nanoarchitectures catalyst for supercapacitor electrode material and methanol oxidation reaction. *Fuel* **2023**, *334*, 26685. [CrossRef]
21. Kim, S.; Ahn, C.; Karuppannan, M.; Sung, Y.; Kwon, O.J.; Cho, Y. Structural modification of electrode for anion exchange membrane fuel cell by controlling ionomer dispersion. *Int. J. Energy Res.* **2021**, *46*, 6471–6479. [CrossRef]
22. Gong, C.; Zhao, S.; Tsen, W.-C.; Hu, F.; Zhong, F.; Zhang, B.; Liu, H.; Zheng, G.; Qin, C.; Wen, S. Hierarchical layered double hydroxide coated carbon nanotube modified quaternized chitosan/polyvinyl alcohol for alkaline direct methanol fuel cells. *J. Power Sources* **2019**, *441*, 227176. [CrossRef]
23. Askari, M.B.; Rozati, S.M. Construction of Co_3O_4-Ni_3S_4-rGO ternary hybrid as an efficient nanoelectrocatalyst for methanol and ethanol oxidation in alkaline media. *J. Alloys Compd.* **2021**, *900*, 163408. [CrossRef]
24. Zhao, G.; Fang, C.; Hu, J.; Zhang, D. Platinum-Based Electrocatalysts for Direct Alcohol Fuel Cells: Enhanced Performances toward Alcohol Oxidation Reactions. *Chempluschem* **2021**, *86*, 574–586. [CrossRef] [PubMed]
25. Tian, H.; Yu, Y.; Wang, Q.; Li, J.; Rao, P.; Li, R.; Du, Y.; Jia, C.; Luo, J.; Deng, P.; et al. Recent advances in two-dimensional Pt based electrocatalysts for methanol oxidation reaction. *Int. J. Hydrogen Energy* **2021**, *46*, 31202–31215. [CrossRef]
26. Yang, C.; Jiang, Q.; Huang, H.; He, H.; Yang, L.; Li, W. Polyelectrolyte-Induced Stereoassembly of Grain Boundary-Enriched Platinum Nanoworms on Ti_3C_2T x MXene Nanosheets for Efficient Methanol Oxidation. *ACS Appl. Mater. Interfaces* **2020**, *12*, 23822–23830. [CrossRef]
27. Wei, S.; Zhan, W.; Ma, L.; Gan, M. $NiMoO_4$ nanorods derives carbon layers wrapped NiCo alloy decorated with Mo2C platinum-based catalyst for efficient methanol electrooxidation. *J. Alloys Compd.* **2022**, *927*, 166963. [CrossRef]
28. Wang, H.; Yang, Y.; Ren, Y.; Chen, D.; Wei, J.; Wang, L.; Xie, A.; Luo, S. Electrochemical synthesis of Pt nanoparticles on ZrO2/MWCNTs hybrid with high electrocatalytic performance for methanol oxidation. *J. Electroanal. Chem.* **2021**, *898*, 115641. [CrossRef]
29. Vulcu, A.; Radu, T.; Porav, A.; Berghian-Grosan, C. Low-platinum catalyst based on sulfur doped graphene for methanol oxidation in alkaline media. *Mater. Today Energy* **2020**, *19*, 100588. [CrossRef]

30. Kianfar, S.; Golikand, A.N.; ZareNezhad, B. Bimetallic-metal oxide nanoparticles of Pt-M (M: W, Mo, and V) supported on reduced graphene oxide (rGO): Radiolytic synthesis and methanol oxidation electrocatalysis. *J. Nanostructure Chem.* **2020**, *11*, 287–299. [CrossRef]
31. Askari, M.B.; Salarizadeh, P.; Beitollahi, H.; Tajik, S.; Eshghi, A.; Azizi, S. Electro-oxidation of hydrazine on $NiFe_2O_4$-rGO as a high-performance nano-electrocatalyst in alkaline media. *Mater. Chem. Phys.* **2021**, *275*, 125313. [CrossRef]
32. Hernández, J.; Solla-Gullón, J.; Herrero, E.; Aldaz, A.; Feliu, J.M. Methanol oxidation on gold nanoparticles in alkaline media: Unusual electrocatalytic activity. *Electrochim. Acta* **2006**, *52*, 1662–1669. [CrossRef]
33. Chrzanowski, W.; Wieckowski, A. Surface structure effects in platinum/ruthenium methanol oxidation electrocatalysis. *Langmuir* **1998**, *14*, 1967–1970. [CrossRef]
34. Ali, A.; Shen, P.K. Recent advances in graphene-based platinum and palladium electrocatalysts for the methanol oxidation reaction. *J. Mater. Chem. A* **2019**, *7*, 22189–22217. [CrossRef]
35. Sun, H.; Xu, X.; Kim, H.; Jung, W.; Zhou, W.; Shao, Z. Electrochemical water splitting: Bridging the gaps between fundamental research and industrial applications. *Energy Environ. Mater.* **2023**, e12441. [CrossRef]
36. Song, S.; Mu, L.; Jiang, Y.; Sun, J.; Zhang, Y.; Shi, G.; Sun, H. Turning Electrocatalytic Activity Sites for the Oxygen Evolution Reaction on Brownmillerite to Oxyhydroxide. *ACS Appl. Mater. Interfaces* **2022**, *14*, 47560–47567. [CrossRef]
37. Sun, H.; Li, L.; Chen, Y.; Kim, H.; Xu, X.; Guan, D.; Hu, Z.; Zhang, L.; Shao, Z.; Jung, W. Boosting Ethanol Oxidation by NiOOH-CuO Nano-Heterostructure for Energy-Saving Hydrogen Production and Biomass Upgrading. *Appl. Catalysis B Environ.* **2023**, *325*, 122388. [CrossRef]
38. Zhang, G.; Huang, C.; Qin, R.; Shao, Z.; An, D.; Zhang, W.; Wang, Y. Uniform Pd–Pt alloy nanoparticles supported on graphite nanoplatelets with high electrocatalytic activity towards methanol oxidation. *J. Mater. Chem. A* **2015**, *3*, 5204–5211. [CrossRef]
39. Hu, Y.; Mei, T.; Li, J.; Wang, J.; Wang, X. Porous SnO_2 hexagonal prism-attached Pd/rGO with enhanced electrocatalytic activity for methanol oxidation. *RSC Adv.* **2017**, *7*, 29909–29915. [CrossRef]
40. Ye, J.; Cheng, B.; Yu, J.; Ho, W.; Wageh, S.; Al-Ghamdi, A.A. Hierarchical Co_3O_4-NiO hollow dodecahedron-supported Pt for room-temperature catalytic formaldehyde decomposition. *Chem. Eng. J.* **2021**, *430*, 132715. [CrossRef]
41. Nie, Y.; Wang, Y.; Zheng, X.; Yang, T.; Wen, Q.; Fang, Y.; Cheng, X.; Li, R.; Li, L. Minutely surficial functionalization of Ce-O-Pt linkages on Pt/C for enhanced electrocatalytic methanol oxidation. *Appl. Surf. Sci.* **2022**, *602*, 154194. [CrossRef]
42. Khalafallah, D.; Alothman, O.Y.; Fouad, H.; Khalil, K.A. Hierarchical Co_3O_4 decorated PPy nanocasting core-shell nanospheres as a high performance electrocatalysts for methanol oxidation. *Int. J. Hydrogen Energy* **2018**, *43*, 2742–2753. [CrossRef]
43. Askari, M.B.; Salarizadeh, P.; Di Bartolomeo, A.; Zadeh, M.H.R.; Beitollahi, H.; Tajik, S. Hierarchical nanostructures of MgCo2O4 on reduced graphene oxide as a high-performance catalyst for methanol electro-oxidation. *Ceram. Int.* **2021**, *47*, 16079–16085. [CrossRef]
44. Zaiman, N.F.H.N.; Shaari, N. Review on flower-like structure nickel based catalyst in fuel cell application. *J. Ind. Eng. Chem.* **2023**, *119*, 1–76. [CrossRef]
45. Sheikhi, S.; Jalali, F. Hierarchical $NiCo_2O_4$/CuO-C nanocomposite derived from copper-based metal organic framework and Ni/Co hydroxides: Excellent electrocatalytic activity towards methanol oxidation. *J. Alloys Compd.* **2022**, *907*, 164510. [CrossRef]
46. Subramanian, V.; Luo, C.; Stephan, A.M.; Nahm, K.S.; Thomas, S.; Wei, B. Supercapacitors from Activated Carbon Derived from Banana Fibers. *J. Phys. Chem. C* **2007**, *111*, 7527–7531. [CrossRef]
47. Soltani, N.; Bahrami, A.; Pech-Canul, M.; González, L. Review on the physicochemical treatments of rice husk for production of advanced materials. *Chem. Eng. J.* **2015**, *264*, 899–935. [CrossRef]
48. Shen, Z.; Feng, J. Preparation of thermally conductive polymer composites with good electromagnetic interference shielding efficiency based on natural wood-derived carbon scaffolds. *ACS Sustain. Chem. Eng.* **2019**, *7*, 6259–6266. [CrossRef]
49. Askari, N.; Askari, M.B.; Di Bartolomeo, A. Electrochemical Alcohol Oxidation and Biological Properties of Mn_3O_4-Co_3O_4-rGO. *J. Electrochem. Soc.* **2022**, *169*, 106511. [CrossRef]
50. Azizi, S.; Askari, M.B.; Moghadam, M.T.T.; Seifi, M.; Di Bartolomeo, A. Ni_3S_4/NiS/rGO as a promising electrocatalyst for methanol and ethanol electro-oxidation. *Nano Futur.* **2023**, *7*, 015002. [CrossRef]
51. Das, A.K.; Jena, S.; Sahoo, S.; Kuchi, R.; Kim, D.; Aljohani, T.; Nayak, G.C.; Jeong, J.-R. Facile synthesis of $NiCo_2O_4$ nanorods for electrocatalytic oxidation of methanol. *J. Saudi Chem. Soc.* **2020**, *24*, 434–444. [CrossRef]
52. El-Deeb, M.M.; El Rouby, W.M.; Abdelwahab, A.; Farghali, A.A. Effect of pore geometry on the electrocatalytic performance of nickel cobaltite/ carbon xerogel nanocomposite for methanol oxidation. *Electrochim. Acta* **2018**, *259*, 77–85. [CrossRef]
53. Zhang, K.; Han, Y.; Qiu, J.; Ding, X.; Deng, Y.; Wu, Y.; Zhang, G.; Yan, L. Interface engineering of Ni/NiO heterostructures with abundant catalytic active sites for enhanced methanol oxidation electrocatalysis. *J. Colloid Interface Sci.* **2023**, *630*, 570–579. [CrossRef]
54. Li, W.; Song, Z.; Deng, X.; Fu, X.-Z.; Luo, J.-L. Decoration of NiO hollow spheres composed of stacked nanosheets with CeO_2 nanoparticles: Enhancement effect of CeO_2 for electrocatalytic methanol oxidation. *Electrochim. Acta* **2020**, *337*, 135684. [CrossRef]
55. Yang, B.; Yu, Y.; Qiao, J.; Yuan, L.; Shen, X.; Hu, X. Solution plasma method for the preparation of Cu-Ni/CuO-NiO with excellent methanol electrocatalytic oxidation performance. *Appl. Surf. Sci.* **2020**, *513*, 145808. [CrossRef]

56. Luo, Q.; Peng, M.; Sun, X.; Asiri, A.M. Hierarchical nickel oxide nanosheet@nanowire arrays on nickel foam: An efficient 3D electrode for methanol electro-oxidation. *Catal. Sci. Technol.* **2015**, *6*, 1157–1161. [CrossRef]
57. Baruah, B.; Kumar, A. PEDOT: PSS/MnO_2/rGO ternary nanocomposite based anode catalyst for enhanced electrocatalytic activity of methanol oxidation for direct methanol fuel cell. *Synth. Met.* **2018**, *245*, 74–86. [CrossRef]

coatings

Article

A Simple and Efficient Strategy for Preparation of Flexible Strain Sensors Based on Marangoni Effect

Xuqiu Bai [1], Zhichun Xu [1], Xianyi Li [1], Tiantian Zhao [1], Xiang Ge [2,*] and Caideng Yuan [1,3,*]

[1] School of Chemical Engineering and Technology, Tianjin University, Tianjin 300350, China; baixuqiu@tju.edu.cn (X.B.); 2021207592@tju.edu.cn (Z.X.); 3019207325@tju.edu.cn (X.L.); 3017207113@tju.edu.cn (T.Z.)
[2] School of Mechanical Engineering, Tianjin University, Tianjin 300350, China
[3] Guangdong Laboratory of Chemistry and Fine Chemical Industry Jieyang Center, Jieyang 522000, China
* Correspondence: gexiang.hkust@gmail.com (X.G.); cdyuan@tju.edu.cn (C.Y.)

Abstract: The Marangoni effect is a phenomenon of mass transfer between two fluids with different surface tensions, which has been used in many fields. In this paper, we prepared ultrathin conductive films with graphene (GN) and carbon nanotubes (CNTs) based on the Marangoni effect. The Marangoni self-assembled film exhibited excellent properties, showing a conductivity of 8.3 $k\Omega \cdot sq^{-1}$, a transparency of 74% at 550 nm and a thickness of 28 nm when the mass ratio of CNTs and GN was 1:1. The conductive films were transferred to flexible substrates twice and fabricated face to face as strain sensors. The 3M4910-based strain sensors, which were prepared with a simple process and high material utilization rate, exhibited good sensitivity (GF = 5.7), a wide working range (193%) and satisfactory cyclic stability. The PDMS-based GN sensor showed high sensitivity (GF = 34), a wide working range (78%) and excellent stability (ε = 10%, > 8000 cycles). It has been proved that the sensors can be used to detect different joint movements of the human body and subtle movements, showing good application prospects in physiological signal detection.

Keywords: Marangoni effect; flexible strain sensors; graphene; carbon nanotubes

Citation: Bai, X.; Xu, Z.; Li, X.; Zhao, T.; Ge, X.; Yuan, C. A Simple and Efficient Strategy for Preparation of Flexible Strain Sensors Based on Marangoni Effect. *Coatings* **2023**, *13*, 1101. https://doi.org/10.3390/coatings13061101

Academic Editors: Gianfranco Carotenuto and Emerson Coy

Received: 22 April 2023
Revised: 3 June 2023
Accepted: 11 June 2023
Published: 15 June 2023

1. Introduction

The Marangoni effect is a phenomenon of mass transfer between two fluids with different surface tensions where the fluid flows from a region of low surface tension to a region of high surface tension [1,2]. In nature, some insects can propel themselves rapidly by using the Marangoni effect without employing the oscillatory movements of legs [1]. The Marangoni effect is also responsible for the formation of "wine tears" on glass walls. As the alcohol in the wine evaporates from the surface continuously, the alcohol concentration of the liquid on the glass wall drops even faster, causing the surface tension of the liquid on the glass wall to be greater than that of the liquid in the glass, so that the wine moves upward along the glass wall and eventually forms "wine tears". The Marangoni effect can be used to induce nanosheets spread out into a thin single film. Compared with the films prepared by drip casting and spin coating, the film based on the Marangoni effect has a significant advantage in uniformity, a fast film-formation rate and simple operation [2].

Shim et al. [2] demonstrated a rapid interfacial assembly strategy for large-area graphene sheets. When EA (ethyl acetate) was injected into a water/N-methylpyrrolidone suspension of graphene, EA triggered the graphene sheets' convective transport rapidly and assembled into a uniform graphene film of arbitrarily large areas in a matter of minutes. The Marangoni effect has important applications in different fields. For example, Wu et al. [3] used Marangoni self-assembly technology to prepare large-area graphene films with a low friction coefficient (about 0.05) and developed a new lubrication system, which has broad prospects in engineering applications. Yoshida et al. [1] proposed a Marangoni propelling microrobot integrated with a wireless photonic colloidal crystal hydrogel sensor for detecting water environments and transmitting environmental information.

Recently, the Marangoni effect has been used in the fabrication of flexible strain sensors, which convert mechanical strains into electrical signals [4]. As the "nerve endings" in the Internet of Things world, flexible strain sensors are the key components of intelligent devices and wearable devices, which have a wide range of applications in human–computer interaction [5–7], electronic skin [8], health monitoring [9–11], etc.

According to sensing principles, flexible sensors can generally be divided into resistance sensors [12,13], capacitive sensors [14] and piezoelectric sensors [15,16]. Resistance sensors, which convert strains to resistance changes, have been widely studied because of their simple structures, high sensing performance, simple signal conversion mechanism and stable signal output. Moreover, flexible sensors can be roughly classified according to their microstructures, including full-filling [17,18], sandwich-like [9,19] and adsorption sensors [20,21]. The sandwich-like sensors, consisting of conductive films and two layers of flexible substrates, have received extensive attention owing to their high sensitivity and stability. The common methods of sensor preparation include spinning coating [22], spraying [9,23], scraping [24], rod coating [25], printing [12,19], swelling/permeating [26–28], self-assembly [5,29], layer-by-layer (LBL) assembly [20,30,31], laser inducement [32–34], chemical vapor deposition (CVD) [35,36], electrodeposition (ED) [37], etc. Flexible strain sensors are generally composed of conductive materials and flexible substrates. Conductive materials play an important role in constructing conductive networks and generating resistance change under strain. Graphene (GN) [12,25], carbon nanotubes (CNTs) [8,9,20], carbon black (CB) [38], silver nanowires (AgNWs) [29,39] and conductive polymers [37,40] have been widely used as conductive materials. Flexible substrates show the function of supporting and connecting conductive materials, responding to stress and strain, which is crucial to the flexibility and stretchability of sensors. Flexible substrates such as polydimethylsiloxane (PDMS) [9,22], polyurethane (PU) [8,12,15] and fabric [41,42] have been widely applied in the electronic field. Gauge factor (GF) is a factor used to estimate the sensitivity of strain sensors, which is defined as $GF = (\Delta R/R_0)/\varepsilon$, where R_0 (Ω), ΔR (Ω) and ε (%) represent the initial resistance without strain, and the resistance change with strain and applied strain, respectively [43,44]. Sensitivity and the working range are a pair of parameters that restrict each other. The strategy of increasing sensitivity often reduces the working range and vice versa. Generally, the sensing performance of sensors is synthetically evaluated by their conductivity, sensitivity, working range, response time and cyclic stability [43,44].

Most of the sensors based on the Marangoni effect employ ultrathin graphene films as sensitive layers, all of which show high sensitivity and excellent sensing performance. Li et al. [43] injected graphene/ethanol dispersion onto the surface of deionized (DI) water. Due to the Marangoni effect, ethanol with graphene sheets flowed from the region of low surface tension (ethanol) to that of high surface tension (DI water). As ethanol evaporated, graphene sheets collided and bonded at the liquid/air interface through π–π interactions. "Fish scale" graphene film was formed on the water surface with a thickness of 2.5–5.0 nm and high transparency (86%–94% at 550 nm). Ultrathin graphene film (UGF) strain sensors with a "fish scale" microstructure showed an ultrahigh sensitivity of 1037 GF at 2% strain and could be used to detect electrical signals generated by small deformation, such as pulse and sound waves. Similarly, Jia et al. [44] skimmed the assembled graphene film to pre-stretched PDMS substrates. The strain sensor (pre-strain, 50%) based on the double-layer pleated graphene films showed high sensitivity (GF = 37.1), a wide working range (>50%) and excellent cyclic stability (ε = 20%, >5000 times). Jiang et al. [45] transferred Marangoni self-assembled graphene films to patterned PDMS by skimming, and assembled them onto an interdigitated Ni/Au electrode to fabricate a high-performance piezoresistive pressure sensor. The sensor exhibited high sensitivity (1.04–1875.5 kPa^{-1}) and high durability (15,000 cycles) over a large linear detection range (1–40 kPa).

Inspired by the Marangoni effect, we prepared Marangoni-assembled ultrathin conductive films with GN and CNTs to exert their synergistic effect. After transferring the films twice onto flexible substrates and assembling them face to face, we obtained flexible strain sensors with high conductivity. Expensive instruments and complicated operations are not necessary in the fabrication progress, and the sensitivity, working range and cyclic stability of strain sensors are excellent. Compared with the reported Marangoni-based sensors, our fabrication process improves the utilization of carbonous nanomaterials and exerts the synergistic effect of GN and CNTs to adjust the sensitivity and working range of sensors.

2. Materials and Methods

2.1. Materials

The graphite paper was supplied by Beijing Jinglong Special Carbon Technology Co., Ltd. (Beijing, China). CNTs (carbon purity: >99 wt%; diameter: 5–15 nm; length: 10–30 μm) was purchased from Chengdu Organic Chemicals Co., Ltd. (Chengdu, China). 3M4910 tape was obtained from 3M China Co., Ltd. (Shanghai, China). PDMS (Sylgard 184 Silicone Elastomer) was provided by Dow Corning Corp. (Midland, MI, USA). Conductive silver paste was supplied by Shenzhen Woweisi Electronic Technology Co., Ltd. (Shenzhen, China). NaOH (superior purity) was provided by Damao Chemical Reagent Factory (Tianjin, China). Ethanol (95%, analytical purity) was purchased from Tianjin Jiangtian Chemical Technology Co., Ltd. (Tianjin, China).

2.2. Preparation of the Sensor

Preparation of graphene. GN was produced by electrochemical exfoliation method. The graphite paper (anode) was electrolyzed at 5.5 V, using the platinum electrode as the contrast electrode (cathode) and 1 $\text{mol}\cdot\text{L}^{-1}$ NaOH solution as the electrolyte. The electrolysis process was carried out in an ice bath and more than 100 mg product was obtained within 20 min. After the electrolysis process, the electrolyte solution was filtered through a 0.22 μm PTFE microporous filter membrane, and then the filter cake was washed to neutral with DI water. After drying at 50 °C for about 6 h, GN was obtained.

Fabrication of Marangoni-driven conductive film. We used GN and CNTs as conductive materials. A certain volume of carbonous nanomaterials/ethanol dispersion with the concentration of 1 $\text{mg}\cdot\text{mL}^{-1}$ was added dropwise onto the surface of 100 cm^2 DI water in a plastic square petri dish. As the dispersion dropped in, the carbonous nanomaterials (GN or CNTs) gradually covered the water surface, forming a layer of continuous film in a few seconds. Then we put the matching lid on the petri dish tightly and flipped it carefully to transfer the film onto the lid. After that, the film on the lid was dried at 50 °C for 20 min.

Transfer of Marangoni-driven conductive film. The dried conductive film on the petri dish lid was pasted onto 3M4910 tape. A scraping plate was used to drive out the bubbles so as to make a thorough transfer of conductive film. After freezing at −20 °C for 15 min, the 3M tape (lost elasticity temporarily to avoid being stretched) was torn off, and the conductive film was transferred onto the stretchable 3M tape. In addition, the paste progress can be repeated again to increase their electrical conductivity. Moreover, the conductive film on water can be transferred to PDMS (main agent to hardener mass ratio 10:1, spun at 300 $\text{r}\cdot\text{min}^{-1}$ on the spin coater, cured at 45 °C for 6 h) by skimming method, which skims a layer of conductive film by PDMS with the plane size of 0.8 cm × 2.5 cm on a glass sheet.

Fabrication procedures of the strain sensor. A strain sensor was fabricated by combining two pieces of composite films face to face. The substrate of the composite film was 3M tape (3M4910) or PDMS, where only one layer of conductive film could be pasted to PDMS, while one or two layers of conductive film could be pasted to 3M4910 tape. In order to distinguish the number of the conductive film layers of the sensor, we named the 3M4910-based sensors composed of different layers of conductive film as the (m + n) sensor, where m and n, respectively, represented the number of layers of conductive film pasted on the 3M tapes. For example, (2 + 1) represented the sensor formed by a piece of 3M tape with two conductive layers and another piece of 3M tape with one conductive layer, while (1 + 0) represented a sensor composed of a piece of 3M tape with one layer of conductive layer and another piece of clean 3M tape without conductive film. For 3M4910-based sensors, if their names were not specified, they were (2 + 2)-type sensors. Copper wires were drawn by conductive silver paste at both ends of the conductive layer to form electrodes. The width of the conductive layer was 0.8 cm and the distance between the two electrodes was 2 cm. For clarity, a schematic diagram for the fabrication procedures of the 3M4910-based strain sensor and photos are presented in Figure 1.

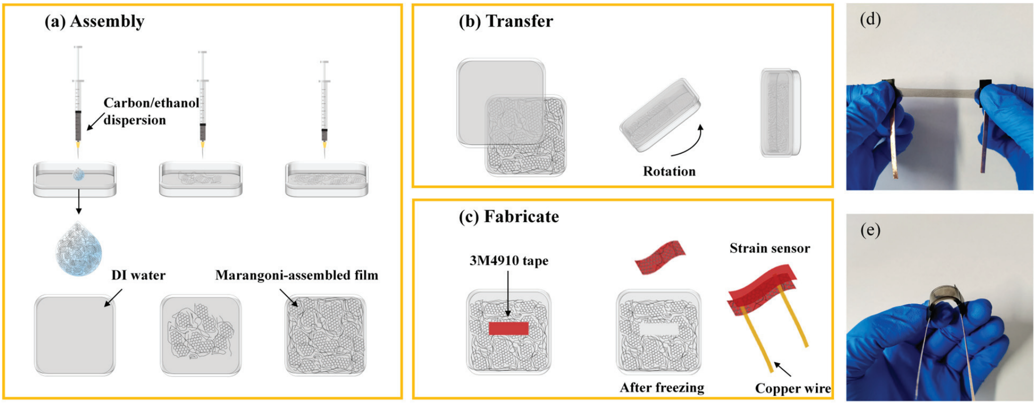

Figure 1. Fabrication procedures of 3M4910-based flexible strain sensor using Marangoni effect. (**a**) A certain volume of carbon/ethanol dispersion was dripped onto the surface of DI water in plastic square petri dish to assemble Marangoni-driven conductive film. (**b**) The lid of the petri dish was closed tightly and the petri dish was turned gently to transfer the conductive film on water to the lid. (**c**) The conductive film was pasted onto 3M4910 tape, and freezing for 15 min is helpful to peel off the tape without stretching. Copper wires were drawn by conductive silver paste at both ends of the conductive layer to form electrodes. Two layers of conductive tapes were combined face to face to form a strain senor. The picture of a (**d**) stretched and (**e**) bent strain sensor.

2.3. Characterization and Measurement

The morphologies of GN and CNTs were characterized by field emission scanning electron microscope (SEM, Regulus 8100, Hitachi, Tokyo, Japan) at an accelerating voltage of 3.0 kV, transmission electron microscopy (TEM, Talos F200x, FEI, Brno, Czechia) and atomic force microscope (AFM, Dimension Icon, Bruker, Karlsruhe, Germany). A thin layer of platinum was sputter-coated before SEM measurements. Raman spectrometer (inVia, Renishaw, Wotton-under-Edge, UK) was employed to characterize the quality of CNTs and GN with 532 nm laser. The thickness of Marangoni-assembled films was measured by an ellipsometer (M-2000v, J. A. Woollam Co., Inc., Lincoln, NE, USA). Sheet resistances of the conductive films were measured by a four-probe resistivity tester (RTS-8, Guangzhou Four Probe Technology Co., Ltd., Guangzhou, China) under 25 °C and 60% RH. A UV-visible spectrophotometer (TU-1900, Beijing Purkinje General Instrument Co., Ltd., Beijing, China) was employed to measure the light transmittance of the samples in the range of 400–800 nm. The strain-sensing behaviors were measured using an electrochemical workstation (VERTEX V16407, Ivium Technologies, Eindhoven, Netherlands) coupled with a universal electronic tensile machine (WDW-05L, Jinan Spai Technology Co., Ltd., Jinan, China) with the rate of 50 mm·min^{-1}.

3. Results and Discussion

3.1. *The Characterization of CNTs and GN*

SEM, AFM and TEM were used to characterize the microstructure of carbon materials. As can be seen from Figures 2 and S1a,b, CNTs are a one-dimensional structure with a pipe diameter of about 10–20 nm. In the natural state, CNTs are curled and intertwined, forming an interconnected network. GN exhibits a two-dimensional layered structure in Figures 2b,c and S1c,d. Moreover, GN is composed of multiple stacked layers together with a large number of folds. These folds are easily disperses under a strong ultrasound, thus forming small transverse lamellae and causing cracks around the GN. TEM was used to analyse the microstructure of GN (Figure 2d). The TEM image shows that the surface of the GN is relatively flat and the transverse size of the lamellae is about 1–2 µm. In Figure 2e, the AFM image further proves that the transverse size of GN is about 1–3 µm and the thickness is about 1.4 nm, which means the GN has a large lateral dimension and thin thickness and may be composed of 1–3 layers of a GN monolayer [43]. The cracks were observed around the graphene lamellar layer as well.

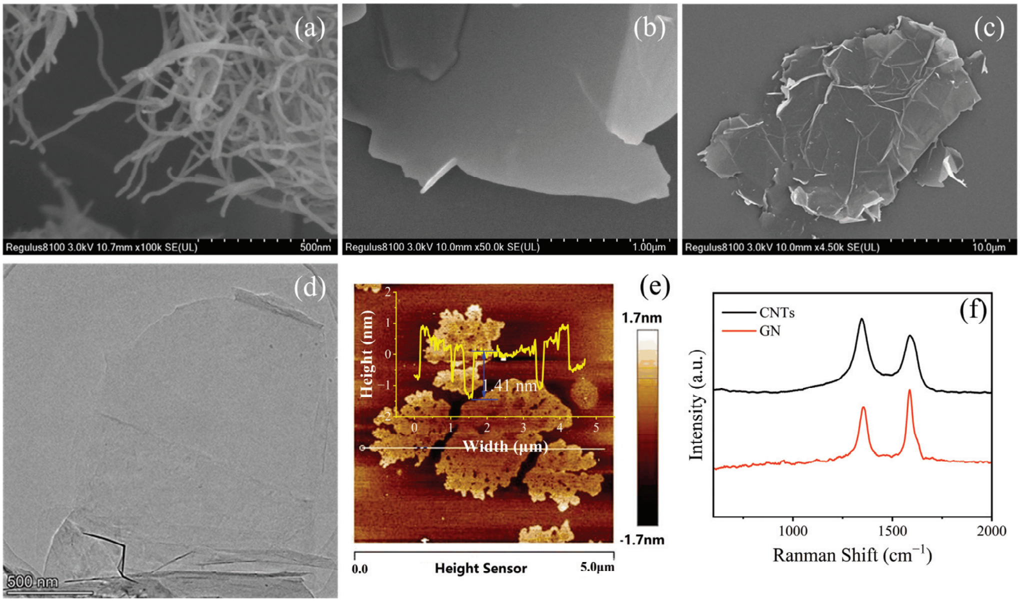

Figure 2. SEM images of (**a**) CNTs and (**b**,**c**) GN, magnified 100 k, 50 k, 4.5 k, respectively. (**d**) TEM images of GN. (**e**) AFM images of GN. The inset of panels shows the thickness of GN. (**f**) Raman spectra of CNTs and GN.

Raman spectroscopy was used to assess the quality of CNTs and GN, as shown in Figure 2f. The value of I_D/I_G is critical to evaluate the degree of crystal defects of graphene derivatives. The larger the value of I_D/I_G, the more defects exist in the material; conversely, the smaller the value of I_D/I_G, the fewer defects exist and the more structured the material. The I_D/I_G values of CNTs and GN were 1.29 and 0.75, respectively, indicating the high quality of the CNTs and GN with few defects.

3.2. *Effects of the Proportions of CNTs and GN*

One-dimensional CNTs and two-dimensional GN can be combined as conductive materials to enhance their synergy. Marangoni-assembled films exhibit different structures and performance when CNTs and GN are mixed in different proportions, which is crucial for sensor design. GN nanosheets can easily slip during stretching, resulting in damage to the conductive network, which is beneficial to the sensitivity but limits the working range of sensors. CNTs have a certain tensile property due to their one-dimensional structure with a high length–diameter ratio, and are curly and tangled in their natural state. Even the sensor based on CNTs is stretched due to large strains, although the CNTs' network is not completely destroyed, which benefits the conductivity and working range of the sensor.

In the process of Marangoni assembly, we injected 1 mg·mL^{-1} carbonous nanomaterials/ethanol dispersion with the volume of 0.5 mL, in which the CNTs' mass proportions were 25%, 50%, 75% and 100%, respectively. When GN was used alone without CNTs, the Marangoni self-assembly phenomenon of the carbon nanomaterials was completely different to the GN/CNTs composite, so we will discuss the situation separately.

Compared with the 25% CNTs film (Figures 3a and S2a,e), there were more CNTs distributed on the surface of the GN nanosheets when the mass ratio of CNTs and GN increased to 1:1, as shown in Figures 3b and S2b. It could be clearly observed that the junctions between GN nanosheets were also overlapped by CNTs, and the conductive pathways were further increased. It is worth noting that the GN network was formed while CNTs were too sparse to form a single CNT network. Figures 3c and S2c,f show the microstructure of the conductive film with 75% CNTs. It can be seen that it was not only GN nanosheets that were connected to a network, but CNTs were also connected to form a CNT network. While using 100% of CNTs, the conductive network obtained by self-assembly with the same mass of carbonous materials was tighter, as shown in Figures 3d and S2d.

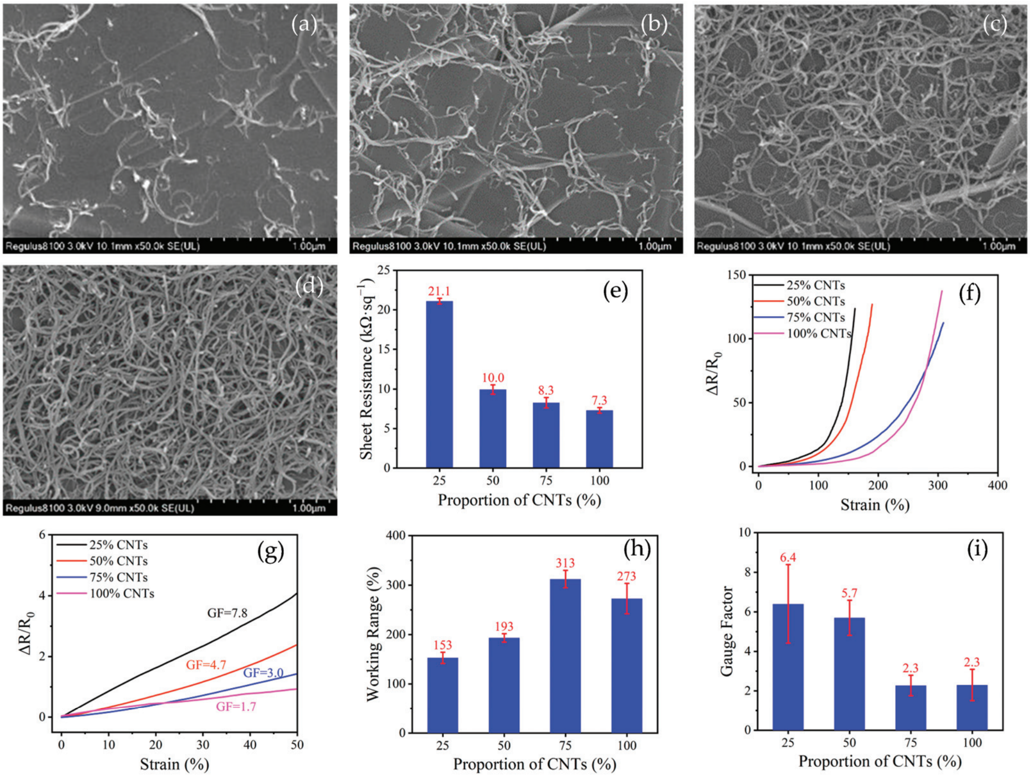

Figure 3. Effects of proportions of CNTs and GN on microstructure of conductive films and properties of sensors. SEM images of Marangoni self-assembled conductive films with different proportions of CNTs: (**a**) 25% CNTs, (**b**) 50% CNTs, (**c**) 75% CNTs, (**d**) 100% CNTs. (**e**) Sheet resistance of Marangoni self-assembled conductive films. (**f**) Strain−ΔR/R$_0$ curves and (**g**) enlarged strain−ΔR/R$_0$ curves of strain sensors. (**h**) Working range diagram and (**i**) sensitivity diagram of strain sensors.

The thicknesses of the films with 50% CNTs and 100% CNTs were 28 nm and 38 nm, respectively, tested by the ellipsometer on polished silicon wafer substrates. Four kinds of conductive films were transferred to quartz plates, and the resistance of the films was measured by a four-probe resistivity tester. As can be seen from Figure 3e, the sheet resistances of the conductive films with CNTs of 25%, 50%, 75% and 100% were 21.1 $k\Omega \cdot sq^{-1}$, 10.0 $k\Omega \cdot sq^{-1}$, 8.3 $k\Omega \cdot sq^{-1}$ and 7.3 $k\Omega \cdot sq^{-1}$, respectively. The conductivity increased successively mainly because the electrical conductivity of the CNTs (0.12 $\Omega \cdot cm$) used in the experiment was higher than that of the GN (1.57 $\Omega \cdot cm$).

We used 3M4910 tape as a flexible substrate, and pasted the self-assembled films twice on the tape. Two pieces of composite conductive films were assembled face to face with copper tapes as electrodes, then a strain sensor was obtained. We stretched the sensors using a tension machine with the rate of 50 $mm \cdot min^{-1}$, and recorded the resistance change. As shown in Figure 3f–i, the ratio of GN and CNTs affected the working range and sensitivity of the sensors. The working range broadened as the CNTs' proportion increased, while the sensitivity decreased. GN has a lamellar structure, which means it can easily slip during stretching and result in damage to the conductive network [43,44]. When the composite film was stretched to large strains, CNTs worked as "bridges", which was helpful to reduce the agglomeration between GN nanosheets, increase the number of conductive paths and enhance the overall electrical conductivity to a large extent. Therefore, a higher proportion of CNTs is helpful to protect the network and increase the working range.

The working range of the sensor with 75% CNTs was broader than that of the sensor with 100% CNTs because of the synergistic effect of GN and CNTs. When the CNTs' network was completely destroyed under a large strain, GN with a large area could still play a role in connecting the CNTs. Therefore, the conductive network with 75% CNTs was less likely to be damaged than that with 100% CNTs.

3.3. Effect of Carbonous Nanomaterials/Ethanol Dispersion Volume on Properties of Sensors

The volume of the added dispersion affects the density of the self-assembled film when the water surface is limited. A total of 1 $mg \cdot mL^{-1}$ 50% CNTs/ethanol dispersion with different volumes was added dropwise to a 100 cm^2 water surface. In the self-assembly process, when less than 0.3 mL dispersion was used, the conductive film could not cover the entire water surface, while when more than 0.6 mL dispersion was added, the excess carbon material aggregated on the water surface or sank in the water.

Figures 4a–d and S3 show the SEM images of Marangoni-assembled films formed by 50% CNTs dispersion in different volumes. It can be seen that GN and CNTs completely covered the silicon substrate at the addition of the volume of 0.3 mL, forming good conductive paths. CNTs were also evenly distributed on the GN layer when the added volume was successively increased to 0.4, 0.5 and 0.6 mL. The sheet resistances of films self-assembled by different volumes of dispersions were 17.7 $k\Omega \cdot sq^{-1}$, 12.9 $k\Omega \cdot sq^{-1}$, 10.0 $k\Omega \cdot sq^{-1}$ and 8.5 $k\Omega \cdot sq^{-1}$, respectively, as shown in Figure 4e. The more carbon materials that were used in self-assembly, the denser the conductive network, and the better the conductivity of the film.

As shown in Figure 4f, the transmittance of the conductive film was tested with an ultraviolet–visible spectrophotometer. The films self-assembled from 0.3 mL and 0.5 mL dispersion had light transmittances of 83% and 74% at 550 nm, respectively. As the volume of dispersion increased, the density of the film increased, so the light transmittance decreased gradually.

As can be seen from Figure 4g–i, the working ranges of sensors prepared by different volumes of dispersion are all over 170%, and the sensitivities are 2.9, 3.6, 5.7 and 3.9, respectively. With more and more carbon materials assembled on films, the GN and CNTs connected with each other even tighter, with a certain overlap area. The tighter the conductive network, the less likely it was to be broken. Therefore, when the sensor was stretched to large strains, the overlapped nanosheets and numerous CNTs were more helpful to avoid the network being damaged totally, which increased the working range and decreased the sensitivity of the sensor. However, the sensitivity of the sensor from 0.5 mL dispersion was higher than that of the sensor from 0.4 mL dispersion, possibly because the aggregation between nanomaterials made the sheets slip more easily, resulting in the film being more prone to fracturing.

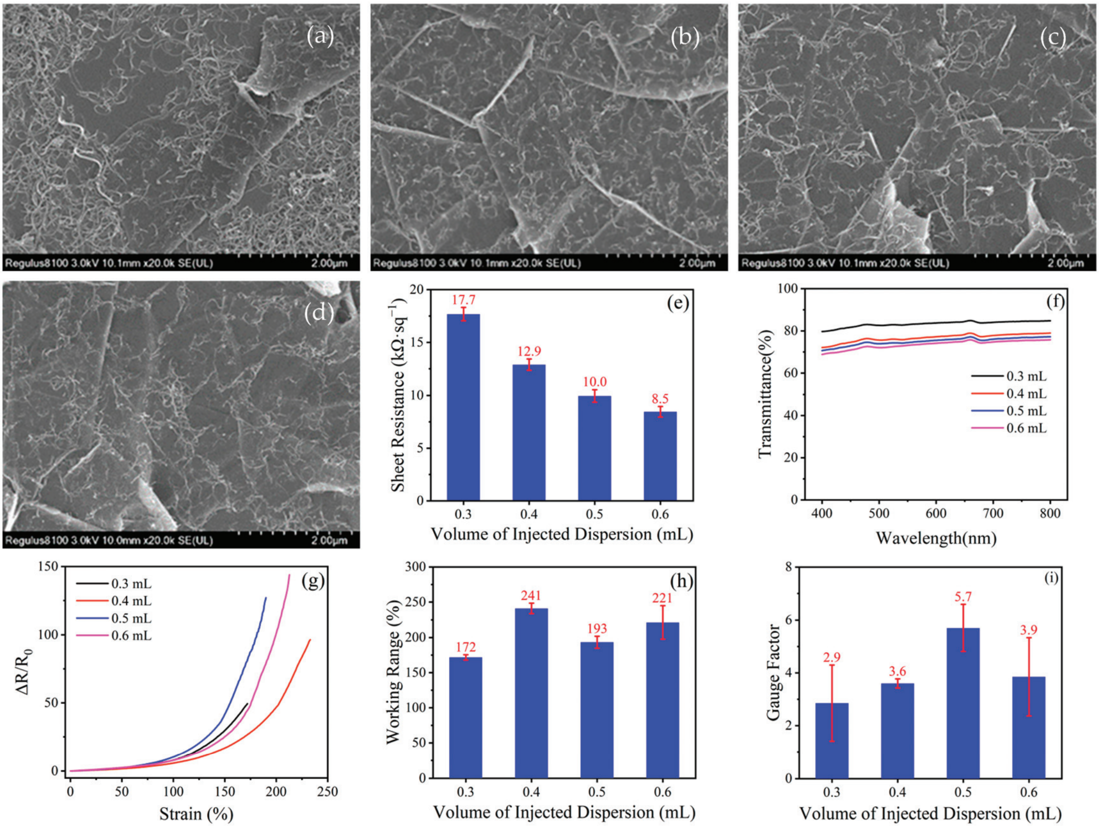

Figure 4. SEM images of Marangoni self-assembled conductive films made by different volumes of 50% CNTs/ethanol dispersion (**a**) 0.3 mL, (**b**) 0.4 mL, (**c**) 0.5 mL, (**d**) 0.6 mL. (**e**) Sheet resistance of 50% CNT conductive films made by different volumes of dispersion. (**f**) Transmittance spectra in the wavelength range from 400 to 800 nm of 50% CNT conductive films made by different volumes of dispersion. (**g**) Strain−$\Delta R/R_0$ diagram of 50% CNT strain sensors made of Marangoni self-assembled conductive films with different volumes of dispersion. (**h**) Working range diagram and (**i**) sensitivity diagram of 50% CNT strain sensors made of Marangoni self-assembled conductive films with different volumes of dispersion.

3.4. Effect of Layers of Conductive Films on Properties of Sensors

The number of conductive films transferred to the substrate has an important effect on the conductivity of the sensor. In the experiment, we pasted conductive films (50% CNTs film assembled by 0.5 mL dispersion) at different times with the 3M tape and assembled them face to face to fabricate sensors with different layers of conductive films. It is worth mentioning that the conductive film could be completely transferred using the 3M tape firstly, and a small part of the film was left in the second pasting because the stickiness of the 3M tape reduced a lot after the first pasting. After pasting twice, the stickiness of the tape was too weak to paste any film.

As shown in Figure 5a, the transparency of the films decreased together with the total paste times. The (2 + 2) sensor still exhibited good transparency and the printed words "strain sensor" under the films could be observed clearly. The resistance of the sensors with different layers of conductive films increased in turn with the decrease in conductive film layers, shown in Figure 5b. In other words, the more conductive materials that were transferred to the substrate, the conductive layer was thicker, and the conductivity of the sensor was better.

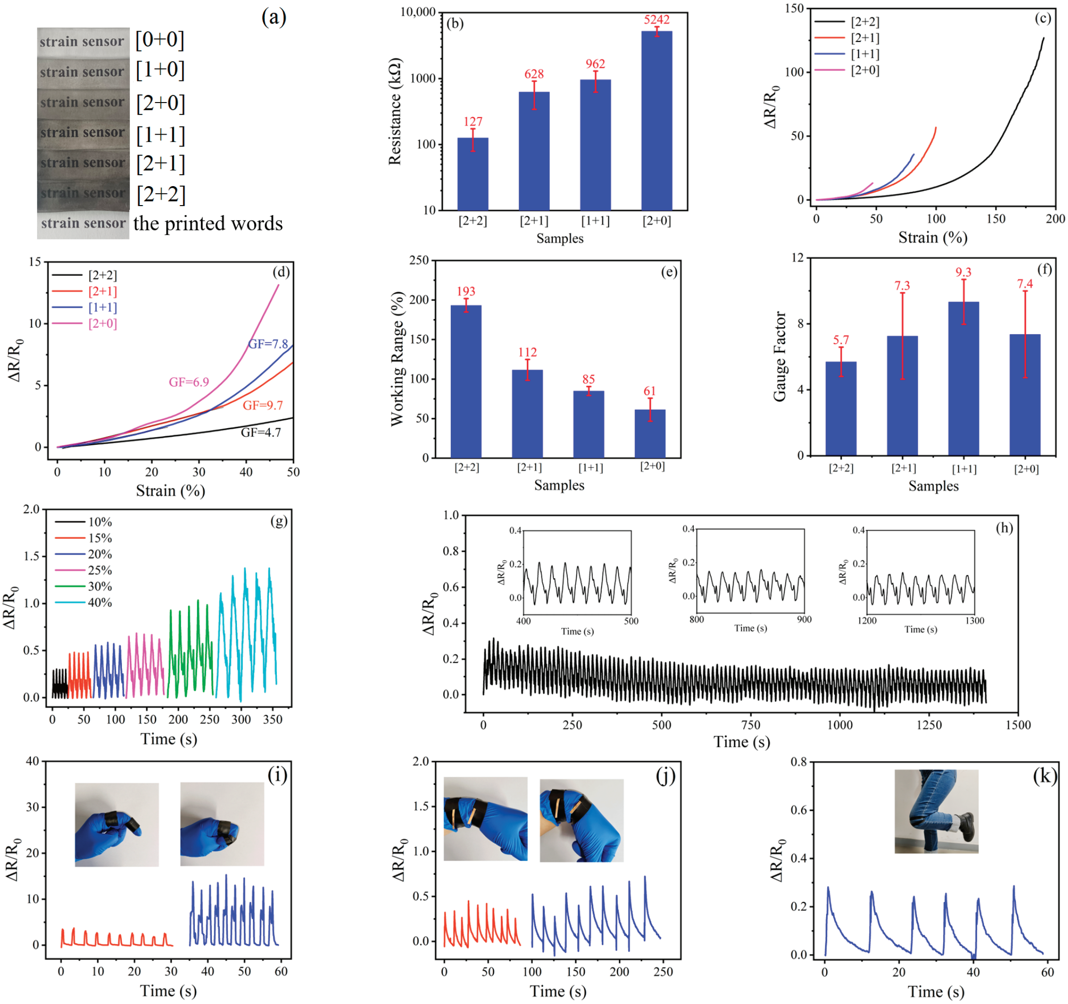

Figure 5. (**a**) The transparency of 3M tapes with different layers of Marangoni self-assembled conductive films made by 0.5 mL 50% CNTs/ethanol dispersion. (**b**) Resistance of strain sensors made by different layers of conductive films. (**c**) Strain−ΔR/R$_0$ diagram and (**d**) enlarged strain−ΔR/R$_0$ diagram of strain sensors made by different layers of conductive films. (**e**) Working range diagram and (**f**) sensitivity diagram of strain sensors made by different layers of conductive films. (**g**) Resistance changes of the 50% CNTs strain sensor made by 0.5 mL dispersion under different strains. Three insets are the enlarged figures of several cycles at different times. (**h**) Stability test of 50% CNTs strain sensor at ε = 10%, with the rate of 20 mm·min^{-1}. The relative resistance changes of the 50% CNTs strain sensor in response to (**i**) finger bend, (**j**) wrist bend and (**k**) knee bend. The illustration shows the corresponding actions.

Electrical signals were collected under constant tension, and the resistance change is shown in Figure 5c–f. The working ranges of sensors with different layers of conductive films were 193% (2 + 2), 112% (2 + 1), 85% (1 + 1) and 61% (2 + 0). As the thickness of the conductive layer and the content of carbon materials increased, the network was harder to break and the working range of the sensor increased as a result.

The sensitivity of the sensors (2 + 2), (2 + 1) and (1 + 1) increased from 5.7 to 7.3 and 9.3, respectively. In other words, the sensors' sensitivities became higher and higher as the thickness of the conductive layers and the content of carbon materials decreased because the conductive network became easier to break. Moreover, the (2 + 0) sensor was less sensitive than the (1 + 1) one because these two layers of conductive films were pressed tightly together and the conductive network was not so easy to damage.

The (2 + 2) sensors responded to different strains repeatedly with the rate of 50 $mm \cdot min^{-1}$, as shown in Figure 5g. $\Delta R/R_0$ increased as the sensor was stretched, and exhibited basically consistent performance under the same strain, showing good recovery performance and stability. The microstructure of the film after repeated stretching and recovery with the strain of 30% is shown in Figure S4.

Cyclic stability is an important performance measurement for sensors. In Figure 5h, the 3M-based sensor (made of 0.5 mL 50% CNTs/ethanol dispersion) was repeatedly stretched to $\varepsilon = 10\%$ at a rate of 20 $mm \cdot min^{-1}$. After cycle testing for a long time, the electrical signal basically remained stable and the peak shape remained consistent.

The (2 + 2) sensor was applied to the joints of the human body to detect the resistance change during movement, as shown in Figure 5i–k. When the sensor was fixed at the second joint of the index finger and bent to about 45°, the sensor responded quickly and sensitively, with $\Delta R/R_0$ reaching 4. When the bend degree increased to the maximum (about 120°), $\Delta R/R_0$ raised to about 15. In addition, when the finger repeated the same bending motion several times, the electrical signals were similar, due to the sensor's good accuracy and repeatability.

The sensor was affixed to the wrist and knee to detect changes in electrical signals caused by different joints, as shown in Figure 5j,k. The relative resistance increased as the wrist joint gradually bent, and decreased as the joint gradually returned to the straight state. When the wrist was bent inward by about 30°, $\Delta R/R_0$ increased to about 0.4, and when it bent inward by about 45° (maximum), $\Delta R/R_0$ increased to about 0.7. Moreover, when the tester subjected the sensor on the knee to a kick back motion, the electronic signal responded quickly, and $\Delta R/R_0$ reached about 0.2. The sensor made from 50% CNTs proved its ability to detect human body action.

3.5. Effect of Substrates on Properties of Sensors

A flexible substrate is an important part of a sensor, as it affects the structure and function of the sensor. In order to explore the influence of substrate types on the performance of the sensor, the sensors based on 3M4910 and PDMS were fabricated using the conductive films formed by carbonous materials/ethanol dispersion with 50% CNTs and 100% CNTs, respectively.

The 3M4910-based sensor was fabricated by using 3M4910 tape to paste a 50% CNTs film twice face to face, while the PDMS-based sensor was fabricated by skimming the conductive film twice. No matter which kind of material was used as the flexible substrate, the sensitivity and working range of the sensors showed the same trend as the proportion of CNTs; that is, the sensor with 100% CNTs, exhibited a wider working range and lower sensitivity than that with 50% CNTs, as shown in Figure 6.

When the proportion of CNTs was the same, the working range of the 3M4910-based sensor was much larger than that of the PDMS-based sensor because 3M tape has a higher fracture strain (more than 1100%). Even if the 3M4910-based sensor was stretched to an extremely high strain and lost its conductivity totally, the 3M tape remained unbroken. When the PDMS-based sensor was stretched so there was a sharp increase in resistance, the PDMS ruptured at the same time. The sensitivity of the PDMS-based sensor was slightly higher than that of the 3M4910-based sensor, which may be caused by the harder PDMS material and there being less carbon material.

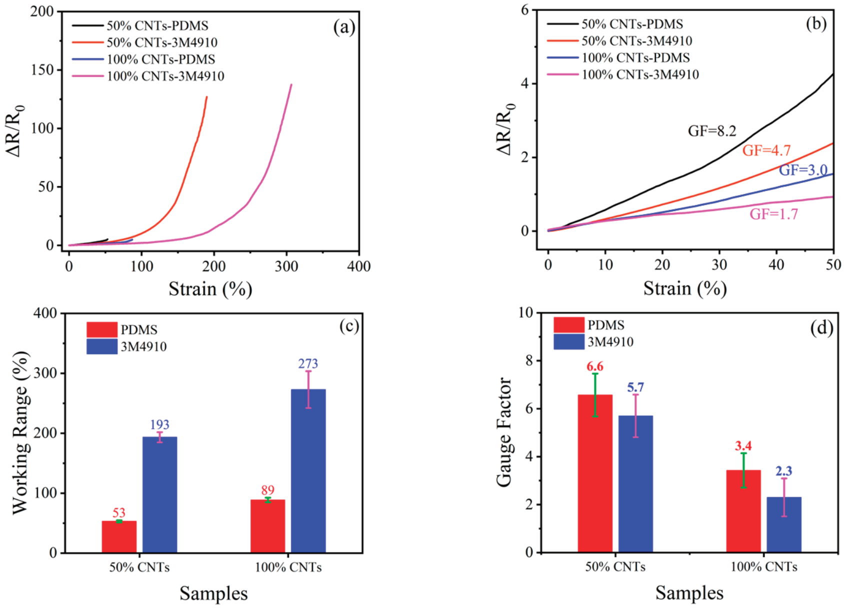

Figure 6. (**a**) Strain—$\Delta R/R_0$ diagram and (**b**) enlarged strain—$\Delta R/R_0$ diagram of strain sensors based on different substrates. (**c**) Working range diagram and (**d**) sensitivity diagram of strain sensors based on different substrates.

3.6. GN Strain Sensor

When using GN/ethanol dispersion without CNTs to prepare conductive films through Marangoni self-assembly, the experimental results were completely different from the case with CNTs. At least 3 mL of GN/ethanol dispersion was required to form a dense GN film on a 100 cm^2 water surface, while when using the dispersion containing 50% CNTs and 50% GN, only 0.5 mL dispersion was needed to form a self-assembled film of the same area. The SEM images, as shown in Figure 7a,b, exhibit GN nanosheets stacked on the top of each other similar to “fish scales”. The GN film was as thick as 4 μm, and the average sheet resistance of the GN films was 1.4 kΩ·sq^{-1}, measured by AFM and a four-probe resistivity tester, respectively. A large number of bubbles and cracks occurred frequently when we transferred the GN films on water to petri dish lids, which limited the transfer of the GN films to 3M tape by pasting. Therefore, we used PDMS as the flexible substrate to skim the GN films repeatedly, and the average resistance of the GN sensors fabricated face to face was 10.9 kΩ.

We stretched the GN sensors at the rate of 50 mm·min^{-1} and recorded the change in resistance to obtain the strain—$\Delta R/R_0$ relationship diagram, as shown in Figure 7c. GN sensors exhibited a smaller working range (78%) and higher sensitivity (GF = 34) than GN/CNTs sensors, mainly due to the GN nanosheets slipping very easily and causing resistance changes when the film was stretched without the overlapping of CNTs.

The GN sensor was repeatedly stretched to different strains and recovered at the stretching rate of 50 mm·min^{-1}, and the results are shown in Figure 7d,e. The $\Delta R/R_0$ was obviously different under different strains, and was basically consistent under the same strain, showing good recovery performance and stability. As shown in Figure 7f, the response and recovery time of the GN sensor were about 110 ms and 250 ms, respectively, which means the sensor responses were fast enough to be applied in reality.

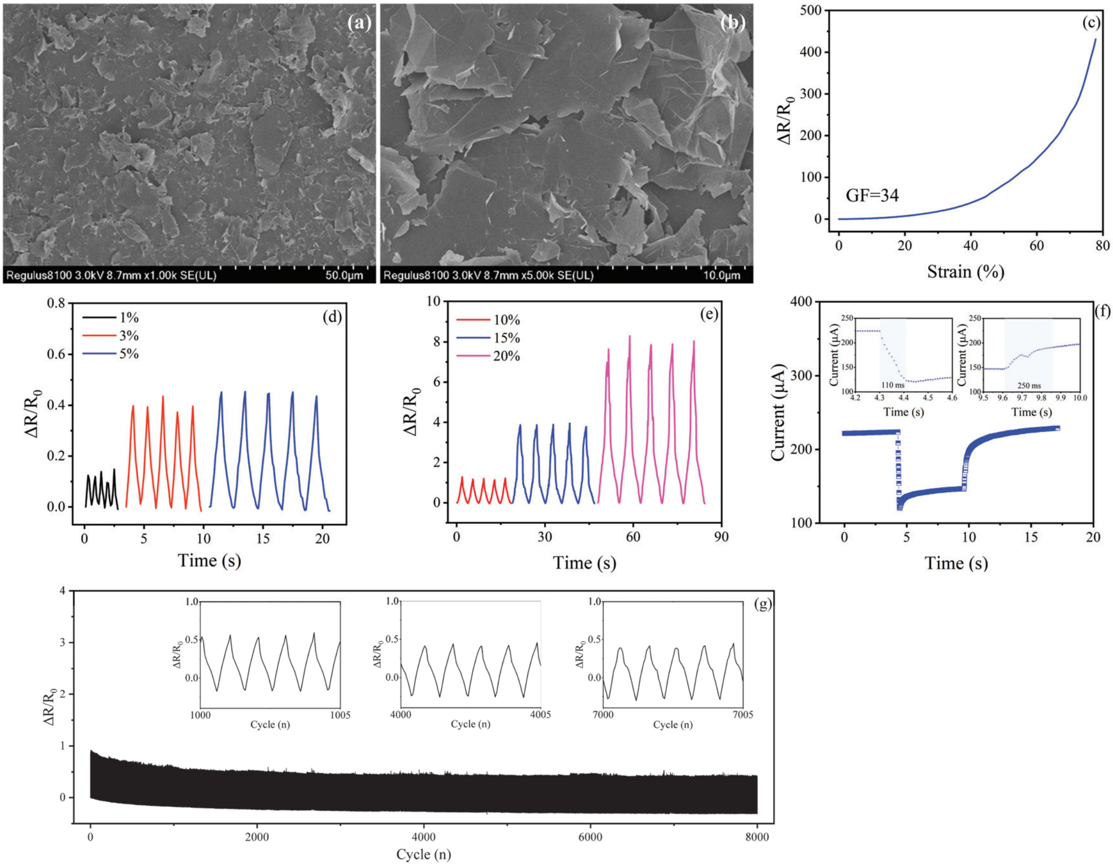

Figure 7. (**a**,**b**) SEM images of Marangoni self-assembled GN film, magnified 1 k and 5 k, respectively. (**c**) Strain−$\Delta R/R_0$ diagram of the GN sensor. (**d**) Resistance changes of the GN sensor under small strains and (**e**) large strains. (**f**) Response time and recovery time of the GN sensor (ε = 5%, with the rate of 500 mm·min^{-1}). The inserts are the enlarged figures of response time and recovery time, respectively. (**g**) Stability test of the GN sensor at ε = 10%, with the rate of 100 mm·min^{-1}. Three insets are the enlarged figures of several cycles at different times.

The GN sensor also exhibited excellent cyclic stability. In Figure 7g, the sensor was stretched to ε = 10% with the rate of 100 mm·min^{-1}. After 8000 cycles of testing, the electrical signal remained stable. In conclusion, the test shows that the sensors have excellent cyclic stability and can meet the requirements of electronic devices.

As shown in Figure 8a–c, when the GN sensor was stretched together with the bend and recover of the finger, wrist and knee, the resistance changed quickly and $\Delta R/R_0$ was higher than that of the 50% CNTs sensor because of the high sensitivity of the GN sensor. In addition, the GN sensor could detect subtle movements of the human body. In Figure 8d–i, the sensor was successfully applied to detect the mouth opening, swallowing, saying "hi", a frown, a blink and the pulse beating, and all of these output stable and reliable electrical signals. The experiments have proved that our strain sensors show great potential in real-time motion detection and can hopefully be applied in reality.

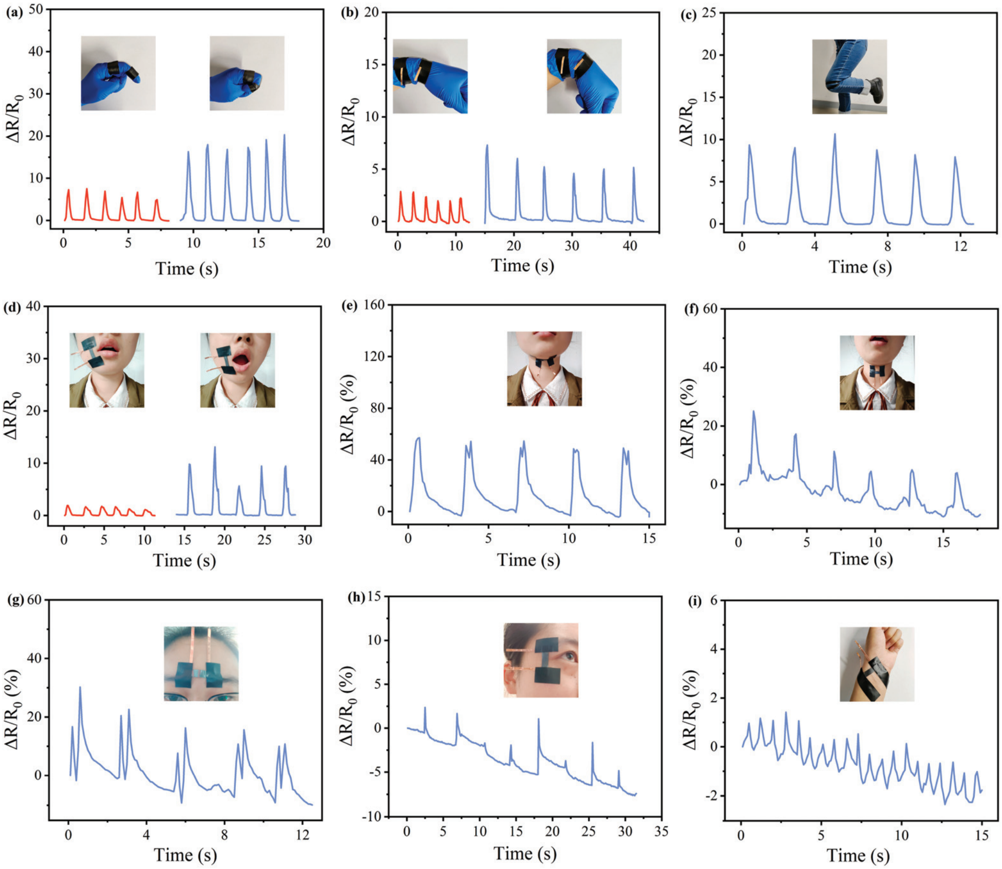

Figure 8. Practical applications of strain sensors. The relative resistance changes of the GN sensor in response to (**a**) finger bend, (**b**) wrist bend, (**c**) knee bend, (**d**) mouth open, (**e**) swallow, (**f**) saying "hi", (**g**) frown, (**h**) blink and (**i**) pulse beating. The illustration shows the corresponding actions.

4. Conclusions

In this paper, we designed high-performance flexible strain sensors with a simple strategy. Ultrathin GN/CNTs conductive films were self-assembled on the water surface in a few seconds due to the Marangoni effect. The sheet resistance, optical transmittance (at 550 nm) and thickness of the Marangoni self-assembled film (with the mass ratio of CNTs and GN 1:1) were 8.3 $k\Omega \cdot sq^{-1}$, 74% and 28 nm, respectively. After transferring the films to flexible substrates twice and packaging them face to face, flexible strain sensors with high sensing performance were obtained. The mass ratio of CNTs and GN and overall carbon content exhibited an enormous influence on sensors' properties, especially their sensitivity, working range, conductivity and transparency. The synergistic effect between CNTs and GN was helpful for the conductivity and working range of sensors because of the combined network structure. With the increase in overall carbon content, the conductivity and working range of sensors increased, while their sensitivity and optical transmittance decreased, for the reason that tighter and thicker conductive networks were vulnerable to being destroyed. The sensors made of the Marangoni self-assembled film using 0.5 mL carbonous nanomaterials/ethanol dispersion with 50% CNTs based on 3M4910 showed satisfactory sensitivity (GF = 5.7), a large working range (193%) and good cyclic stability. The sensors made of the film assembled by 3 mL GN/ethanol dispersion based on PDMS exhibited high sensitivity (GF = 34), a wide working range (78%) and excellent cyclic stability (ε = 10%, >8000 cycles). In addition, they both performed outstandingly in sensing different strains with a short response and recovery time. The experimental results indicate the remarkable potential for the strain sensors to be applied in human motion detection.

Supplementary Materials: The following supporting information can be downloaded at: https://www.mdpi.com/article/10.3390/coatings13061101/s1, Figure S1. SEM images of (a,b) CNTs and (c,d) GN. Figure S2. SEM images of Marangoni self-assembled conductive films made by different proportions of CNTs and GN. (a) 25% CNTs, (b) 50% CNTs, (c) 75% CNTs, (d) 100% CNTs, magnified 5 k, (e) 25% CNTs and (f) 75% CNTs, magnified 1 k. Figure S3. SEM images of Marangoni self-assembled conductive films made by different volumes of 50% CNTs/ethanol dispersion. (a) 0.3 mL, (b) 0.4 mL, (c) 0.5 mL, (d) 0.6 mL, magnified 1 k. Figure S4. The SEM images of Marangoni self-assembled films based on 3M4910 after stretching and recovery repeatedly with the strain of 30%.

Author Contributions: Conceptualization, X.B. and C.Y.; data curation, X.B.; formal analysis, X.B. and Z.X.; investigation, X.B., Z.X., X.L. and T.Z.; methodology, X.B., X.G. and C.Y.; project administration, C.Y.; resources, X.G. and C.Y.; supervision, C.Y.; validation, X.B., X.L. and T.Z.; visualization, X.B.; writing—original draft, X.B.; writing—review and editing, X.G. and C.Y. All authors have read and agreed to the published version of the manuscript.

Funding: This research was funded by the National Natural Science Foundation of China (No. 31971250 and 52075371).

Institutional Review Board Statement: Not applicable.

Informed Consent Statement: Not applicable.

Data Availability Statement: Not applicable.

Conflicts of Interest: The authors declare no conflict of interest.

References

1. Yoshida, K.; Onoe, H. Marangoni-propulsion micro-robots integrated with a wireless photonic colloidal crystal hydrogel sensor for exploring the aquatic environment. *Adv. Intell. Syst.* **2022**, *4*, 2100248. [CrossRef]
2. Shim, J.; Yun, J.M.; Yun, T.; Kim, P.; Lee, K.E.; Lee, W.J.; Ryoo, R.; Pine, D.J.; Yi, G.R.; Kim, S.O. Two-minute assembly of pristine large-area graphene based films. *Nano Lett.* **2014**, *14*, 1388–1393. [CrossRef]
3. Wu, P.; Li, X.; Zhang, C.; Chen, X.; Lin, S.; Sun, H.; Lin, C.T.; Zhu, H.; Luo, J. Self-assembled graphene film as low friction solid lubricant in macroscale contact. *ACS Appl. Mater. Interfaces* **2017**, *9*, 21554–21562. [CrossRef] [PubMed]
4. Amjadi, M.; Kyung, K.; Park, I.; Sitti, M. Stretchable, skin-mountable, and wearable strain sensors and their potential applications: A review. *Adv. Funct. Mater.* **2016**, *26*, 1678–1698. [CrossRef]
5. Dong, H.; Sun, J.; Liu, X.; Jiang, X.; Lu, S. Highly sensitive and stretchable MXene/CNTs/TPU composite strain sensor with bilayer conductive structure for human motion detection. *ACS Appl. Mater. Interfaces* **2022**, *14*, 15504–15516. [CrossRef] [PubMed]
6. Nela, L.; Tang, J.; Cao, Q.; Tulevski, G.; Han, S.J. Large-area high-performance flexible pressure sensor with carbon nanotube active matrix for electronic skin. *Nano Lett.* **2018**, *18*, 2054–2059. [CrossRef]
7. Chen, Q.; Xiang, D.; Wang, L.; Tang, Y.; Harkin-Jones, E.; Zhao, C.; Li, Y. Facile fabrication and performance of robust polymer/carbon nanotube coated spandex fibers for strain sensing. *Compos. Part A Appl. Sci. Manuf.* **2018**, *112*, 186–196. [CrossRef]
8. Moheimani, R.; Aliahmad, N.; Aliheidari, N.; Agarwal, M.; Dalir, H. Thermoplastic polyurethane flexible capacitive proximity sensor reinforced by CNTs for applications in the creative industries. *Sci. Rep.* **2021**, *11*, 1104. [CrossRef]
9. Chen, J.; Zhu, Y.; Jiang, W. A stretchable and transparent strain sensor based on sandwich-like PDMS/CNTs/PDMS composite containing an ultrathin conductive CNT layer. *Compos. Sci. Technol.* **2020**, *186*, 107938. [CrossRef]
10. Sun, Z.; Yang, S.; Zhao, P.; Zhang, J.; Yang, Y.; Ye, X.; Zhao, X.; Cui, N.; Tong, Y.; Liu, Y.; et al. Skin-like ultrasensitive strain sensor for full-range detection of human health monitoring. *ACS Appl. Mater. Interfaces* **2020**, *12*, 13287–13295. [CrossRef] [PubMed]
11. Lee, J.; Pyo, S.; Kwon, D.S.; Jo, E.; Kim, W.; Kim, J. Ultrasensitive strain sensor based on separation of overlapped carbon nanotubes. *Small* **2019**, *15*, 1805120. [CrossRef] [PubMed]
12. Li, Z.; Li, B.; Chen, B.; Zhang, J.; Li, Y. 3D printed graphene/polyurethane wearable pressure sensor for motion fitness monitoring. *Nanotechnology* **2021**, *32*, 395503. [CrossRef]
13. Xu, M.; Li, F.; Zhang, Z.; Shen, T.; Qi, J. Piezoresistive sensors based on rGO 3D microarchitecture: Coupled properties tuning in local/integral deformation. *Adv. Electron. Mater.* **2019**, *5*, 1800461. [CrossRef]
14. Kim, S.; Dong, Y.; Hossain, M.M.; Gorman, S.; Towfeeq, I.; Gajula, D.; Childress, A.; Rao, A.M.; Koley, G. Piezoresistive graphene/P(VDF-TrFE) heterostructure based highly sensitive and flexible pressure sensor. *ACS Appl. Mater. Interfaces* **2019**, *11*, 16006–16017. [CrossRef]

15. Lv, B.; Chen, X.; Liu, C. A highly sensitive piezoresistive pressure sensor based on graphene oxide/polypyrrole@polyurethane sponge. *Sensors* **2020**, *20*, 1219. [CrossRef] [PubMed]
16. Chen, Z.; Wang, Z.; Li, X.; Lin, Y.; Luo, N.; Long, M.; Zhao, N.; Xu, J.B. Flexible piezoelectric-induced pressure sensors for static measurements based on nanowires/graphene heterostructures. *ACS Nano* **2017**, *11*, 4507–4513. [CrossRef]
17. Meng, X.Y.; Zhao, S.F.; Zhang, Z.; Zhang, R.L.; Li, J.H.; Leng, J.F.; Cao, D.X.; Zhang, G.P.; Sun, R. Nacre-inspired highly stretchable piezoresistive Cu-Ag nanowire/graphene synergistic conductive networks for strain sensors and beyond. *J. Mater. Chem. C* **2019**, *7*, 7061–7072. [CrossRef]
18. Luo, Y.; Zhao, P.; Yang, Q.; He, D.; Kong, L.; Peng, Z. Fabrication of conductive elastic nanocomposites via framing intact interconnected graphene networks. *Compos. Sci. Technol.* **2014**, *100*, 143–151. [CrossRef]
19. Zhu, W.B.; Xue, S.S.; Zhang, H.; Wang, Y.Y.; Huang, P.; Tang, Z.H.; Li, Y.Q.; Fu, S.Y. Direct ink writing of a graphene/CNT/silicone composite strain sensor with a near-zero temperature coefficient of resistance. *J. Mater. Chem. C* **2022**, *10*, 8226–8233. [CrossRef]
20. Ma, Z.; Wei, A.; Ma, J.; Shao, L.; Jiang, H.; Dong, D.; Ji, Z.; Wang, Q.; Kang, S. Lightweight, compressible and electrically conductive polyurethane sponges coated with synergistic multiwalled carbon nanotubes and graphene for piezoresistive sensors. *Nanoscale* **2018**, *10*, 7116–7126. [CrossRef]
21. Tian, Y.; Wang, D.; Li, Y.; Tian, H.; Yang, Y.; Ren, T.L. Highly sensitive, wide-range, and flexible pressure sensor based on honeycomb-like graphene network. *IEEE Trans. Electron Devices* **2020**, *67*, 2153–2156. [CrossRef]
22. Zhang, F.; Wu, S.; Peng, S.; Sha, Z.; Wang, C.H. Synergism of binary carbon nanofibres and graphene nanoplates in improving sensitivity and stability of stretchable strain sensors. *Compos. Sci. Technol.* **2019**, *172*, 7–16. [CrossRef]
23. Liu, Y.; Zhang, D.; Wang, K.; Liu, Y.; Shang, Y. A novel strain sensor based on graphene composite films with layered structure. *Compos. Part A Appl. Sci. Manuf* **2016**, *80*, 95–103. [CrossRef]
24. Amjadi, M.; Turan, M.; Clementson, C.P.; Sitti, M. Parallel microcracks-based ultrasensitive and highly stretchable strain sensors. *ACS Appl. Mater. Interfaces* **2016**, *8*, 5618–5626. [CrossRef] [PubMed]
25. Zhang, M.; Wang, C.; Wang, Q.; Jian, M.; Zhang, Y. Sheath-core graphite/silk fiber made by dry-meyer-rod-coating for wearable strain sensors. *ACS Appl. Mater. Interfaces* **2016**, *8*, 20894–20899. [CrossRef]
26. Zhang, X.; Ke, L.; Zhang, X.; Xu, F.; Hu, Y.; Lin, H.; Zhu, J. Breathable and wearable strain sensors based on synergistic conductive carbon nanotubes/cotton fabrics for multi-directional motion detection. *ACS Appl. Mater. Interfaces* **2022**, *14*, 25753–25762. [CrossRef]
27. Zhang, R.; Ying, C.; Gao, H.; Liu, Q.; Fu, X.; Hu, S. Highly flexible strain sensors based on polydimethylsiloxane/carbon nanotubes (CNTs) prepared by a swelling/permeating method and enhanced sensitivity by CNTs surface modification. *Compos. Sci. Technol.* **2019**, *171*, 218–225. [CrossRef]
28. Wang, Y.; Jia, Y.; Zhou, Y.; Wang, Y.; Zheng, G.; Dai, K.; Liu, C.; Shen, C. Ultra-stretchable, sensitive and durable strain sensors based on polydopamine encapsulated carbon nanotubes/elastic bands. *J. Mater. Chem. C* **2018**, *6*, 8160–8170. [CrossRef]
29. Chen, S.; Wei, Y.; Wei, S.; Lin, Y.; Liu, L. Ultrasensitive cracking-assisted strain sensors based on silver nanowires/graphene hybrid particles. *ACS Appl. Mater. Interfaces* **2016**, *8*, 25563–25570. [CrossRef]
30. Zheng, X.; Hu, Q.; Wang, Z.; Nie, W.; Wang, P.; Li, C. Roll-to-roll layer-by-layer assembly bark-shaped carbon nanotube/$Ti_3C_2T_x$ MXene textiles for wearable electronics. *J. Colloid Interface Sci.* **2021**, *602*, 680–688. [CrossRef]
31. Zhang, R.; Pan, P.; Dai, Q.; Yang, X.; Yang, Z.; Wei, J.; Liu, J.; Yuan, Q. Sensitive and wearable carbon nanotubes/carbon black strain sensors with wide linear ranges for human motion monitoring. *J. Mater. Sci.-Mater. Electron.* **2018**, *29*, 5589–5596. [CrossRef]
32. Lin, J.; Peng, Z.; Liu, Y.; Ruiz-Zepeda, F.; Ye, R.; Samuel, E.L.; Yacaman, M.J.; Yakobson, B.I.; Tour, J.M. Laser-induced porous graphene films from commercial polymers. *Nat. Commun.* **2014**, *5*, 5714. [CrossRef]
33. Zhu, Y.; Cai, H.; Ding, H.; Pan, N.; Wang, X. Fabrication of low-cost and highly sensitive graphene-based pressure sensors by direct laser scribing polydimethylsiloxane. *ACS Appl. Mater. Interfaces* **2019**, *11*, 6195–6200. [CrossRef] [PubMed]
34. Luong, D.; Subramanian, A.; Silva, G.; Yoon, J.; Cofer, S.; Yang, K.; Owuor, P.S.; Wang, T.; Wang, Z.; Lou, J.; et al. Laminated object manufacturing of 3D-printed laser-induced graphene foams. *Adv. Mater.* **2018**, *30*, 1707416. [CrossRef] [PubMed]
35. Shi, J.; Hu, J.; Dai, Z.; Zhao, W.; Liu, P.; Zhao, L.; Guo, Y.; Yang, T.; Zou, L.; Jiang, K.; et al. Graphene welded carbon nanotube crossbars for biaxial strain sensors. *Carbon* **2017**, *123*, 786–793. [CrossRef]
36. Shi, J.; Li, X.; Cheng, H.; Liu, Z.; Zhao, L.; Yang, T.; Dai, Z.; Cheng, Z.; Shi, E.; Yang, L.; et al. Graphene reinforced carbon nanotube networks for wearable strain sensors. *Adv. Funct. Mater.* **2016**, *26*, 2078–2084. [CrossRef]
37. Choi, E.J.; Drago, N.P.; Humphrey, N.J.; Van Houten, J.; Ahn, J.; Lee, J.; Kim, I.-D.; Ogata, A.F.; Penner, R.M. Electrodeposition-enabled, electrically-transduced sensors and biosensors. *Mater. Today* **2023**, *62*, 129–150. [CrossRef]
38. Huang, Y.; He, X.; Gao, L.; Wang, Y.; Liu, C.; Liu, P. Pressure-sensitive carbon black/graphene nanoplatelets-silicone rubber hybrid conductive composites based on a three-dimensional polydopamine-modified polyurethane sponge. *J. Mater. Sci.-Mater. Electron.* **2017**, *28*, 9495–9504. [CrossRef]
39. Dong, X.; Wei, Y.; Chen, S.; Lin, Y.; Liu, L.; Li, J. A linear and large-range pressure sensor based on a graphene/silver nanowires nanobiocomposites network and a hierarchical structural sponge. *Compos. Sci. Technol.* **2018**, *155*, 108–116. [CrossRef]
40. Muhammad, W.; Kim, S.D. Highly stretchable PPy/PDMS strain sensors fabricated with multi-step oxygen plasma treatment. *Polymers* **2023**, *15*, 1714. [CrossRef] [PubMed]

41. Wang, Y.; Hao, J.; Huang, Z.; Zheng, G.; Dai, K.; Liu, C.; Shen, C. Flexible electrically resistive-type strain sensors based on reduced graphene oxide-decorated electrospun polymer fibrous mats for human motion monitoring. *Carbon* **2018**, *126*, 360–371. [CrossRef]
42. Yin, B.; Wen, Y.; Hong, T.; Xie, Z.; Yuan, G.; Ji, Q.; Jia, H. Highly stretchable, ultrasensitive, and wearable strain sensors based on facilely prepared reduced graphene oxide woven fabrics in an ethanol flame. *ACS Appl. Mater. Interfaces* **2017**, *9*, 32054–32064. [CrossRef] [PubMed]
43. Li, X.; Yang, T.; Yang, Y.; Zhu, J.; Li, L.; Alam, F.E.; Li, X.; Wang, K.; Cheng, H.; Lin, C.T.; et al. Large-area ultrathin graphene films by single-step Marangoni self-assembly for highly sensitive strain sensing application. *Adv. Funct. Mater.* **2016**, *26*, 1322–1329. [CrossRef]
44. Jia, Y.; Chen, W.; Ye, C.; Yang, R.; Yang, L.; Zhang, Z.; Hu, Q.; Liang, B.; Yang, B.-R.; Tang, Z.; et al. Controllable formation of periodic wrinkles in Marangoni-driven self-assembled graphene film for sensitive strain detection. *Sci. China Mater.* **2020**, *63*, 1983–1992. [CrossRef]
45. He, J.; Xiao, P.; Lu, W.; Shi, J.; Zhang, L.; Liang, Y.; Pan, C.; Kuo, S.W.; Chen, T. A universal high accuracy wearable pulse monitoring system via high sensitivity and large linearity graphene pressure sensor. *Nano Energy* **2019**, *59*, 422–433. [CrossRef]

coatings

Article

Sol–Gel Silica Coatings for Corrosion Protection of Aluminum Parts Manufactured by Selective Laser Melting (SLM) Technology

Luciano Macera [1,*], Daniele Pullini [2], Alberto Boschetto [1], Luana Bottini [1], Claudio Mingazzini [3] and Gian Luca Falleti [4]

[1] Mechanical and Aerospace Engineering Department, Sapienza University of Rome, Via Eudossiana 18, 00184 Roma, Italy; alberto.boschetto@uniroma1.it (A.B.); luana.bottini@uniroma1.it (L.B.)
[2] Centro Ricerche Fiat Scpa, Strada Torino 50, 10043 Orbassano, Italy; daniele.pullini@crf.it
[3] Nalucoat Benefit Srl, Via Canale 300, 42013 Casalgrande, Italy; info@nalucoat.it
[4] Nanoprom Chemicals Srl, Via Canale 300, 42013 Casalgrande, Italy; gianluca@nanoprom.it
* Correspondence: luciano.macera@uniroma1.it

Abstract: Metal additive manufacturing is a rapidly growing field based on the fabrication of complex parts with improved performance. The advantages of using this technology include the production of shapes that cannot be produced by traditional machining technologies, the possibility of using trabecular reinforcing structures, and the ability to make parts with topological optimization that allow for increased performance and decreased mass of the parts produced. Metal parts produced by selective laser melting technology exhibit high surface roughness, which limits their direct implementation. Corrosion protection of these surfaces is difficult, especially for galvanic processes. This paper analyzes the possibility of using sol–gel silica (silicon oxide) coatings to effectively protect various surfaces of aluminum alloys produced by selective laser melting technology. Silicon oxide sol–gel protective coatings have demonstrated excellent chemical stability and corrosion resistance, being able to be applied in very thin layers. These properties make them excellent candidates for protecting additive-manufactured metal parts, especially as-built surfaces with a high surface roughness. Nanostructured silica sol–gel protective coatings have demonstrated excellent corrosion resistance and have the potential to replace the highly toxic chromium-based galvanic treatments. Using nanostructured silica sol–gel coatings, aluminum parts can be seamlessly integrated into circular-economy cycles.

Keywords: selective laser melting; sol–gel coatings; circular economy

Citation: Macera, L.; Pullini, D.; Boschetto, A.; Bottini, L.; Mingazzini, C.; Falleti, G.L. Sol–Gel Silica Coatings for Corrosion Protection of Aluminum Parts Manufactured by Selective Laser Melting (SLM) Technology. *Coatings* **2023**, *13*, 1081. https://doi.org/10.3390/coatings13061081

Academic Editor: Peter Rodič

Received: 13 March 2023
Revised: 6 June 2023
Accepted: 7 June 2023
Published: 11 June 2023

1. Introduction

In recent decades, industry has made great strides in the production of consumer goods, thanks in part to the availability of cheap energy from fossil fuels and the development of industrial control systems based on increasingly sophisticated and effective computer systems (e.g., vision systems, robotic systems, etc.) [1].

The steady improvement in economic and social conditions has also pushed markets toward an assumption of continued growth, which is also corroborated by the expansion of new customers resulting from the globalization of markets [2].

Unfortunately, the industry's strong expansionary drive has led to the indiscriminate use of natural resources without regarding the global impacts; this aspect, combined with the extensive use of fossil fuels, causes sudden and significant changes in the ecosystem, especially at the atmospheric level [3,4]. Moreover, pollution of water and soil by microplastics is an incontrovertible phenomenon, which is constantly and worryingly increasing [5,6].

Additive manufacturing (AM), also known as 3D printing, uses a Computer-Aided Design (CAD) model to define objects in 3D and then fabricate them layer by layer [7].

It was initially used for prototyping parts, but technological evolution has transformed this field [8,9], making it a mainstream manufacturing sector. One of the main advantages of AM is that the entire process chain can be completely digital. The product is designed with CAD software and the processed files can be sent via the Internet to a 3D printer to print the object anywhere in the world. As a result, logistical and warehousing impacts are reduced, and stored parts can be drastically minimized and printed as needed [10].

Unlike traditional industrial manufacturing, AM enables the efficient use of resources [11], reducing energy costs and special waste typically produced by traditional technologies such as casting, machining, and plastic deformation.

Through the production of AM-made metal parts, used resources and wastes are minimized, and when a product reaches the end of its life cycle, it is modified so that it can be reused, creating new value [12].

AM is therefore also seen as a powerful enabler of the circular economy, enabling the reduction of energy consumption to reduce operating costs and greenhouse gas emissions. In fact, producing aluminum from recycled sources requires 95 percent less energy than production from mined ore [13].

Aluminum's characteristic properties make it an ideal material for the purposes of the new market drivers embodied in the concepts of circular economy and environmental sustainability [14].

Its high strength-to-stiffness-to-weight ratios, good formability, good corrosion resistance, and recycling potential make it an ideal candidate to replace heavier materials, e.g., steel, in industry. The extensive use of aluminum alloys helps to reduce the weight of fabricated components by enabling improved point-of-view efficiency and resulting in lower energy consumption and, thus, less air pollution [15].

Aluminum alloy parts made by traditional manufacturing methods (casting, forging, and extrusion) have several process-related issues which generally contribute to a medium-to-large microstructure. Conversely, parts produced by SLM technology have a very fine microstructure [16], which allows for improved mechanical performance [17]. A lower fatigue strength remains a drawback, which can be solved by using high-pressure heat treatments [18].

SLM technology is used to produce high-value parts with very complex designs, which cannot be made with conventional technologies; the high cost of this process prevents its extensive use in industry, but combined parts made in AM with parts made with conventional technologies at low production costs make its use in industrial production possible, making hybrids that use AM technology only where it is really needed [19].

The aluminum parts' corrosion resistance is typically increased by a protection technology which must not contrast principles of sustainability and material reuse of the circular economy. Historically, aluminum parts were protected by chromate conversion coating. It primarily serves as a corrosion inhibitor which is made by conversion and used to passivate alloys of stainless steel, aluminum, zinc, and other metals [20]. Chromate conversion coatings are usually applied by soaking the part in a chemical bath of acidic solution of chromate and fluoride until a film of the desired thickness is formed, removing the part, rinsing it, and allowing it to dry. The process is usually performed at room temperature, with a few minutes of soaking. Bath composition varies widely depending on the material to be coated and the desired effect. The main components of the solutions used for forming chromate-conversion-coating films are trivalent and hexavalent chromium [21]; the base metal; various oxides; water; and several additional components, such as phosphates, sulfates, and fluorides. These elements are highly toxic, the hexavalent chromium is carcinogenic, and trivalent chromium tends to migrate to the hexavalent formulation [22]; hence, the parts coated by this process are classified as special waste at the end of their operating life and cannot be disposed of in ordinary waste cycles (landfill or recycling).

With a view to environmental sustainability and the circular economy, it is necessary to find other coatings for the corrosion protection of metals and, in particular, aluminum alloys, which are the perfect candidate for the circular economy because, at the end of its life, an aluminum-alloy component can be re-melted to become raw material for processing or, in the case of AM technology, can be atomized into powders for use with SLM technology [23].

In the late 1990s, silanes encountered great interest sparked by the possibility of using these compounds as “coupling agents” between metals and their coatings, as well as between metals and conventional painting. Moreover, these primers can be used by themselves or nano-additivated in various ways, as corrosion inhibitors [24,25].

Sol–gel coatings can be deposited to the metal substrate through various techniques, such as dip-coating, spin-coating, and spraying, which do not need a high temperature and vacuum conditions. In recent years, sol–gel coatings have been studied extensively for the replacement of the toxic and carcinogenic chromate-containing coatings [26,27].

One methodology for the formation of thin and strong sol–gel films at room temperature is based on the use of sol–gel nanoparticles that are pre-formed in a solution. These pre-assembled nanoparticles (SNAP: Self-Assembled Nanoscale Particle) polymerize without forming the porosities associated with hydrolysis and condensation products [28].

This technology enables the fabrication of silicon-based sol–gel coatings whose coating formation properties, barrier properties, performance, and morphology are formulated to provide thin, dense films using only the room-temperature process based on standard organic crosslinking reactions to form the film after application [29].

A set of corrosion tests were conducted on aluminum alloy specimens made with SLM technology in order to validate the protection effectiveness of a commercial coating made in silica sol–gel technology. The expected results aim to confirm that this corrosion-protection system is effective and can replace chromic-conversion treatments to make aluminum parts eco-friendly and enable them for use in the circular-economy supply chain.

2. Materials and Methods

The AlSi10Mg and Al6061 alloy specimens tested in this work were fabricated by using SLM technology. The specimens are sheets of various sizes: 250 × 75 × 1 mm^3, 50 × 50 × 2 mm^3, 150 × 75 × 2 mm^3, and 80 × 80 × 2 mm^3.

The used machine is an EOS M280 (EOS GmbH, Krailling, Germany) equipped with a 400 W ytterbium fiber continuum laser (wavelength 1060–1100 nm) that is characterized by a beam spot diameter of 100 μm and a building volume of 250 × 250 × 325 mm^3.

For AlSi10Mg specimens, a commercial EOS Aluminum AlSi10Mg powder was used; for Al6061 specimens, a commercial A6061-RAM2 (Elementum 3D, Erie, CO, USA) powder was used. The employed process parameters for the two alloys are reported in Table 1.

Table 1. Employed SLM process parameters for the two considered alloys.

	SLM Process Parameters				**Energy Density (J/mm^3)**
	Laser Power (W)	**Scan Speed (mm/s)**	**Hatch Distance (mm)**	**Layer Thickness (mm)**	
AlSi10Mg	370	1300	0.19	0.03	49.9
Al6061-RAM2	350	1400	0.11	0.03	75.8

A commercial silica sol–gel coating, commercially called Polysil® SC, produced by Nanoprom Chemicals, was used to test the corrosion-protection performance of the SLM specimens.

The coating was applied by spray in a spray booth without any specific special precautions. Polysil® crosslinks at room temperature due to moisture in the air; after about 60 min, the coating is dry to the touch; however, at least 72 h is required to achieve complete crosslinking, or it can be cured at 80° in an oven for 2 h, as recommended by Nanoprom.

The main test is the 168-hour salt-spray test according to ASTM B117 [30]/UNI EN ISO 9227 [31]. The geometric dimensions of the used specimen are 250 × 75 × 1 mm^3. In addition to the salt-spray test, further tests were carried out to verify corrosion resistance and to evaluate static and dynamic adhesion (thermal cycling) on a partly as-built surface and partially milled specimens.

Specifically, the additional tests that were carried out are as follows:

- Adhesion, according to ASTM d3359-17

Adhesion refers to the ability of a coating or paint to stick to a substrate or surface. ASTM D3359-17 [32] is a standard test method for measuring the adhesion of coatings to substrates. It is commonly used in the paint and coating industry to evaluate the quality and durability of coatings on a variety of substrates. The ASTM D3359-17 test method involves applying a grid pattern on the coating's surface with a cutting tool and then applying an adhesive tape over the grid pattern. The tape is then removed quickly, at a 90-degree angle to the surface, and the amount of coating that remains on the surface is evaluated based on the grid pattern. The specimen dimensions are $50 \times 50 \times 2\ \text{mm}^3$.

- Thickness analysis, according to UNI EN ISO 2808:2019

This test was performed according to UNI EN ISO 2808:2019, with method 6A, based on the principle of magnetic induction. The Elcometer 456 F/NF probe was used for coating-thickness measurement; this is a digital coating-thickness gauge that is capable of measuring the thickness of magnetic (ferrous) and nonmagnetic (nonferrous) coatings on a variety of substrates. The specimen size is $140 \times 100 \times 2\ \text{mm}^3$.

- Neutral salt-spray test, according to MIL-STD-810G w/change 1 Method 509.6

The neutral salt-spray test is a test method used to evaluate the corrosion resistance of materials and coatings. MIL-STD-810G w/change 1 Method 509.6 is the standard that was used and specifies the procedures for conducting the neutral salt-spray test.

The test involves exposing the test specimen, which can be a material or a coated surface, to a salt-spray mist in a controlled environment for a set period of time. The salt-spray mist was composed of a 5% sodium chloride solution. The test was performed in an Angelantoni ACS Mod. DCTC 600P chamber for neutral salt-spray testing, using the following parameters:

(a) 24 h of salt spray (T 35 °C, pH 7.0);
(b) 24 h under drying conditions at 23 °C +/−5 °C and humidity of 50%UR +/−10%UR;
(c) 24 h salt spray (T 35 °C, pH 7.0);
(d) 24 h under drying conditions at 23 °C +/−5 °C and humidity of 50%UR +/−10%UR.

During the test, the specimen is inspected periodically to assess the extent of corrosion or damage to the surface. The size of the specimen is $150 \times 75 \times 2\ \text{mm}^3$.

- Determination of thermal-cycling resistance

The determination of thermal-cycling resistance is a test method used to evaluate the ability of a material or product to withstand changes in temperature over time. This test method is important in determining the durability and reliability of a coating that will be exposed to temperature changes during its lifetime.

The reference application is aerospace; therefore, the reference cycles simulate flight conditions for aircraft. The following thermal conditioning was performed:

Repetition of 5 times for the first cycle:

- Ramp of 1 h down to the temperature of −54 °C;
- Maintain the temperature of −54 °C for 3 h;
- Ramp of 1 h up to the temperature of 23 °C;
- Maintain the temperature of 23 °C for 10 min.

Repetition of 5 times for the second cycle:

- Ramp of 1 h down to the temperature of −110 °C;
- Maintain the temperature of −110 °C for 3 min;
- Ramp of 1 h up to the temperature of 23 °C;
- Maintain the temperature of 23 °C for 3 h.

During the test, the test specimen is monitored for any changes or damage that may occur as a result of the temperature changes. This can include cracking, delamination, or other forms of physical or chemical degradation. The specimen size is 140 × 100 × 2 mm^3.

The tests were performed on as-is AlSi10Mg and Al6061 SLM specimens. For the additional tests, after the fabrication, specific AlSi10Mg specimens were processed by shot-peening and milling. The former was provided using a Lampugnani shot-peening LC/S machine loaded by glass-sphere particles at 5 bar pressure for 30 s. The milling operation was performed using a C.B. Ferrari 5-axis machining center mod. S616. The used tool was a Sandvik CoroMill R245-050Q22-12H mill, 50 mm in diameter, equipped with five R245-12T3ECD10 coated tungsten carbide inserts; the process parameters were set at a 300 m/min cutting speed and a 0.08 mm/round/tooth feed rate. The specimens for adhesion, thickness, neutral salt-spray, and thermal-cycle tests were partially machined to investigate the effect of the machining on the same material in the same conditions (Figure 1).

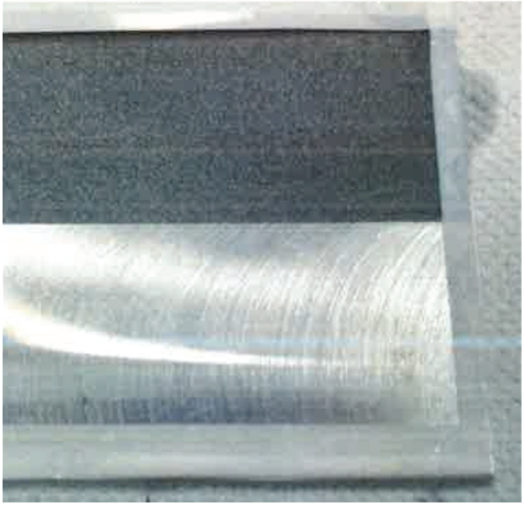

Figure 1. Partially machined AlSi10Mg specimen for additional tests.

The observations of the surface specimens were performed using both a stereomicroscope WILD M3Z FA10780 (Leica Microsystems GmbH, Wetzlar, Germany) and an optical microscope Nikon ECLIPSE LV150N (Nikon, Tokyo, Japan).

Observations of surface specimens in Figures 6 and 7 were made using a Keyence VHX-6000 digital microscope (Keyence, Osaka, Japan) with dual-objective zoom lens (20× to 2000×).

3. Results and Discussion

3.1. Salt-Spray Test

The main test is the verification of corrosion resistance by salt-spray test of the sol–gel silica-based coating, applied on one side of the three following specimens as-is AlSi10Mg specimen, shot-peened AlSi10Mg specimen, and as-is Al6061 specimen.

In Figure 2, these three specimens, before the salt-spray test, are shown. Some peculiar features of SLM technology can be identified: For the as-is AlSi10Mg, the speckled appearance of the surface is due to microgeometrical defect aggregates (satellites, trapped powders, etc.), and these issues are much less evident on the shot-peened specimen, where the scanning lines of the SLM process arose. The speckled appearance is less obvious on the third specimen due to the different aluminum alloy characterized by a different light-diffusion property than that expected for an SLMed surface characterized by high energy. In fact, the higher energy density employed for the processing lowered the surface roughness [33]; as a consequence, the multiple surface reflections were reduced, and the scattering was improved in all directions [34].

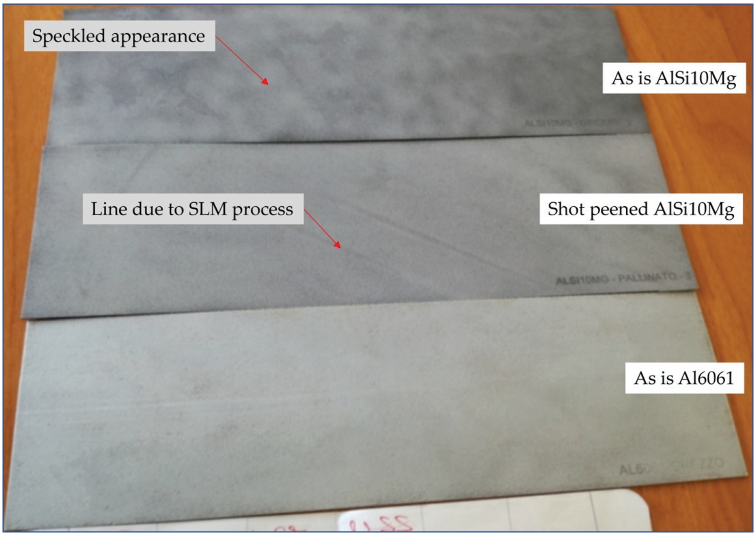

Figure 2. As-is AlSi10Mg, shot-peened AlSi10Mg, and as-is Al6061 specimens before test.

The same specimens, after the salt-spray test, can be observed in Figure 3. On the side protected by the silica coating, it was observed that a browning of the surfaces is more noticeable for the as-is AlSi10Mg specimen, milder for the shot-peened AlSi10Mg specimen, and almost absent for the as-is Al6061 specimen.

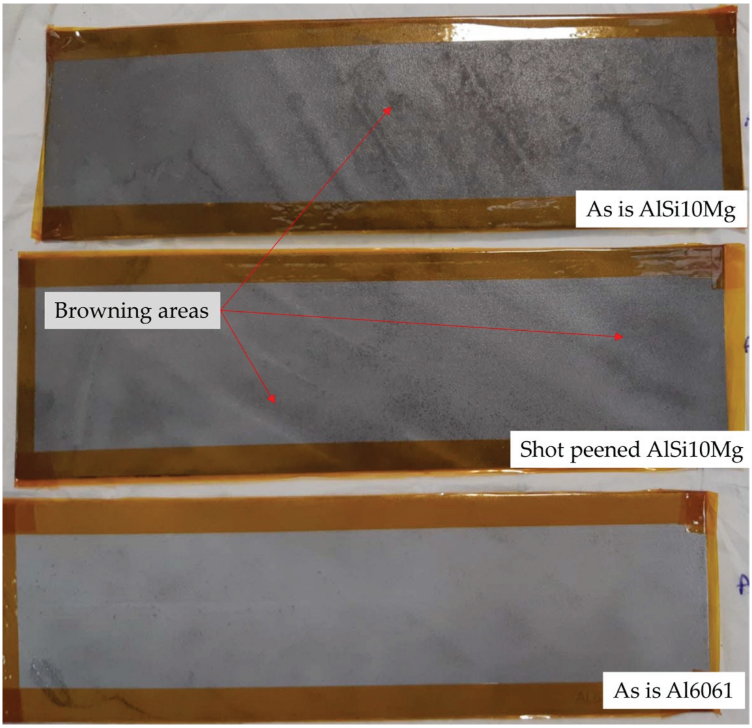

Figure 3. As-is AlSi10Mg, shot-peened AlSi10Mg, and as-is Al6061 specimens after 168 h salt-spray test.

All specimens passed the salt-spray tests, with no signs of corrosion on the surface after 168 h, the darkening phenomena of the coating could be due to the fact that the coating was added with functionalizing elements to increase heat transfer [35].

The evaluation of the other side of the specimens (not treated by the coating) although not of interest was left for comparison in order to highlight the improved effect, in terms of surface protection (Figure 4).

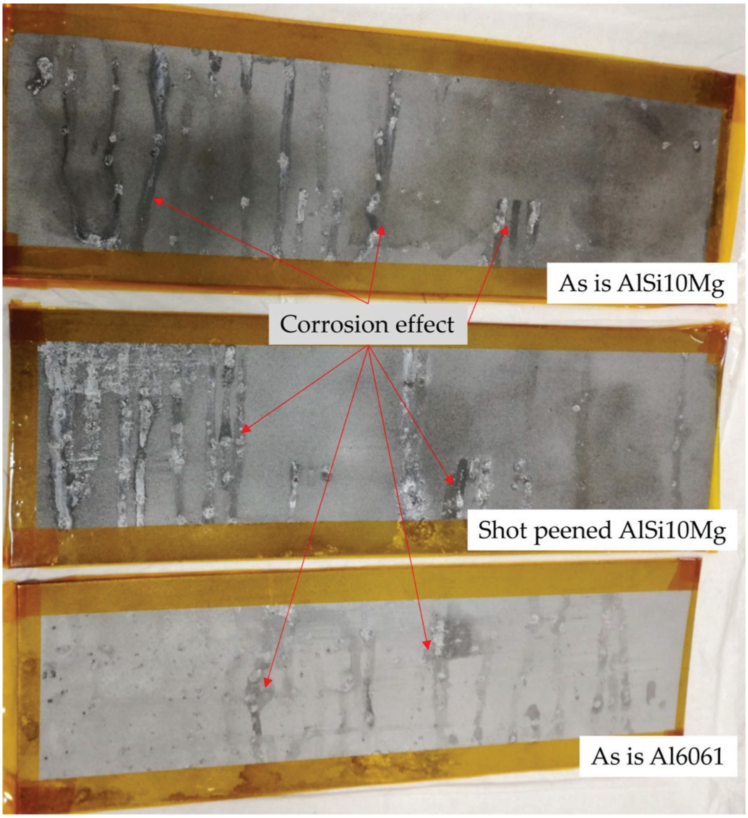

Figure 4. Aspects of non-coated surfaces of the tested specimens after 168 h salt-spray test.

Figure 5 shows, in detail, this side for the investigated specimens. The as-is AlSi10Mg exhibits a marked irregular corrosion phenomenon (Figure 5a) after the 168 h test. The same material subjected to the shot-peening is characterized by a more regular corrosion attack, as shown in Figure 5b; this is probably due to the stress-induced damage, which triggers a more localized beginning of the corrosion [36]. Analogously, the Al6061 surface is affected by a local crater with regular rims (Figure 5c) ascribable to the employed Volumetric Energy Density (VED), greater than the AlSi10Mg case, and resulting in increased defects on the fabricated surfaces [37].

A more in-depth analysis of coated surfaces, i.e., side "A", allows us to investigate how the coating was effective on different surface morphologies. Figure 6a shows the as-is AlSi10Mg, which is characterized by a number of bumps; it is well-known that the balling phenomenon, i.e., a protrusion of material in the form of balls caused by the Maragoni effect, is typical of SLM process because of the high temperature gradients, which lead to a high surface tension gradient [38]. Between the bumps, some salt deposits were trapped without altering the corrosion capability of the coated surface. These phenomena are enhanced on the shot-peened AlSi10Mg surfaces: the mechanical action of the glass-sphere impacts increases the probability to have local damages, which can be observed in the dark regions in Figure 6b; also, the light small area comprises salt crystals that are incorporated into the bumpy surface [39,40]. Total different behavior is observed on the Al6061 specimen, where the balling phenomenon is marginal, and a small circular porosity is visible on the surface (Figure 6c). The previously mentioned browning areas are present on all the specimens and are apparently due to defects initially present on the fabricated part; however, by zooming into a particular area of these zones (Figure 6d), it may be assumed that there was a reaction between the coating pigment and some intermetallic components coming from the SLM process. In fact, it is well-known that the high-energy laser consolidation can produce a wide range of microstructures and promote reaction intermediates of the elements that compose the alloy [38].

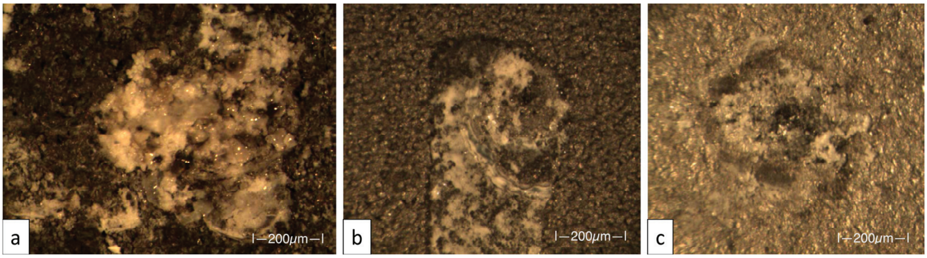

Figure 5. Corrosion results after 168 h salt-spray test of not coating side “B” for as-is AlSi10Mg (**a**), shot-peened AlSi10Mg (**b**), and Al6061 (**c**).

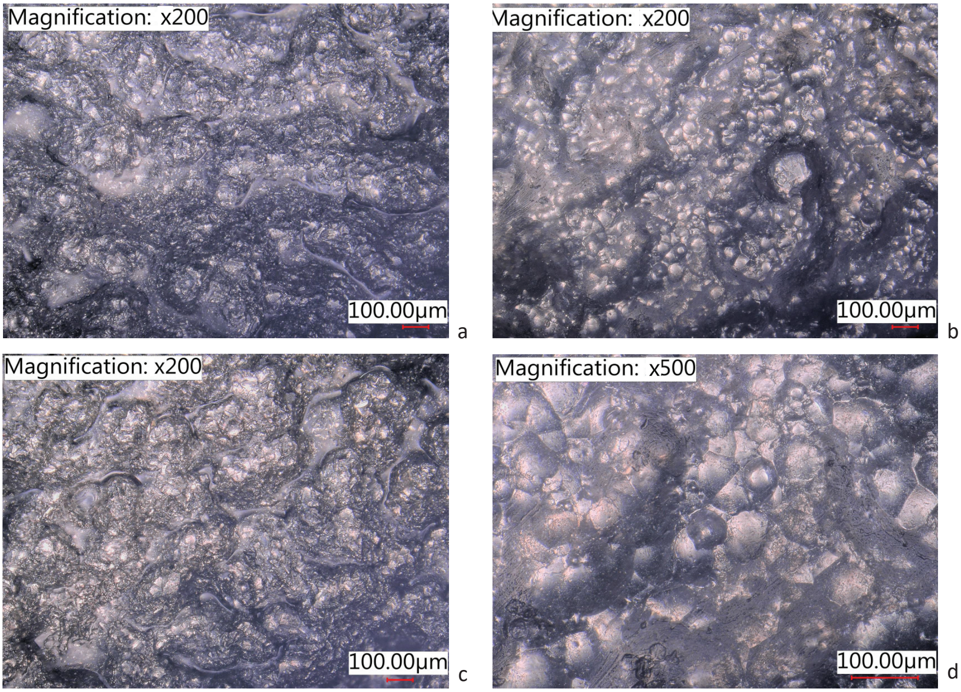

Figure 6. Corrosion results after 168 h salt-spray test of coated side “A” for as-is AlSi10Mg (**a**), shot-peened AlSi10Mg (**b**), Al6061 (**c**), and 500× shot-peened AlSi10Mg (**d**).

3.2. Adhesion Test

This test aims to assess the capability of a relatively ductile coating film to adhere to a metallic substrate. The removal of pressure-sensitive tape over cuts made in the coating may cause damages which are classified according to the standardized method ASTM D3359-23 [41]. The results observed on the coated surfaces showed a very good adhesion result for quite all the not-machined specimens, whilst a lower capability was detected for the machined ones. In Table 2, the results are presented according to the classification codes and with respect to the percent area removed.

Table 2. Adhesion-test results for the investigated specimens.

Specimen	ID	Machined	Classification	Percent Area Removed
As-is AlSi10Mg	1	No	5B	0%, none
As-is AlSi10Mg	2	No	5B	0%, none
As-is AlSi10Mg	3	No	5B	0%, none
Shot-peened AlSi10Mg	4	No	5B	0%, none
Shot-peened AlSi10Mg	5	No	5B	0%, none
Shot-peened AlSi10Mg	6	No	2B	15%–35%
Al6061	7	No	5B	0%, none
Al6061	8	No	5B	0%, none
Al6061	9	No	5B	0%, none
As-is AlSi10Mg	1	Yes	5B	0%, none
As-is AlSi10Mg	2	Yes	4B	0%, none
As-is AlSi10Mg	3	Yes	5B	0%, none
Shot-peened AlSi10Mg	4	Yes	5B	0%, none
Shot-peened AlSi10Mg	5	Yes	0B	Greater than 65%
Shot-peened AlSi10Mg	6	Yes	4B	Less than 5%
Al6061	7	Yes	5B	0%, none
Al6061	8	Yes	3B	5%–15%
Al6061	9	Yes	5B	0%, none

The as-is AlSi10Mg returned 5B classification, meaning that no area was removed for both the machined and non-machined status. Figure 7a shows one of these cases that is characterized by excellent outcomes with high repeatability. The shot-peened specimen made of the same material exhibited, in one case, some issues: Specimen 5 was characterized by a good performance of the non-machined surface, whilst wide detachments, greater than 65%, were detected on the machined one; also, Specimen 6 exhibited a small number of defects in both the conditions. Regarding the Al6061, only the machined surface, in one case, resulted in a 3B classification, meaning that between 5 and 15% of the area was removed.

3.3. Thickness Analysis

The test, based on magnetic induction, was carried out on 140 × 100 × 2 mm^3 specimens. Ten measurements were taken that were uniformly distributed over the entire surface.

The results are reported in Table 3. A marked scattering is observed for surfaces fabricated in SLM, as expected. In fact, the attainable roughness for an SLMed aluminum part is in the range of 5–8 μm for horizontal surfaces, and the peak-to-valley height can reach 40 μm. As a consequence, the coating reflects this variability, and a higher average thickness is obtained to cover the profile well. A thinner coating is observed for machined areas characterized by a roughness, Ra, in the range of 0.8–1.2 μm.

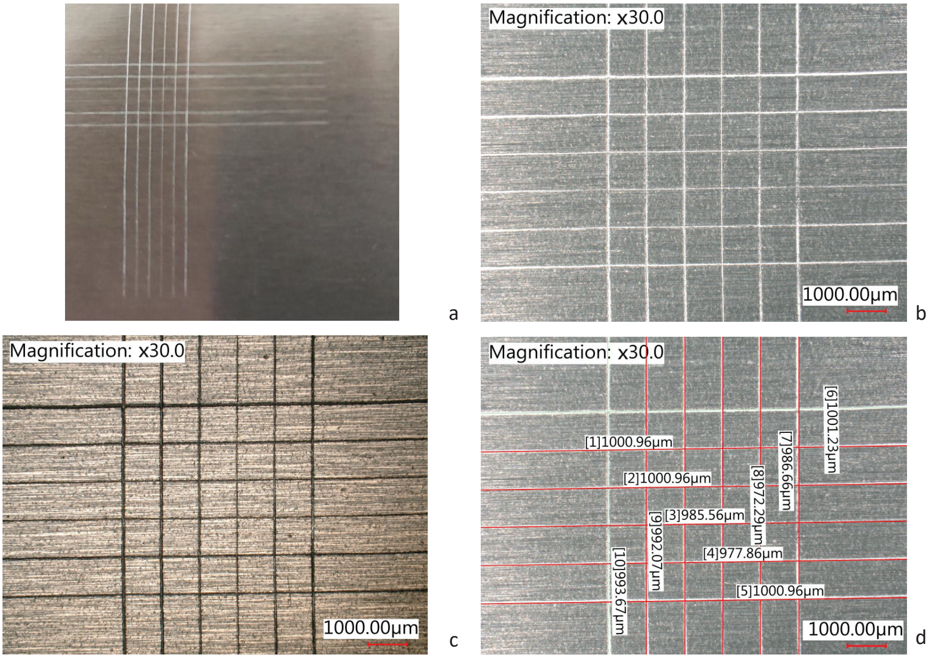

Figure 7. Adhesion test specimens for as-is AlSi10Mg (**a**), 30× magnification AlSi10Mg (**b**), 30× magnification with polarized light (**c**), and grid measurement (**d**).

Table 3. Measurement of coating thicknesses for investigated specimens at rough and machined areas.

Specimen	ID	Thickness in the Rough Area (μm)	Thickness in the Machined Area (μm)
As-is AlSi10Mg	T1	28, 17.1, 50, 39.2, 84, 56.8, 40.8, 28.1, 32.9, 57.6	12.9, 11.4, 13.8, 13.5, 9.8, 13.9, 13.8, 13.1, 14.3, 12.9
As-is AlSi10Mg	T2	51.5, 31.5, 29.8, 32.8, 42.9, 42.1, 37.7, 45.1, 57.9, 43	14.9, 14.3, 14.2, 15.5, 15.1, 13.7, 12.3, 14.7, 16.5, 9.2
As-is AlSi10Mg	T3	31.9, 19.4, 32, 41.3, 39.9, 19.6, 60.2, 38.	9.3, 11.3, 11.8, 14.7, 13.6, 14.2, 15.1, 12.9, 12.5, 13.5
Shot-peened AlSi10Mg	T4	61.8, 53, 50.3, 53.7, 47.8, 50.6, 30.7, 35, 48.9, 46.9	10.5, 11.1, 11.9, 10.1, 13.2, 11.8, 12.2, 14.3, 13.8, 7.2
Shot-peened AlSi10Mg	T5	55.2, 42.8, 56.9, 48.5, 50.6, 73.1, 69.2, 58.3, 41.2, 59.7	9.9, 8.6, 10.6, 8.3, 11.6, 7, 11, 7.2, 9.9, 7.4
Shot-peened AlSi10Mg	T6	54.4, 59.9, 38.5, 42.1, 58.8, 43.7, 41.8, 54.3, 54.4, 50.9	14, 13.5, 14.8, 15.4, 14.4, 15.5, 14.7, 15.6, 15.8, 14.4
Al6061	T7	32, 26.5, 29.5, 45.5, 29.8, 26.4, 36.4, 34.5, 29.9, 28.7	12.4, 10.9, 11.1, 10.2, 10.7, 9.7, 10. 7, 9.4,10.7, 9.6
Al6061	T8	35.7, 35.1, 60.8, 31.4, 39, 33.9, 53.4, 30.5, 32.1, 33.4	13.6, 12.5, 13.5, 11.8, 13.6, 11.9, 13.0, 12.2, 12.3, 11.9
Al6061	T9	32.6, 26.2, 31.7, 31.3, 23.3, 29.8, 27.1, 33, 40.7, 19.8	10.4, 10.7, 10.9, 10.6, 10.2, 10.3, 9.6, 11.4, 10.1, 9.9

The data trends are described by the box-and-whiskers charts reported in Figures 8 and 9 for rough and machined areas, respectively. The as-is AlSi10Mg shows a big scattering of thickness but good repeatability. The shot-peened surface is characterized by a lower variability since many particles and satellites were removed from the surface; however, the coating's average thickness is bigger. In this case, some outliers (i.e. the points lying outside 1.5 times the interquartile range) are observed in the first replicate, meaning that some dips can be related to the dark areas shown in Figure 6b. The as-is Al6061 shows a better surface finishing due to the higher VED, which leads to a smoother surface. In this case, the found outliers can be attributed to the typical SLM defects due to the balling effects, which increase with a high processing energy.

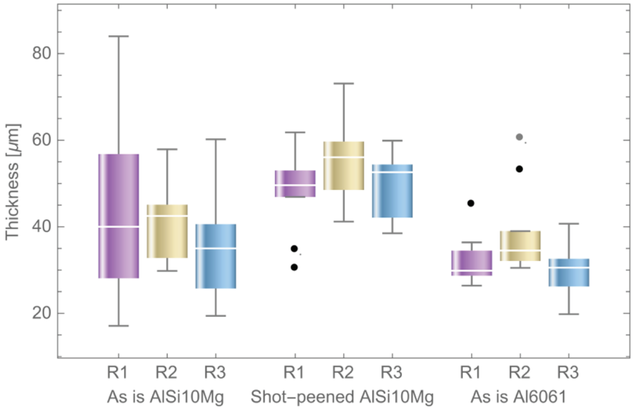

Figure 8. Box-and-whiskers chart of thickness measurements for rough surfaces.

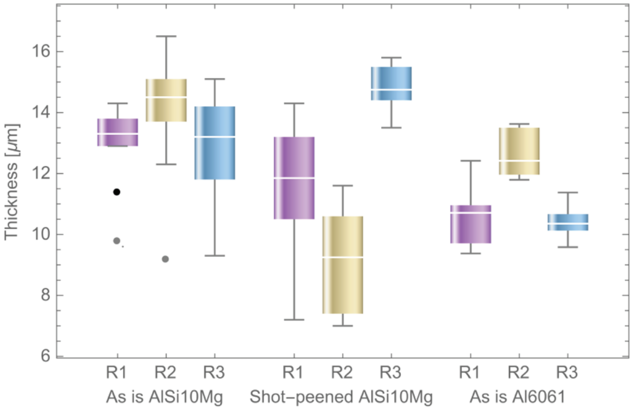

Figure 9. Box-and-whiskers chart of thickness measurements for machined surfaces.

The coating thicknesses measured on machined surfaces are markedly smaller than the rough ones. Figure 9 shows the outcomes for different replicates and specimens. The AlSi10Mg is characterized by good repeatability, with some bottom outliers, meaning some defects, such as an SLM porosity which is not completely filled by the coating. The repeatability is good since the median variation is less than 1 μm. Conversely, the shot-peened specimens exhibit a greater scattering of data, with distributions positioned 5 μm apart. This can be due to the mechanical action the shot-peening can induce on the surface [42,43]. Low variability is observed for the as-is Al6061 without outliers.

As a conclusive remark, expected differences are observed between rough and machined surfaces. Different variabilities between materials and surface conditions can be included. The as-is AlSi10Mg shows the worst result, with a scattering in the measure of an interquartile more than 20 μm. Other rough specimens have an interquartile of about 10 μm. This is markedly reduced for machined surfaces (3 μm). Considering that the application was manually performed, we can assess that the deposition is sufficiently homogeneous.

3.4. Neutral Salt-Spray Test

This test is designed to measure the resistance of a component to the exposure of salt. Test: A typical effect on aluminum is the surface damages and corrosion degradations, which may be observed by inspection with the naked eye. According to the standard, the test was performed for four days. A 24-h spray of a 5% salt solution was performed. The temperature was monitored, and it did not exceed the range of 35 ± 0.1 °C. The drying was provided for 24 h, and then the specimens went back into the chamber for a 5% salt spray for another 24 h. Finally, they came out and were subjected to another 24-h dry. The specific weight of the solution was measured each day and was in the range of 1.0341 ± 0.001 kg/dm^3, with a pH ranging between 6.9 and 7. Figure 10 shows one of the repetitions for each specimen type. This test was brilliantly passed by all the specimens: no alteration, no corrosion attack, and no local damage were observed on all the surfaces, whether machined or rough.

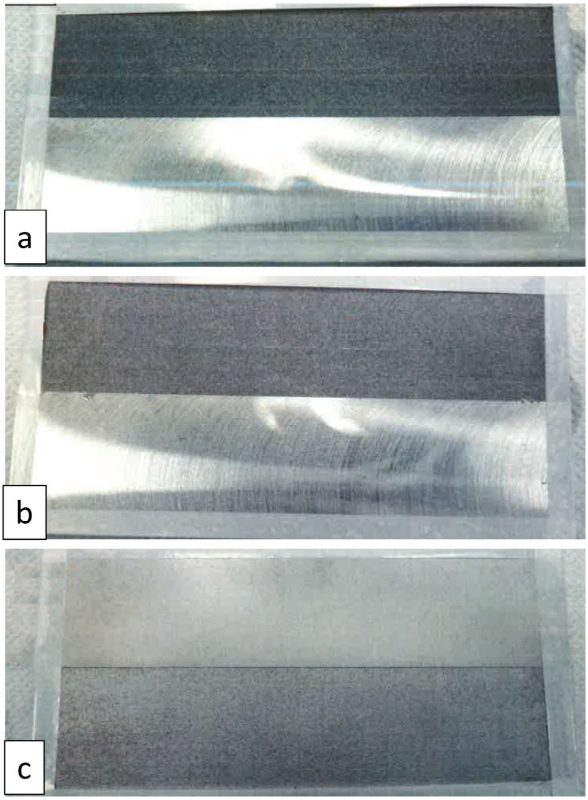

Figure 10. Specimens after neutral salt-spray test: as-is AlSi10Mg (**a**), shot-peened AlSi10Mg (**b**), and as-is Al6061 (**c**).

3.5. Determination of Thermal Cycling Resistance

A thermal cycle through two temperature extremes was applied to the coated specimens to assess the suitability for service in severe conditions. This accelerated laboratory testing can damage the coating because of the increased stress coming from the expansion and contraction of the substrate with a different coefficient of expansion from the coating, leading to crack formation and early failure [44]. Rapid ramps are applied for this purpose. The previously described procedure was applied. The temperature values were monitored, leading to the trends reported in Figure 11.

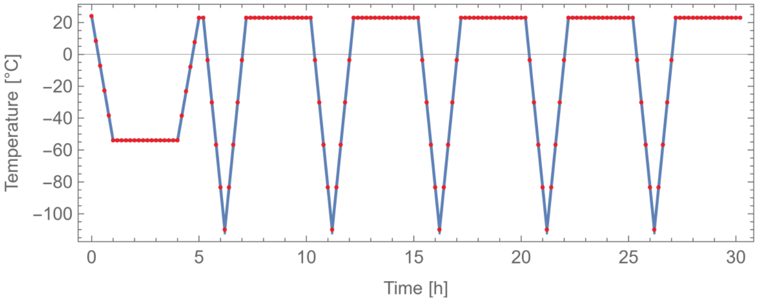

Figure 11. Measured temperature values during the thermal-cycle test.

At the end of the cycle, a photograph was taken of each specimen, and a visual inspection was achieved to verify the presence of macro-defects on the surfaces.

Figure 12 shows the results for the investigated specimens. The as-is AlSi10Mg passed the test, with no or negligible defects (Figure 12a). Conversely, the shot-peened AlSi10Mg ones were characterized by dark areas and matting (Figure 12b). Minor issues were found on the Al6061, which was affected by some halos (Figure 12c).

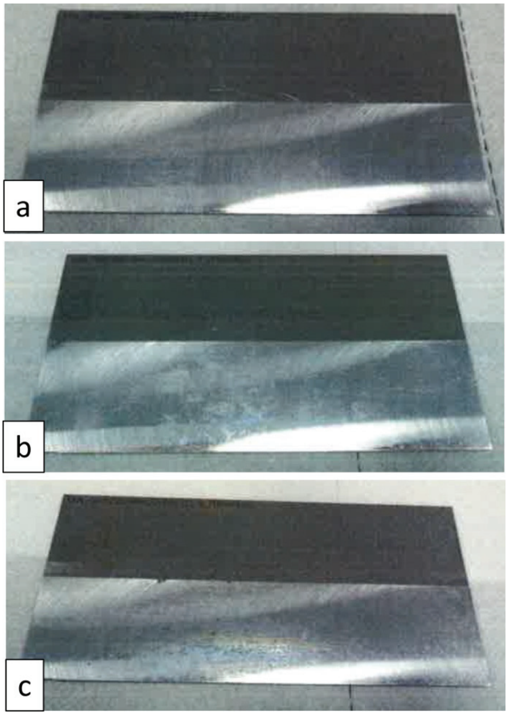

Figure 12. Specimen after the thermal-cycling resistance test: as-is AlSi10Mg (**a**), shot-peened AlSi10Mg (**b**), and as-is Al6061 (**c**).

The damaged areas were measured and are reported in Figure 13. The as-is AlSi10Mg, which was fabricated by using standard EOS exposure parameters, maintained its surface morphology till the end of the thermal cycle both for rough and machined zones. A slight increase of the defect is notable for the latter since the machining can increase the surface's residual stress. The shot-peened AlSi10Mg exhibited an average defected area of 16% and 11% for rough and machined specimens, respectively. This is attributed to the stress induced by the finishing operation, which reduces the material capacity to resist the additional severe expansion and compression cycle. The machined surfaces, in this case, show a better result, probably due to the partial elimination of the stress-induced zone by machining. The as-is Al6061 fabricated by high VED exhibits an intermediate behavior with about 5% defected area. This is an important indication about the selection of the exposure parameters in the SLM fabrication: the enhancing of the surface roughness by selecting a higher energy density can limit the ability of the coated surface to resist high thermal cycles. The surface stresses, in this case, are not reduced if machining is applied. In fact, the damaged area is 8% of the total specimen's surface.

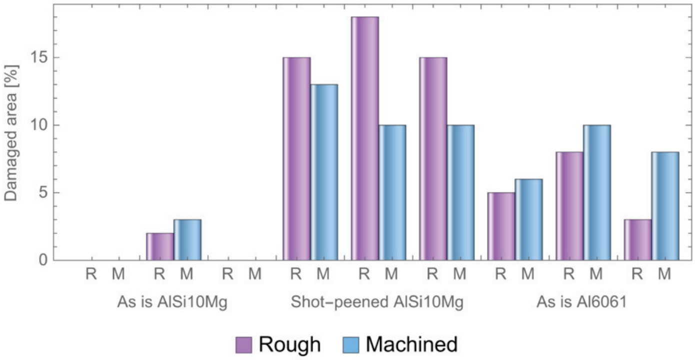

Figure 13. Damaged areas after thermal-cycle test for investigated specimens.

4. Conclusions

Nanostructured silica sol–gel protective coatings demonstrated excellent chemical stability and corrosion resistance, and they can be applied in very thin layers that can effectively protect SLM-manufactured parts thanks to the filling characteristics of the coating. This peculiarity makes nanostructured silica sol–gel an excellent candidate for the protection of Selective Laser Melting as-built surfaces. In fact, the non-coated SLM surfaces exhibit aggressive corrosion, as shown in the salt-spray test. This research highlights some distinctive features depending upon the aluminum alloy and the surface conditioning post fabrication. The rough as-is AlSi10Mg showed very good results for the adhesion and thermal-cycle tests, but a large scattering in the coating thickness measurement was observed. This material, subjected to preliminary shot-peening, is affected by a stress-induced condition which reduces the performances achieved in the salt-spray test and in the thermal cycle. The better surface properties achieved by high VED in the SLM fabrication of as-is Al6061 specimens were attributed to the good results in the thickness analysis and adhesion test; however, the salt spray and thermal cycle pointed out some small defects after the testing. The machined specimens were characterized by a very small average coating thickness, as expected, but in some cases, the adhesion capability was reduced. The machining allowed a slight increase in the thermal-cycle capability; however, the opposite behavior was detected for shot-peened specimens.

Silica sol–gel coating is an environmentally friendly surface-protection technique and has the potential to replace the highly toxic chromium-based galvanic treatments traditionally used to increase the corrosion resistance of metals. In particular, aluminum parts protected with silica sol–gel coatings can be seamlessly integrated into circular economy cycles.

Author Contributions: Conceptualization, L.M., A.B. and L.B.; Methodology, A.B. and L.B.; Validation, D.P.; Investigation, L.M. and G.L.F.; Writing—original draft preparation, L.M.; Writing—review & editing, D.P., A.B., L.B. and C.M. All authors have read and agreed to the published version of the manuscript.

Funding: This research received no external funding.

Institutional Review Board Statement: Not applicable.

Informed Consent Statement: Not applicable.

Data Availability Statement: Not applicable.

Conflicts of Interest: The authors declare no conflict of interest.

References

1. Yao, X.; Zhou, J.; Lin, Y.; Li, Y.; Yu, H.; Liu, Y. Smart manufacturing based on cyber-physical systems and beyond. *J. Intell. Manuf.* **2019**, *30*, 2805–2817. [CrossRef]
2. Levitt, T. The Globalization of Markets. *Harvard Business Review*, May–June 1983; 92–102.
3. Elshkaki, A. The implications of material and energy efficiencies for the climate change mitigation potential of global energy transition scenarios. *Energy* **2023**, *267*, 126596. [CrossRef]
4. Yang, M.; Chen, L.; Wang, J.; Msigwa, G.; Osman, A.I.; Fawzy, S.; Rooney, D.W.; Yap, P.-S. Circular economy strategies for combating climate change and other environmental issues. *Environ. Chem. Lett.* **2023**, *21*, 55–80. [CrossRef]
5. Wang, C.; Tang, J.; Yu, H.; Wang, Y.; Li, H.; Xu, S.; Li, G.; Zhou, Q. Microplastic Pollution in the Soil Environment: Characteristics, Influencing Factors, and Risks. *Sustainability* **2022**, *14*, 13405. [CrossRef]
6. Sajjad, M.; Huang, Q.; Khan, S.; Khan, M.A.; Liu, Y.; Wang, J.; Lian, F.; Wang, Q.; Guo, G. Microplastics in the soil environment: A critical review. *Environ. Technol. Innov.* **2022**, *27*, 102408. [CrossRef]
7. Gibson, I.; Rosen, D.W.; Stucker, B.; Khorasani, M. *Additive Manufacturing Technologies*; Springer: New York, NY, USA, 2021; ISBN 978-3-030-56127-7. [CrossRef]
8. Westerweel, B.; Basten, R.J.; Van Houtum, G.J. Traditional or Additive Manufacturing? Assessing Component Design Options through Lifecycle Cost Analysis. *Eur. J. Oper. Res.* **2018**, *2270*, 570–585. [CrossRef]
9. Yang, S.; Tang, Y.; Zhao, Y.F. A new part consolidation method to embrace the design freedom of additive manufacturing. *J. Manuf. Process.* **2015**, *20*, 444–449. [CrossRef]
10. Debnath, B.; Shakur, M.S.; Tanjum, F.; Rahman, M.A.; Adnan, Z.H. Impact of Additive Manufacturing on the Supply Chain of Aerospace Spare Parts Industry—A Review. *Logistics* **2022**, *6*, 28. [CrossRef]
11. Peng, T.; Kellens, K.; Tang, R.; Chen, C.; Chen, G. Sustainability of additive manufacturing: An overview on its energy demand and environmental impact. *Addit. Manuf.* **2018**, *21*, 694–704. [CrossRef]
12. Colorado, H.; Velásquez, E.; Monteiro, S. Sustainability of additive manufacturing: The circular economy of materials and environmental perspectives. *J. Mater. Res. Technol.* **2020**, *9*, 8221–8234. [CrossRef]
13. Green, J.A. *Aluminum Recycling and Processing for Energy Conservation and Sustainability*; ASM International: Materials Park, OH, USA, 2007.
14. Nordheim, E.; Barrasso, G. Sustainable development indicators of the European aluminium industry. *J. Clean. Prod.* **2007**, *15*, 275–279. [CrossRef]
15. Fontaras, G.; Samaras, Z. On the way to 130gCO_2/km—Estimating the future characteristics of the average European passenger car. *Energy Policy* **2010**, *38*, 1826–1833. [CrossRef]
16. Yan, Q.; Song, B.; Shi, Y. Comparative study of performance comparison of AlSi10Mg alloy prepared by selective laser melting and casting. *J. Mater. Sci. Technol.* **2020**, *41*, 199–208. [CrossRef]
17. Trevisan, F.; Calignano, F.; Lorusso, M.; Pakkanen, J.; Aversa, A.; Ambrosio, E.P.; Lombardi, M.; Fino, P.; Manfredi, D. On the Selective Laser Melting (SLM) of the AlSi10Mg Alloy: Process, Microstructure, and Mechanical Properties. *Materials* **2017**, *10*, 76. [CrossRef] [PubMed]
18. Schneller, W.; Leitner, M.; Springer, S.; Grün, F.; Taschauer, M. Effect of HIP Treatment on Microstructure and Fatigue Strength of Selectively Laser Melted AlSi10Mg. *J. Manuf. Mater. Process.* **2019**, *3*, 16. [CrossRef]
19. Tommasi, A.; Maillol, N.; Bertinetti, A.; Penchev, P.; Bajolet, J.; Gili, F.; Pullini, D.; Mataix, D.B. Influence of Surface Preparation and Heat Treatment on Mechanical Behavior of Hybrid Aluminum Parts Manufactured by a Combination of Laser Powder Bed Fusion and Conventional Manufacturing Processes. *Metals* **2021**, *11*, 522. [CrossRef]
20. Osborne, J.H. Observations on chromate conversion coatings from a sol–gel perspective. *Prog. Org. Coat.* **2001**, *41*, 280–286. [CrossRef]
21. Zhang, X.; van den Bos, C.; Sloof, W.G.; Hovestad, A.; Terryn, H.; de Wit, J. Comparison of the morphology and corrosion performance of Cr(VI)- and Cr(III)-based conversion coatings on zinc. *Surf. Coat. Technol.* **2005**, *199*, 92–104. [CrossRef]
22. Apte, A.; Tare, V.; Bose, P. Extent of oxidation of Cr(III) to Cr(VI) under various conditions pertaining to natural environment. *J. Hazard. Mater.* **2006**, *128*, 164–174. [CrossRef]
23. Asgari, H.; Baxter, C.; Hosseinkhani, K.; Mohammadi, M. On microstructure and mechanical properties of additively manufactured AlSi10Mg_200C using recycled powder. *Mater. Sci. Eng. A* **2017**, *707*, 148–158. [CrossRef]
24. Brinker, C.J.; Scherer, G.W. *Sol-Gel Science: The Physics and Chemistry of Sol-Gel Processing*; Academic Press: Boston, MA, USA, 1990. [CrossRef]
25. Mutin, P.H.; Vioux, A. Nonhydrolytic processing of oxide-based materials: Simple routes to control homogeneity, morphology, and nanostructure. *Chem. Mater.* **2009**, *21*, 582–596. [CrossRef]

26. Liu, Y.; Sun, D.Z.; You, H.; Chun, J.S. Corrosion resistance properties of organic-inorganic hybrid coatings on 2024 aluminum alloy. *Appl. Surf. Sci.* **2005**, *246*, 82–89. [CrossRef]
27. Zheludkevich, M.L.; Serra, R.; Montemor, M.F.; Salvado, I.M.M.; Ferreira, M.G.S. Corrosion protective properties of nanostructured sol–gel hybrid coatings to AA2024-T3. *Surf. Coat. Technol.* **2006**, *200*, 3084–3094. [CrossRef]
28. Vreugdenhil, A.J.; Balbyshev, V.N.; Donley, M.S. Nanostructured silicon sol-gel surface treatments for Al 2024-T3 protection. *J. Coat. Technol.* **2001**, *73*, 35–43. [CrossRef]
29. Voevodin, N.N.; Kurdziel, J.W.; Mantz, R. Corrosion protection for aerospace aluminum alloys by Modified Self-assembled NAnophase Particle (MSNAP) sol–gel. *Surf. Coat. Technol.* **2006**, *201*, 1080–1084. [CrossRef]
30. *ASTM B117-19*; Standard Practice for Operating Salt Spray (Fog) Apparatus; Book of Standards Volume: 03.02. American National Standards Institute: Washington, DC, USA, 2019. [CrossRef]
31. *ISO 9227:2017*; Corrosion Tests in Artificial Atmospheres—Salt Spray Tests. ISO: Geneva, Switzerland, 2017.
32. *ASTM D3322-82(2017)*; Standard Practice for Testing Primers and Primer Surfacers Over Preformed Metal; Book of Standards Volume: 06.02. ASTM: West Conshohocken, PA, USA, 2017. [CrossRef]
33. Yang, T.; Liu, T.; Liao, W.; MacDonald, E.; Wei, H.; Chen, X.; Jiang, L. The influence of process parameters on vertical surface roughness of the AlSi10Mg parts fabricated by selective laser melting. *J. Mater. Process. Technol.* **2019**, *266*, 26–36. [CrossRef]
34. Whitehouse, D.J. *Handbook of Surface and Nanometrology*; CRC Press: Boca Raton, FL, USA, 2010. [CrossRef]
35. Wu, L.; Baghdachi, J. *Functional Polymer Coatings: Principles, Methods, and Applications*; John Wiley & Sons, Inc.: New York, NY, USA, 2015. [CrossRef]
36. Tan, M.Y. *Localized Corrosion in Complex Environments*; John Wiley & Sons: New York, NY, USA, 2023.
37. Giovagnoli, M.; Silvi, G.; Merlin, M.; Di Giovanni, M.T. Optimisation of process parameters for an additively manufactured AlSi10Mg alloy: Limitations of the energy density-based approach on porosity and mechanical properties estimation. *Mater. Sci. Eng. A* **2021**, *802*, 140613. [CrossRef]
38. Gu, D. *Laser Additive Manufacturing of High-Performance Materials*; Springer: Berlin/Heidelberg, Germany, 2015. [CrossRef]
39. Vargel, C. *Corrosion of Aluminium*, 2nd ed.; Elsevier Science: Amsterdam, The Netherlands, 2020. [CrossRef]
40. During, E.D.D. *Corrosion Atlas—A Collection of Illustrated Case Histories*, 3rd ed.; Elsevier: Amsterdam, The Netherlands, 2018.
41. *ASTM D3359-23*; Standard Test Methods for Rating Adhesion by Tape Test. ASTM: West Conshohocken, PA, USA, 2023. [CrossRef]
42. Uzan, N.E.; Ramati, S.; Shneck, R.; Frage, N.; Yeheskel, O. On the effect of shot-peening on fatigue resistance of AlSi10Mg specimens fabricated by additive manufacturing using selective laser melting (AM-SLM). *Addit. Manuf.* **2018**, *21*, 458–464. [CrossRef]
43. Maamoun, A.H.; Elbestawi, M.A.; Veldhuis, S.C. Influence of Shot Peening on AlSi10Mg Parts Fabricated by Additive Manufacturing. *J. Manuf. Mater. Process.* **2018**, *2*, 40. [CrossRef]
44. Doerner, M.F.; Nix, W.D. Stresses and deformation processes in thin films on substrates. *Crit. Rev. Solid State Mater. Sci.* **2006**, *14*, 225–268. [CrossRef]

coatings

Article

Electrical Method for the On-Line Monitoring of Zeolite-Based Thermochemical Storage

Gianfranco Carotenuto

Institute for Polymers, Composites and Biomaterials (IPCB-CNR), National Research Council, Piazzale E. Fermi, 1-80055 Portici, Italy; gianfranco.carotenuto@cnr.it

Abstract: Zeolites are used to store sunlight energy in the form of latent heat of adsorption. The energy is stored by dehydration of the substance and released by its rehydration. The availability of an online monitoring technique for this hydration/dehydration process is an extremely useful potentiality for an optimal exploitation of such technology, since it allows establishment of the degree of activation and saturation of the material. Here, an electrical method has been developed and used for monitoring the hydration/dehydration process of a sample of natural clinoptilolite. Clinoptilolite has been selected as a model zeolitic material for testing this monitoring technique since it is a widely spread, very inexpensive, and highly mechanically stable zeolite type, that could be used for such a purpose. The study has been performed in the presence of pure water vapor and wet air (75RH) after having dehydrated the sample by exposition to sunlight for 12 h. The developed monitoring method has also allowed us to have information on the kinetics of the process (Lagergren pseudo-first order), to establish the specific rate of hydration (3.3×10^{-3} min^{-1}), and to have an idea of the involved adsorption mechanism. The sample of natural clinoptilolite was also chemically and structurally characterized by EDS, XRD, DSC, and TGA.

Keywords: zeolite; online hydration monitoring; clinoptilolite; thermochemical storage; adsorption latent head; Lagergren pseudo-first order kinetics

Citation: Carotenuto, G. Electrical Method for the On-Line Monitoring of Zeolite-Based Thermochemical Storage. *Coatings* **2023**, *13*, 392. https://doi.org/10.3390/coatings13020392

Academic Editor: Xuanpeng Wang

Received: 17 December 2022
Revised: 28 January 2023
Accepted: 5 February 2023
Published: 8 February 2023

1. Introduction

The Greek noun zeolite means: 'the boiling stone' (from the words: Zein = to boil and Lithos = stone) [1], and it originates from the important characteristic of such a substance to lose water when it is heated [2]. In fact, water desorption from the zeolite surface (cationic sites) is an endothermic process that can be induced by heating this substance, while water adsorption on the same adsorption sites is an exothermic process. The amount of heat that can be stored by zeolite during the dehydration process is so large that it has been possible even to cook some tender foods, such as fish and vegetables, by using this very innovative and unusual approach known as 'zeocooking' [2,3]. The possibility to store sunshine energy in the form of latent heat in zeolitic materials and to reuse such energy simply by adding some water to it represents a very important technological potentiality. Zeolites are widely spread in nature (e.g., phillipsite, mordenite, and clinoptilolite), and they are being studied (principally faujasite) as materials to conveniently store the large quantity of sunshine energy available during the summer period (dehydration is induced by exposition to sunlight concentrated by means of mirrors or lenses) [4]. Then the stored energy is recovered by a controlled rehydration process obtained, for example, by exposing the material to a water vapor flow [5–10]. Clinoptilolite is a natural zeolite that could be preferred for investigating such a type of application principally because of its high mechanical stability (usually the structural porosity of zeolites makes them as highly friable solids) and large availability on the market, at a very low cost. Optimal zeolitic systems based on this principle (e.g., adsorption chillers, adsorption heat pumps, and other thermochemical storage systems) have reached energy densities of 150–200 kWm^{-3}.

Cations contained in zeolites are responsible for the molecular adsorption of water and other small polar molecules. In particular, owing to the presence of extra-framework cations (i.e., the charge-balancing cations) in their crystal lattice, natural zeolites are minerals capable to absorb polar molecules having very small kinetic diameter (e.g., water, ammonia, methanol, ethanol, and formaldehyde) on their external and internal surface (i.e., micro-channels and meso-porosity) [11]. The small size is required for the permeation of molecules in the ordered porosity of the mineral, and the molecular adsorption takes place by ion–dipole interaction. In particular, zeolites have a very high capability to absorb water vapor molecules, and such a property has been exploited in different technological applications (e.g., desiccant materials [12,13], thermal energy storage [4–10,14], and humidity sensors [15,16]). The reason is that zeolites can potentially adsorb a number of small polar molecules on the own extra-framework cations by ion–dipole interaction; however, water molecules result preferentially adsorbed on zeolite for different reasons. Owing to the small size of the zeolite channels (for example, for clinoptilolite the maximum pore diameter is 7.4 Å), the small water molecules (kinetic diameter of ca. 2.75 Å) quickly permeate the crystal lattice. Diffusion rate depends on the pore size and large molecules are excluded or move very slowly in these channels. In addition, the dipole moment of the v-shaped water molecule is very high compared to that of other small polar molecules. Moreover, the special shape of water molecules has a role in facilitating their physical adsorption (shape selectivity effect) [2]. Consequently, this special molecule can displace almost all types of adsorbed polar molecules from the cationic sites.

Usually, alkali (Na^+, K^+) and alkaline-earth (Ca^{2+}, Mg^{2+}, etc.) metal cations are contained in the crystal lattice of the natural zeolites (e.g., clinoptilolite), and these species can act as charge carriers for the electrical transport in these materials. The amount of cations contained in the crystal lattice is related to the Si/Al atomic ratio, and consequently the electrical conductivity depends on this important structural parameter, which changes with the type of zeolite. However, the Coulomb interactions acting among these cations and the negatively charged aluminum atoms present in the framework (actually, the full nucleophilic areas is involved since, according to the resonance theory, the negative charge is not localized but it is spread among the aluminum atom and the four oxygen atoms bonded to it) are quite strong, and consequently the electrical conductivity of anhydrous zeolites is very low at room temperature [17]. The natural zeolite electrical conductivity can be significantly increased by exposing the mineral to a wet environment because cation hydration by one or more water molecules decreases the intensity of the electrostatic interaction with the nucleophilic area in the lattice, thus allowing cations to easily move under the application of an electric field [18]. When zeolite is exposed to moisture, such an increase in the cation mobility readily takes place.

Since cations can play the double role (i) to adsorb polar molecules and (ii) to allow electrical transport in zeolites, simple electrical measurements performed on pieces of natural zeolite (e.g., clinoptilolite) exposed to a constant and known humidity environment can be used to monitor the adsorption/desorption process and to investigate the kinetics of these adsorption processes with the intent of measuring the specific rate, reaction order, etc., and to clarify the mechanism of polar molecule adsorption on cations trough ion–dipole forces.

As proved by the large number of articles that have recently appeared in the literature, the long-term storage of thermal energy by natural zeolitic materials is an extremely actual and relevant topic for the technological development of new strategies for energy production and storage. In particular, the idea to develop a simple technique for real-time monitoring of the amount of water loaded by zeolite during the heat release process or the residual water content in the zeolite during the thermal activation process derives from the technological necessity to opportunely design the operation cycles of this promising innovative technological solution (i.e., the time required for the full zeolite activation at the different temperatures and/or the residual service time). In other words, the availability of a way to "visualize" the evolution of the process of water loading/unloading from the zeolite mineral is absolutely of a mandatory importance. Also relevant for the present technological application is the possibility to exploit abundant natural sources of this special mineral substance, since they are available in most of the world's countries at a very low price and clinoptilolite is the most common.

To the best of our knowledge, an electrical method has never been proposed for the cycle assessment of zeolite thermal storage materials. In addition, this technique represents a universal approach (indeed, clinoptilolite is only one example of zeolitic material potentially useful for heat storage) and can be applied to all types of natural and synthetic zeolites.

Here, a method for monitoring the hydration and sunlight-induced dehydration processes and therefore the saturation/activation level of the zeolitic material has been described and used. Clinoptilolite was selected as model material and samples of natural clinoptilolite were exposed to sunlight for 12 h before testing. Then, the hydration process was investigated in presence of pure water vapor and under mild humidity conditions (i.e., constant humidity environment with 75RH) by following the temporal behavior of the electrical transport in the material (i.e., intensity of the current in the sample biased by a 20 V_{pp}, 5 kHz sinusoidal voltage). The hydration kinetics under mild humidity conditions (i.e., 75RH) has been also investigated. The tested mineral sample has been chemically structurally characterized by energy dispersive X-ray spectroscopy (EDS), powder diffraction (XRD), and thermal analysis (DSC, TGA), in order to know its composition.

2. Experimental Part

The clinoptilolite mineral was selected as model material for this study, because it is a mechanically stable hydrophilic zeolite. In addition, this mineral represents the most common type of natural zeolite, widely spread on the market at a very low cost. The mineral was provided by the TIP Technische Industrie-Produkte, GmbH (Waibstadt, Germany) and it was investigated in its pristine form. The mineral was chemically analyzed by Energy Dispersive X-ray Spectroscopy (EDS, FEI Quanta 200 FEG microscope, equipped with EDS Oxford Inca Energy System 250, equipped with INCAx-act LN2-free detector, Oxford, UK) in order to value the Si/Al ratio, cation types and relative amounts, minimum chemical formula, etc. Four different samples were chemically analyzed by measuring a surface area of ca. 900 μm^2. The total water content was measured by thermogravimetric analysis (TGA, TA-Instrument Q500, TA Instrument, New Castle, PA, USA). Tests were performed on powdered clinoptilolite samples by using a TA-Instruments Q500, operating in flowing nitrogen with a constant rate of 10 °C/min. The desorption process of water molecules from the mineral was also investigated by differential scanning calorimetry tests (DSC, TA-Instrument Q200, TA Instrument, New Castle, PA, USA). The percentage of clinoptilolite present in the mineral was established by X-ray diffraction (X'Expert PRO, PANalytical, Oxford, UK).

Impedance spectroscopy, I–V characteristics, and time-resolved current intensity measurements were performed on the surface of rectangular monoliths obtained by cutting the raw material (electrical mini-grinder, 130W, VUM-40, Vigor, Fossano, Italy, with diamond cutting disc). The two electrical contacts were obtained by using a silver paint (ENSON, EN-0638, Beijing, China). For time-resolved measurements, a sinusoidal voltage signal (20 V_{pp}, 5 kHz), generated by a direct digital synthesis (DDS) function generator (GW Instek, mod. SFG-1013, Good Will Instrument Co., Ltd., New Taipei, Taiwan, China) was applied to the silver electrodes and the generated effective current intensity was measured by using a True-RMS digital multimeter (DMM) (Brymen, BM869s, New Taipei, Taiwan, China, 100 kHz bandwidth). Current intensity was recorded by a devoted multimeter data logger (Brymen, BU-86x, New Taipei, Taiwan, China, with the software: Bs86x Data Logging System, Ver. 6.0.0.3s, Brymen, New Taipei, Taiwan, China). For the hydration tests, zeolite samples were exposed to the vapor tension of pure water and to air having a constant humidity content (75RH), obtained by saturating water with sodium chloride salt (i.e., the saturated-salt solution technique, based on wet NaCl crystals).

3. Results and Discussion

Before to monitor the clinoptilolite water adsorption process and to study the related kinetics, the clinoptilolite sample was chemically characterized by Energy Dispersive X-ray Spectroscopy (EDS). EDS analysis is a simple spectroscopic technique, associated with a scanning electron microscope (SEM), capable to provide the most important chemical information on this mineral, for example: the characteristic Si/Al atomic ratio, type and relative amount of cations present in it, type of clinoptilolite mineral, chemical formula, content of empty nucleophilic sites, etc. The elemental composition of the sample achieved by EDS analysis is given in Table 1 in atomic, weight and molar percentages.

Table 1. Atomic, weight, and molar percentages of the different elements contained in the clinoptilolite sample as determined by EDS (colors indicate the elements belonging to covalent framework or extra-framework region).

Element Type	at.%	wt.%	mol.%
Silicon (Si)	23.38	32.67	23.38
Aluminium (Al)	4.27	5.74	4.27
Oxygen (O)	69.01	54.94	69.01
Potassium cation (K^+)	1.55	3.02	1.55
Calcium cation (Ca^{2+})	1.03	2.06	1.03
Magnesium cation (Mg^{2+})	0.34	0.41	0.34
Iron cation (Fe^{3+})	0.41	1.14	0.41

This elemental composition of the mineral substance can be compactly represented by using a Kiviat chart in semi-logarithmic scale, as shown in Figure 1. In particular, the framework elements have been grouped on the right-side of the regular polygon, while the extra-framework elements have been grouped on the left-side. For those inorganic compounds that count a quite large number of elements such as zeolites, this type of diagram is very convenient as representation method because it gives at a glance the idea of the system composition. Indeed, the irregular polygon inscribed within the regular polygon leans toward the most abundant elements contained in the substance. The semi-logarithmic scale is needed since the framework elements (i.e., oxygen, silicon, and aluminum) are largely more abundant than the extra-framework species (some element such as iron are present just at an impurity level). According to the measured Si and Al atomic percentages, the characteristic value of the Si/Al ratio was 5.3, which agrees with the values commonly observed for this type of mineral substance [19]. According to this Si/Al ratio, the clinoptilolite mineral is a hydrophilic zeolite type that should show enough water adsorption capability.

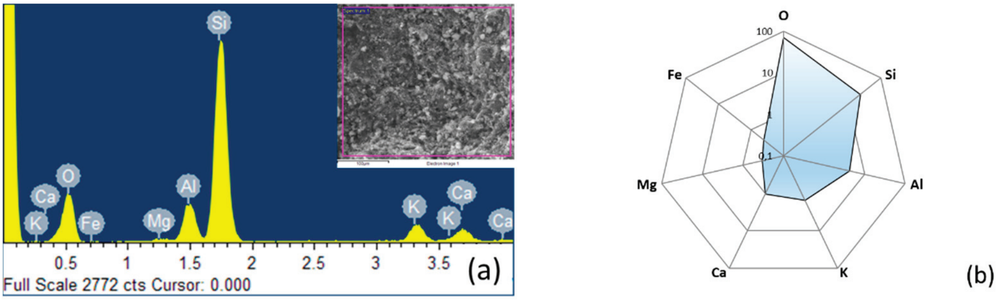

Figure 1. EDS-spectrum of the clinoptilolite sample with the analyzed area in the inset (**a**) and Kiviat chart of the elemental composition (**b**). Framework elements have been conventionally grouped on the right-side, while extra-framework elements are on the left-side.

Four types of cations are present in the mineral: K^+, Ca^{2+}, Fe^{3+}, and Mg^{2+}. Calcium and potassium ions are the most abundant types and, therefore, the sample could be classified as clinoptilolite-K, Ca. These two ions are present in the system in comparable quantities, but owing to the lower charge density of K^+, this ion is the only active charge-carrier in the electrical transport mechanism. Potassium ion moves by hopping among the free nucleophilic sites present in the framework, that are originated because of the presence of multi-charged cations (i.e., Ca^{2+}, Mg^{2+}, and Fe^{3+}). In particular, the EDS analysis can provide the approximate value of the ratio between the amount of empty cationic sites and charge-carriers (i.e., K^+ cations), which is given by the quantity:

$$\frac{at.\%\mathrm{Ca} + at.\%\mathrm{Mg} + 2 \cdot at.\%\mathrm{Fe}}{at.\%\mathrm{K}} = 1.4$$

Therefore, there are almost one and half empty sites for the hopping of each hydrated K^+ cation. Such information is important because, when the conductive mechanism in a material is based on hopping, the electrical transport depends not only on the charge-carrier concentration but also on the quantity of available empty sites.

The common chemical formula of the clinoptilolite mineral is well-known and it corresponds to $(K_2,Ca)_3Al_6Si_{30}O_{72}.24H_2O$ [20]. Since the EDS technique also provides the atomic percentage (or molar percentage) of the oxygen present in the compound, it is possible to compare the experimentally found mineral stoichiometric composition with that expected for the clinoptilolite by calculating the atomic ratio: $\frac{\mathrm{O}\%}{\mathrm{Si}\%+\mathrm{Al}\%}$, which results: 2.67 (see Table 1). Therefore, a good accordance has been found between experimental and theoretically expected (i.e., 96/(30 + 6) = 2.67) stoichiometric compositions.

The EDS analysis has been also used to test the homogeneity of the natural sample composition by performing the elemental analysis in different points of the same sample surface (see Figure 2). As visible, the composition data achieved by EDS are mostly consistent (low fluctuation of the measured values), especially for the most abundant elements.

However, EDS information should be quite approximate since natural zeolites, like many other mineral substances, are heterogeneous systems, that include a number of crystalline solid-phases, and the zeolite phase is only the most abundant component. Powder diffraction (XRD) represents the standard structural characterization approach for crystalline materials, and it is used to identify each crystalline phase contained in the mineral. According to the XRD analysis performed on our sample, the main mineral components were clinoptilolite (48.4% by weight), anorthite (42.0% by weight), and cristobalite (8.9% by weight). A little amount of another zeolite named stilbite (0.7% by weight) has also been detected in the XRD diffractogram. Similarly, to the elemental composition of the mineral established by EDS, the distribution of the different crystalline solid-phases in the composite mineral can be conveniently represented by using the Kiviat chart in semi-logarithmic scale (see Figure 3). It must be pointed out that the anorthite presence in this mineral does not affect the clinoptilolite chemical composition determined by EDS because it is a silico-aluminate compound with equal quantities of aluminum, silicon, and oxygen.

Since water is involved in the heat storage mechanism it is important to quantify its amount in the mineral. The total amount of water contained in the clinoptilolite sample, when it is in equilibrium with air, was established by Thermo-Gravimetric Analysis (TGA). A typical TGA-thermogram of the clinoptilolite sample is shown in Figure 4a. According to this TGA result, natural clinoptilolite is a hygroscopic substance and the percentage of water present in the sample was ca. 10% by weight. Water can be completely removed from the sample by heating it at a temperature higher than 500 °C, and therefore the effectiveness of the sample exposition to sunlight in the dehydration process depends on the geographic collocation and the used light concentration technology.

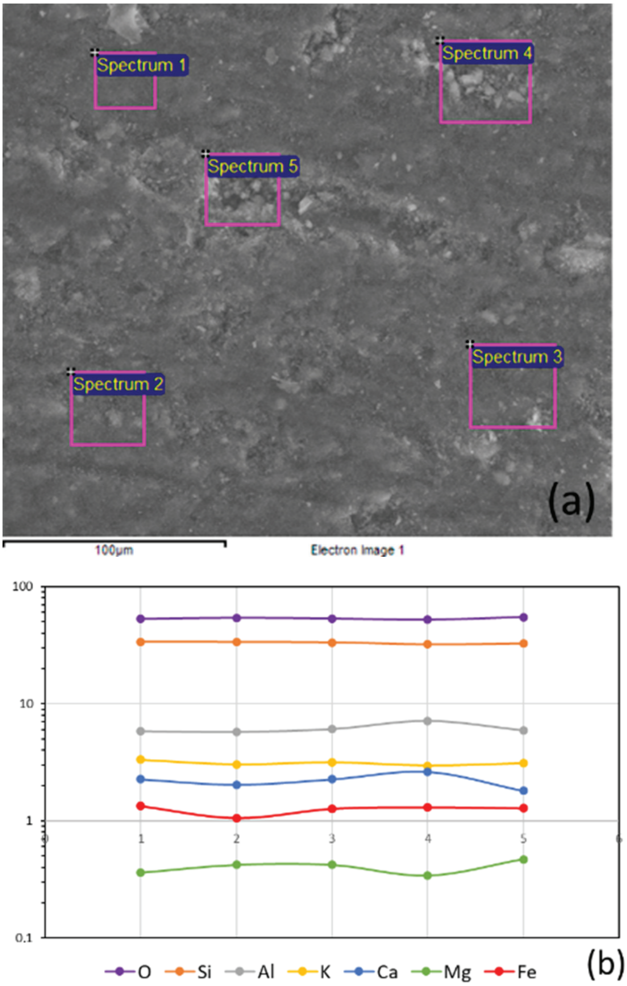

Figure 2. EDS analysis performed in different points of the sample surface (**a**) and consistency of the achieved measurements (**b**).

The water contained in the natural clinoptilolite sample has been also qualitatively investigated by using DSC, with the aim to establish the nature of the different water types. The DSC thermogram of the mineral is given in Figure 4b. The very broad endothermic signal visible in the DSC thermogram, which extends from ca. 100 °C to ca. 450 °C, is generated by the desorption of at least three different types of physically adsorbed water molecules (i.e., water molecules adsorbed on the external surface and in the mesoporosity (1), water molecules adsorbed in the super-cages of the microporosity (2), and water molecules adsorbed in the sodalite cages of the microporosity (3)). It is important to observe that water adsorbed on the external surface and in mesoporosity is the most abundant fraction of the total water present in clinoptilolite and it is fully desorbed at a temperature close to 100 °C.

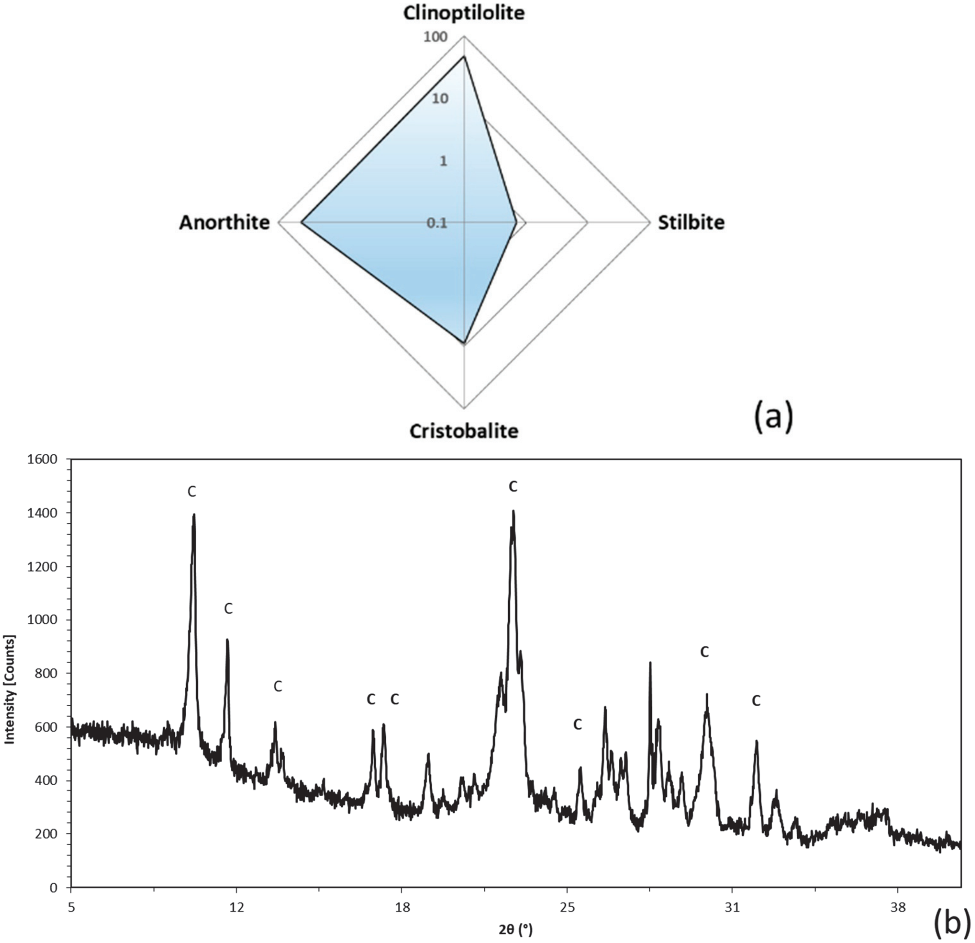

Figure 3. Kiviat chart of the crystalline solid-phase percentages present in the mineral, as obtained by the XRD analysis (**a**), and XRD diffractogram (**b**).

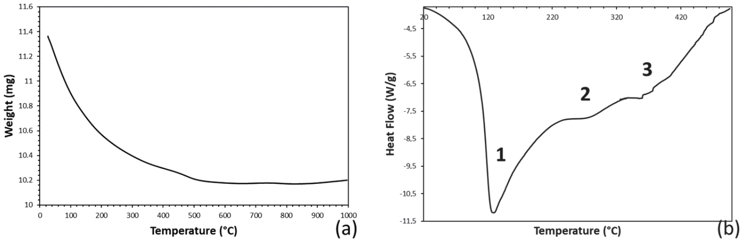

Figure 4. TGA (**a**) and DSC (**b**) thermograms of the studied clinoptilolite sample.

The impedance spectrum of the clinoptilolite sample in a 100 Hz–10 kHz frequency range is shown in Figure 5a. Such a type of electrical characterization allows to understand the behavior of the material electrical transport in a.c. conditions. According to the obtained curve profile, the clinoptilolite sample has a reactive nature and its equivalent circuit is a RC series model with a capacitance, C, of ca. 490pF and a resistance, R, of ca. 100 kΩ (for the sample geometry shown in Figure 6a). Figure 6b shows a detail of the surface of electrodes fabricated on clinoptilolite by silver paint. As visible, the electrode is made by a percolative structure of silver nanoparticles. As a consequence, the reactive contribution to the total sample impedance, $X_C = 1/\omega \cdot C$, rapidly reduces with increasing of the frequency and it can be considered as negligible at a frequency equal or higher than 5 kHz (consequently, the measured sample impedance, Z, reduces to its resistance, $Z \approx R$). In other words, at a frequency lower than 5 kHz the charge carriers (cations) are involved in the electrical transport, but they also partially accumulate at the sample-electrode interface; differently above 5 kHz all charge carriers participate to the electrical transport mechanism. As a consequence, at 5 kHz the charge carrier concentration is directly proportional to the current density, $J = I/S$, according to the law: $J = z \cdot e \cdot \mu \cdot E$ [21], where z is the cation charge (i.e., 1 for the potassium cation), e is the elementary charge (1.6×10^{-19} C), E is the local electric field, and μ is a characteristic property of the cation known as mobility. This condition allows the electrical monitoring of the cation hydration/dehydration process by simple current intensity measurement.

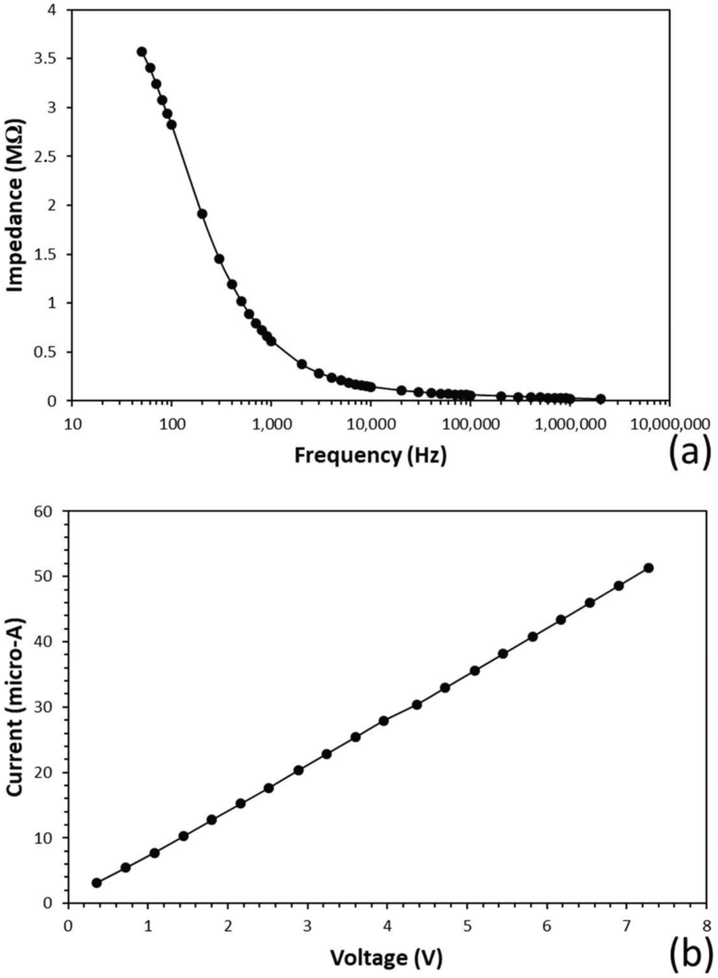

Figure 5. Impedance spectrum of the natural clinoptilolite sample (**a**) and I–V characteristics of the same sample at a frequency of 5 kHz (**b**).

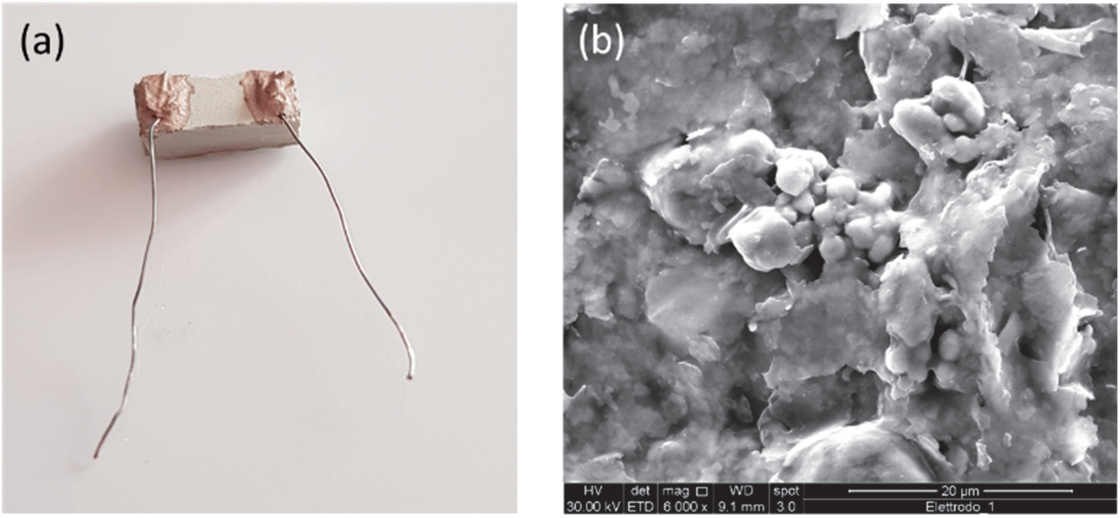

Figure 6. Photograph of the electrically tested sample (**a**) and SEM-micrograph of the silver electrode surface (**b**).

The I–V characteristics of the same clinoptilolite sample at equilibrium with an environment of 75RH is shown in Figure 5b. As visible, the sample biased by a sinusoidal voltage with a frequency of 5 kHz behaved like an ohmic conductor up to a voltage of 7 V_{eff} (20 V_{pp}) and its surface resistance was of 93 kΩ.

The kinetic study of the water adsorption process on K^+ ions in clinoptilolite allows to determine the specific rate of the process. This kinetic study can be performed by measuring the temporal evolution of the electrical transport in the sample, when it is exposed to a wet atmosphere. Time-resolved measurements were made on clinoptilolite samples biased by a sinusoidal voltage (20 V_{pp}, 5 kHz). Since the two electrodes have been placed on the external surface of the piece of clinoptilolite (see Figure 6a), diffusion of the water molecules in the clinoptilolite micro- and meso-porosity is not necessary to have electrical transport in the material. As visible in Figure 7, when the sample is exposed to water vapor, a raising in the current intensity moving at the sample surface (and in the immediately sub-surface region) is readily observed. Since current intensity in clinoptilolite and therefore carrier concentration was promptly affected by exposing it to this wet environment, the role played by cations in the water adsorption mechanism is confirmed. In particular, if the electrically contacted sample is exposed to pure water vapor (tap water) inside a closed box, the current intensity raises very quickly and in a nonlinear manner, in a few seconds the sample transforms from a dielectric material to an electrical conductor. In order to slow down the hydration process, thus allowing an easier monitoring of the current intensity increase, the humidity content of the atmosphere in the box has been lowered to a known value, corresponding to 75RH, by using the saturated salt method based on wet NaCl crystals. Owing to the lower humidity content present in the atmosphere of the closed container, the current intensity showed a slower temporal increase, and it was easier to accurately record it. This very simple measurement allows to have an index evolving proportionally to the quantity of adsorbed water and therefore it is useful to establish when the material has saturated all surface adsorption sites. A different positioning of the electrodes could allow to obtain the same type of information also on the material bulk. Owing to the effect of the applied sinusoidal electrical field, the cations that are located in the region of the sample involved in the measurement make an oscillatory movement. The amplitude of such oscillations should be quite limited because of the very high voltage frequency that is applied during the measurements (i.e., 5 kHz). However, the phenomenon of water molecule adsorption on these oscillating cations should not be significantly affected by their movement, principally because of the very intensive ion–dipole interaction forces that are involved in the adsorption process [22]. Ion–dipole interactions represent a fundamental attractive force (300–40 kcal/mol), indeed such a type of physical interaction is responsible for the highly stable protein ternary and quaternary structure [22]. Finally, when the physical adsorption phenomenon is monitored by the here present electrical method, the heat storage performance of the mineral should not be affected, and the recorded temporal behaviour of the electrical current intensity could be considered as reliable.

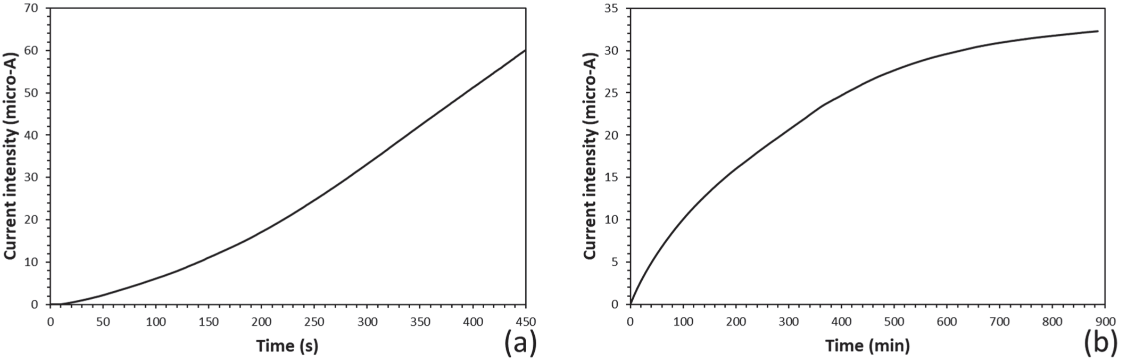

Figure 7. Temporal evolution of the current intensity during the hydration in presence of pure water vapour (**a**) and at 75RH (**b**).

It is possible to establish the type of kinetic control that is active in the adsorption process and to formulate an hypothesis on the involved reaction mechanism, by mathematically elaborating the current intensity temporal behavior shown in Figure 7b. Owing to the current intensity proportionality with the concentration of the charge carriers (i.e., $I\infty\left[KOH_2^+\right]$), the current intensity measurements can be used to calculate the numerical value of the ratio between the carrier concentration at t time and at equilibrium (i.e., $\frac{I_t}{I_{eq}} = \frac{\left[KOH_2^+\right]_t}{\left[KOH_2^+\right]_{eq}}$). The complementary value of this ratio corresponds to the unsolvated K^+ ions (i.e., $1 - \frac{I_t}{I_{eq}} = 1 - \frac{\left[KOH_2^+\right]_t}{\left[KOH_2^+\right]_{eq}} = \frac{\left[K^+\right]_t}{\left[K^+\right]_{tot}}$), that become charge carriers only after solvation by water. As visible in Figure 8, the logarithm of this quantity behaves linearly vs. time (a linear best-fitting with a correlation factor R of 0.9989 has been found). As a consequence, the water adsorption process follows a Lagergren pseudo-first kinetic order and, according to the performed linear best-fitting of the experimental data, the specific adsorption rate is 3.3×10^{-3} min^{-1} at a temperature of 25 °C.

Usually, the adsorption reaction involves a bimolecular interaction between the adsorption site (K^+) and the water molecule and consequently it should have a second-order kinetics. However, since in this experiment the water vapor concentration is kept constant (75RH) during the time by using the saturated salt method, the adsorption reaction becomes of the first kinetic order. Therefore, the kinetic behavior observed in a condition of low humidity content is compatible with an adsorption mechanism based on the following elementary step that involves a single water molecule addition to the cation:

$$K^+ + H_2O \leftrightarrows [KOH_2]^+ \tag{1}$$

An important point concerning the positioning of the water molecule adsorbed on the potassium cation. According to thermodynamics, physical interactions must be maximized in the final chemical conformation of the adsorption site, in order to lower the system energy content at a minimum value. Consequently, the adsorbed water molecule must be placed at the interface between framework and cation. In particular, when the cation bonds the oxygen atom of the water molecule (ion–dipole interaction), its positive charge transfers to the oxygen and consequently the resulting molecular adduct should prefer to electrostatically interact with the negative site (aluminum atom) through the water molecule oxygen atom. Therefore, the water molecule spontaneously moves at the interface with the alumino-silicate framework (see Scheme 1).

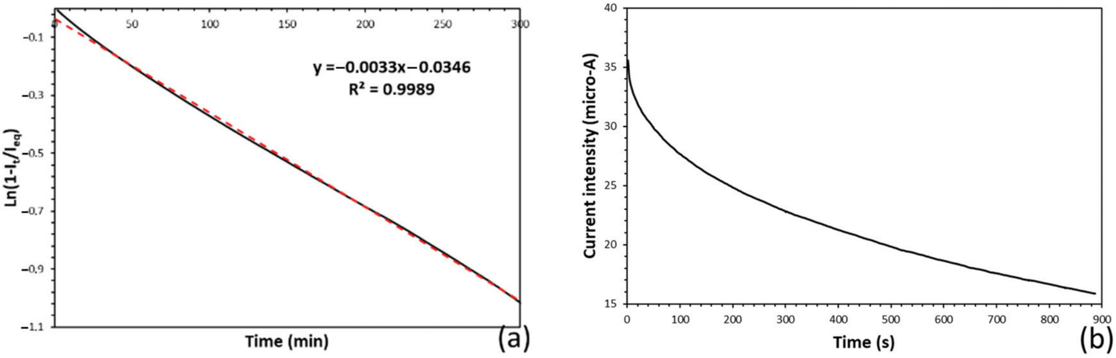

Figure 8. Experimental data elaboration and calculation of the specific kinetic rate of water adsorption on clinoptilolite (**a**) and monitoring of the water desorption from the clinoptilolite sample (**b**).

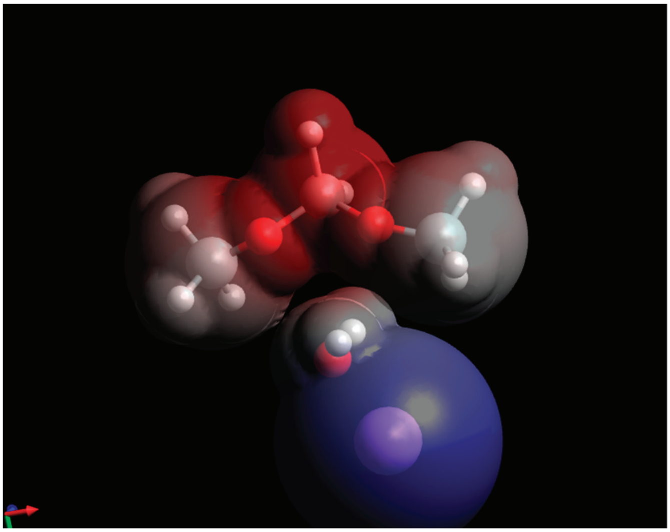

Scheme 1. Chemical structure of the cationic site in the hydrated state.

Obviously, reaction (1) is reversible because the hydrated cations spontaneously decompose, giving back K^+ and water. Moreover, desorption in air under sunlight can be monitored by the same electrical technique (see Figure 8b) and the kinetic rate of the inverse reaction can be measured too.

Owing to the present need for new energy sources, the use of zeolite as heat storage material is an actual and relevant research field [23–25]. Monitoring of the extent of the hydration/dehydration process represents a determining aspect that has been carried out by using different physical approaches in an off-line manner. The zeolite hydration kinetics has been principally investigated by using differential scanning calorimetry (DSC) in a humid gas stream [26]. Tests are typically performed under hysothermal conditions within a thermal analysis device that records simultaneously DSC and thermogravimetric analysis (TGA) signals. Monitoring changes in sample mass (corresponding to the extent of reaction progress) coincident with a quantitative measurement of heat flow allows for direct detection of ΔH as a function of the extent of hydration, which can be integrated to determine ΔH_{tot}. The behaviour of natrolite, analcime, and chabazite have been investigated by using this strategy [26]. Such a characterization method allows to have direct information on the heat generated during the hydration process; however it is a quite expensive and complex approach that requires to minimize the errors associated with significant baseline uncertainties (see Figure 4). Other calorimetric techniques and regression of phase equilibrium data have also been used [27–29]. Adsorption has been investigated also by other off-line approaches, for example, the gravimetrical method [30], finding a perfect accordance with the behaviours obtained by the here presented electrical method (i.e., the Lagergren pseudo first-order kinetic behaviour). Moreover, the dehydration process has been studied by DSC [31] and more complex approaches, for example, by in situ synchrotron powder diffraction [32].

4. Conclusions

The capability of zeolite to absorb water can be conveniently exploited for a number of technological applications, for example, water vapor sensing, dehydration, and humidity control in buildings. However, zeolites can be also used in the energy field as heat storage material based on the latent heat of the zeolite hydration process. For such a reason, it is very useful to make available a method for monitoring the progress of the zeolite hydration, that can offer also the possibility to study the kinetics and the mechanism of this process. Clinoptilolite is a very common type of natural zeolite, potentially useful to fabricate zeolite-based heat storage systems; consequently, it has been selected for this study as model material. The clinoptilolite hydration process can be easily monitored by measuring the intensity of a sinusoidal electric current moving in it during the hydration process (for example, the surface current intensity, resulting from a.c. biasing, can be monitored). An a.c. current of convenient frequency (5 kHz) is required, and its generation and measurement can be achieved by a simple electronic setup (i.e., low-frequency sinusoidal generator and broadband a.c. micro-ammeter connected in series with the sample). Based on this electrical monitoring approach the kinetics of the hydration process for clinoptilolite has been studied and the hydration specific rate has been determined ($k = 3.3 \times 10^{-3}$ min^{-1}). A hypothesis on the hydration mechanism could be formulated on the basis of the found kinetic order (pseudo-first order) and it should correspond to the addition of a single water molecule to each K^+ cation.

Funding: This research received no external funding.

Institutional Review Board Statement: Not applicable.

Informed Consent Statement: Not applicable.

Data Availability Statement: Data sharing is not applicable to this article.

Conflicts of Interest: The author declare no conflict of interest.

References

1. Derbe, T.; Temesgen, S.; Bitew, M. A short review on synthesis, characterization, and applications of zeolites. *Adv. Mater. Sci. Eng.* **2021**, *2021*, 6637898. [CrossRef]
2. Ghobarkar, H.; Schaf, O.; Guth, U. Zeolites—From kitchen to space. *Prog. Solid St.* **1999**, *27*, 29–73. [CrossRef]
3. Shibano, Y. Cooking Equipment Using Zeolite. JP Patent JPH07148073A, 1993. Available online: https://patents.google.com/patent/JPH07148073A/en (accessed on 28 January 2023).
4. Bilgin, O. Natural zeolite minerals as storage of solar energy. *Int. J. Eng. Res. Technol.* **2014**, *3*, 741–744.
5. Jung, D.; Khelifa, N.; Lävemann, E.; Sizmann, R. Energy Storage in Zeolites and Application to Heating and Air Conditioning. *Stud. Surf. Sci. Catal.* **1985**, *24*, 555–562.
6. Aiello, R.; Nastro, A.; Colella, C. Solar energy storage through water adsorption-desorption cycles in zeolitic tuffs. *Thermochim. Acta* **1984**, *79*, 271–278. [CrossRef]

7. Di Palo, M.; Sabatelli, V.; Buzzi, F.; Gabbrielli, R. Experimental and Numerical Assessment of a Novel All-In-One Adsorption Thermal Storage with Zeolite for Thermal Solar Applications. *Appl. Sci.* **2020**, *10*, 8517. [CrossRef]
8. Fasano, M.; Bergamasco, L.; Lombardo, A.; Zanini, M.; Chiavazzo, E.; Asinari, P. Water/Ethanol and 13X Zeolite Pairs for Long-Term Thermal Energy Storage at Ambient Pressure. *Front. Energy Res.* **2019**, *7*, 148. [CrossRef]
9. Vasta, S.; Brancato, V.; La Rosa, D.; Palomba, V.; Restuccia, G.; Sapienza, A.; Frazzica, A. Adsorption Heat Storage: State-of-the-Art and Future Perspectives. *Nanomaterials* **2018**, *8*, 522. [CrossRef]
10. Henninger, S.K.; Jeremias, F.; Kummer, H.; Schossig, P.; Henning, H.-M. Novel Sorption Materials for Solar Heating and Cooling. *Energy Procedia* **2012**, *30*, 279–288. [CrossRef]
11. Ackley, M.W.; Rege, S.U.; Saxena, H. Application of natural zeolites in the purification and separation of gases. *Microporous Mesoporous Mater.* **2003**, *61*, 25–42. [CrossRef]
12. Djaeni, M.; Kurniasari, L.; Sasongko, S. Preparation of natural zeolite for air dehumidification in food drying. *Int. J. Sci. Eng.* **2015**, *8*, 80–83.
13. Djaeni, M.; Kurniasari, L.; Purbasari, A.; Sasongko, S. Activation of natural zeolite as water adsorbent for mixed-adsorption drying. In Proceeding of the 1st International Conference on Materials Engineering (ICME) and 3rd AUN/SEED-Net Regional Conference on Materials (RCM), Yogyakarta, Indonesia, 25–26 November 2010.
14. Rönsch, S.; Auer, B.; Kinateder, M.; Gleichmann, K. Zeolite Heat Storage: Key Parameters from Experimental Results with Binder-Free NaY. *Chem. Eng. Technol.* **2020**, *43*, 2530–2537. [CrossRef]
15. Xu, X.; Wang, J.; Long, Y. Zeolite-based Materials for Gas Sensors. *Sensors* **2006**, *6*, 1751–1764. [CrossRef]
16. Nagai, M.; Hibino, M.; Nishino, T. Humidity Sensor Characteristics of Porous Zeolite Ceramics at Elevated Temperatures. *J. Ceram. Soc. Jpn.* **1989**, *97*, 1296–1299. [CrossRef]
17. Kelemen, G.; Schon, G. Ionic conductivity in dehydrated zeolites. *J. Mater. Sci.* **1992**, *27*, 6036–6040. [CrossRef]
18. Schaf, O.; Ghobarkar, H.; Adolf, F.; Knauth, P. Influence of ions and molecules on single crystal zeolite conductivity under in situ conditions. *Solid State Ion.* **2001**, *143*, 433–444. [CrossRef]
19. Deshpande, V.; Bhoskar, B. Dielectric study of zeolite clinoptilolite. *Int. J. Eng. Res. Technol.* **2012**, *1*, 2278.
20. Hajialigol, S.; Taher, M.A.; Malekpour, A. A New Method for the Selective Removal of Cadmium and Zinc Ions from Aqueous Solution by Modified Clinoptilolite. *Adsorpt. Sci. Technol.* **2006**, *24*, 487–496. [CrossRef]
21. Kasap, S.; Capper, P. (Eds.) *Springer Handbook of Electronic and Photonic Materials*; Springer Science & Business Media, Inc.: Wurzburg, Germany, 2017. [CrossRef]
22. Sippel, K.H.; Quiocho, F.A. Ion-dipole interactions and their functions in proteins. *Protein Sci.* **2015**, *24*, 1040–1046. [CrossRef]
23. De Gennaro, B.; Cappi, A.; de Gennaro, M.; Bianco, N.; Langella, A.; Cappelletti, P.; Marocco, A.; Aprea, P.; Pansini, M. Use of Zeolites in the Capture and Storage of Thermal Energy by Water Desorption—Adsorption Cycles. *Materials* **2022**, *15*, 5574. [CrossRef]
24. Banaei, A.; Zanj, A. A Review on the Challenges of Using Zeolite 13X as Heat Storage Systems for the Residential Sector. *Energies* **2021**, *14*, 8062. [CrossRef]
25. Kouchachvili, L.; Bardy, D.A.; Djebbar, R.; Hogg, L.E.W. Natural zeolite as host matrices for the development of low-cost and stable thermochemical energy storage materials. *J. Porous Mater.* **2023**, *30*, 163–173. [CrossRef]
26. Neuhoff, P.S.; Wang, J. Isothermal measurement of heats of hydration in zeolites by simultaneous thermogravimetry and differential scanning calorimetry. *Clays Clay Miner.* **2007**, *55*, 239–252. [CrossRef]
27. Carey, J.W.; Bish, D.L. Calorimetric measurement of the enthalpy of hydration of clinoptilolite. *Clays Clay Miner.* **1997**, *45*, 826–833. [CrossRef]
28. Chipera, S.J.; Bish, D.L. Rehydration behavior of natural analcime. In *Clay Minerals Society, 28th Annual Meeting*; Lunar and Planetary Institute: Huston, TX, USA, 1991; p. 29.
29. Gatta, G.D. Direct determination of adsorption heats. *Thermochim. Acta* **1985**, *96*, 349–363. [CrossRef]
30. Zettl, B.; Englmair, G.; Somitsch, W. An open sorption heat storage concept and materials for building heat supply. *Energy Procedia* **2015**, *73*, 297–304. [CrossRef]
31. Drebushchak, V. Measurements of Heat of Zeolite Dehydration by Scanning Heating. *J. Therm. Anal. Calorim.* **1999**, *58*, 653–662. [CrossRef]
32. Cruciani, G.; Gualtieri, A. Dehydration dynamics of analcime by in situ synchrotron powder diffraction. *Am. Miner.* **1999**, *84*, 112–119. [CrossRef]

coatings

Article

Fabrication and Characterization of Ag–Ta Thin Films by Co-Magnetron Sputtering as Alternative Layer for High Reflection of NIR Radiation

Wuttichai Phae-Ngam [1], Tanattha Rattana [2], Surachart Kamoldilok [3,*], Kanokporn Kohmun [4], Hideki Nakajima [5], Narit Triamnak [6], Chanunthorn Chananonnawathorn [7], Wantanee Hincheeranan [7] and Mati Horprathum [7]

[1] Physics Program, Faculty of Science and Technology, Phranakhon Rajabhat University, Bangkok 10220, Thailand
[2] Department of Physics, Faculty of Science, Burapha University, Chonburi 20131, Thailand
[3] Department of Physics, Faculty of Science, King Mongkut's Institute of Technology Ladkrabang, Bangkok 10520, Thailand
[4] Faculty of Science and Technology, Rajamagala University of Technology Tawan-ok, Chonburi 20110, Thailand
[5] Synchrotron Light Research Institute, Muang, Nakhon Ratchasima 30000, Thailand
[6] Department of Materials Science and Engineering, Faculty of Engineering and Industrial Technology, Sipakorn University, Nakhon Pathom 73000, Thailand
[7] Opto-Electrochemical Sensing Research Team, National Electronics and Computer Technology Center, Pathum Thani 12120, Thailand
* Correspondence: surachart.ka@kmitl.ac.th

Abstract: Silver–tantalum (Ag–Ta) thin films were fabricated by magnetron co-sputtering on silicon (Si) wafer (100) and glass slide substrates at room temperature. The Ag–Ta thin films were prepared at various deposition times of 5, 10, 20 and 30 s and the physical, structural and optical properties of the Ag–Ta thin films were investigated. It was determined that the thicknesses of the films were 7, 9, 17 and 33 nm, respectively. The results revealed that an increase in the film thickness leads to a monotonic increase in FCC and BCC phase of Ag and Ta, respectively. The work function and stoichiometric of the Ag–Ta thin films were investigated by ultraviolet and X-ray photoemission spectroscopies (UPS and XPS), respectively. The potential of Ag–Ta thin films to be used as low-emission coating was investigated using a spectrophotometer. A UV–VIS–NIR spectrophotometer was used to measure the spectral reflectance in the wavelength range from 300 to 2000 nm. The results showed that the Ag–Ta thin film deposited for 30 s exhibited higher reflectance in NIR region than those of 5, 10, 20 and 30 s. It demonstrated an average reflectance of about 80% and slightly decreased to 75% after being kept in the air atmosphere for 28 days. It can be likewise proposed as an alternative thin film with high reflectance of NIR radiation single layer to develop industrial low-emission coating for cost-effective, clean, and easy adaptation to a large area coating.

Keywords: Ag–Ta thin film; low-emissivity coating; reflectance; NIR radiation

Citation: Phae-Ngam, W.; Rattana, T.; Kamoldilok, S.; Kohmun, K.; Nakajima, H.; Triamnak, N.; Chananonnawathorn, C.; Hincheeranan, W.; Horprathum, M. Fabrication and Characterization of Ag–Ta Thin Films by Co-Magnetron Sputtering as Alternative Layer for High Reflection of NIR Radiation. *Coatings* **2023**, *13*, 43. https://doi.org/10.3390/coatings13010043

Academic Editors: Christian Mitterer and Gianfranco Carotenuto

Received: 24 November 2022
Revised: 21 December 2022
Accepted: 22 December 2022
Published: 26 December 2022

1. Introduction

At present, the tall buildings in a big city such as Bangkok have been constructed and many more buildings are under construction. In most of those buildings, the walls are made of glass. The glass walls are the major opening parts of the building that absorb the solar radiation and contribute more than 50% of the energy exchange through conduction, convection and radiation [1,2]. Therefore, the absorbed solar radiation in the form of heat transfers into the building. This results in the increase of energy consumption by the air conditioners which are generally used in big buildings.

One way to reduce the transmission of infrared radiation into the building is the coating of low-emissivity materials on the glass building [3]. Low-emissivity coatings display good properties on high reflectance of solar infrared radiation and high visible transmittance. They have been widely used for coating on architectural and automotive flat glass products [4].

Two types of films were used as low-emissivity coatings for energy saving glasses; metal films and transparent conductive oxide (TCO) films [5]. The emissivity of metal films is high, but their visible transmittance is low [5,6]. The weakness of metal films is poor stability due to the oxidation by the air atmosphere and resulting in the low reflectance of solar infrared radiation [5]. For TCO film, it is more stable and transparent than those of metal film, but its infrared emissivity is higher [5,7]. Among all TCO films, indium tin oxide (ITO) film is the most widely used due to it yielding a low infrared emissivity of about 0.2 [8,9]. However, ITO is too expensive for low-emissivity coating on the large-scale glasses.

Therefore, in the past decade, low-emissivity coating methods have been proposed by using the protective layer on both surfaces of metal films. The transparent oxide and sulfide films of various materials including TiO_2, SnO_2, ZnO, ITO and ZnS have been used in a protective layer in dielectric–metal–dielectric multilayer structure [10]. The low-emissivity coatings of dielectric–metal–dielectric multilayer structure have been widely studied such as $TiO_2/Ag/TiO_2$, $SnO_2/Ag/SnO_2$, ZnO/Ag/ZnO, ITO/Ag/ITO and ZnS/Ag/ZnS [10–12].

Since the Ag atoms can diffuse through the dielectric layer and react with the oxygen of dielectric layer at high temperature and lead to poor low-emissivity property, chemical durability, corrosion resistance and thermal stability [13,14]. A simple method to solve this problem is the coating of a single-layer Ag-based alloy such as Ag–Ti, Ag-Nb and Ag–Ta alloys [15–18]. However, those works mainly focus on antibacterial and protective coating applications. Nevertheless, the optical property of Ag-based alloy film as well as the reflectance of NIR radiation of the Ag-based alloy materials still needs to be studied. In addition, alloying with Ta could produce high structure stability [19].

This work studies a series of Ag–Ta thin films prepared by magnetron co-sputtering on silicon wafer and glass slide substrates. The crystalline structure, surface and cross-sectional morphologies were characterized. The deep investigation on work function and stoichiometric of the Ag–Ta thin Films were investigated by ultraviolet and X-ray photoemission spectroscopies (UPS and XPS), respectively. The reflectance of the Ag–Ta thin films deposited on glass slides at different deposition times were measured by UV–VIS–NIR spectrometer in the wavelength range from 300 to 2000 nm.

2. Experimental Details

Silver–tantalum (Ag–Ta) thin films were deposited on 1.5 cm × 1.5 cm Si(100) wafers and glass slides, each with a dimension of 2.5 cm × 2.5 cm using a DC magnetron co-sputtering system as shown in Figure 1. Ag (99.99% purity) and Ta (99.99% purity), each with a diameter of 2 inch and a thickness of 0.25 inch, were used as the targets. The substrates were ultrasonically cleaned in acetone and methanol for 10 min and dried with nitrogen before being installed in the vacuum chamber. The distance from Ag target to substrate (D_{s-t}(Ag)) and Ta target to substrate (D_{s-t}(Ta)) were 10.7 and 9.2 cm, respectively.

A home-built vacuum chamber was evacuated to achieve a base pressure of about 3×10^{-6} Torr by a pumping system consisting of a rotary pump and a diffusion pump. Prior to the deposition, the targets were pre-sputtered with Ar ions for 5 min in order to clear out impure gases in the chamber and to remove the contaminants from the target surface. Then, for sputter-cleaning of the targets, Ar (99.99% purity) was flowed into the chamber with a flow rate of 20 sccm. The Ag target was supplied with a 100 W DC power supply while the Ta target was supplied with a 100 W, 3 kHz DC pulsed power supply. The pressure during deposition was about 5×10^{-3} Torr. The films were deposited for various times of 5, 10, 20 and 30 s.

The crystalline structure of Ag–Ta thin films deposited on Si substrates was characterized by a X-ray diffractometer (XRD:Bruker D8 Discover AXS, Billerica, MA, USA) using CuKα radiation (λ = 0.1542 nm) operated at 40 kV and 40 mA. The XRD patterns were recorded at a glancing incidence angle of 2θ with the 2° range from 20° to 80° and a scanning speed of 2°/min. The surface and cross-sectional morphologies of the films deposited on the Si substrates were investigated by a field emission scanning electron microscope (FE-SEM: JEOL, JSM 660 LV, Tokyo, Japan).

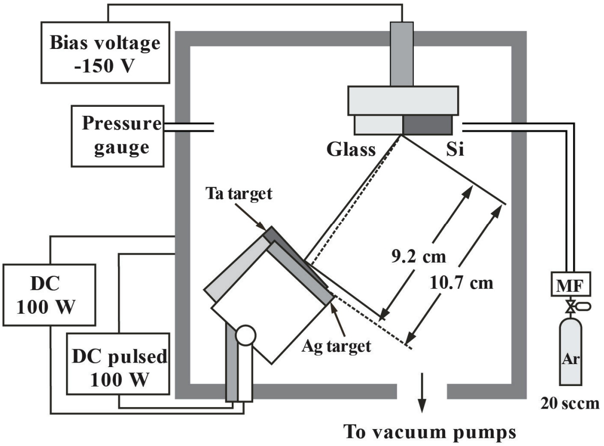

Figure 1. Schematic diagram of DC magnetron co-sputtering system.

The ultraviolet and X-ray photoemission spectroscopy (UPS and XPS) were performed at BL3.2Ua in the Synchrotron Light Research Institute, Nakhon Ratchasima, Thailand. The beamline delivers the soft X-rays ranging from 40 to 1040 eV linearly polarized [20]. The incident angle is 20 degrees and its polarization is usually parallel to the surface. The CLAM2 electron energy analyzer (Thermo VG Scientific, West Sussex, England) was used to measure the electron energy at an emission angle of 70 degrees. The CLAM2 analyzer was calibrated in the Fermi edge and Au4f7/2 peak at zero and 84 eV, respectively. The samples were loaded into the vacuum chamber and characterized under the pressure of 10–7 Pa at room temperature. The total energy resolutions of UPS and XPS were 0.2 and 2.0 eV, respectively. No changer neutralizer or argon ion etching was applied prior to the measurement. The work function and valence band spectra were measured in the UPS mode at the photon energy of 60 eV on the sample negatively biased at about 10 V. The binding energy is referenced from the Fermi edge of gold. The elemental and chemical compositions of samples were measured in the XPS mode at a photon energy of 600 eV. The binding energy of spectra is referenced from the work function method described elsewhere [21,22].

The films deposited on the glass substrates were used for spectral reflectance measurements by a UV–VIS–NIR spectrophotometer (Shimadzu, UV–VIS–NIR 3600, Kyoto, Japan) in the wavelength range from 300 to 2000 nm.

3. Results and Discussion

3.1. Crystal Structure

Figure 2 shows the X-ray diffraction patterns of Ag–Ta thin films deposited on Si substrates with the deposition times of 5, 10, 20 and 30 s. It revealed that the films exhibited preferred orientations of (111) plane for Ag and (110) plane for Ta according to the JCPDS data of the FCC structure of Ag (No. 04-0783) and the BCC structure of Ta (No. 89-5158). It is observed that X-ray intensity of Ag (111) peak is higher than that of Ta (110) peak. This is due to the fact that the atomic number of Ag (47) is lower than that of Ta (73), even though the Ag target was sputtered with 100 W DC supply, whereas Ta target was sputtered with 100 W DC pulsed supply. When the deposition time was increased to 30 s, it revealed that the X-ray intensity of Ag (111) peak and Ta (110) peak increased.

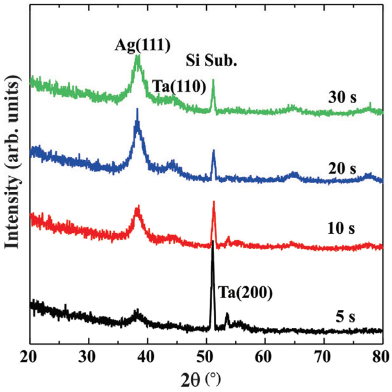

Figure 2. XRD patterns of Ag–Ta thin films on Si substrates deposited with different times.

3.2. Surface and Cross-Sectional Morphologies

Figure 3a shows the FE-SEM micrographs of the Ag–Ta films and Figure 3b shows the cross-sectional FE-SEM images of the Ag–Ta films deposited on Si substrates at various deposition times of 5, 10, 20 and 30 s. From Figure 3a, the grain size was measured by image-J program and determined to be 4.4, 5.7, 6.8 and 9.5 nm for the deposition times of 5, 10, 20 and 30 s, respectively. From Figure 3b, the thicknesses for the films deposited at 5, 10, 20 and 30 s were determined to be 7 ± 0.6, 9 ± 0.5, 17 ± 0.9 and 33 ± 1.1 nm, respectively.

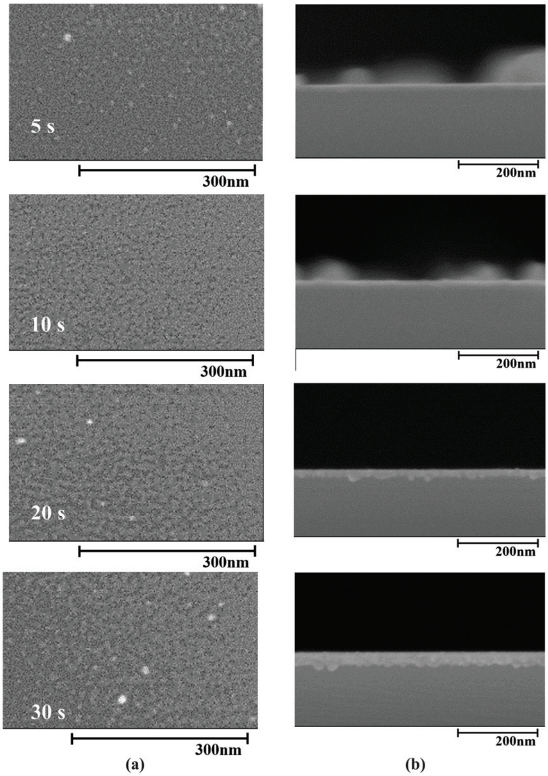

Figure 3. (**a**) Surface and (**b**) cross-sectional FE-SEM images of Ag–Ta thin films deposited on Si substrates at various deposition times.

3.3. Work Function and Stochiometric

The basic theory related to measuring work function has been reviewed by Helander et al. [23]. The UPS spectra were measured for the secondary electron cutoff to evaluate the work function of films as shown in Figure 4a,b. Note that the Fermi level was obtained by gold standard sample. The work function and C1s C–C reference binding energy are listed in Table 1. The work function of films is ranged from 4.91 to 4.98 eV, which is higher than that of metallic silver and tantalum crystal surfaces. These high work functions tell us that the surface of films is quite flat and uniform [23]. It might also be due to the formation of alloy film between silver and tantalum.

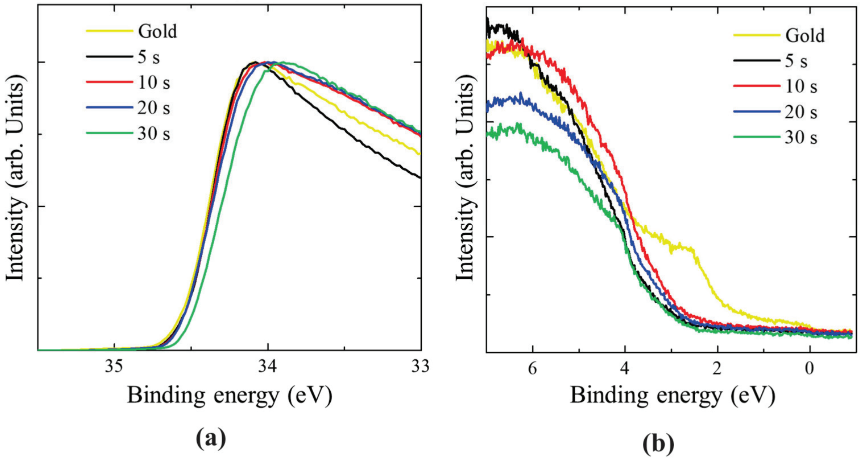

Figure 4. UPS spectra of prepared Ag–Ta thin films at different deposition times: (**a**) high-energy and (**b**) low-energy cut-off point.

Table 1. Work function and C1s C–C reference binding energy of prepared Ag–Ta thin films at different deposition times.

Deposition Time (s)	PE (eV)	Cut-Off (eV)	WF (eV)	C1s (C–C) (eV)
5	39.5	34.55	4.95	284.63
10	39.5	34.55	4.95	284.63
20	39.5	34.59	4.91	284.67
30	39.5	34.52	4.98	284.60

Figure 5a,b shows the survey XPS spectra and atomic concentration of elements. As shown in Figure 5a, the secondary electron background increases the baseline of spectra in the low kinetic energy range overlapped with the Auger transitions of C KLL, Ag MNN, and Ta NOO. XPS is sensitive to surface region probed in 3 nm below surface because the inelastic mean free path is short [24]. Carbon contamination cannot be avoided during the sample transfer from deposition to XPS analysis chamber. Because the films were deposited under the low vacuum condition, the oxidation of films could not be avoided. Atomic concentration of oxygen is ranged from 40 to 50%, and those of other elements are approximately 20% including adventitious carbon at the surface.

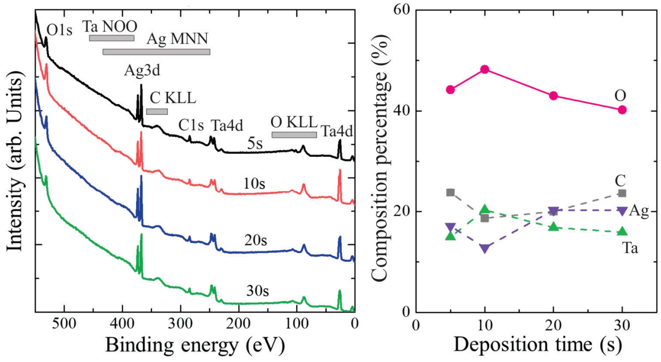

(a)

(b)

Figure 5. (**a**) XPS survey spectra and (**b**) composition percentage of the prepared Ag–Ta thin films.

Figure 6a–d shows the C1s, O1s, Ta4f, and Ag3d spectra to evaluate the elemental and chemical compositions. The spectral background was removed by the Shieley's method mixed with polynomial curve in the active background approach [25]. The peaks were fitted with Gaussian for C1s and O1s spectra at the full width at half maximum (FWHM) of 2 eV. Ta4f peaks were synthesized from Gaussian in the range of FWHM between 1.5 and 3 eV. Ag3d peaks were fitted with the pseudo-Voigt based on the summation of Gaussian (80%) and Lorentzian (20%) at FWHM of about 1.6 eV.

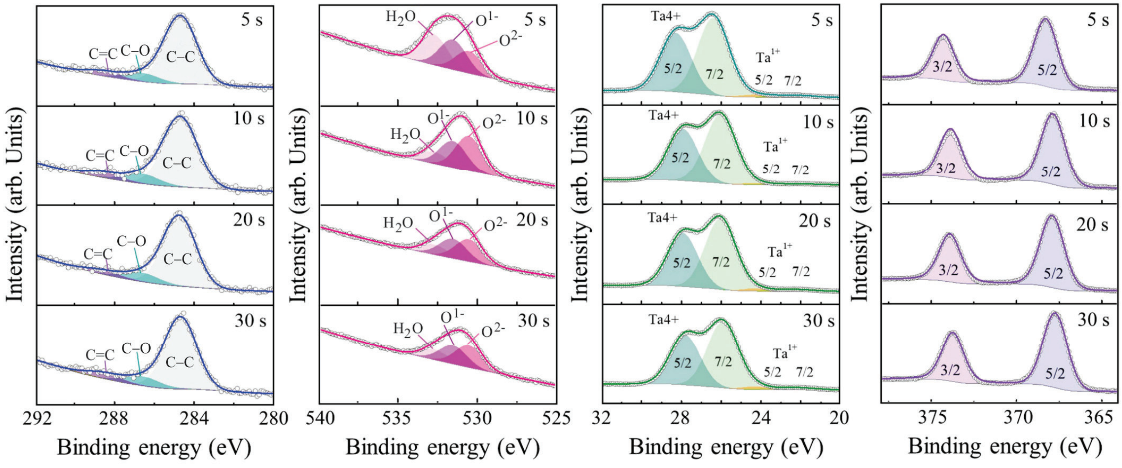

(a) C1s (b) O1s (c) Ta4f (d) Ag3d

Figure 6. XPS deconvoluted spectra.

The C1s spectra display the C–C/C–H peak at about 284.6 eV as a major contribution because the carbon originates from the contamination based on the hydrocarbon. Minor contributions of C–O at 1.9 eV below C–C peak and C=O at 3.9 eV below C–C peak were also discovered in the fitting process [23]. The O1s spectra are derived from three components at 530.5 eV for O^{2-}, 531.5 eV for O^{1-}, and 532.7 eV for H_2O [26]. O^{2-} content is primarily attributed to the metal oxides with tantalum and silver. O1- content can originate from the O–H/C–O bonds and possibly single metallic bond with tantalum and silver. H_2O content is the highest contribution in TaAg film deposited for 5 s. However, the O^{2-} content becomes higher than the other contents in the TaAg films deposited for 10–30 s.

The Ta4f spectra illustrate two phases of tantalum compositions in the films [27]. Tantalum oxide (TaO_2, Ta^{4+}) is identified at the double peaks ranging from 26 to 28 eV. The Ta4f doublet peaks are separated by the spin splitting (1.9 eV) between 7/2 and 5/2, and their amplitudes are constrained at a ratio of 4:3. The other tantalum oxide (Ta_2O, Ta^{1+}) is also observed from the double peaks from 22 to 24 eV fitted with the same parameters described in tantalum oxide. However, the percentage of Ta^{1+} against Ta^{4+} is approximately 3–5% at the film surface. The Ag3d spectra appear to be the single phase of metallic silver based on the binding energies of 7/2 peak at 367.7–368.3 eV and 5/2 peak at 373.7–374.3 eV, which are separated by the spin splitting (6.0 eV) and fixed at 3:2 of the amplitude ratio. However, it is difficult to identify the oxidation or chemical state of silver from the peak energy [28]; no energy loss peak or satellite was determined besides the main peak, so the silver might be partly oxidized or alloyed with tantalum.

3.4. Reflectance Spectra

Figure 7 shows the reflectance spectra of the Ag–Ta thin films deposited on the glass substrates at various deposition times of 5, 10, 20 and 30 s in the wavelength range from 300 to 2000 nm. The spectral reflectance data (R(λ)) were used to calculate the average reflectance in the visible range (λ = 380–780 nm) and near-infrared range (780–2000 nm).

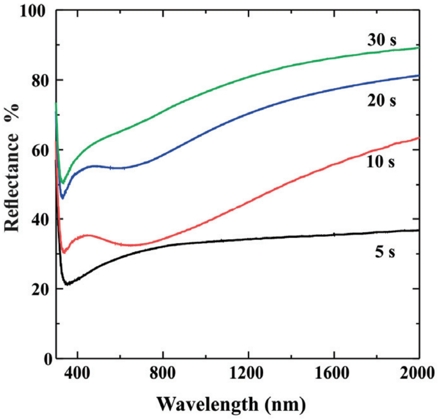

Figure 7. Reflectance spectra of Ag–Ta thin films.

Figure 8 shows the average reflectance in the visible and near-infrared ranges. It can be observed that the film deposited at 30 s can reflect the radiation in the visible range and NIR range by about 60% and 80%, respectively.

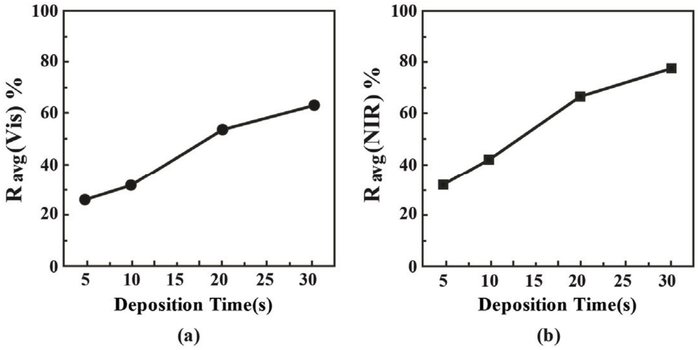

Figure 8. Average spectral reflectance in (**a**) Vis and (**b**) NIR ranges.

3.5. Durability Test

The durability test of the films deposited on the glass substrates was performed by keeping the samples in the air atmosphere for about one month. The reflection measurements were carried out on the days 7, 14, 21 and 28 and average reflectance in the visible range and NIR were measured, and the results are shown in Figure 9.

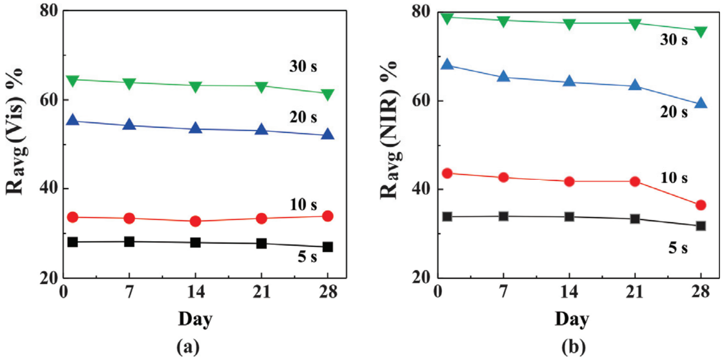

Figure 9. Variations of average reflectance in (**a**) Vis and (**b**) NIR ranges for the films after being kept in the air for 7 to 28 days.

From Figure 9, it can be observed that the average reflectance for all the films deposited on the glass substrates slightly decreased after being kept in the air atmosphere for 28 days. Furthermore, the film deposited for 30 s has a high average reflectance of more than 75% after being kept in the air for 28 days. The results show that all the films deposited in this work have a good durability, particularly the film deposited for 30 s has an additional property of high NIR reflectance.

4. Conclusions

In this work, single-layer Ag–Ta thin films were deposited on the glass and Si (100) substrates using co-sputtering method for high reflection of NIR radiation. Ag and Ta were used as sputtering targets. The Ag and Ta targets were supplied by a 100 W DC power supply and a 100 W DC pulsed power supply, respectively. The films were deposited at various times of 5, 10, 20 and 30 s.

The thicknesses of the films deposited at 5, 10, 20 and 30 s, as determined from the cross-sectional FE-SEM images, were determined to be 7.16, 9.81, 17.43 and 33.93 nm, respectively. The reflectance spectra showed that the film deposited at 30 s had an average reflectance of about 80% in the NIR range and it decreased to 75% after the films were kept in the air atmosphere for 28 days. The atomic concentration of elements of Ag–Ta films as investigated by XPS showed that the concentrations of Ag, Ta, O_2 and C were determined to be about 20, 20, 40 and 20%, respectively, in all prepared films. This means that Ag and Ta oxide films were formed during the deposition or the waiting time for characterization in which this problem is unavoidable. For the overall result, it can be concluded that the Ag–Ta thin films prepared in this work are acceptable for high NIR reflection. They can be coated on the glass building for saving energy in the building.

Author Contributions: Conceptualization, W.P.-N. and M.H.; methodology, N.T. and C.C.; validation, H.N., N.T. and C.C.; formal analysis, W.P.-N. and S.K.; investigation, K.K. and W.H.; resources, W.H.; data curation, K.K., S.K. and W.H.; writing—original draft preparation, S.K.; writing—review and editing, S.K.; supervision, W.P.-N.; project administration, W.P.-N. and S.K.; funding acquisition, W.P.-N., T.R. and M.H. All authors have read and agreed to the published version of the manuscript.

Funding: This research was funded by Biodiversity-Based Economy Development Office (Public Organization), Grant No. BEDO-NRCT 47/2562.

Institutional Review Board Statement: Not applicable.

Informed Consent Statement: Not applicable.

Data Availability Statement: Not applicable.

Acknowledgments: This research work was supported by Phranakhon Rajabhat University and Biodiversity-Based Economy Development Office (Public Organization). The authors would like to thank National Electrics and Computer Technology Center for providing the deposition system and spectrophotometer.

Conflicts of Interest: The authors declare no conflict of interest.

References

1. Su, J.; Yin, L.; Qin, L.; Ma, N.; Huang, J. Preparation and performance of ZrAlN antireflective coatings for low-emissivity glasses. *Ceram. Int.* **2017**, *43*, 14616–14622. [CrossRef]
2. Kumar, G.K.; Saboor, S.; Babu, T.P.A. Investigation of various low emissivity glass materials for green energy building construction in indian climatic zones. *Mater. Today Proc.* **2017**, *4*, 8052–8058. [CrossRef]
3. Gläser, H.J.; Ulrich, S. Condensation on the outdoor surface of window glazing calculation methods, key parameters and prevention with low-emissivity coatings. *Thin Solid Film.* **2013**, *532*, 127–131. [CrossRef]
4. Park, S.H.; Lee, K.S.; Reddy, A.S. Low emissivity Ag/Ta/Glass multilayer thin films deposited by sputtering. *J. Appl. Phys.* **2011**, *110*, 063501–063508. [CrossRef]
5. Sun, K.; Tang, X.; Yang, C.; Jin, D. Preparation and performance of low-emissivity Al-Doped ZnO films for energy-saving glass. *Ceram. Int.* **2018**, *44*, 19597–19602. [CrossRef]
6. Loka, C.; Yu, H.T.; Lee, K.S. The preparation of thermally stable TiNx/Ag(Mo)/TiNx ultrathin films by magnetron sputtering. *Thin Solid Film.* **2014**, *570*, 178–182. [CrossRef]
7. Giovannetti, F.; Föste, S.; Ehrmann, N.; Rockendorf, G. High transmittance, low emissivity glass covers for flat plate collectors: Applications and performance. *Energy Procedia* **2012**, *30*, 106–115. [CrossRef]
8. Sibin, K.P.; Swain, N.; Chowdhury, P.; Dey, A.; Sridhara, N.; Shashikala, H.D.; Sharma, A.K.; Barshilia, H.C. Optical and electrical properties of ITO thin films sputtered on flexible FEP substrate as passive thermal control system for space applications. *Sol. Energy Mater. Sol. Cells* **2016**, *145*, 314–322. [CrossRef]
9. Shi, Z.; Song, L.; Zhang, T. Terahertz reflection and visible light transmission of ITO films affected by annealing temperature and applied in metamaterial absorber. *Vacuum* **2018**, *149*, 12–18. [CrossRef]
10. Chiba, K.; Kaminishi, S. Fabrication and optical properties of low-emissivity coatings of AlSiN and AgCuNd-Alloy multilayer films on glass. *Jpn. J. Appl. Phys.* **2008**, *47*, 240–243. [CrossRef]
11. Dhar, A.; Alford, T.L. High quality transparent $TiO_2/Ag/TiO_2$ composite electrode films deposited on flexible substrate at room temperature by sputtering. *APL Mater.* **2013**, *1*, 12102–12107. [CrossRef]
12. Kim, J.H.; Kim, D.H.; Kim, S.K.; Bae, D.; Yoo, Y.Z.; Seong, T.Y. Control of refractive index by annealing to achieve high figure of merit for $TiO_2/Ag/TiO_2$ multilayer films. *Ceram. Int.* **2016**, *42*, 14071–14076. [CrossRef]
13. Kulczyk-Malecka, J.; Kelly West, P.J.G.; Clarke, G.C.B.; Ridealgh, J.A.; Almtoft, K.P.; Greer, A.L.; Barber, Z.H. Investigation of silver diffusion in $TiO_2/Ag/TiO_2$ coatings. *Acta Mater.* **2014**, *66*, 396–404. [CrossRef]
14. Loka, C.; Yu, H.T.; Lee, K.S. Effect of TiNx Inter/Outer layer on Ag(Cr) thin films at elevated temperatures for low emissivity applications. *Jpn. J. Appl. Phys.* **2014**, *53*, 3014–3017. [CrossRef]
15. Kao, K.S.; Cheng, D.L.; Chang, S.H.; Hsieh, P.T.; Chin, H.S.; Lin, H.K. Effect of mesh fatterning with UV pulsed-laser on optical and electrical properties of ZnO/Ag–Ti thin Films. *Appl. Surf. Sci.* **2010**, *256*, 7446–7450. [CrossRef]
16. Wojcieszak, D.; Mazur, M.; Kaczmarek, D.; Mazur, P.; Szponar, B.; Domaradzki, J.; Kepinski, L. Influence of the surface properties on bactericidal and fungicidal activity of magnetron sputtered Ti–Ag and Nb–Ag thin films. *Mater. Sci. Eng. C* **2016**, *62*, 86–95. [CrossRef]
17. Wang, J.; Li, J.; Li, H.; Zhang, X.; Huang, J.; Xiong, D. Friction and wear properties of amorphous and nanocrystalline Ta-Ag films at elevated temperatures as function of working pressure. *Surf. Coat. Technol.* **2018**, *353*, 135–147. [CrossRef]
18. Jianliang, L.; Jun, W.; Ameet, K.; Hang, L.; Dangsheng, X. High temperatures tribological properties of Ta-Ag films deposited at various working pressures and sputtering powers. *Surf. Coat. Technol.* **2018**, *349*, 186–197. [CrossRef]
19. Jianliang, L.; Xiafei, Z.; Jun, W.; Hang, L.; Jiewen, H.; Heguo, Z.; Dangsheng, X. Mechanical and frictional performance of Ta and Ta-Ag alloy films deposited at different sputtering powers. *J. Mater. Eng. Perform.* **2019**, *28*, 5037–5046. [CrossRef]
20. Hideki, N.; Sarunyu, C.; Porntip, S.; Surachet, R.; Watcharapon, J.; Ratchadaporn, S.; Narong, C.; Prayoon, S. Commissioning of the soft X-Ray undulator beamline at the siam photon laboratory. In Proceedings of the 12th International Conference on Synchrotron Radiation Instrumentation SRI2015, New York, NY, USA, 6–10 July 2015; AIP Publishing: Melville, NY, USA, 2016; Volume 1741, pp. 020040-1–020040-4. [CrossRef]
21. Greczynski, G.; Hultman, L. X-ray photoelectron spectroscopy: Towards reliable binding energy referencing. *Prog. Mater. Sci.* **2019**, *107*, 100591. [CrossRef]

22. Greczynski, G.; Hultman, L. C 1s peak of adventitious carbon aligns to the vacuum level: Dire consequences for material's bonding assignment by photoelectron spectroscopy. *ChemPhysChem* **2017**, *18*, 1507–1512. [CrossRef] [PubMed]
23. Helander, M.G.; Greiner, M.T.; Wang, Z.B.; Lu, Z.H. Pitfalls in measuring work function using photoelectron spectroscopy. *Appl. Surf. Sci.* **2010**, *256*, 2602–2605. [CrossRef]
24. Powell, C.J.; Jablonski, A. Surface sensitivity of X-ray photoelectron spectroscopy. *Nucl. Instrum. Methods Phys. Res. A* **2009**, *601*, 54–65. [CrossRef]
25. Engelhard, M.H.; Baer, D.R.; Herrera-Gomez, A.; Sherwood Peter, M.A. Introductory guide to backgrounds in XPS spectra and their impact on determining peak intensities. *J. Vac. Sci. Technol. A* **2020**, *38*, 063203–063224. [CrossRef]
26. Jean-Charles, D.; Danielle, G.; Philippe, V.; Alain, L. Systematic XPS studies of metal oxides, hydroxides and peroxides. *Phys. Chem. Chem. Phys.* **2000**, *2*, 1319–1324. [CrossRef]
27. Robin, S.; Richard, W.; John, W.; Mark, B. XPS investigation of monatomic and cluster argon ion sputtering of tantalum pentoxide. *Appl. Surf. Sci.* **2017**, *405*, 79–87. [CrossRef]
28. Maria, A.; Ferraria Patrícia Carapeto, A.; Maria Botelho do Rego, A. X-ray photoelectron spectroscopy: Silver salts revisited. *Vacuum* **2012**, *86*, 1988–1991. [CrossRef]

coatings

Article

Effects of Graphene Morphology on Properties of Carbon Nanotube/Polyurethane Film Strain Sensors

Chen Liu [1], Xiang Ge [2], Jiaqi Geng [1], Yuanli Men [1] and Caideng Yuan [1,*]

[1] School of Chemical Engineering and Technology, Tianjin University, Tianjin 300350, China
[2] School of Mechanical Engineering, Tianjin University, Tianjin 300350, China
* Correspondence: cdyuan@tju.edu.cn

Abstract: The film flexible sensors can convert tiny changes in size or force into electrical signals. They are key components of intelligent devices and wearable devices, and are widely used in human-computer interaction, electronic skin, health monitoring, implantable diagnosis, and other fields. This kind of sensor is generally composed of polymer matrix and conductive components, while carbon nanotubes (CNT) and graphene (GN), as typical one-dimensional and two-dimensional conductive carbon nano-materials, respectively, have been used to build film flexible sensors. In order to explore the relationship between the GN size and thickness, and the performance of film sensors, the GN-CNT/PU composite film sensors were prepared by in situ polymerization of polyurethane (PU) in the presence of GN and CNT. A highly sensitive GN-CNT/PU flexible film sensor was prepared with a high gauge factor (GF) up to 13.15 in a strain range of 0–20%; an exceptionally low percolation threshold of GN is about 0.04 vol% when the CNT content is fixed at 0.2 vol%, which is below the percolation threshold of CNT/PU nanocomposites. The size of the GN layer affects the GFs of the flexible film sensors; a GN with a smaller size can achieve a greater GF. This study paves the way for the better application of different qualities of GN in flexible sensors.

Keywords: carbon nanotubes; graphene; film sensors; composite materials; polyurethane

Citation: Liu, C.; Ge, X.; Geng, J.; Men, Y.; Yuan, C. Effects of Graphene Morphology on Properties of Carbon Nanotube/Polyurethane Film Strain Sensors. *Coatings* **2022**, *12*, 1889. https://doi.org/10.3390/coatings12121889

Academic Editor: Gianfranco Carotenuto

Received: 30 October 2022
Accepted: 1 December 2022
Published: 5 December 2022

1. Introduction

The emergence of film sensors has completely changed human life. The flexible sensors are continuously improved and innovated, which play a vital role in environmental monitoring [1], liquid detection [2], food detection [3], and other fields. The most important application is monitoring human health, collecting real-time characteristics of life parameters changes to understand human behavior better. Connecting the flexible sensor to the human skin can monitor pulse, heartbeat, blood pressure, finger bending, tiny facial muscle movements, vocal cord vibration, and so on [4–9], to complete multi-directional accurate monitoring of human life and health. In addition to applications in the medical and health field, flexible strain sensors can also be integrated into the intelligent robot arm, endowing the robotic arm with a human-like sense of touch, perceiving the size and spatial distribution of pressure [10].

Carbon materials have a broad prospect as conductive fillers for film sensors, especially graphene (GN) and carbon nanotubes (CNT), which have excellent electrical conductivity among carbon materials; these have attracted the extensive attention of researchers. The combination of GN or CNT with polymers in a specific way can form an electron transport channel in the polymer, while maintaining the flexibility of the polymer [11–15]. Vertuccio et al. [16] used simple film casting technology to produce CNT/epoxy resin composites for preparing strain sensors with GFs between 0.67 and 4.45. In order to increase the strain range of the sensor, using 3D printing technology, Christ et al. [17] prepared a multi-walled carbon nanotube/polyurethane highly elastic deformation sensor with a high GF.

Polyurethane (PU) elastomers have been proven to be used as substrates for film flexible sensors [18–21]. GN and CNT can be regularly and directionally arranged in polyurethane through the CVD method [19], the biological stretching process [20], and 3D spraying [21]. The physicochemical properties of GN prepared by different methods are much different and they show different conductivities when doped into film sensors; however, there are few reports on the effects of GN prepared with different methods on the performance of film sensors.

In this paper, we prepared three kinds of graphene with different sheet sizes and thicknesses by the ultrasonic-assisted electrochemical method and chemical redox method. Different types of GN and CNT were dropped into PU to prepare PU-based composite films. The dispersion state of carbon nanomaterials in PU was characterized by SEM and XRD; the volume conductivity of PU composite flexible films was deeply analyzed; the GFs of PU flexible sensors were tested and calculated so that different qualities of GN can be better used in flexible sensors.

2. Materials and Methods

2.1. Materials

Graphite foils were provided by Jinglong Special Carbon Co., Ltd. (Beijing, China). NaOH and $(NH_4)_2SO_4$ were purchased from Tianjin Kemiou Chemical Reagent Co., Ltd. (Tianjin, China). Isophorone diisocyanate (IPDI) was purchased from Macklin Biochemical Technology Co., Ltd. (Shanghai, China). Polyether polyols were purchased from SINOPEC Tianjin Branch. Dibutyltin dilaurate (DBTDL) and L-ascorbic acid (L-AA, 99%) were purchased from Heowns Chemical Co., Ltd. (Tianjin, China). N, N-Dimethylformamide (DMF, AR, 99.5%) was provided by Bohua Chemical Reagent Co., Ltd. (Tianjin, China). Multi-walled carbon nanotubes (CNT, 99 wt%, OD = 5–15 nm, length = 10–30 um) were provided by Chengdu Organic Chemicals Co. Ltd (Chengdu, China).

2.2. Preparation of GNs

Three kinds of GN samples were prepared, one of which was prepared by the chemical redox method. Graphene oxide was prepared by the modified Hummers' process reported by the previous work of our team [22]; then, reduced graphene oxide (rGO) was obtained after being reduced with environmentally friendly L-AA at 25 °C for 24 h.

Another two GN samples were prepared by the ultrasonic-assisted electrochemical method in different electrolyte solutions (1.0 mol/L NaOH solution or 0.1 mol/L $(NH_4)_2SO_4$ solution). Graphite foils were used as the active electrodes; the insert electrode was platinum electrode (15 mm × 10 mm). The electrolysis time was 2 h. The black dispersion obtained by electrolysis was filtered under reduced pressure with a 0.22 μm polytetrafluoroethylene microporous filter membrane, and the solid was washed with distilled water until the pH of the filtrate was about 7. After drying, GN samples were obtained. The two GN samples prepared in 1.0 mol/L NaOH electrolyte solution and 0.1 mol/L $(NH_4)_2SO_4$ electrolyte solution were named G1 and G2, respectively.

2.3. Fabrication of PU-Based Films and Film Strain Sensors

A certain amount of GN and CNT powder were added into 100 mL of dewatered DMF, ultrasonically dispersed for 1 h. GN-CNT/DMF solution was mixed into polyurethane monomers with a certain ratio; then, the catalyst DBTDL was dripped. The polymerization was carried out at 85 °C for 3 h. To obtain GN-CNT/PU films, the GN-CNT/PU solutions were finally cured in PTFE mold at 60 °C for 4 h, and at 80 °C for 2 h to obtain films with a length of 4 cm, a width of 1 cm, and a thickness of 0.5–1.0 mm. Copper foil and silver wire were assembled on both ends of the film to obtain strain sensors. The film sample was named as $\text{Graphene}_{\text{volume fraction}}\text{-CNT}_{\text{volume fraction}}\text{/PU}$; for example, $\text{G1}_{0.01}\text{-CNT}_{0.2}\text{/PU}$ means graphene G1-CNT/PU composite film, and the volume fraction of G1 and CNT are 0.01 vol% and 0.20 vol%, respectively. The schematic diagram of the preparation process of GN-CNT/PU film strain sensors is shown in Figure 1.

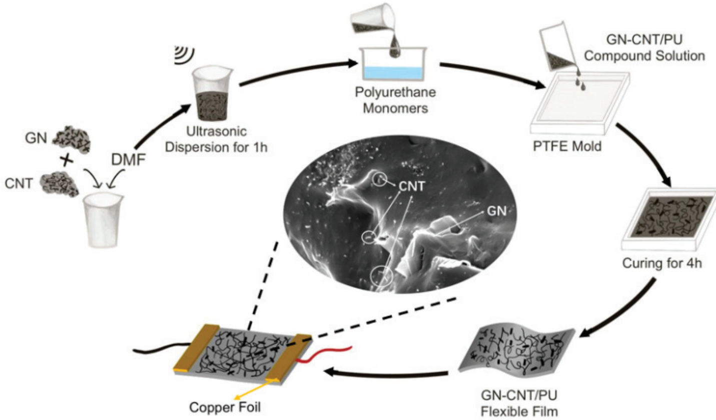

Figure 1. Schematic diagram of preparing GN-CNT/PU film strain sensors.

2.4. Characterizations

The surface morphology of graphene was observed by an atomic force microscope (AFM, Dimension Icon, Bruker, Karlsruhe, Germany) and field-emission scanning electron microscope (FESEM; Gemini 300, Carl Zeiss, Oberkochen, Germany). The chemical characteristics of prepared carbon materials was conducted by an X-ray photoelectron spectrometer (XPS; ESCALAB-250Xi, Thermo Fisher Scientific, Waltham, MA, USA). The dispersion of GN and CNT in PU films was characterized by XRD (MiniFlex600, Rigaku Corporation, Tokyo, Japan). The sensitivities of the film flexible strain sensors were tested by a universal testing machine (WDW-05L, Jinan Spai Technology Co., Ltd., Jinan, China), and the electrical conductivities were synchronously and automatically recorded by an electrochemical workstation (VERTEX V16407, Ivium Technologies, Eindhoven, The Netherlands) with a data acquisition frequency of 50 Hz.

3. Results and Discussion

3.1. Morphologies of GN

It can be seen from Figure 2a,d,g that the horizontal size of G1 is about 1 μm; the thickness is about 1.76 nm, around 3 to 4 layers of graphene; and the thickness of the graphene sheets is uniform, with the edges of G1 being relatively smooth. From Figure 2b,e,h, the horizontal size of G2 is about 0.7 μm and the sheets size is relatively uniform. The thickness of G2 is about 1.20 nm, with 2~3 layers of graphene. G2 has a smaller sheet size and fewer graphene layers than G1. The horizontal size of rGO sheets reduced with L-AA is about 1.5–2 μm and the thickness is about 2.00 nm in Figure 2c,f. The sizes of G1 and G2 are significantly smaller than that of rGO, and the defects of G1 and G2 are fewer; the surfaces are flatter and the structures are more complete.

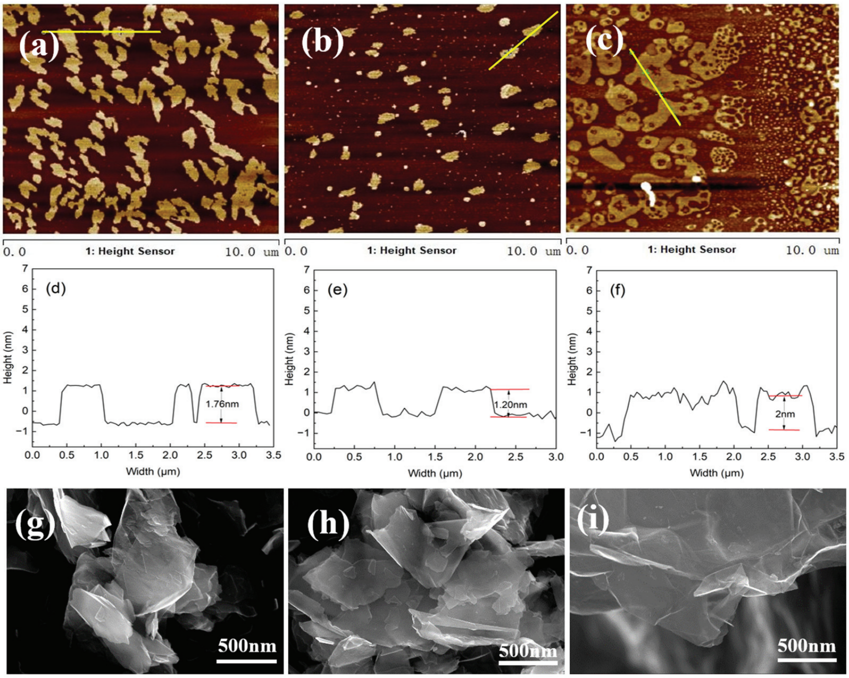

Figure 2. AFM 2D images of graphene (**a**) G1, (**b**) G2, and (**c**) rGO; the thickness (height) of graphene (**d**) G1, (**e**) G2, and (**f**) rGO; and FESEM images of graphene (**g**) G1, (**h**) G2, and (**i**) rGO.

3.2. Chemical Characteristics of Prepared GN and GO

The carbon and oxygen content in carbon material samples is usually obtained by XPS. By analyzing C 1s to O 1s peak in the XPS spectra of GO and GN, the atomic ratios of C/O were obtained. The precise oxygen content and C/O ratios of four carbon materials are listed in Table 1. It can be seen that the oxygen content of samples G1, G2, and rGO is increasing. The oxygen content of G1 is only 4.03 atom %, with a high C/O ratio of 23.81. The oxygen content of G2 (9.99 atom %) is slightly higher than that of G1. rGO reduced by L-AA contains more oxygen than GN prepared by the electrochemical method.

Table 1. XPS compositions of prepared GN and GO.

	C Content (Atomic %)	O Content (Atomic %)	C/O Ratios
G1	95.97	4.03	23.81
G2	90.01	9.99	9.01
GO	68.04	31.96	2.12
rGO	89.44	10.56	8.47

Figure 3 shows the high-resolution spectra of C 1s of three kinds of graphene and GO. The peaks of C-C, C-OH, C=O, and (C=O)-O groups are about 284.6 eV, 285.5 eV, 287.6 eV, and 288–290 eV, respectively [23–25]. Figure 3c shows that the sample GO contains a large number of oxygen-containing functional groups, with the oxygen content of 31.96%. The peak intensity of oxygen-containing functional groups in rGO is much weaker than that of GO, indicating that some oxygen-containing functional groups in GO have been successfully reduced by L-AA.

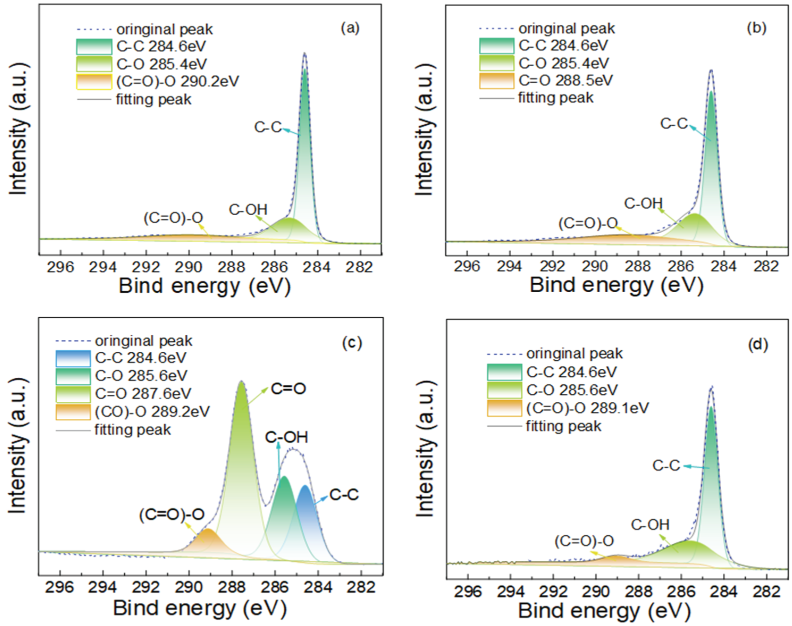

Figure 3. Curve-fitting of C 1s XPS spectra of (**a**) G1, (**b**) G2, (**c**) GO, and (**d**) rGO.

3.3. Dispersion of GN and CNT in PU Films

Figure 4a–d are FESEM images of the cross section in thickness direction of PU and $CNT_{0.2}$/PU films, respectively. The cross section of the PU film is relatively clean; only brittle fracture lines can be observed. The cross section of the sample $CNT_{0.2}$/PU exposes a lot of carbon nanotubes (bright spots and lines), indicating that the carbon nanotubes can be uniformly mixed in the PU through ultrasonic and mechanical stirring. From Figure 4c–j, it can be observed that many carbon nanotubes are randomly dispersed around GN sheets with a light yarn-like structure, which is the connection between the sheet-shaped GN and the linear carbon nanotubes to form a conductive path. The addition of graphene prevents CNT from agglomeration in PU to varying degrees. By comparing with Figure 4e,i,j the agglomeration of CNT in G2-doped composite film is significantly less than that in G1- and rGO-doped films.

The dispersion degree of graphene and carbon nanotubes in PU films can be explained laterally by XRD patterns in Figure 5. As expected, it is observed that the carbon nanotubes exhibit broad diffraction peaks at 25.8° and 43.1°; the former is the diffraction peak of the (002) crystal plane perpendicular to the diameter of the carbon nanotube, and the latter is the characteristic diffraction peak of the (100) crystal plane parallel to the diameter of the carbon nanotube. Graphene G1 and G2 have obvious diffraction peaks at $2\theta = 26.5°$, and rGO has characteristic peaks at $2\theta = 23.6°$. The diffraction peak of pure PU film appears near $2\theta = 19.1°$, which is mainly related to the short-range orderly and regular structure of the hard and soft segments of PU, and the existence of the disordered structure of the PU amorphous phase. After CNT and GN are doped in PU film, the XRD patterns of the composites show the characteristic peak of PU at 19.1°, while the characteristic peaks of CNT and GN disappear. It can be explained that when GN and CNT are doped in PU, the stacked GN sheets and agglomerated CNT will disperse under the action of Van der Waals force. Therefore, the crystal lattice of GN and CNT will be distorted, the XRD peaks will broaden, and the peaks intensity will decrease. When crystallite size become smaller with the increase of crystal lattice distortion, carbon material will be an amorphous structure, completely disordered, and the diffraction peaks of GN and CNT disappear. Therefore, it can be said that the graphene and carbon nanotubes can be well dispersed in PU film through ultrasonic dispersion and mechanical dispersion.

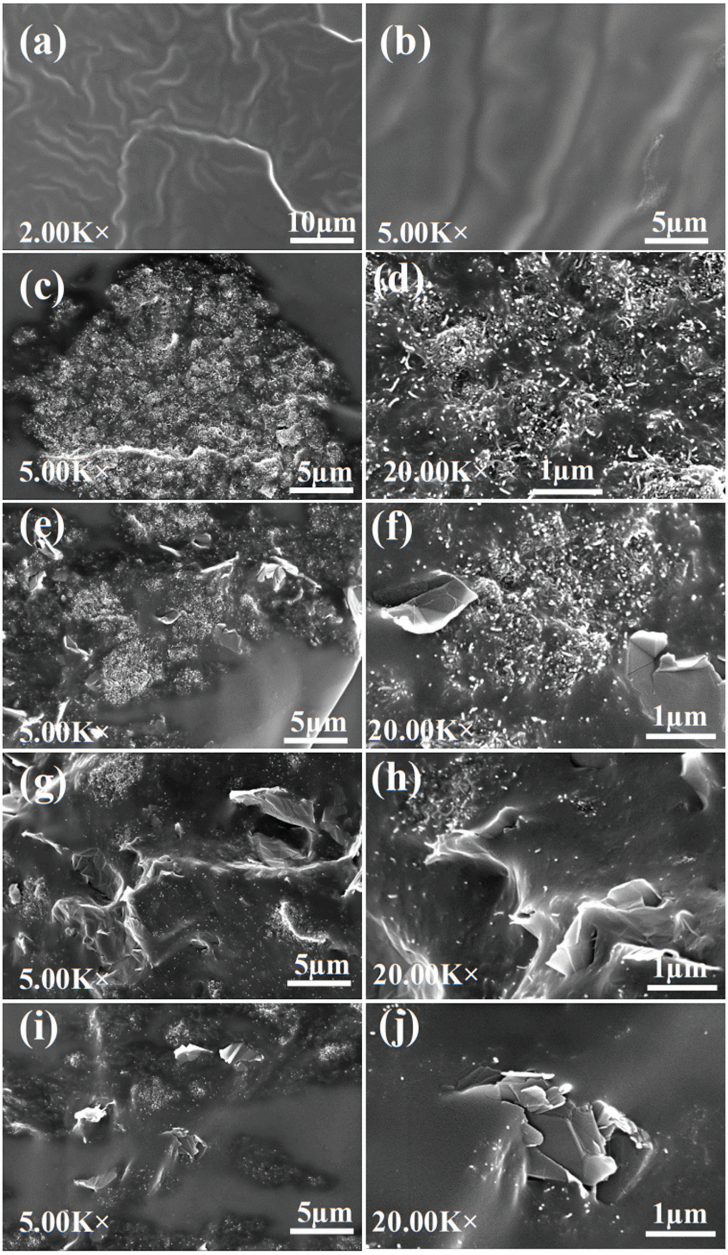

Figure 4. FESEM images of the cross section in thickness direction of PU and modified PU conductive films with different GN and CNT: (**a**,**b**) PU; (**c**,**d**) $CNT_{0.2}$/PU; (**e**,**f**) $G1_{0.1}$-$CNT_{0.2}$/PU; (**g**,**h**) $G2_{0.1}$-$CNT_{0.2}$/PU; (**i**,**j**) $rGO_{0.1}$-$CNT_{0.2}$/PU.

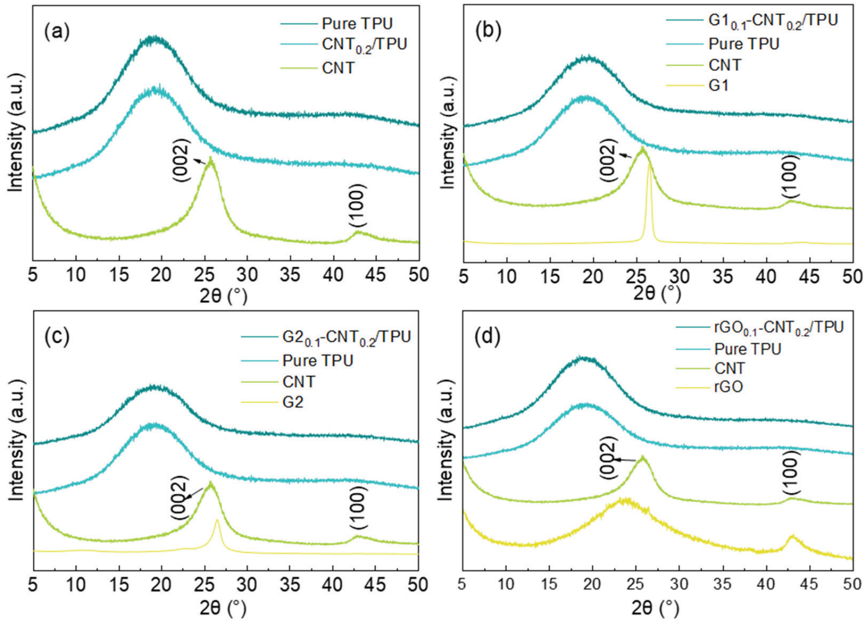

Figure 5. XRD patterns of pure PU film and PU composite films, with GN and CNT (**a**) $CNT_{0.2}$/PU, (**b**) $G1_{0.1}$- $CNT_{0.2}$/PU, (**c**) $G2_{0.1}$-$CNT_{0.2}$/PU, and (**d**) $rGO_{0.1}$-$CNT_{0.2}$/PU.

3.4. Electrical Properties of GN-CNT/PU Composite Films and Flexible Sensors

According to the percolation theory, the electrical conductivity of the composite and the volume fraction of the filler usually satisfy the following equation:

$$\sigma = \sigma_0 (V - V_c)^t$$

where σ and σ_0 are the volume conductivities of composites and the fillers (S/cm); *V* and V_c are the volume fraction and volume percolation threshold of the fillers (%); and *t* is a constant, relating to the dimension of conductivity path.

It can be seen from Figure 6a that when the content of CNT increased from 0.127 vol% to 0.255 vol%, the volume conductivities of the composites increased from 5.13×10^{-12} S/cm to 5.12×10^{-7} S/cm, having a 5-order magnitude improvement. According to the percolation theory, the volume percolation threshold of the fillers (V_c, %) of CNT doped in PU film is about 0.296 vol%. The constant *t* of CNT/PU flexible films is 1.16, calculated by percolation theory from Figure 6b. It can be said that CNT forms a good 2D conductive network in PU substrate and has a low percolation threshold.

The experiments set the doping content of CNT as 0.200 vol%, far less than that of its percolation threshold. The volume conductivity of the sample $CNT_{0.2}$/PU film is 2.19×10^{-11} S/cm. As shown in Figure 7a, the volume conductivity of the GN-$CNT_{0.2}$/PU film increased with the addition of GN. When the addition amount of G1, G2, and rGO was 0.020 vol% (1/10 of CNT content), the volume conductivities of $GN_{0.02}$-$CNT_{0.2}$/PU films were 5.77×10^{-7} S/cm, 1.41×10^{-7} S/cm, and 1.70×10^{-6} S/cm, for G1, G2, and rGo, respectively. Compared with $CNT_{0.2}$/PU, doping a minute amount of GN in $CNT_{0.2}$/PU can make the volume conductivities of flexible films increased by 4 to 5 orders of magnitude, and the effect of enhancing the conductivity is obvious. With the further increase of the addition of GN, the conductivities of composites increase linearly. It can be seen from Figure 7b that the constant t (slopes of the lines in Figure 7b) of G1, G2, and rGO in the $CNT_{0.2}$/PU system are 2.06, 1.31, and 1.36, respectively, which are higher than the t value of the CNT/PU film. It can confirm the role of graphene in CNT/PU composite film, as expected, forming a stronger 2D and 3D hybrid conductive network, or 3D conductive network with CNT. Compared with the need to dope about 0.100 vol% CNT to obtain a decent volume conductivity, adding less than 0.020 vol% of graphene can obtain the same conductive effect. This phenomenon may be caused by the smaller graphene flakes; this not only can assist in forming a more complete conductive path, but also prevent CNT entanglement or formation of CNT bundles, making the dispersion of CNT more uniform.

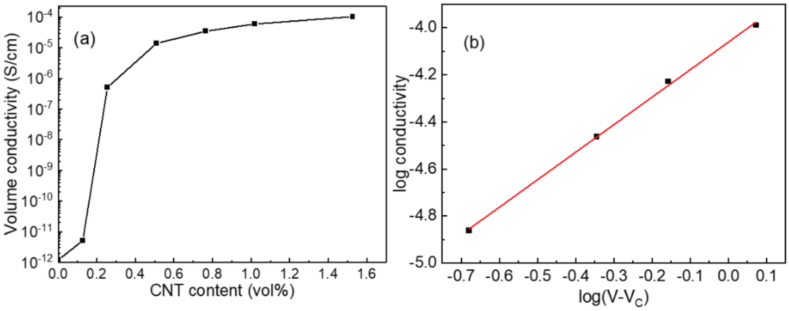

Figure 6. (**a**) Volume conductivity plotted as a function of CNT content; (**b**) log(σ) plotted as a function of log(V-Vc).

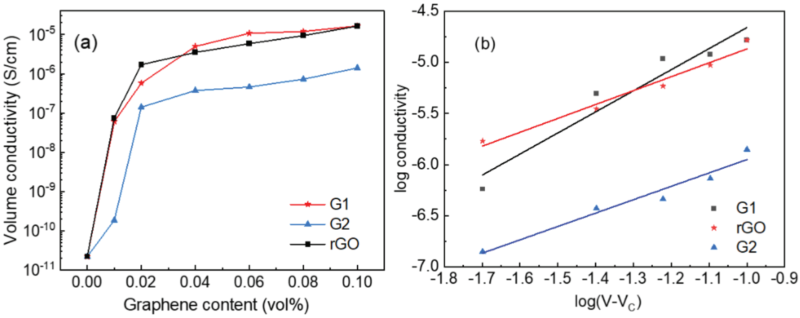

Figure 7. (**a**) Volume conductivity of GN-CNT$_{0.2}$/PU composite film as a function of the volume fraction of GN; (**b**) log(σ)-log(V-V$_c$) curves of CNT$_{0.2}$/PU composite film doped with different kinds of graphene.

From Figure 8a, the GFs of G1$_x$-CNT$_{0.2}$/PU sensors (x = 0.01, 0.02, 0.04, 0.06) are 1.14, 4.18, 13.15, and 1.88, respectively, showing a trend of increasing firstly and then, decreasing. To explore the influence of graphene prepared by different methods on the GFs of the flexible sensors, the current change of the GN$_{0.06}$-CNT$_{0.2}$/PU sensors were tested within a strain of 20%, and the results are shown in Figure 8b. The GFs of G1$_{0.06}$-CNT$_{0.2}$/PU, G2$_{0.06}$-CNT$_{0.2}$/PU, and rGO$_{0.06}$-CNT$_{0.2}$/PU are 1.88, 3.47, and 1.41, respectively. The G2-doped film flexible sensor has the highest GF. From the AFM results of GN, G2 has the smallest sheet size, followed by G1, and rGO has the largest size. It is assumed that CNTs in PU are untwisted, oriented, and without overlapping distribution. In an ideal state, according to the outside diameter and length of carbon nanotubes, when the volume fraction of CNT in PU film is 0.2 vol%, the estimated gap between carbon nanotubes is about 200–500 nm. The smaller the graphene sheet, the greater the probability of graphene being inserted into the gap between the CNT. The greater the overlap density with the CNT, the more obvious the resistance change during stretching; and therefore, the greater the GF. When the GN layer is large, according to estimated gap between CNT, the smaller the probability of GN inserting into the gap, the less the hybrid conductive network formed between GN and CNT; thus, GF will also be smaller.

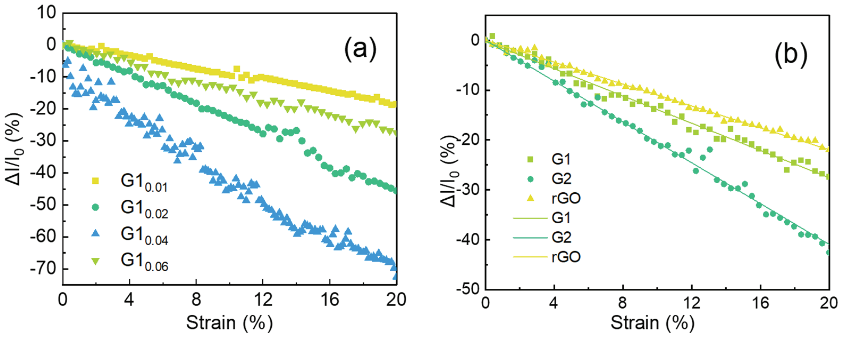

Figure 8. (**a**) Normalized current change $\Delta I/I_0$ plotted as a function of tensile strain (20%) of G1$_x$-CNT$_{0.2}$/PU composites; (**b**) $\Delta I/I_0$ plotted as a function of tensile strain (20%) of GN$_{0.06}$-CNT$_{0.2}$/PU composites.

The performance comparison between the flexible sensors assembled in this work and the PU-based sensors previously reported are shown in Table 2. It is found that, compared to others' works that use PU as substrate, and the combination of conductive fillers and PU in a simple and uniform mixture, the flexible sensors of this work can reach the GF at a higher level when the content of the added conductive fillers is very small.

Table 2. Performance of flexible sensors based on PU matrix.

Conductive Fills	Content	Strain (%)	GF	References
Carbon black	3 wt%	30%	3.5	[26]
GN	0.6 wt%	30%	0.78	[13]
CNT	2 wt%	5%	20	[27]
rGO/Fe_3O_4	1 wt%	12%	6.2	[18]
G1/CNT	0.04 vol%/0.2 vol%	20%	13.15	This work

Cyclic tensile tests (strain from 15% to 50% and circulated 100 times) were carried out on the G1$_{0.06}$-CNT$_{0.2}$/PU sensor. It can be seen from the Figure 9a that after the sample is stretched for dozens of times, the curve tends to be flat; however, there are still fluctuations. $\Delta R/R_0$-time and the corresponding elongation–time curves of the sample after 21–25 cycles and 91–95 cycles are shown in Figure 9b. It can be observed that the normalized resistance of the sample increases with the elongation of the G1$_{0.06}$-CNT$_{0.2}$/PU film sensor. When the sensor elongation is 50%, the change in resistance value reaches the maximum; that is, a higher peak in the curve. As the elongation of the sample decreases, the value of $\Delta R/R_0$ decreases first and then, increases; in addition, a secondary peak appears when the strain recovers to 15%. The sensors made of G2- and rGO-doped CNT/PU films showed almost the same secondary peak phenomenon in the cycle tests; however, the G1-CNT/PU film sensor showed better stability during the long cyclic tensile tests. Therefore, the cyclic test results of the G1-CNT/PU film sensor were reported. The main reason for the secondary peak is that during the rebound process of the composite, although the conductive network reconstruction in the sample mainly occurs as the strain decreases, the conductive network of the carbon material will be subjected to secondary damage due to residual stress and creep. When the residual stress is greater than the reconstruction of the conductive network in the PU itself, the resistance will increase again, and the secondary peak appears.

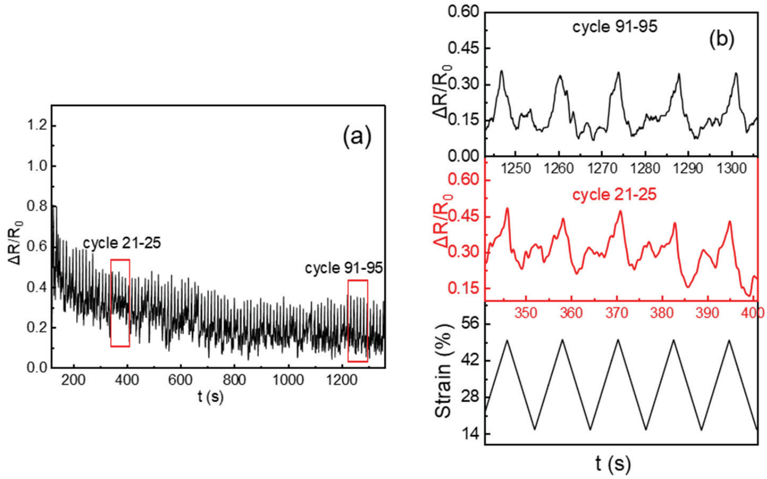

Figure 9. (**a**) normalized resistance change $\Delta R/R_0$-time curves in correspondence of strain varies from 15% to 50% of $G1_{0.06}$-$CNT_{0.2}$/PU composite; (**b**) $\Delta R/R_0$-time curves and tensile strain–time curve of $G1_{0.06}$-$CNT_{0.2}$/PU sensor.

4. Conclusions

Three kinds of GN samples with different sheet sizes and thicknesses were prepared and composited with CNT and PU to manufacture film flexible sensors. The size of the GN layers affected the GF of the flexible sensors; that means the appropriate size of a GN sheet is essential to obtain a flexible sensor with an excellent GF. With the same amount of graphene added, a higher GF of sensors can be obtained by reducing graphene size. These results have an excellent reference for the application of graphene with different sheet sizes in flexible sensors.

Author Contributions: Conceptualization, C.L. and C.Y.; data curation, C.L.; formal analysis, C.L.; investigation, C.L., J.G. and Y.M.; methodology, C.L., X.G. and C.Y.; project administration, C.Y.; resources, X.G. and C.Y.; supervision, C.Y.; validation, C.L., J.G. and Y.M.; visualization, C.L.; writing—original draft, C.L.; writing—review and editing, X.G. and C.Y. All authors have read and agreed to the published version of the manuscript.

Funding: This research was funded by the Independent Innovation Fund of Tianjin University (No. 2021XZS-0017).

Institutional Review Board Statement: Not applicable.

Informed Consent Statement: Not applicable.

Data Availability Statement: Not applicable.

Conflicts of Interest: The authors declare no conflict of interest.

References

1. Yunus, M.; Mukhopadhyay, S.C. Development of planar electromagnetic sensors for measurement and monitoring of environmental parameters. *Meas. Sci. Technol.* **2011**, *22*, 025107. [CrossRef]
2. Tashiro, K.; Wakiwaka, H.; Mori, T.; Nakano, R.; Harun, N.H.; Misron, N. Experimental confirmation of cylindrical electromagnetic sensor design for liquid detection application. In *Sensing Technology: Current Status and Future Trends IV*; Mason, A.S., Mukhopadhyay, S., Jayasundera, K., Eds.; Springer International Publishing: Cham, Switzerland, 2015; Volume 12, pp. 119–137. [CrossRef]
3. Zia, A.I.; Rahman, M.; Mukhopadhyay, S.C.; Yu, P.L.; Al-Bahadly, I.H.; Gooneratne, C.P.; Kosel, J.; Liao, T.S. Technique for rapid detection of phthalates in water and beverages. *J. Food Eng.* **2013**, *116*, 515–523. [CrossRef]
4. Park, J.J.; Hyun, W.J.; Mun, S.C.; Park, Y.T.; Park, O.O. Highly stretchable and wearable graphene strain sensors with controllable sensitivity for human motion monitoring. *ACS Appl. Mater. Inter.* **2015**, *7*, 6317–6324. [CrossRef] [PubMed]

5. Wu, X.; Han, Y.; Zhang, X.; Lu, C. Highly sensitive, stretchable, and wash-durable strain sensor based on ultrathin conductive layer@polyurethane yarn for tiny motion monitoring. *ACS Appl. Mater. Inter.* **2016**, *8*, 9936–9945. [CrossRef] [PubMed]
6. Jian, Z.; Xu, X.; Hu, Y.; Lubineau, G. Deformable and wearable carbon nanotube microwire-based sensors for ultrasensitive monitoring of strain, pressure and torsion. *Nanoscale* **2017**, *9*, 604–612. [CrossRef]
7. Tao, X.M.; Wang, F.; Liu, S.; Shu, L. Low-dimensional carbon based sensors and sensing network for wearable health and environmental monitoring. *Carbon* **2017**, *121*, 353–367. [CrossRef]
8. Yin, B.; Wen, Y.W.; Hong, T.; Xie, Z.S.; Yuan, G.L.; Ji, Q.M.; Jia, H.B. Highly stretchable, ultrasensitive, and wearable strain sensors based on facilely prepared reduced graphene oxide woven fabrics in an ethanol flame. *ACS Appl. Mater. Inter.* **2017**, *9*, 32054–32064. [CrossRef]
9. Yan, T.; Wang, Z.; Wang, Y.Q.; Pan, Z.J. Carbon/graphene composite nanofiber yarns for highly sensitive strain sensors. *Mater Design.* **2018**, *143*, 214–223. [CrossRef]
10. Chun, S.; Son, W.; Kim, H.; Lim, S.K.; Pang, C.; Choi, C. Self-powered pressure- and vibration-sensitive tactile sensors for learning technique-based neural finger skin. *Nano Lett.* **2019**, *19*, 3305–3312. [CrossRef]
11. Zhu, B.; Niu, Z.; Wang, H.; Leow, W.R.; Wang, H.; Li, Y.; Zheng, L.; Wei, J.; Hou, F.; Chen, X. Microstructured graphene arrays for highly sensitive flexible tactile sensors. *Small* **2014**, *10*, 3625–3631. [CrossRef]
12. Wei, Y.; Qiao, Y.; Jiang, G.; Wang, Y.; Ren, T.L. A wearable skin-like ultra-sensitive artificial graphene throat. *ACS Nano* **2019**, *13*, 8639–8647. [CrossRef] [PubMed]
13. Liu, H.; Li, Y.; Dai, K.; Zheng, G.; Liu, C.; Shen, C.; Yan, X.; Guo, J.; Guo, Z. Electrically conductive thermoplastic elastomer nanocomposites at ultralow graphene loading levels for strain sensor applications. *J. Mater. Chem. C* **2015**, *4*, 157–166. [CrossRef]
14. Liu, L.; Zhang, D. The sensitive electrical response of reduced graphene oxide-polymer nanocomposites to large deformation. *Compos. Part A Appl. Sci. Manuf.* **2015**, *75*, 46–53. [CrossRef]
15. Tian, Y.; Wang, D.Y.; Li, Y.T.; Tian, H.; Ren, T.L. Highly sensitive, wide-range, and flexible pressure sensor based on honeycomb-like graphene network. *IEEE Trans. Electron Devices* **2020**, *67*, 2153–2156. [CrossRef]
16. Vertuccio, L.; Vittoria, V.; Guadagno, L.; Santis, F.D. Strain and damage monitoring in carbon-nanotube-based composite under cyclic strain. *Compos. Part A Appl. Sci. Manuf.* **2015**, *71*, 9–16. [CrossRef]
17. Christ, J.F.; Aliheidari, N.; Ameli, A.; Pötschke, P. 3D printed highly elastic strain sensors of multiwalled carbon nanotube/thermoplastic polyurethane nanocomposites. *Mater. Design* **2017**, *131*, 394–401. [CrossRef]
18. Tung, T.T.; Robert, C.; Castro, M.; Feller, J.F.; Kim, T.Y.; Suh, K.S. Enhancing the sensitivity of graphene/polyurethane nanocomposite flexible piezo-resistive pressure sensors with magnetite nano-spacers. *Carbon* **2016**, *108*, 450–460. [CrossRef]
19. Slobodian, P.; Riha, P.; Kondo, H.; Cvelbar, U.; Olejnik, R.; Matyas, J.; Sekine, M.; Hori, M. Transparent elongation and compressive strain sensors based on aligned carbon nanowalls embedded in polyurethane. *Sens. Actuat. A Phys.* **2020**, *306*, 111946. [CrossRef]
20. Chen, X.; Xiang, D.; Li, J.; Zhang, X.; Jones, E.H.; Wu, Y.; Zhao, C.; Li, H.; Li, Z.; Wang, P.; et al. Flexible Strain Sensors with Enhanced Sensing Performance Prepared from Biaxially Stretched Carbon Nanotube/Thermoplastic Polyurethane Nanocomposites. *ACS Appl. Electron. Mater.* **2022**, *4*, 3071–3079. [CrossRef]
21. Tran, M.T.; Tung, T.T.; Sachan, A.; Losic, D.; Castro, M.; Feller, J.F. 3D sprayed polyurethane functionalized graphene/carbon nanotubes hybrid architectures to enhance the piezo-resistive response of quantum resistive pressure sensors. *Carbon* **2020**, *168*, 564–579. [CrossRef]
22. Zhang, X.; Su, J.; Wang, X.Y.; Tong, X.L.; Yao, F.L.; Yuan, C.D. Synthesis of graphene aerogels using cyclohexane and n-butanol as soft templates. *RSC Adv.* **2020**, *10*, 14283–14290. [CrossRef] [PubMed]
23. Srivastava, S.; Kashyap, P.K.; Singh, V.; Senguttuvan, T.D.; Gupta, B.K. Nitrogen doped high quality CVD grown graphene as a fast responding NO_2 gas sensor. *New J. Chem.* **2018**, *42*, 9550–9556. [CrossRef]
24. Parvez, K.; Wu, Z.S.; Li, R.; Liu, X.; Graf, R.; Feng, X.; Müllen, K. Exfoliation of graphite into graphene in aqueous solutions of inorganic salts. *J. Am. Chem. Soc.* **2014**, *136*, 6083–6091. [CrossRef] [PubMed]
25. Zhang, Y.; Xu, Y. Simultaneous electrochemical dual-electrode exfoliation of graphite toward scalable production of high-quality graphene. *Adv. Funct. Mater.* **2019**, *29*, 1902171. [CrossRef]
26. Qiu, A.; Jia, Q.; Yu, H.; Oh, H.; Li, D.; Hsu, H.; Kawashima, N.; Zhuge, Y.; Ma, J. Highly sensitive and flexible capacitive elastomeric sensors for compressive strain measurements. *Mater. Today Commun.* **2021**, *26*, 102023. [CrossRef]
27. Zhang, R.; Deng, H.; Valenca, R.; Jin, J.; Fu, Q.; Bilotti, E.; Peijs, T. Strain sensing behaviour of elastomeric composite films containing carbon nanotubes under cyclic loading. *Compos. Sci. Technol.* **2013**, *74*, 1–5. [CrossRef]

coatings

MDPI

Article

Photoresist Microlens Arrays Fabricated by Nanoimprint Technique to Improve the Photoelectric Conversion Efficiency of Solar Cells

Xuehua Zhang [1,*], Liangwei Lv [1], Xinwen Zhang [1] and Fangren Hu [1,2,*]

[1] College of Electronic and Optical Engineering & College of Microelectronics, Nanjing University of Posts and Telecommunications, Nanjing 210023, China
[2] Peter Grunberg Research Center, Nanjing 210023, China
* Correspondence: zhangxuehua@njupt.edu.cn (X.Z.); hufr@njupt.edu.cn (F.H.); Tel.: +86-25-8586-6402 (F.H.)

Abstract: Silicon solar cells have the advantages of non-toxicity, reliability, low price, and stability. Microlens arrays (MLAs) are widely used in solar cells to improve photoelectrical conversion efficiency (PCE). In this research, different MLAs mold was designed by a method of thermal reflow. Then the photoresist film MLAs structure was replicated on the surface of silicon solar cells through UV nanoimprint technology. The optical transmission and surface morphology of these photoresist films were respectively measured by using a UV spectrometer and an atomic force microscope. The surface morphology and imaging capabilities of photoresist film MLAs were respectively measured by using a scanning electron microscope and optical microscope. Finally, the photovoltaic performance of the silicon solar cell with the photoresist film MLAs was investigated, and the PCE value of the silicon solar cell improved from 11.53% for the sample without MLAs to 13.19% for the sample with the square MLAs and the PCE improvement is about 14.40%. All these results above show that the photoresist film MLAs can significantly improve the efficiency of silicon solar cells and have great application potential in the field of solar cells.

Keywords: MLAs; solar cell; photoresist film; UV nanoimprint technology

Citation: Zhang, X.; Lv, L.; Zhang, X.; Hu, F. Photoresist Microlens Arrays Fabricated by Nanoimprint Technique to Improve the Photoelectric Conversion Efficiency of Solar Cells. *Coatings* **2022**, *12*, 1812. https://doi.org/10.3390/coatings12121812

Academic Editor: Gianfranco Carotenuto

Received: 19 October 2022
Accepted: 23 November 2022
Published: 24 November 2022

1. Introduction

Solar energy, a non-polluting renewable green energy, has received extensive attention [1]. Many kinds of solar cells have been designed, including silicon solar cells [2], allium arsenide cells [3], perovskite cells [4–6], dye-sensitized solar cells [7], and so on. Moreover, silicon solar cells have already owned the highest market share in recent years owing to their non-toxicity, low price, stability, high conversion efficiency, reliability, and mature manufacturing technology [8–10].

There are two processes in the silicon solar cells that generate photoelectrical power. The absorption of photons causes the excitation of electron-hole pairs and the transport and separation of electron-hole pairs to external electrodes. Two main factors influence the efficiency of these silicon solar cells. One factor is the reflectance of the surface of the silicon solar cell, which affects the total amount of light absorption, and another factor is the collection of the photo-generated carriers and the loss of photo-generated carrier recombination.

In order to effectively collect photo-generated carriers and suppress the recombination loss of photo-generated carriers, many high-efficiency silicon solar cells were produced, such as the passivated emitter rear cell (PERC), the heterojunction solar cells with interdigitated back contacts (HBC), and the interdigitated back contact cell (IBC) [11]. However, these solar cells involve complicated technologies and may not be suitable for extensive production. Micro/nanostructures are generally used to decrease the reflectivity of the surface of silicon solar cells. These structures are usually used on the surface of silicon solar cells by etching technology or UV nanoimprint technology. These methods are relatively simple to operate and are suitable for extensive applications in solar cells.

Many kinds of methods can fabricate micro/nanostructures, such as microspheres self-assembly, partial-filling hot embossing technique, femtosecond laser direct writing, and the thermal reflow method. Compared with other methods, the advantages of nanoimprint technique has the advantages of simple operation, high feasibility, and low price. Many kinds of microstructures, such as micro/nanocones [12], nanowires [13,14], nanospheres [15], inverted pyramids [16], and nanopillars [17], have been proposed to reduce surface reflection to improve the PCE of the solar cells. Microlens arrays (MLAs) are used in solar cells to improve photoelectric conversion efficiency due to their excellent optical properties. For example, Gao et al. fabricated a Moth-eye nanostructure, which increased the reflectivity by 46.6% and improved the PCE of ultra-thin c-Si solar cells by 42.3% [18]. Huang et al. fabricated double-layer nano-pyramid arrays on thin-film solar cells [19]. The integrated absorption and PCE of the solar cell were increased by 45.31% and 15.77%. Osama et al. fabricated the 2D non-close-packed nanopore arrays on the perovskite layer, and the devices achieved a champion PCE of 11.64% [20].

In this work, we fabricated original MLAs molds of three different shapes using the thermal reflow method [21]. Photoresist film MLAs were replicated from the original MLAs mold by using UV nanoimprinting and applied on silicon solar cells [22]. The surface topography and optical properties of the photoresist film were investigated. The photoresist film MLAs can reduce the reflectivity of the substrate and have a great application value in the field of optics. Then the properties of current voltage, fill factor, and power of silicon solar cells with different shapes of photoresist film MLAs were measured, and it was found that the photoelectrical conversion efficiency (PCE) of the solar cells with square film MLAs has the maximum improvement of about 14.40%. Finally, the change in the conversion efficiency of solar cells under different incident angles of sunlight was studied.

2. Materials and Methods

2.1. The Design of MLAs Mask

The MLAs mask with three different microlens shapes was designed as shown in Figure 1. It can be easily found from Figure 1 that the circular and hexagonal MLAs have the regular hexagon arrangement, and the square MLAs have the square arrangement. D_1, D_2, and D_3, respectively, are the diameter lengths of the MLAs. d_1, d_2, and d_3 represent the spacing between adjacent MLAs. The filling factors of these MLAs have been calculated as 80.11%, 89.23%, and 86.58%, respectively, for the circular, square, and hexagonal MLAs. The detailed parameters of the MLAs, including the diameter and spacing, can be found in Table 1.

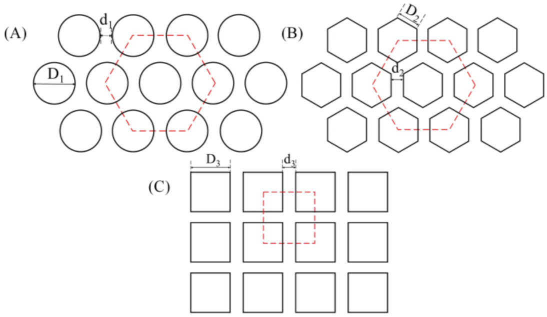

Figure 1. The arrangement diagram of the special-shaped microlens array mold. (**A**) the circular, (**B**) the hexagonal, and (**C**) the square MLAs.

Table 1. The detailed parameters of these MLAs mask.

MLAs Shape	Diameter/Side Length (μm)	Space (μm)
Circular	15	3
Square	15	3
Hexagonal	15	3

2.2. Fabrication Process of Photoresist Film MLAs on Silicon Solar Cells

The process of preparing photoresist film MLAs on silicon solar cells is demonstrated in Figure 2. The whole process concludes in two steps. First, a photoresist thermal reflow method is used to prepare the original MLAs mold, as shown in Figure 2A–D. Second, the photoresist film MLAs were fabricated on silicon solar cells using UV nanoimprint technology, as shown in Figure 2E–I.

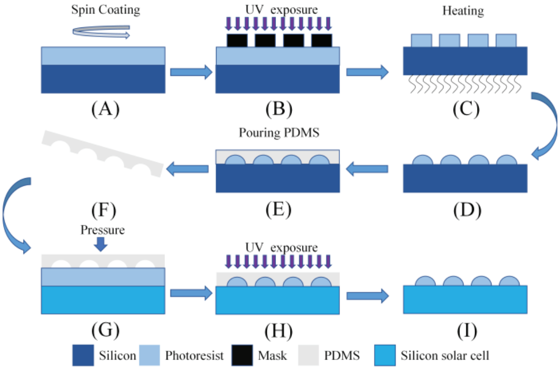

Figure 2. Flow chart of the manufacturing process of the photoresist film MLAs on silicon solar cells. (**A**) Spin coating photoresist film on this silicon substrate, (**B**) exposure of the photoresist film to the UV light with Ge mask, (**C**) thermal reflow, (**D**) original photoresist mold, (**E**) replicating PDMS mold, (**F**) peeling off this mold, (**G**) pressing a PDMS mold on this photoresist film, (**H**) exposing this sample for solidification, (**I**) obtained silicon solar cells with MLAs.

2.3. Preparation of Original MLAs Mold

The original MLAs mold was fabricated by the thermal reflow method. This is shown in Figure 2A–D. First, the photoresist (AZ4620) was spin-coated on a circular substrate at a high speed of 2000 rpm for 30 s. This film was then prebaked at 100 °C for 10 min so that the excess solvent from the photoresist could be removed. The Ge mask was placed under a 300 W UV high-pressure mercury lamp for the exposure of the photoresist film. The exposure time of UV light (365 nm) was 180 s. We dropped the sample in the developer (AZ300MIF) for 300 s; then, photoresist cylindrical islands were formed on the substrate. Then, we rinsed the sample with DI water. Finally, the sample was placed on the plate at 140 °C for 45 min for the photoresist thermal reflow process and finally obtained the original MLAs mold. It should be emphasized that the experimental conditions of the different structural MLAs molds are the same.

2.4. Fabrication of Photoresist Film MLAs on Silicon Solar Cells

Figure 2E–I show the fabrication of MLAs on silicon solar cells by UV nanoimprinting technology. PDMS monomer (Sylgard 184) was blended with the curing agent at a weight ratio of 10:1. Then, this mixture was poured slowly onto an original MLA mold. We placed the sample in a vacuum drying oven and heated it at 80 °C for 45 min. After the sample was cooled, the PDMS soft template was removed from the original MLA mold. Next, we used a spin coater to deposit a photoresist (NOA63) film on the surface of a silicon solar cell at a high spin coating speed of 2000 rpm for 60 s. The PDMS mold with the MLAs was pressed onto a photoresist film; then, this sample was exposed to ultraviolet light (365 nm) for 10 min under a xenon lamp (300 w), and the intensity of the light was 1200 mW/cm^2. In the end, this PDMS mold with the MLAs was peeled off, and the photoresist film MLAs were prepared on the silicon solar cells. Silicon solar cells were purchased from Anyang Sunshine Science and Education Energy Co., Ltd. (Anyang, China).

2.5. Characterizations

The surface topography and roughness of the photoresist films were investigated with an atomic force microscope (AFM, Bruker Dimension Icon, Karlsruhe, Germany).

The optical transmittance of these photoresist films, which were fabricated on glass substrates, was characterized with a UV spectrometer (USA UNICO UV-2800A, Shanghai Bayu Co., Ltd., Shanghai, China). We measured the surface profile of the photoresist film MLA with a step profiler (Alpha-Step D-500 KLA, Shanghai, China). The surface topography of these photoresist film MLAs was measured by scanning electron microscopy (SEM, S-4800, Hitachi, Tokyo, Japan). These imaging capabilities of photoresist film MLAs were all investigated by an inverted optical microscope (Ti2-E, Nikon, Japan). The photovoltaic performance of the solar cells was investigated by a solar workstation (SAN-EI, Hitachi, Tokyo, Japan) at AM 1.5.

3. Results

3.1. Optical Properties of The Photoresist Films

In this work, the optical character of these photoresist films was investigated. Figure 3A demonstrates an AFM image of this photoresist film with an area of 10 µm × 10 µm. Furthermore, these films were fabricated on glass substrates at the high spinning speed of 2000 rpm for 60 s. Then these films were exposed to the UV light for 10 min. As can be observed from Figure 3A that the surface of this photoresist film was clean and smooth. Furthermore, the roughness Ra of this photoresist film is 2.51 nm. Figure 3B manifests the optical transmittance of this photoresist film, which was fabricated on a glass substrate. As can be observed from Figure 3B that this transmittance value of the film in the light region from 350 to 800 nm is higher than 95%, which has great application value in the field of photovoltaic cells.

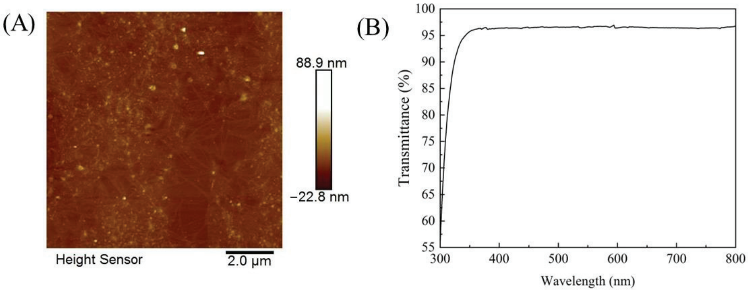

Figure 3. (**A**) The AFM image and (**B**) the optical transmittance of the photoresist film.

3.2. The Optical Transmittance of Photoresist Film MLAs

Figure 4 shows the optical transmittance of the photoresist film MLAs with different shapes and deposited on glass substrates. It can be clearly observed that the photoresist film MLAs have a suitable light transmittance of about 90%. It has great application value in the field of photovoltaic cells.

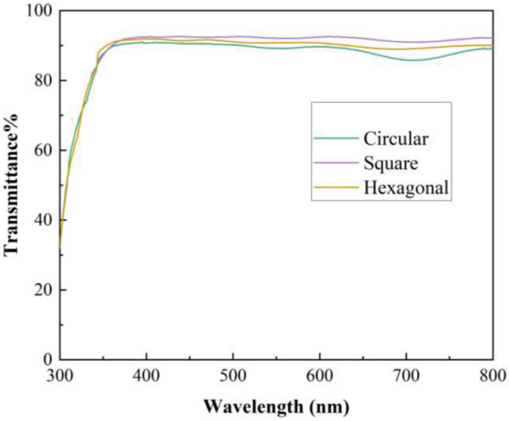

Figure 4. The optical transmittance of the photoresist film MLAs with different shapes and deposited on glass substrates.

3.3. The Surface Topography of Photoresist Film MLAs

The SEM images and surface profiles of the photoresist film MLAs are manifested in Figure 5. As can be observed clearly from Figure 5A–C, these photoresist film MLAs are on a smooth surface, the MLAs are tightly arranged, and there is no obvious damage. Figure 5D–F displays that the diameter of the circular microlens is about 16.50 μm, the side length of the hexagonal and square microlens, respectively, is 15.63 and 15.1 μm, and the heights are 3.20, 2.98, and 3.18 μm, respectively. There is some size difference between the photoresist film MLAs and the original mask, which is mainly caused by the thermal reflow and UV nanoimprint process.

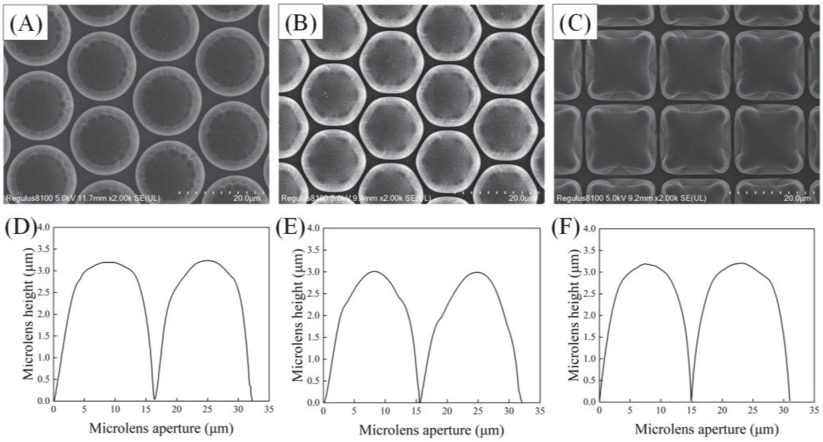

Figure 5. The SEM images and the surface profiles of (**A**,**D**) circular, (**B**,**E**) hexagonal, and (**C**,**F**) square photoresist film MLAs.

3.4. Optical Imaging Capabilities of Photoresist Film MLAs

Optical imaging properties of the photoresist film MLAs were investigated by an inverted optical microscope system. Moreover, Figure 6 manifests (A) the schematic of the imaging system and the virtual images of (B) circular, (C) hexagonal, and (D) square photoresist film MLAs. It should be mentioned that the photoresist film MLAs were fabricated on glass substrates. The test procedure is as follows: the photoresist film MLAs were first put on the optical platform. Furthermore, a tin foil mask in the shape of the letter

"T" was placed between the microscope light source and these photoresist film MLAs. A CCD camera can be applied to catch the light penetrating through this "T"-shaped mask and the photoresist film MLAs. Figure 5 manifests virtual images of the (B) circular, (C) hexagonal, and (D) square photoresist film MLAs, which show suitable imaging capabilities.

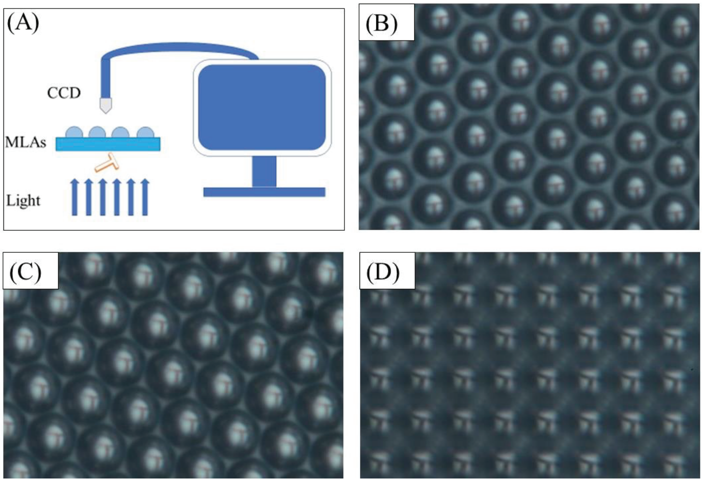

Figure 6. (**A**) The schematic of the imaging system and the virtual images of (**B**) circular, (**C**) hexagonal, and (**D**) square photoresist film MLAs.

3.5. The Transport Mechanism of Sunlight on Silicon Solar Cells

The fabricated photoresist film MLAs are applied to silicon solar cells. Figure 7A,B show the photographs of the silicon solar cells (A) without the photoresist film MLAs and (B) with the photoresist film MLAs. The size of both solar cells is 2 cm × 2 cm. Figure 7C,D show the transmission principle of the light on the silicon solar cell device. As shown in Figure 7C, when the light is incident vertically on the bare solar cell device, it will return back to the original path. As shown in Figure 7D, if the light hits the surface of the solar cell device with the photoresist film MLAs vertically, there will be three kinds of reflection paths (I, II, III). Light I, II will be reflected and dissipated in the air, but light III will be absorbed by the silicon solar cells. The utilization of light energy will be improved.

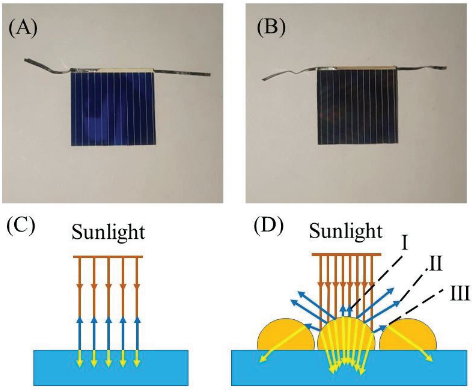

Figure 7. Photographs of the solar cells (**A**) without photoresist film MLAs and (**B**) with the photoresist film MLAs, and the light path of the incident sunlight on (**C**) a bare solar cell and (**D**) a solar cell with the photoresist film MLAs and three kinds of reflected light (I, II, III).

3.6. Photovoltaic Properties of These Solar Cells

Photovoltaic properties of these silicon solar cells were characterized. Figure 8 shows (A) I-V curves and (B) P-V curves of the silicon solar cells with flat photoresist film and photoresist film MLAs compared with the original silicon solar cells without photoresist film MLAs. As can be observed from Figure 8A that the short-circuit current of the solar cell with a flat photoresist film has a small increase than that of an original solar cell. Moreover, this short-circuit current of the solar cell with the photoresist film MLAs has an obvious increase to that of an original solar cell. The properties of the solar cell with a flat photoresist film have a small increase than an original solar cell. Then the current of these silicon solar cells with photoresist film MLAs from 0 to 0.5 voltage is significantly larger than the original silicon solar cell. It can also be obtained from Figure 8B that the power of the silicon solar cells with the photoresist film MLAs is larger than that of the original silicon solar cell and the solar cell with a flat photoresist film within the voltage of 0.1–0.5 V. The current voltage, fill actor, current density, and photoelectric conversion efficiency of the original solar cell have been measured as 570.0 mV, 65.93%, 30.85 mA/cm^2, and 11.53%. The maximum power (Pmax) value of the silicon solar cells with circular, hexagonal, and square MLAs is 49.24, 50.91, and 52.75 mW, respectively. Table 2 shows that the photoresist film MLAs increased the short-circuit current density J_{sc} by 6.74% for circular photoresist film MLAs, 6.35% for hexagonal photoresist film MLAs, and 7.39% for square photoresist film MLAs, and the open-circuit voltage V_{oc} has minor changes. The fill factor of the silicon solar cells with the photoresist film MLAs has great improvement, especially the silicon solar cell with square MLAs, in which the value was increased from 65.93% to 70.25%. The PCE value for the silicon solar cells with circular, hexagonal, and square photoresist film MLAs can be calculated respectively as 12.31%, 12.73%, and 13.19%. The maximum PCE improvement of the silicon solar cell is improved from 11.53% for the sample without the microstructure to 13.19% for the sample with the square MLAs, and the PCE improvement is about 14.40%. This is probably because the square MLAs have the highest fill factor. The above results display that the photoresist film MLAs can improve the capability of silicon solar cells, especially the square MLAs.

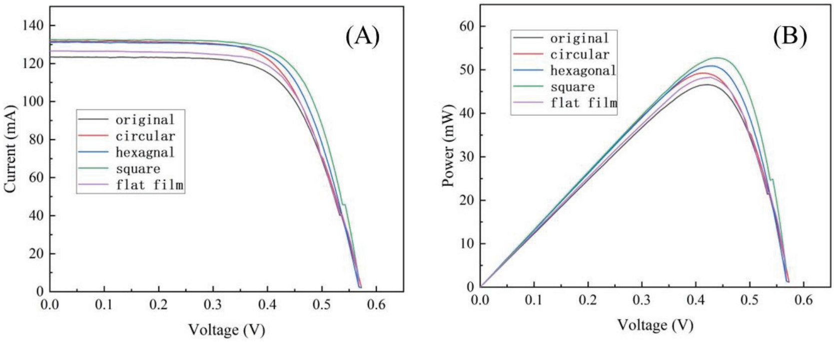

Figure 8. (**A**) The I-V curves and (**B**) the P-V curves of silicon solar cells with flat film, circular, hexagonal, and square MLAs films compared with the silicon solar cells without photoresist film MLAs.

Table 2. Specific parameters of silicon solar cells with different shapes of MLAs.

Solar Cell with or without MLA	V_{OC} (mV)	J_{SC} (mA cm^2)	Fill Actor (%)	Efficiency (%)
Reference	570.0	30.85	65.93	11.53
Circular	574.5	32.93	65.08	12.31
Hexagonal	569.4	32.81	68.12	12.73
Square	566.6	33.13	70.25	13.19
Flat film	559.2	31.64	68.39	12.10

Figure 9 shows the change in the photoelectric conversion efficiency of solar cells under different incident angles of sunlight. As the angle of incidence increases, the PCE of these silicon solar cells gradually decreases, while these solar cells with photoresist film MLAs exhibit superior solar power generation over a wide incident angle range of 0–60°. Moreover, the solar cell with a flat photoresist film also has a slight improvement to that of the original solar cell. This is because the photoresist film MLAs reduce the reflection and increase the incident light. The results show that the photoresist film MLAs can also improve the photoelectric conversion efficiency of solar cells under different incident angles of the sunlight and have strong adaptability.

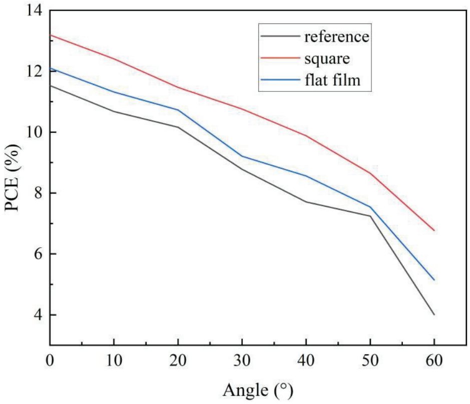

Figure 9. Dependence of the solar cell PCEs on an incident angle with and without the photoresist film MLAs.

4. Conclusions

Three types of photoresist film MLAs were successfully fabricated on silicon solar cells by UV nanoimprint technology. These prepared photoresist films have a smooth surface and a suitable optical transmittance of above 95% in the visible light range. The photoresist film MLAs also have a clear surface and suitable imaging properties. Moreover, the photovoltaic performance of these solar cells with photoresist film MLAs was investigated, including the current voltage, fill actor, current density, and photoelectric conversion efficiency. The results show that the photoresist film MLAs can improve the short-circuit current density, fill actor, resulting in considerable enhancement of PCE, and the silicon solar cells with square MLAs have the maximum PCE improvement of about 14.40%. These findings demonstrate the promising application of photoresist film MLAs in solar cell devices.

Author Contributions: Writing—review and editing, X.Z. (Xuehua Zhang); writing—original draft preparation, L.L.; data curation, X.Z. (Xinwen Zhang); project administration, X.Z. (Xuehua Zhang) and F.H. All authors have read and agreed to the published version of the manuscript.

Funding: National Natural Science Foundation of China (NSFC) (Grant Nos.: 61605086, 51602160, 61574080, 61274121).

Institutional Review Board Statement: Not applicable.

Informed Consent Statement: Not applicable.

Data Availability Statement: Not applicable.

Conflicts of Interest: The authors declare no conflict of interest.

References

1. Hossain, M.K.; Gazi, A.R.; Md, A.A.; Mirza, H.K.R.; Mohammad, H.A.; Khan, M.I.; Shahadat, H.; Sapan, K.S.; Jalal, M.I.E.; El-Denglawey, A. Current Applications and Future Potential of Rare Earth Oxides in Sustainable Nuclear, Radiation, and Energy Devices: A Review. *ACS Appl. Electron. Mater.* **2022**, *4*, 3327–3353. [CrossRef]
2. Zhong, S.; Shen, W. Quasi-omnidirectional crystalline silicon solar cells. *J. Phys. D Appl. Phys.* **2020**, *53*, 483001. [CrossRef]
3. Obaid, S.; Lu, L. Highly Efficient microscale gallium arsenide solar cell arrays as optogenetic power options. *IEEE Photonics J.* **2019**, *11*, 8400108. [CrossRef]
4. Yu, Y.; Zhang, F.; Yu, H. Self-healing perovskite solar cells. *Sol. Energy* **2020**, *209*, 408–414. [CrossRef]
5. Wali, Q.; Iftikhar, F.J.; Khan, M.E.; Ullah, A.; Lqbal, Y.; Jose, R. Advances in stability of perovskite solar cells. *Org. Electron.* **2020**, *78*, 105590. [CrossRef]
6. Bencherif, H.; Mwddour, F.; Elshorbagy, M.H.; Hossain, M.K.; Cuadrado, A.; Abdi, M.A.; Bendib, T.; Kouda, S.; Alda, J. Performance enhancement of $(FAPbI_3)_{1-x}(MAPbBr_3)_x$ perovskite solar cell with an optimized design. *Micro. Nanostruct.* **2022**, *171*, 207403. [CrossRef]
7. Javed, A.H.; Shahzad, N.; Khan, M.A.; Ayub, M.; Lqbal, N.; Hassan, M.; Hussain, N.; Rameel, M.I.; Shahzad, M.I. Effect of ZnO nanostructures on the performance of dye sensitized solar cells. *Sol. Energy* **2021**, *230*, 492–500. [CrossRef]
8. Son, H.J.; Hong, K.K.; Ju, B.K.; Kim, S.H. Oxidation-resistant Cu-Based metallisation for Si solar cells. *Energy Sci. Eng.* **2022**, *10*, 1264–1271. [CrossRef]
9. Lu, L.; Adel, N.; Wang, K.; Du, M.Y.; Liu, S.Z. Perovskite Quantum Dots in solar Cells. *Adv. Sci.* **2022**, *9*, 2104577. [CrossRef]
10. Hsu, C.H.; Zhang, X.Y.; Zhao, M.J.; Lin, H.J.; Zhu, W.Z.; Lien, S.Y. Silicon Heterojunction Solar Cells with p-Type Silicon Carbon Window Layer. *Crystals* **2019**, *9*, 402. [CrossRef]
11. Liu, J.J.; Yao, Y.; Xiao, S.Q.; Gu, X.F. Review of status developments of high-Efficiency crystalline silicon solar cells. *J. Phys. D Appl. Phys.* **2018**, *51*, 123001. [CrossRef]
12. Yang, D.; Zhang, T.R.; Wang, C.B.; Yu, T.T.; Wang, J.; Xu, Z.P. Enhanced electro-Optical properties of TiO_2 Nanocone Arrays for ultrathin GaAs Solar cells. *Opt. Commun.* **2019**, *452*, 281–285. [CrossRef]
13. Chen, W.H.; Cabarrocas, P.R.I. Rational design of nanowire solar cells: From single nanowire to nanowire arrays. *Nanotechnology* **2019**, *30*, 194002. [CrossRef]
14. Adibzadeh, F.; Olyaee, S. Nanostructure back reflector for enhancing the performance of InP nanowire array solar cells. *Opt. Quant. Electron.* **2022**, *54*, 303. [CrossRef]
15. Wei, P.K.; Hao, Z.W.; Yang, Y.; Liu, L. Hollow $NiSe_2$ nanospheres grown on graphene with unconventional dual-Vacancies in dye-Sensitized solar cells. *Appl. Surf. Sci.* **2021**, *553*, 149567. [CrossRef]
16. Tang, H.B.; Liu, Y.P.; Chen, Q.S.; Wang, Y.; Chen, W.; Wu, J.T.; Zhao, Y.; Du, X.L. Optical Design of Inverted Pyramid Textured PERC Solar Cells. *ACS Appl. Electron. Mater.* **2019**, *1*, 2684–2691. [CrossRef]
17. Sun, P.; Qu, G.P.; Hu, Q.K.; Ma, Y.C.; Liu, H.S.; Xu, Z.X.; Huang, Z.F. Highly Efficient Large-Area Flexible Perovskite Solar Cells Containing Tin Oxide Vertical Nanopillars without Oxygen Vacancies. *ACS Appl. Energ. Mater.* **2022**, *5*, 3568–3577. [CrossRef]
18. Gao, Z.L.; Lin, G.L.; Chen, Y.C. Moth-eye nanostructure PDMS films for reducing reflection and retaining flexibility in ultra-thin c-Si solar cells. *Sol. Energy* **2020**, *205*, 275–281. [CrossRef]
19. Huang, Z.S.; Wang, B. Thin-Film Solar Cells by Silicon-Based Nano-Pyramid Arrays. *Adv. Theor. Simul.* **2022**, *5*, 2100586. [CrossRef]
20. Osama, M.A.; Amal, A.; Muhamad, Z.M.; Ben, F.S.; Qian, C.; Andrew, G.T.; Nigel, W.H.; Wang, X.L.; Patrick, H.; Janet, J.; et al. High efficiency semitransparent perovskite solar cells containing 2D nanopore arrays deposited in a single step. *J. Mater. Chem. A* **2022**, *10*, 10227–10241.
21. Shi, J.; Huang, Y.S.; Peng, L.N.; Ni, Z.J.; Zhang, D.W. Grating/microlens arrays fabricated by hot-melting, self-Assembly and replication. *Opt. Mater.* **2020**, *104*, 109733. [CrossRef]
22. Baek, S.; Kim, K.; Sung, Y.; Jung, P.; Ju, S.; Kim, W.; Kim, S.J.; Hong, S.H.; Lee, H. Solution-processable multi-color printing using UV nanoimprint lithography. *Nanotechnology* **2020**, *31*, 125301. [CrossRef] [PubMed]

coatings

Review

Development of Hetero-Junction Silicon Solar Cells with Intrinsic Thin Layer: A Review

Nikolay Chuchvaga *, Kairat Zholdybayev, Kazybek Aimaganbetov, Sultan Zhantuarov and Abay Serikkanov

Institute of Physics and Technology, Satbayev University, Almaty A25A1G8, Kazakhstan
* Correspondence: chuchvaga@sci.kz or nikolay.chuchvaga@gmail.com

Abstract: This paper presents the history of the development of heterojunction silicon solar cells from the first studies of the amorphous silicon/crystalline silicon junction to the creation of HJT solar cells with novel structure and contact grid designs. In addition to explanation of the current advances in the field of research of this type of solar cells, the purpose of this paper is to show possible ways to improve the structure of the amorphous silicon/crystalline silicon-based solar cells for further improvement of the optical and electrical parameters of the devices by using of numerical simulation method and current hypotheses. This paper briefly describes the history, beginning from the first studies of and research of HJT-structure solar cells. It raises questions about the advantages and existing problems of optimization of HJT solar cells. The authors of this paper are proposing further ways of design development of HJT solar cells.

Keywords: HIT; HJT; solar cell; quantum wall; modeling; review

Citation: Chuchvaga, N.; Zholdybayev, K.; Aimaganbetov, K.; Zhantuarov, S.; Serikkanov, A. Development of Hetero-Junction Silicon Solar Cells with Intrinsic Thin Layer: A Review. *Coatings* **2023**, *13*, 796. https://doi.org/10.3390/coatings13040796

Academic Editor: Alessandro Latini

Received: 27 February 2023
Revised: 30 March 2023
Accepted: 17 April 2023
Published: 19 April 2023

1. Introduction

The current challenges associated with the general growth of the world's population, political, economic and environmental circumstances put before humanity the search for new solutions in the field of production, processing and consumption of world resources. One of the key solutions to this problem is the development of green energy. The concept of "green energy" means energy resources that do not harm the environment and are, therefore, meant as environmentally friendly resources. The development of this industry is associated with the development of more highly efficient technologies for energy production and energy consumption of resources, the search for new materials, the training of specialists and the creation of infrastructure and jobs, as well as the creation of favorable conditions for the development of the green energy market.

One of the brightest and rapidly developing representatives is solar energy. This type of energy is associated with the conversion of solar energy, both for heat generation and with the use of semiconductor systems, for direct conversion of solar radiation into electricity. The main advantages of these systems are their efficiency, noiselessness, environmental friendliness and the ability to work in cloudy conditions and even in the rain. For the development of solar energy and its implementation in everyday life, there are tasks to increase efficiency, scale up production, search for new materials and, most importantly, reduce the cost of electricity produced. One of the most interesting materials capable of solving the presented problems is silicon. This is primarily due to the fact that silicon is the second most abundant chemical element on Earth. Despite the fact that silicon technology is the most traditional representative of solar energy, there are further technological ways to optimize the use of this material. One of the most prominent representatives of silicon technologies are silicon solar cells based on HIT and PERC technology.

In recent years, HIT structure solar cells (heterojunction with thin intrinsic layer) or, as it is also called—HJT—have gained great popularity. Such a big interest in this design is related to high efficiency of devices, low-temperature production technology (up to

200 degrees Celsius), as well as low degradation of photovoltaic structure properties. In this article, we would like to show the world achievements in the development of HJT technology, as well as speculate what engineering and technical perspectives await it.

2. Review

2.1. History

The technology of heterojunction silicon solar cells, also known as HJT solar cells (heterojunction technology), combines the advantages of crystalline and amorphous silicon, demonstrating the ability to achieve high efficiency of solar energy conversion when using less silicon and lower manufacturing temperatures that do not exceeding 200–250 °C compared to traditional diffusion technologies [1]. The first HJT solar cells were developed in the 1990s by Sanyo Company with an efficiency of 12% [2]. Since then, HJT technology has evolved, reaching new heights in terms of efficiency every year [3–5]. This technology has become one of the most promising for use in large-scale ground-based photovoltaics in a relatively short period, demonstrating record-breaking efficiency values of over 26% for all silicon technologies [6].

According to the calculations made by William Shockley and Hans-Joachim Quiesser, the theoretical efficiency limit for a semiconductor structure with one p–n junction is 33.7% [7]. Then, according to estimations presented on the work [8], it was shown that for silicon based solar cells, the maximum efficiency limit is 29.4%. The above-presented research works have set a goal for many engineers and scientists to strive for in silicon photovoltaics. Today, one of the fastest growing photovoltaic cell technologies is HJT technology.

Today the most popular on the market are solar cells based on crystalline silicon, in which a p–n junction is created by diffusion. This type of solar cell has advantages such as relatively high efficiency; it is also technologically well established. At the same time, this technology has big disadvantage of high temperatures up to 1000 °C; as a consequence, there is a high manufacturing cost. Crystalline silicon wafers of such solar cells must meet the requirements for high purity of the material. Together, all these parameters ensure high efficiency of solar cells. Amorphous silicon is a material that is perfectly suited as a cheaper alternative to crystalline silicon. Nevertheless, the efficiency of laboratory solar cells based on amorphous silicon does not exceed 14% [9].

In the first design version of these solar cells, the heterojunction was formed by using the flat n-type crystalline silicon wafer with a thin layer of p-type amorphous hydrogenated silicon (a-Si:H) deposited on its surface [2].

The efficiency of this structure reached 12.3%. This maximum value of efficiency was obtained for the thickness of the amorphous layer of the order of 100 Å (10 nm). It was also found that the introduction of intrinsic conductivity a-Si:H thin film between the n- and p-type silicon layers can reduce the density of surface defects at the interface between crystalline and amorphous silicon, which is reflected in simultaneously increasing the open circuit voltage, short-circuit current and solar cell fill factor. In this case, the efficiency of such a structure increased up to 14.8%, while the optimal thickness of the intrinsic amorphous silicon layer turned out to be 60–70 Å. Another innovation made by Sanyo was the creation of textured surface of the crystalline silicon wafer for more efficient absorption of light, as well as for the ability to absorb incident light on the wafer at low angles. Texturing conditions were not specified, but it was mentioned that silicon crystalline wafer was treated to hydrogen plasma before deposition of a-Si:H. In addition, a-Si:H layer of n-type conductivity was deposited on the back side of the silicon wafer to create an electric field on the back side of the solar cell. As a result, the efficiency of the solar cell reached a value of 18.1% for a 1 cm^2 sample.

Further improvement of the HJT technology was aimed at improving passivation of crystalline silicon surface by optimizing the amorphous silicon deposition conditions [10]. In 2009, Tsunomura and colleagues reported the creation of a high-efficiency HJT solar cell with dimension of 100.5 cm^2 [11]. The main factors used for the improvement were optimization of the characteristics of the amorphous silicon–crystalline silicon heterojunction, reducing the thickness of the fingers and contact grid bars and reducing optical losses. In the fall of 2009, Sanyo presented a HJT-structure solar cell with silicon wafer thickness of 98 μm and an area of 100.3 cm^2 [12]. In early 2014, Panasonic achieved record efficiency of HJT cells by using a high-quality monocrystalline silicon wafer [13].

The essence of heterojunction solar cells is the formation of p–n junctions from materials with different values of the band gap. One of the main features of heterojunction silicon solar cells is passivation with a wide-gap semiconductor layer between the ohmic contacts and the active elements of the structure, which creates a high voltage when current flows through it; the voltage must be high enough to reduce the probability of recombination [14,15]. Silicon-based heterojunction semiconductor devices have a similar structure to metal-dielectric-semiconductor (MDS) devices based on the tunneling of charge carriers through a dielectric layer [16]. All this does not exclude the diffusion transport of charge carriers, which can play a major role in the current flow through the structure [17]. According to the information mentioned above, we can say that hydrogenated thin layers of amorphous silicon (a-Si:H) with thickness of a few nanometers are perfectly suitable as a buffer layer for semiconductor silicon multilayer solar cells. The bandgap width of amorphous silicon is larger than the bandgap of monocrystalline silicon, and it can easily be doped to achieve n- or p-type conductivity, which makes this material as suitable candidate for the role of buffer layer [18].

In 1974, V. Fuss conducted the first studies of a-Si/c-Si crystalline-silicon–amorphous-silicon heterojunction [19]. The first studies of passivation of crystalline silicon surface by amorphous silicon were shown in [20]. In 1983, the research group, in their work [21], presented a tandem-type solar cell with a-Si/c-Si structure. Sanyo (Japan) started introducing heterojunction solar cells with a-Si/c-Si structure of such structure in the 1980s. The manufactured devices consisted of n-type silicon wafers and emitters made of p-type conductivity amorphous silicon doped with boron. These solar cells had an efficiency of about 12%. Such small values of efficiency were due to the small value of fill factor caused by the high values of parasitic current [22]. However, one of the most significant steps made for creation of new high-efficiency HJT structure solar cells was the idea of the using of the intrinsic conductivity a-Si:H as a buffer layer between the doped emitter and the silicon wafer which led to reduction of the dangling bond densities and densities of defects at the interface. This structure is called a heterojunction with intrinsic thin layer (HIT). The efficiency of the first elements of the HIT structure was 14.8% ([2], p. 3521). In the work ([2], p. 3522), a created similar heterojunction structure solar cell was presented. The solar cell held, at that time, a record efficiency of 18%. The novelty of this work was the application of intrinsic amorphous layer on the back side of the solar cell.

The authors of this work have clearly demonstrated what design a modern heterojunction solar cell should have; namely, it should have buffer passivation layers on both sides of the silicon wafer, as well as an integrated thin layer of intrinsic conductivity between the doped emitter layer and the crystalline wafer.

2.2. Degradation and Passivation of Surfaces Defects

An integrated intrinsic conductivity a-Si thin layer plays the role of passivation of the surface states of the crystalline silicon. It is applied between the surface of the crystalline silicon and the doped a-Si layer. The doped amorphous layers passivate the surface of the crystalline substrate by themselves, but as shown in [23], intrinsic conductivity amorphous layers passivate the substrate surface much better. It is worth noting that this dependence is explained by changes in the value of the Fermi level [24]. Such a change leads to a decrease in defect formation energy. Consequently, an increase in doping concentration can lead to a higher defect density. Studies on the relationship between doping levels and defect formation are highlighted in [25,26]. One of the effects that negatively affects the efficiency of photocells is the Staebler–Wronski effect [27]. It is known that prolonged illumination of amorphous hydrogenated silicon (a-Si:H) leads to changes in the conductivity of the structure, including photoconductivity. Many studies have been conducted on the subject of the Staebler–Wronski effect [28–32]. Many of these works have shown that the change in photoconductivity of the structure under prolonged illumination is associated with a shift of the Fermi level. The shift is due to increasing defects associated with broken bonds of the amorphous material. However, a model of recombination in a-Si:H p-type was proposed in work [33], which corresponds well to the experimental data. According to the proposed model, for a-Si:H p-type films having the same parameters of valence band tail states, the photoconductivity should not depend on the doping level and total concentration of defects of the broken bond type. The proposed recombination model fully explains the effect of long-term illumination on the temperature dependences of photoconductivity of the a-Si:H p-type.

Therefore, one of the important areas of research in the field of heterostructured solar cells is the study of photoinduced degradation processes. In paper [34], the object of the study was solar cells with a structure of α-Si:H/μc-Si:H, fabricated by the modified technology of OerlikonSolarLtd (Switzerland). Studies of photoinduced degradation at temperatures of 298, 328 and 353 K were conducted. The experimental data obtained were used to estimate the magnitude of the change in the concentration of free (broken) bonds after saturation photoinduced degradation from temperature. The presented model assumes that a large fraction of hydrogen is in the semiconductor in the form of metastable Si–H–H–Si complexes. The formation of free bonds occurs due to the rupture of the weak Si–Si bond in close proximity to the metastable Si–H–H–Si complex. After the rupture of the weak Si–Si bond, the metastable complex breaks and a pair of free bonds and a pair of hydrogenated Si–H bonds are formed. At high temperatures (>345 K), the defects are annealed.

Against the background of the studied materials on the Staebler–Wronski effect, a very interesting work appears in which the abnormal Staebler–Wronski effect is seen in the amorphous silicon [35]. A description of the effect, its justification and the mechanism of this effect were given. The essence of the observed effect is an increase in the photoconductivity of a-Si:H thin films after taking a light bath. The authors showed that such behavior of the material should be well described by the Debye model and Williams–Watts model. Applying this anomalous effect in SHJ solar cells, the authors achieved a power conversion efficiency (PCE) of 25.18% (26.05% on a given area) with an FF of 85.42% on 244.63 cm^2 plates. This PCE is one of the highest values for silicon solar cells with a top/back contact on the total area. The FF value reaches 98.30% of its Shockley–Quisser limit.

2.3. Features of HIT Solar Cells Production

The use of amorphous silicon makes it possible to carry out technological processes for the production of solar cells at low temperatures not exceeding 200 °C, which allows the use of a smaller number of solar cells manufacturing stages and reduces its cost. The process of deposition of amorphous silicon on a crystalline wafer occurs by the method of plasma-chemical vapor deposition (PECVD-plasma enhanced chemical vapor deposition). For creation of the p–n junction, the material is doped by adding another gas agent (C_3H_9B for p-type conductivity and PH_3 for n-type conductivity). The intrinsic layer of amorphous silicon is deposited from silane (SiH_4) with a large proportion of hydrogen (H_2) for hydronization [36]. From the opposite side of the emitter, a thin layer of intrinsic conductivity is similarly deposited and a layer of amorphous silicon of the same type of conductivity as the substrate is deposited. This combination forms the so-called BSF-layer (-back surface field). The BSF is formed in order to prevent minor charge carriers from reaching the external circuit and thereby creating parasitic reverse currents. At the next stage, a layer of TCO (transparent conductive oxide) with a low resistance of less than 100 Ohm/square is formed on top of the finished “sandwich” by magnetron sputtering. Mostly, the material used as TCO in HJT solar cells is indium tin oxide (ITO). After the deposition of ITO layers, metal contacts are applied by screen printing method: (a) on the both sides of the double-sided solar cells; (b) on the front side for single-sided solar cells. For a single-sided solar cell, the back side metal contact is deposited by magnetron sputtering immediately after applying the TCO layer. Further, the resulting cell is connected with other similar solar cells into a module and laminated.

From the above-mentioned information, we can conclude that thin films of amorphous hydrogenated silicon are well suited for passivation of the surface states of a crystalline silicon substrate [20]. The a-Si:H film is deposited by the PECVD method from silane (SiH_4) diluted in hydrogen. The plasma discharge frequency is typically 13.56 MHz [37]. However, it should be noted that different equipment may have different optimal deposition parameters [38].

Passivation of the crystalline wafer surface by the deposition of amorphous silicon occurs by closing of dangling bonds with hydrogen, which leads to a decrease in the density of surface states ([37], p. 4440). Presumably, the defect that is responsible for surface recombination is a dangling bond on the silicon surface. These defects can be neutral, negative or positive. Such a surface recombination model was experimentally confirmed for a-Si:H/c-Si structures [39]. The described passivation of the wafers should rid the surface of defects of this kind, which lead to active surface recombination.

The doped layers in the HJT structure play the role of an n/p-type emitter or p+/n+-type BSF layer. These films are deposited by the PECVD method in the same equipment as the layers of intrinsic amorphous silicon. Usually, different chambers are used for each type of film, but all layers can be deposited in one chamber if the chamber is cleaned and conditioned before deposition. The agent gases used for creation the conduction layer are trimethyl boron (TMB) or biborane (B_2H_6) for p-type films; and phosphine (PH_3) for n-type films. All process gases in the working chambers are highly diluted in hydrogen.

An increase in the lifetime of charge carriers is achieved by passivation of surface states by deposition of thin amorphous layers which allows charges to pass without recombination through all layers of the structure to external metal contacts. High lifetime values (on the order of several thousand microseconds) and the ability to deposit contacts directly over the conducting oxide, avoiding contact between the metal and the emitter, eliminate recombination losses at the interface between the metal and doped amorphous silicon and make it possible to achieve high open-circuit voltage (Uoc). However, since the lifetime of charge carriers in amorphous films is many times shorter than in crystalline silicon, this has a negative effect on the conductivity of the structure. Since visible light is absorbed in the crystalline wafer, the negative effect is felt only from the front side of the solar cell which is expressed by the drop in short-circuit current (Isc) [40].

HJT structure have a sandwich design consisting of five main layers: p-type amorphous silicon layer, a built-in intrinsic amorphous silicon layer, n-type single-crystal silicon layer, a rear amorphous intrinsic layer, and a heavily doped amorphous silicon layer of n-type conductivity (Figure 1). A p-type conductivity layer forms a p–n heterojunction with a layer of crystalline silicon. A heavily doped n-type layer of amorphous silicon creates a back blocking field, which creates an energy barrier for minor charge carriers. Embedded thin amorphous layers of intrinsic conductivity provide passivation of the surface states of the crystalline silicon substrate [41–44].

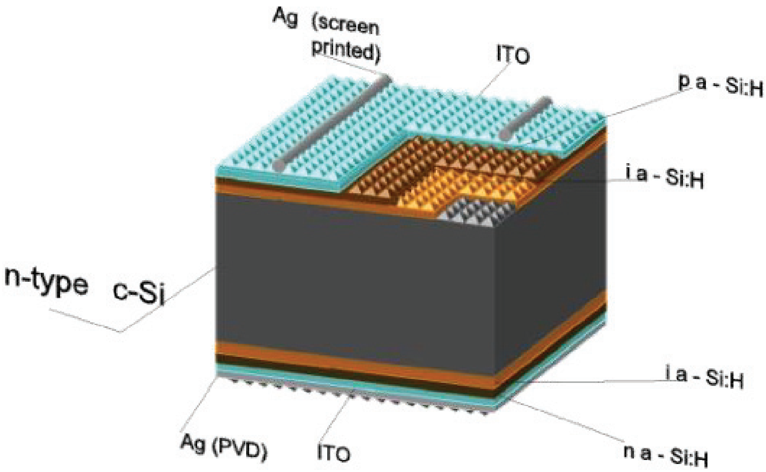

Figure 1. Schematic view of the HJT solar cell [45].

2.4. Design and Parameters of the HIT Structure

One of the first research works showed the importance of determining the most efficient parameters of HJT solar cells. The authors showed the influence of the thickness of the emitter and intrinsic built-in layer of the photocell structure [2]. The authors showed that the solar cell efficiency starts to increase after the deposition of intrinsic amorphous silicon layer. The dependence curve increases to a maximum and then starts to decline. This indicates the importance of the correct selection of the parameters of the solar cell.

In order to achieve a device efficiency that is as high as possible, it is necessary to determine what the main output characteristics of device depend on and find the optimal parameters that can be achieved during the growth of heterostructure. As shown by the authors of some works [46,47], one of the most important parameters is the quality of the crystalline silicon layer in the HJT structure. The density of surface defects D_{it}, as well as the density of bulk defects (in p-type crystalline silicon, such defects are caused by oxygen inclusions D_{od}) are important parameters; the values of these parameters depend on the method and quality of material growth and affect the output characteristics of solar cells. Considering the following structure of solar cell: TCO/a-Si:H(n)/a-Si:H(i)/c-Si(p)/Al-BSF/Al, the authors showed that for the minimum efficiency loss of the solar cell D_{it} should not exceed 10^{11} cm^{-2}, and D_{od} should not exceed 10^{9} cm^{-2}. Similar results were shown in the work in which the TCO/a-Si:H(n)/c-Si(p)/Al/structure was modeled. According to the authors, the optimal value of D_{it} should be no more than 10^{10} cm^{-2}.

One of the parameters controlled during the fabrication of solar cell is the thickness of one or another layer of the structure ([2], pp. 3519–3520). According to the researcher works, the thickness of the crystalline silicon layer in the HJT device should be 50–300 microns, depending on its structure. The optimal thicknesses of the amorphous emitter and intrinsic layer are 5–10 nm and 3–5 nm, respectively [47–50].

One of the most important factors affecting the performance of HJT cell is the material interface between the TCO layer and amorphous material, and between crystalline and amorphous silicon. The studies of these factors are described in some theoretical works devoted to the modeling of solar cells ([48], p. 168).

According to the research works, the optimal energy for breaking the bands in the c-Si/a-Si heterojunction is $\Delta EV = 0.37$ eV and $\Delta Ec = 0.25$ eV, since a larger potential barrier for the main charge carriers leads to a drop in the short circuit current and, consequently, to a drop in the efficiency of the solar cell. It is also shown that when the work function of the TCO layer is WTCO = 5.1–5.2 eV, an increase in the output characteristics is observed; at lower values, a decrease occurs. This is due to the charge distribution in the depletion region, which affects the quasi-Fermi levels in these regions, which leads to a change in the band diagram and a decrease in the efficiency of the solar cell.

An important controllable input parameter of a solar cell that affects its output characteristics is the concentration of charge carriers in each layer of the structure. According to the works ([50], p. 0111), the concentration of the main charge carriers of the p-type emitter layer in the HJT solar cell should be at least 2×10^{20} cm^{-3}. Unfortunately, there are not so many works on the study of the influence of the concentration of charge carriers of the layers on a solar cell operation.

3. Modeling and Optimization of Structure

Recently, quite a lot of work has been devoted to research using computer modeling tools. For example, in paper [45], taking into account the experimental data, as well as using the AFORS-HET program, the optimal design of the HIT photocell structure was calculated (Table 1).

Table 1. Optimized parameters of the HIT solar cells simulated using the AFORS-HET tool [45].

dp-a-Si	7 nm	*Na*, *p-a-Si*	1×10^{20} cm^{-3}
dn-c-Si	260 μm	*Nd*, *n-c-Si*	2×10^{17} cm^{-3}
dn-a-Si	20 nm	*Nd*, *n-a-Si*	1×10^{20} cm^{-3}
di-a-Si, front	5–7 nm	*di-a-Si*, rear	5 nm

The authors also showed that the physics of the heterojunction must be taken into account to advise the validity of the calculations. For this purpose, the authors of the paper used the Anderson heterojunction model [51].

Based on the laboratory optimization of the HIT cell structure, optimal parameters of a HIT-structured solar cell were elucidated for the given wafer quality, and an optimized solar cell was fabricated (Table 2) with the following output characteristics: J_{SC} = 37.51 mA·cm^{-2}; VOC = 713 mV; FF = 77.18%; PCE = 20.64%. The simulated values for comparison were as follows: JSC = 30.33 mA·cm^{-2}; VOC = 781.6 mV; FF = 85.44%; PCE = 20.26%.

Table 2. Final optimized parameters of HIT solar cells [45].

$d_{p\text{-a-Si}}$	10 nm	$N_{\text{a},p\text{-a-Si}}$	3.59×10^{20} cm^{-3}
$d_{n\text{-c-Si}}$	170 μm	$N_{\text{d},n\text{-c-Si}}$	2.15×10^{17} cm^{-3}
$d_{n\text{-a-Si}}$	20 nm	$N_{\text{d},n\text{-a-Si}}$	1×10^{20} cm^{-3}
$d_{i\text{-a-Si, front}}$	7 nm	$d_{i\text{-a-Si, rear}}$	9 nm

In paper [52], the authors presented an analytical study of the effect of light trapping and multilayer anti-reflective coating (ARC) on the electrical characteristics of n(a-Si:H)/i(aSi:H)/p(c-Si)/p+(C-Si) heterojunction solar cells with an internal thin layer (SHJ). Due to the improved light trapping capability provided by the optimized triangular texture morphology, a conversion efficiency of 20.06% was achieved. This result was compared with similar c-Si based structures with a planar structure and a single ARC layer (Figure 2).

Another example of using the AFORS-HET program is paper [53]. In this work, to simulate a solar cell with AZO/Si and TiO_2/Si heterojunction, the AFORS-HET automatic simulation program is used, in which the ultra-thin AZO layer and TiO_2 layer act as n-type layer, and the crystalline silicon wafer of p-type (p-cSi) acts as an absorbing p-type layer. In this paper [53], texturing is performed at different texture angles and the performance of a simulated AZO/Si heterojunction solar cell is optimized. The role of surface texturing at different angles was studied and maximum efficiencies of 17% and 17.5% were obtained for silicon HJ solar cells based on AZO and TiO_2 layers, respectively. A linear increase in the efficiency as a function of the texturing angle is observed, where the efficiency is 14.21% for the AZO layer and 14.45% for silicon HJ solar cells based on the TiO_2 layer when the surface is pyramidally textured. Optimizing the p-cSi thickness at 70 μm and removing the amorphous silicon inner layer can be very cost effective for producing AZO/Si heterojunction solar cells on an industrial scale for commercial production, as deposition of the a-Si i-layer and other similar HJ-based solar cells with an inner layer requires additional processing.

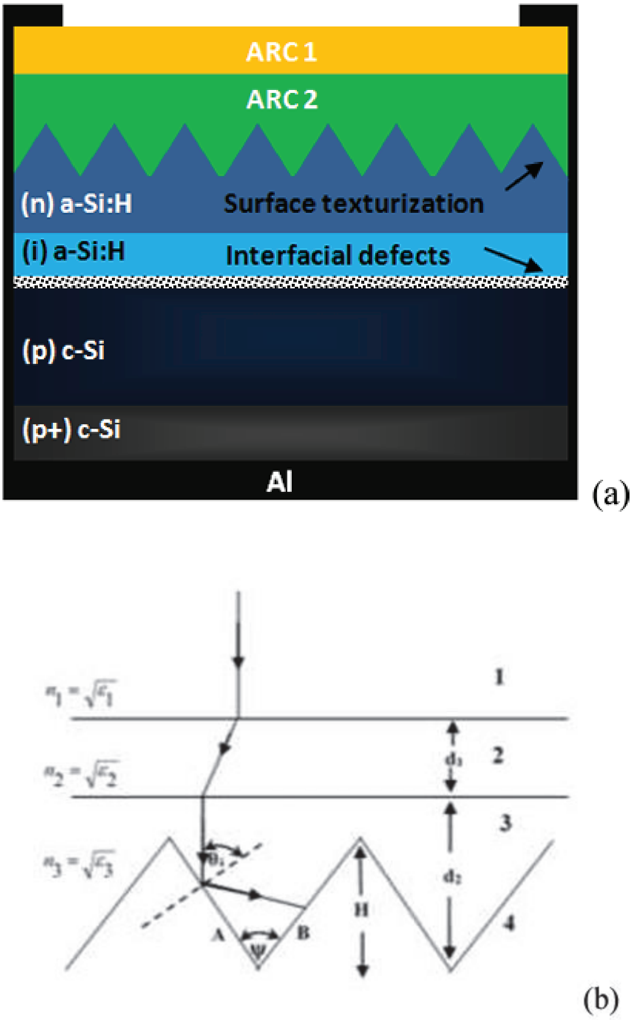

Figure 2. A schematic representation of the double ARC layer and texture morphology of the cell [52]. (**a**) Cross-sectional view of the proposed SHJ solar cell. (**b**) Schematic representation of the double ARC layer and triangular texture morphology.

To the disadvantage of this work and other works related to the use of software packages, I would attribute the exclusive subjectivity of the conclusions based on the analysis of the computer program model without further experimental research. However, even research at this level raises interesting topics and introduces new ideas, which is undoubtedly useful for world science.

To demonstrate the diversity and choice of modeling tools, we offer the review paper [54]. In this paper, the HIT solar cell is simulated by Amorphous Semiconductor Device Modeling Program (ASDMP). The influence of the physical and geometrical parameters of the emitter on the performance of the element, the phenomena of conduction and recombination have been studied. It is shown that when choosing the thickness of the emitter, a compromise must be found: It must not be too thin so it has a sufficient electric field at the p-a-Si:H/n-c-Si junction; and it must not be too thick such that the maximum photons are transferred to the active layer and so that the diffusion length of charge carriers was at least equal to the thickness of the emitter. With a p-Si:H layer thickness of 155 Å, the best values of the cell parameters were achieved, while the efficiency was 18.25%. The performance of the investigated HIT cell is improved by increasing the doping density of the emitter layer of hydrogenated amorphous p-type silicon (p-a-Si:H). Despite the deterioration of material characteristics as a result of doping, the recombination rate decreases on the active layer (n-c-Si) due to the higher electric field strength.

Another interesting paper that talks about a new method [55]. A new method is presented for extracting seven parameters of a two-diode solar cell model using the current-voltage (I–V) characteristics under illumination and in the dark. The algorithm consists of two subroutines that are executed in turn to adjust all cell parameters in an iterative process. The proposed parameter extraction algorithm uses the I–V characteristics in light and darkness so it can predict the MPP and, at the same time, give a better idea of the physical structure of the solar cell, since the accuracy of performance prediction in both conditions is improved. In particular, the proposed parameter extraction algorithm is divided into two subroutines: IIVf (I–V fitting in lighting) and DIVf (I–V fitting in dark), which are executed alternately until a good match is achieved in both conditions. The proposed method can be used to extract the parameters of any photovoltaic device, either commercial or fabricated in research laboratories, as long as their operation relies on the p–n junction.

The novelty of the method should be attributed to the advantages of work [55]. The possibility of using it in conjunction with electrical measuring techniques. The authors of the work also showed the efficiency of the method experimentally.

4. Discussion and Possible Solutions

Finally, we come to the question: "What else can be done to improve the efficiency of the HJT-solar cells?". We are interested in engineering solutions in the design of the structure, and not in improving the quality of semiconductor and metallic materials.

Samples produced in laboratories achieved efficiency up to 26.7% [56]. These record results are the result of optimization and development of the HJT-structure. There are three directions which can be performed for the optimization of the HJT-structure: improving material quality and production methods, optimizing the internal parameters of the device (thickness, concentration of layers) and changing the design.

4.1. Contact Design

For example, several types of metal contact grid designs are developed: "Busbar", "SmartWire" and "IBC". Solar cells with BUSBAR contact design are metallized with thin rectangular strips printed mostly only on the front and rarely, additionally, on the back of the cell. These metal contacts are called "busbars" and have an important purpose: they carry the direct current generated by the solar cell. Perpendicular to the "busbars" are thinner metal "fingers" that collect the generated current and deliver it to the "busbars". The cost of metallization for the production of heterojunction solar cells has been significantly reduced by applying the "SmartWire" contact grid design [57]. This design replaces the busbars with a lot of thin wires. The soldering of such contacts with the "fingers" contacts occurs directly during the lamination of the solar cell.

The third contact design is "IBC", the structure of which is shown in Figure 3. The use of such a design of contacts allows increasing the exposure to sunlight solar cell surface area, which has a positive effect on the short circuit current of the solar cell.

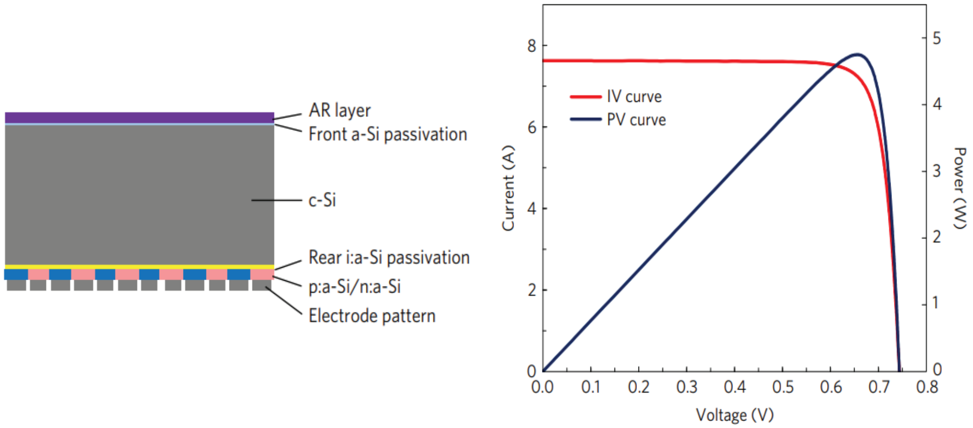

(**a**) (**b**)

Figure 3. Data presented from research work [6]: (**a**) HJT solar cell structure with integrated rear contacts; (**b**) IV-curve of the presented structure.

The highest efficiency values for HJT solar cells are shown by the IBC contact design [6,58]. This assertion can be verified by tracing some works devoted to Sokar Cells Tables [3–5,9,56]. In this architecture, by integrating both P+ and N+ HJT contacts on the back side, good optical and passivation properties can be obtained on the front side of the cell that receives light. As shown in Figure 3a, the amorphous Si p-type layer (p:a-Si) and the amorphous Si n-type layer (n:a-Si) are cut to collect holes and electrons, respectively. The face is coated with an a-Si passivation layer and a dielectric anti-reflection (AR) layer. The incident light generates carriers that are collected by the patterned a-Si layers and electrodes [6].

4.2. Internal Layer Modification and Defect Engineering

The results achieved during the studies have demonstrated the effectiveness of intrinsic amorphous silicon in the surface passivation of crystalline silicon wafers. The built-in layer of amorphous silicon is used in the HJT solar cell and aimed to passivate heterojunction defects. However, the presence of this layer also leads to undesirable consequences for the solar cells; namely, due to the qualities of the amorphous material itself, a drop in the diffusion length of charge carriers in the area is observed and, as a result, reduces the efficiency of the solar cell. One of the possibilities to further improve the efficiency of a heterojunction silicon solar cell is to increase the diffusion path of charge carriers in the heterojunction region [59,60]. The research work [61] presents a model of a solar cell with a very thick i-a-Si-layer, which, according to the authors, increases the generation of electron–hole pairs and prevents overheating of the electronic device. In the work [45,62], the experimental dependences of the output electrical characteristics of the HJT solar cell on the parameters of the internal layers is shown. Based on the research works, as well as to the work [63], it can be concluded that in HJT structure solar cells, an increase in the thickness of the built-in amorphous layer, the efficiency of the solar cell increases, but up to a certain maximum point. The increase in output characteristics is due to an increase in the lifetime of minority charge carriers in the crystalline silicon wafer. This behavior of the system can be explained by better passivation of the surface states on the silicon substrate.

The search and creation of an alternative semiconductor material will make it possible not only to use it in solar energy, but also in other areas of electronics where there is a need for such semiconductor films with high charge mobility and a relatively cheap production method.

The end result of the work is a film or heterojunction, an alternative to the "single-crystal silicon-hydrogenated amorphous silicon" junction. Currently, in a standard HJT solar cell, a photoelectric effect occurs in the p–i–n junction. In this technology, the i-layer performs the role of passivation of surface states on the surface of the crystalline substrate and serves as a buffer layer between p and n. However, with an increase in the geometric dimensions of the field that is created by the p-i-n junction, it is possible to increase the region of useful absorption of photons by the material. Since amorphous silicon is a rather defective material, with an increase in the thickness of its own layer, the efficiency of the solar cell decreases. The main hypothesis is that the pores on the crystalline wafer filled with a thick layer of amorphous silicon will play the role of areas that passivate the dangling bonds of the crystalline surface on themselves, and the places on the surface of crystalline silicon covered with a thin layer of amorphous film will be responsible for the current conductivity in structure. Thus, it will be possible to achieve good conductivity with better passivation of the structure. In addition, possible quantum-size effects, depending on the obtained structures, can affect the final conductivity of the structure. Testing this hypothesis and developing methods for creating such a structure are the priority tasks of our research team at the moment. Today, the work is not fully completed. Recipes for obtaining porous silicon of various topologies are being developed.

The next hypothesis that our research group is proposing is to test is the creation of domain structures with different effective masses of charge carriers or different conductivity. For example, we are proposing the use of composite material as semiconductor material. It is proposed to introduce metal nanocrystals into an amorphous material (which will serve as a matrix for a composite material), somehow "include" such nanocrystals in the structure of an amorphous semiconductor and obtain domains with changed charge carrier parameters in certain areas.

As an example of the successful application of such an approach, I would like to describe the work of scientists from Spain [64]. The authors made a HIT solar cell: in its design, a hyperdoped layer was applied to the surface of crystalline silicon-photovoltaic cell based on intermediate band (IB) semiconductors (IB solar cell, or IBSC) (Figure 4).

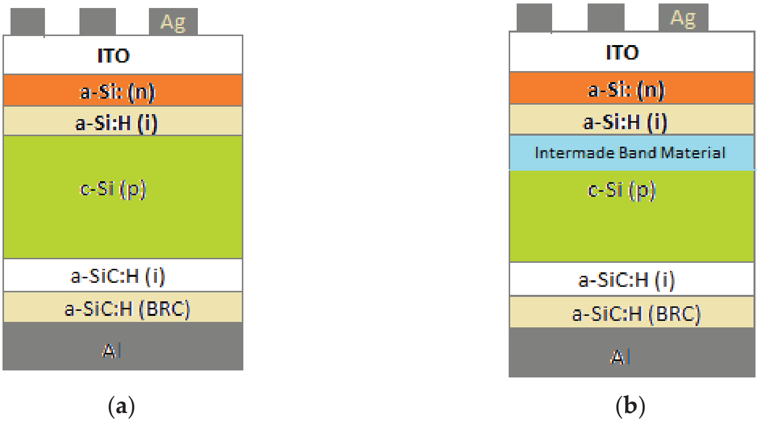

Figure 4. An example of structure of the reference HIT solar cell (**a**) and IBSC (**b**) used in [64].

In this study, the researchers created various IBSCs based on a hyperdoped silicon semiconductor with Ti and V. These cells have an efficiency of 2.6% and 1.9%, respectively, and exhibit a silicon subbandgap EQE. Analysis of J–V measurements showed three main conduction processes and series resistance. The main exponential mechanism observed in all temperature ranges in this study has an ideality coefficient of $1 < n1 < 2$ and an activation energy of Ea (Ti) = 0.55 eV and Ea (V) = 0.56 eV.

In this work [64], the authors failed to increase the efficiency of the HIT solar cell. However, at the same time, we believe that this direction—the direction of engineering and the study of the properties of heterojunctions—is worth moving towards.

4.3. Application of the Properties of Nanoscale Structures

Continuing the theme of changing the properties of the i-layer, let us consider the use of quantum wells in the solar cell structure.

In the work [65], a simulated situation is shown, in which hot electrons in a semiconductor lose their energy, falling on the "shelves" of quantum walls. The negative effect of Auger recombination of electrons on the conductivity of the structure is thereby reduced (Figure 5).

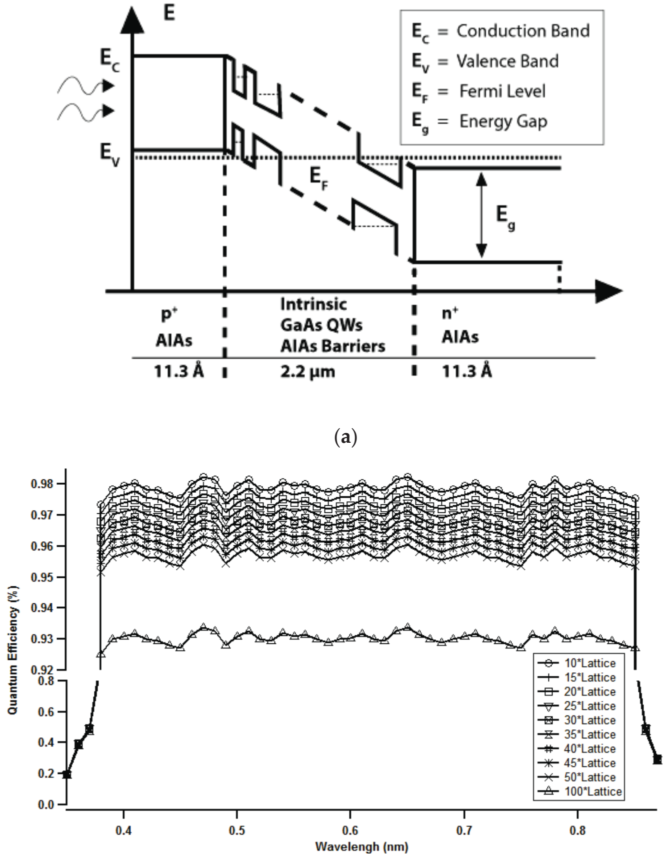

(**a**)

(**b**)

Figure 5. This is a figure data presented from [65] with the permission of AIP Publishing: (**a**) Energy diagram of a heterojunction solar cell with p–i–n QW; (**b**) QW efficiency versus wavelength for all 10 sets of QWs.

If we continue to consider quantum phenomena in a semiconductor, let us consider a superlattice of quantum wells. A superlattice is a solid-state structure in which, in addition to the periodic potential of the crystal lattice, there is an additional periodic potential: the period of which significantly exceeds the lattice constant.

For non-degenerate energy bands, we have:

$$-\frac{\left(\frac{h}{2\pi}\right)^2}{2m_{eff}}\nabla^2\psi(\boldsymbol{r})+\Delta(\boldsymbol{r})\psi(\boldsymbol{r})=\varepsilon\psi(\boldsymbol{r}) \tag{1}$$

where m_{eff} is the effective mass of an electron or hole.

It is shown that the energy spectrum of the superlattice has a band character, determined by the band number and the wave vector [66].

The qualitative properties of the energy structure of a superlattice (SL) are the same for different SLs. The spectrum $\varepsilon j(\boldsymbol{k})$ is a series of non-overlapping minibands. If the energy of the miniband is less than the maximum of the SL potential, then such minibands have a small width, determined by the tunneling transparency of the SL barriers; these minibands can be described in the tight coupling approximation:

$$\varepsilon \mathrm{j}(\boldsymbol{k}) = \varepsilon \mathrm{j} - \Delta j\ \cos \boldsymbol{k}d \tag{2}$$

where εj are the energy levels of a single well; $|\Delta j|$-width of j mini-zones, which are determined by the parameters of the SL.

Figure 6 shows the presence of maxima in the I–V characteristic, which can result in the possibility of a negative differential resistance of the structure. This property of the structure with quantum wells can be used to determine the optimal values of the internal field of the p–n junction of the solar cell.

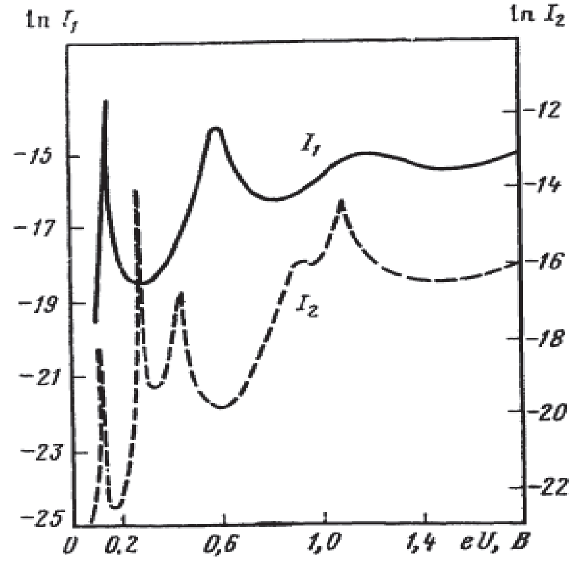

Figure 6. Dependence of the natural logarithm of the current passing along the SL on the voltage for structures with two and three barriers [66].

As it is well known, if the barriers between QWs are sufficiently transparent. That is, the tail of the wave function of an electron in one state of QWn intersects with the tail of the wave function of an electron in the state of QWn + 1. Then, the electron can tunnel to another state through the energy barrier. Moreover, if the energy levels of neighboring states have the same value, then the probability of tunneling increases since it does not imply a change in the electron energy. This suggests that if there is a superlattice inside the p–n junction, it is possible to increase the region of the i-layer of the p–i–n structure due to the tunneling current in the SL.

4.4. Modern Tendencies

In conclusion, we would like to give a graph of the development of solar cell technology from the well-known resource NREL. As you can see from Figure 7, heterojunction technology tends to grow steadily in efficiency, and it has quickly overtaken other technologies. Now, of the solar cell technologies that are designed for civilian applications, only the new perovskite [67] and organic [68] technologies are rapidly gaining the upper hand. However, these technologies have not yet perfected the production process; they have a number of shortcomings at this stage of development [69].

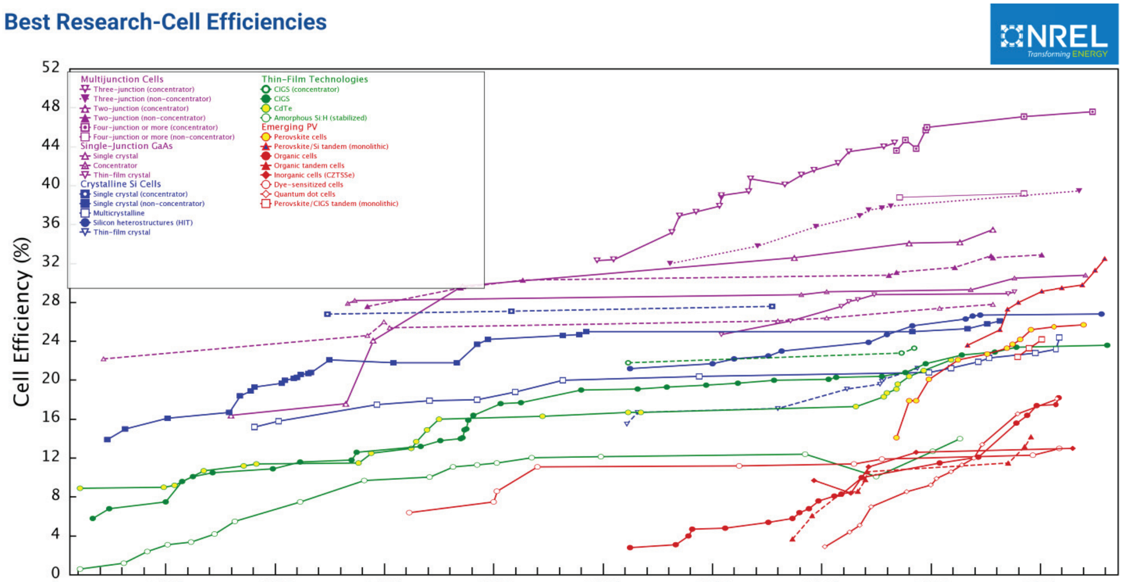

Figure 7. Best Research-Cell Efficiency Chart presented by NREL. The plot is courtesy of the National Renewable Energy Laboratory, Golden, CO [70].

Based on the above, it is not surprising that, at present, there are many works devoted to the tandem of solar cells based on the perovskite structure and other photocells [71,72].

Figure 8 shows variants of tandem solar cells based on silicon and perovskite. Module C is a variant of using the HIT photocell ([71], p. 1561). Figure 7 shows that the record of such a tandem photocell is 32.5% [73]. The connection options for tandem solar cells can be divided into several types. One popular connection type is where the top and bottom cells can independently contribute to the maximum power output, as the top and bottom cells are only connected optically without electrical connection, using the top solar cells as filters (Figure 9a). The other type is the two-terminal (2T) tandem solar cell (Figure 9b), which has the advantage of less parasitic absorption because it is a simple integrated type without an additional glass substrate and a thick transparent electrode for the top perovskite cell. However, it requires sophisticated technology such as process optimization and current matching technology [74]. More details about the possible options for tandems of perovskites and heterotransition silicon elements are found in review [75].

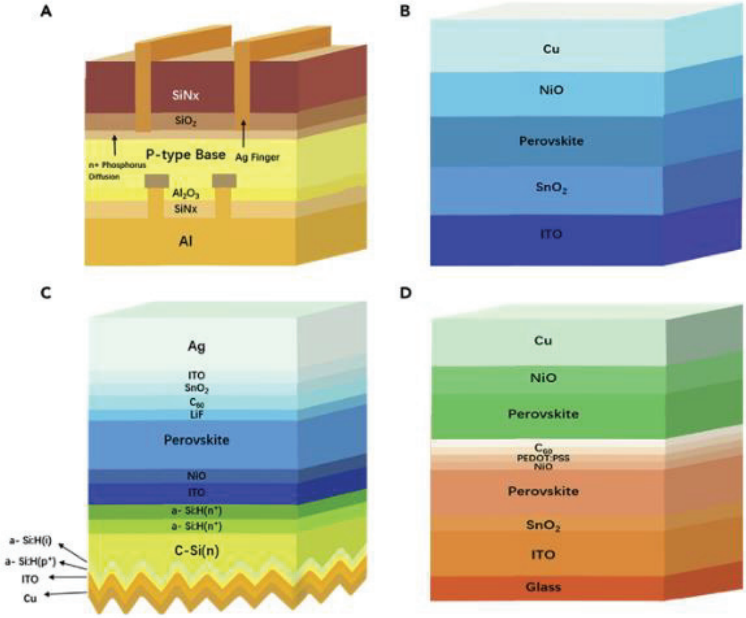

Figure 8. This is a figure data presented from ([71], p. 1561): Schematic diagram of solar cells. (**A**) is composed of traditional silicon cells, (**B**) is composed of planar perovskite cells, (**C**) is composed of silicon/perovskite tandem cells, (**D**) is composed of perovskite/perovskite tandem cells.

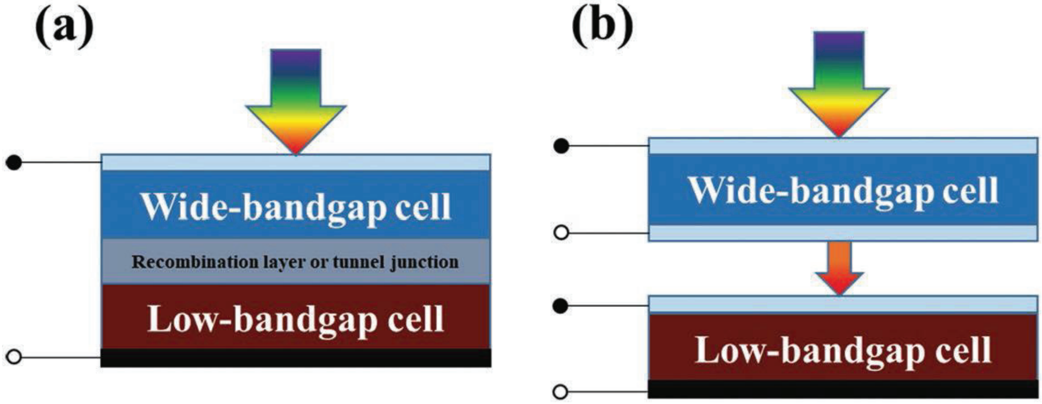

Figure 9. This is a figure data presented from [74]. Schematics of tandem architectures: (**a**) 4-terminal mechanically stacked (**b**) 2-terminal monolithically integrated [74].

4.5. Other Applications with Heterojunction Photocells

Recently, works related to the electrochemical etching of silicon in installations which use photocells have been appearing. In Ref. [76], the paper showed that a heterojunction photocell can be used as a photoanode and a photocathode. The current density in such a setup was 21.48 mA/cm^2. The conversion efficiency was 13.26%. Figure 10 shows a schematic of the cell.

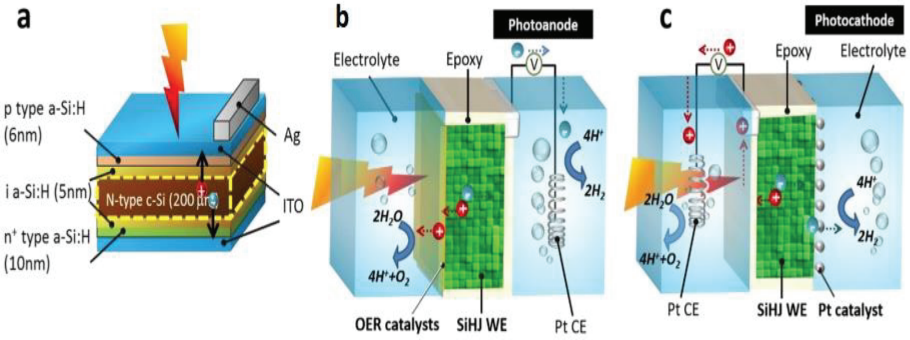

Figure 10. This is a figure data presented from [76]. (**a**) Schematic of the SiHJ solar cell and (**b**) schematic of the SiHJ photoanode; (**c**) schematic of the SiHJ photocathode.

Study [77] suggests a practical way to improve the photoresponse of Si-based planar photocathodes based on the creation of a Si junction. Here, a soft and feasible strategy for fabricating an amorphous Si/crystalline Si (a-Si/c-Si) junction photocathode with a Pt co-catalyst is proposed. The a-Si layer acts as an electron transfer agent to form a deep a-Si/c-Si junction with a large energy band shift, thereby allowing easy charge transfer. Meanwhile, the a-Si layer serves as a growth substrate to obtain controllable Pt nanoparticles. The Pt/a-Si/c-Si photocathode demonstrates an onset potential of 0.42 V. The photocurrent up to -35.0 mA cm^{-2} was obtained on Pt/a-Si/c-Si, which is much higher than without the a-Si layer.

Based on the above, we can conclude that improvements in the production technology of heteroprocessed solar cells and new engineering solutions in the design of photocells also lead to progress in other areas of solid-state engineering and technology.

5. Conclusions

In this paper, we briefly talked about the history of the invention and research of the HJT structure solar cells from the studies of the amorphous silicon/crystalline silicon junctions to the novel designs of the HJT solar cells. This work includes the history of development of solar cells, ranging from small-sized heterojunction amorphous/crystalline silicon solar cells research to finished industrial sized solar cells. It also describes the ways that were performed to possibly increase the main output characteristics and technological solutions that affect them. We also raised questions about the challenges of further optimizing HJT solar cell performance by means of numerical simulation programs and current hypotheses. According to the presented information, the authors of this research work propose further ways of the development of heterojunction solar cells. In accordance with the data presented, possibilities were found to increase the output characteristics by improving the design of the contact grid of solar cells and modifying the structure of heterojunction solar cells. According to this work, the most optimal design of the contact grid is the IBS design; due to this design, it is possible to increase the light-absorbing surface of the solar cell and, thereby, to increase the short circuit current of the device. Another possible approach includes the use of a superlattice of quantum wells in the area of the p–i–n-heterojunction as one way performance development. Another way is the use of an attractive new tandem structure based on use of perovskite materials.

Based on the foregoing information, the authors conclude that HJT technology remains promising in terms of the development and implementation of solar energy of this type in the global share of the energy market.

Author Contributions: N.C.—Head Leader of grant; concept, management, analysis and writing of papers. K.Z.—Main technologist, growth of thin films. K.A.—electrical characterization of simples. S.Z.—organic solar cells, wet chemistry. A.S.—resources, funding acquisition. All authors have read and agreed to the published version of the manuscript.

Funding: This research was funded by Science Committee of the Ministry of Science and Higher Education of the Republic of Kazakhstan, grant number AP09259279.

Institutional Review Board Statement: Not applicable.

Informed Consent Statement: Not applicable.

Data Availability Statement: Not applicable.

Acknowledgments: For help in publishing this article, we sincerely thank the entire staff of the Institute of Physics and Technology (Almaty, Kazakhstan). For foundation and inspiration in the field of HJT Solar Cells research we sincerely thank S.Zh. Tokmoldin, N.S. Tokmoldin, and E.I. Terukov.

Conflicts of Interest: The authors declare no conflict of interest. The funders had no role in the design of the study; in the collection, analyses, or interpretation of data; in the writing of the manuscript; or in the decision to publish the results.

References

1. Green, M.A.; Emery, K.; Hishikawa, Y.; Warta, W.; Dunlop, E.D. Solar cell efficiency tables (version 43). *Prog. Photovolt.* **2014**, *22*, 1–9. [CrossRef]
2. Tanaka, M.; Taguchi, M.; Matsuyama, T.; Sawada, T.; Tsuda, S.; Nakano, S.; Hanafusa, H.; Kuwano, Y. Development of new a-si c-si heterojunction solar-cells-acj-hit (artificially constructed junction-heterojunction with intrinsic thin-layer). *Jpn. J. Appl. Phys. Part 1-Regul. Pap. Short Notes Rev. Pap.* **1992**, *31*, 3518–3522. [CrossRef]
3. Green, M.A.; Emery, K.; Hishikawa, Y.; Warta, W. Solar cell efficiency tables (version 33). *Prog. Photovolt. Res. Appl.* **2009**, *17*, 85–94. [CrossRef]
4. Green, M.A.; Emery, K.; Hishikawa, Y.; Warta, W. Solar cell efficiency tables (version 37). *Prog. Photovolt. Res. Appl.* **2011**, *19*, 84–92. [CrossRef]
5. Green, M.A.; Emery, K.; Hishikawa, Y.; Warta, W.; Dunlop, E.D. Solar cell efficiency tables (Version 45). *Prog. Photovolt. Res. Appl.* **2015**, *23*, 1–9. [CrossRef]
6. Yoshikawa, K.; Kawasaki, H.; Yoshida, W.; Irie, T.; Konishi, K.; Nakano, K.; Uto, T.; Adachi, D.; Kanematsu, M.; Uzu, H.; et al. Silicon heterojunction solar cell with interdigitated back contacts for a photoconversion efficiency over 26%. *Nat. Energy* **2017**, *2*, 17032. [CrossRef]
7. William, S.; Hans, Q. Detailed Balance Limit of Efficiency of p-n Junction Solar Cells. *J. Appl. Phys.* **1961**, *32*, 510–519. [CrossRef]
8. Richter, A.; Hermle, M.; Glunz, S.W. Reassessment of the limiting efficiency for crystalline silicon solar cells. *IEEE J. Photovolt.* **2013**, *3*, 1184–1191. [CrossRef]
9. Green, M.A.; Emery, K.; Hishikawa, Y.; Warta, W.; Dunlop, E.D. Solar cell efficiency tables (version 41). *Prog. Photovolt.* **2013**, *21*, 1–11. [CrossRef]
10. Tanaka, M.; Okamoto, S.; Tsuge, S.; Kiyama, S. Development of hit solar cells with more than 21% conversion efficiency and commercialization of highest performance hit modules. In Proceedings of the 3rd World Conference on Photovoltaic Energy Conversion, Osaka, Japan, 11–18 May 2003; pp. 955–958.
11. Tsunomura, Y.; Yoshimine, Y.; Taguchi, M.; Baba, T.; Kinoshita, T.; Kanno, H.; Sakata, H.; Maruyama, E.; Tanaka, M. Twenty-two percent efficiency HIT solar cell. *Sol. Energy Mater. Sol. Cells* **2009**, *93*, 670–673. [CrossRef]
12. Sanyo Develops HIT Solar Cells with 23% Conversion Efficiency 2009. Available online: http://itnews.com.ua/news/50770-sanyo-sozdala-solnechnye-elementy-s-koeffitsientom-preobrazovaniya-228 (accessed on 17 April 2023).
13. Masuko, K.; Shigematsu, M.; Hashiguchi, T.; Fujishima, D.; Kai, M.; Yoshimura, N.; Yamaguchi, T.; Ichihashi, Y.; Mishima, T.; Matsubara, N.; et al. Achievement of more than 25% conversion efficiency with crystalline silicon heterojunction solar cell. *IEEE J. Photovolt.* **2014**, *4*, 1433–1435. [CrossRef]
14. Yablonovitch, E.; Gmitter, T.; Swanson, R.M.; Kwark, Y.H. A 720 mV open circuit voltage SiO x: C-Si: SiO x double heterostructure solar cell. *Appl. Phys. Lett.* **1985**, *47*, 1211–1213. [CrossRef]
15. Würfel, P. *Physics of Solar Cells: From Principles to New Concepts*; Physics of Solar Cells; John Wiley & Sons: Hoboken, NJ, USA, 2005; p. 186.
16. Green, M.A.; King, F.D.; Shewchun, J. Minority carrier MIS tunnel diodes and their application to electron-and photo-voltaic energy conversion—I. Theory. *Solid-State Electron.* **1974**, *17*, 551–561. [CrossRef]
17. Taguchi, M.; Maruyama, E.; Tanaka, M. Temperature dependence of amorphous/crystalline silicon heterojunction solar cells. *Jpn. J. Appl. Phys.* **2008**, *47*, 814. [CrossRef]
18. Spear, W.E.; Le Comber, P.G. Substitutional doping of amorphous silicon. *Solid State Commun.* **1993**, *88*, 1015–1018. [CrossRef]

19. Fuhs, W.; Niemann, K.; Stuke, J. Heterojunctions of amorphous silicon and silicon single crystals. *AIP Conf. Proc. AIP* **1974**, *20*, 345–350.
20. Pankove, J.I.; Tarng, M.L. Amorphous silicon as a passivant for crystalline silicon. *Appl. Phys. Lett.* **1979**, *34*, 156–157. [CrossRef]
21. Hamakawa, Y.; Fujimoto, K.; Okuda, K.; Kashima, Y.; Nonomura, S.; Okamoto, H. New types of high efficiency solar cells based on a-Si. *Appl. Phys. Lett.* **1983**, *43*, 644–646. [CrossRef]
22. Taguchi, M. Improvement of the conversion efficiency of polycrystalline silicon thin film solar cell. In Proceedings of the Fifth PVSEC, Florida, FL, USA; 1990; pp. 689–692.
23. Korte, L.; Schmidt, M. Investigation of gap states in phosphorous-doped ultra-thin a-Si: H by near-UV photoelectron spectroscopy. *J. Non-Cryst. Solids* **2008**, *354*, 2138–2143. [CrossRef]
24. Schulze, T.; Mingirulli, N.; Leendertz, C.; Beushausen, H.; Rech, B.; Korte, L. Impact of a-si: H structural properties on annealing behavior and voc of a-si: H/c-si heterojunction solar cells. In Proceedings of the 25th European Photovoltaic Solar Energy Conference and Exhibition/5th World Conference on Photovoltaic Energy Conversion, Valencia, Spain, 6–10 September 2010; pp. 6–10.
25. Schmidt, M.; Schoepke, A.; Korte, L.; Milch, O.; Fuhs, W. Density distribution of gap states in extremely thin a-Si: H layers on crystalline silicon wafers. *J. Non-Cryst. Solids* **2004**, *338*, 211–214. [CrossRef]
26. Pierz, K.; Fuhs, W.; Mell, H. On the mechanism of doping and defect formation in a-Si: H. *Philos. Mag. B* **1991**, *63*, 123–141. [CrossRef]
27. Staebler, D.L.; Wronski, C.R. Reversible Conductivity Changes in DischargeProduced Amorphous Si. *Appl. Phys. Lett.* **1977**, *31*, 292–294. [CrossRef]
28. Stutzmann, M.; Jackson, W.B.; Tsai, C.C. Light-induced metastable defects in hydrogenated amorphous silicon: A systematic study. *Phys. Rev. B* **1985**, *32*, 23–47. [CrossRef]
29. Irsigler, P.; Wagner, D.; Dunstan, D.J. On the preparation dependence of the Staebler-Wronski effect in a-Si: H. *J. Non-Cryst. Solids* **1985**, *69*, 207–211. [CrossRef]
30. Kazanski, A.G. The Staebler-Wronski Effect in Amorphous Hydrogenated Silicon Doped with Phosphorus. *Semicond. Phys. Technol.* **1990**, *24*, 1462–1466.
31. Crandall Richard, S. Defect relaxation in amorphous silicon: Stretched exponentials, the Meyer-Neldel rule, and the Staebler-Wronski effect. *Phys. Rev. B* **1991**, *43*, 4057. [CrossRef]
32. Fritzsche, H. Photo-induced structural changes associated with the Staebler-Wronski effect in hydrogenated amorphous silicon. *Solid State Commun.* **1995**, *94*, 953–955. [CrossRef]
33. Kuznetsov, C.V. The Staebler-Wronski effect and temperature dependences of photoconductivity of a-Si: H p-type. *Phys. Technol. Semicond.* **2000**, *34*, 748–752.
34. Emel'yanov, V.M.; Bobyl', A.V.; Terukov, E.I.; Chesta, O.I.; Shvarts, M.Z. Photoinduced degradation of α-Si: H/μ c-Si: H tandem photoconvertes at elevated temperatures. *Tech. Phys. Lett.* **2013**, *39*, 906–909. [CrossRef]
35. Liu, W.; Shi, J.; Zhang, L.; Han, A.; Huang, S.; Li, X.; Peng, J.; Yang, Y.; Gao, Y.; Yu, J.; et al. Abnormal Staebler-Wronski effect of amorphous silicon. *arXiv* **2021**, arXiv:2106.01657.
36. Chuchvaga, N.A.; Schulze, J.; Klimenov, V.V.; Zholdybayev, K.S.; Aimaganbetov, K.P.; Zhantuarov, S.R.; Serikkanov, A.S.; Terukov, E.I.; Tokmoldin, S.Z.; Tokmoldin, N.S. Optimization and Fabrication of Heterojunction Silicon Solar Cells Using an Experimental-Industrial Facility AK-1000 Inline. *J. Russ. Univ. Radioelectron.* **2020**, *23*, 57–62. [CrossRef]
37. Amanatides, E.; Mataras, D.; Rapakoulias, D.E. Deposition rate optimization in SiH4/H2 PECVD of hydrogenated microcrystalline silicon. *Thin Solid Films* **2001**, *383*, 15–18. [CrossRef]
38. Olibet, S.; Vallat-Sauvain, E.; Fesquet, L.; Monachon, C.; Hessler-Wyser, A.; Damon-Lacoste, J.; De Wolf, S.; Ballif, C. Properties of interfaces in amorphous/crystalline silicon heterojunctions. *Phys. Status Solidi (A)* **2010**, *207*, 651–656. [CrossRef]
39. Olibet, S.; Vallat-Sauvain, E.; Ballif, C. Model for a-Si: H/c-Si interface recombination based on the amphoteric nature of silicon dangling bonds. *Phys. Rev. B* **2007**, *76*, 035326. [CrossRef]
40. Holman, Z.C.; Descoeudres, A.; Barraud, L.; Fernandez, F.Z.; Seif, J.P.; De Wolf, S.; Ballif, C. Current losses at the front of silicon heterojunction solar cells. *IEEE J. Photovolt.* **2012**, *2*, 7–15. [CrossRef]
41. Tucci, M.; della Noce, M.; Bobeico, E.; Roca, F.; de Cesare, G.; Palma, F. Comparison of amorphous/crystalline heterojunction solar cells based on n-and p-type crystalline silicon. *Thin Solid Film.* **2004**, *451*, 355–360. [CrossRef]
42. Voz, C.; Muñoz, D.; Fonrodona, M.; Martin, I.; Puigdollers, J.; Alcubilla, R.; Escarre, J.; Bertomeu, J.; Andreu, J. Bifacial heterojunction silicon solar cells by hot-wire CVD with open-circuit voltages exceeding 600 mV. *Thin Solid Film.* **2006**, *511*, 415–419. [CrossRef]
43. Xu, Y.; Hu, Z.; Diao, H.; Cai, Y.; Zhang, S.; Zeng, X.; Hao, H.; Liao, X.; Fortunato, E.; Martins, R. Heterojunction solar cells with n-type nanocrystalline silicon emitters on p-type c-Si wafers. *J. Non-Cryst. Solids* **2006**, *352*, 1972–1975. [CrossRef]
44. Kleider, J.-P.; Chouffot, R.; Gudovskikh, A.; Cabarrocas, P.R.I.; Labrune, M.; Ribeyron, P.-J.; Brüggemann, R. Electronic and structural properties of the amorphous/crystalline silicon interface. *Thin Solid Film.* **2009**, *517*, 6386–6391. [CrossRef]
45. Chuchvaga, N.A.; Zhilina, D.V.; Zhantuarov, S.R.; Tokmoldin, S.Z.; Terukov, E.I.; Tokmoldin, N.S. Study and optimization of heterojunction silicon solar cells. *J. Phys. Conf. Ser.* **2018**, *993*, 012039. [CrossRef]
46. Zhao, L.; Li, H.; Zhou, C.; Diao, H.; Wang, W. Optimized resistivity of p-type Si substrate for HIT solar cell with Al back surface field by computer simulation. *Sol. Energy* **2009**, *83*, 812–816. [CrossRef]

47. Lisheng, W.; Fengxiang, C.; Yu, A. Simulation of high efficiency heterojunction solar cells with AFORS-HET. *J. Phys. Conf. Ser.* **2011**, *276*, 012177. [CrossRef]
48. Wen, X.; Zeng, X.; Liao, W.; Lei, Q.; Yin, S. An approach for improving the carriers transport properties of a-Si: H/c-Si heterojunction solar cells with efficiency of more than 27%. *Sol. Energy* **2013**, *96*, 168–176. [CrossRef]
49. Dwivedi, N.; Kumar, S.; Bisht, A.; Patel, K.; Sudhakar, S. Simulation approach for optimization of device structure and thickness of HIT solar cells to achieve∼ 27% efficiency. *Sol. Energy* **2013**, *88*, 31–41. [CrossRef]
50. Liu, Q.; Ye, X.-J.; Liu, C.; Chen, M.-B. Performance of bifacial HIT solar cells on n-type silicon substrates. *Optoelectron. Lett.* **2010**, *6*, 108–111. [CrossRef]
51. Ilyin, V.I.; Musikhin, S.F.; Shik, A.Y. *Varionic Semiconductors and Heterostructures*; Nauka: Saint Petersburg, Russia, 2000; pp. 21–44. (In Russian)
52. Bencherif, H.; Dehimi, L.; Pezzimenti, F.; Della Corte, F.G. Improving the efficiency of a-Si: H/c-Si thin heterojunction solar cells by using both antireflection coating engineering and diffraction grating. *Optik* **2019**, *182*, 682–693. [CrossRef]
53. Chandan, Y.; Kumar, S. Numerical simulation of novel designed perovskite/silicon heterojunction solar cell. *Opt. Mater.* **2022**, *123*, 111847.
54. Azzemou, F.; Rached, D.; Rahal, W.L. Optimisation of emitter properties for silicon heterojunction solar cell ITO/pa-Si: H/ia-Si: H/nc-Si/BSF/Al. *Optik* **2020**, *217*, 164802. [CrossRef]
55. Fredy, M.-G.; Sanz-Pascual, M.T.; Rosales-Quintero, P.; Moreno-Moreno, M. Solar Cell Parameter Extraction Method from Illumination and Dark I-V Characteristics. *Nanomaterials* **2022**, *12*, 1955. [CrossRef]
56. Green, M.; Dunlop, E.; Hohl-Ebinger, J.; Yoshita, M.; Kopidakis, N.; Hao, X. Solar cell efficiency tables (version 57). *Prog. Photovolt. Res. Appl.* **2021**, *29*, 3–15. [CrossRef]
57. Faes, A.; Despeisse, M.; Levrat, J.; Champliaud, J.; Badel, N.; Kiaee, M.; Söderström, T.; Yao, Y.; Grischke, R.; Gragert, M.; et al. SmartWire solar cell interconnection technology. In Proceedings of the 29th European Photovoltaic Solar Energy Conference and Exhibition, Amsterdam, The Netherlands, 22–26 September 2014; pp. 2555–2561.
58. Lammert, M.D.; Schwartz, R.J. The interdigitated back contact solar cell: A silicon solar cell for use in concentrated sunlight. *IEEE Trans. Electron Devices* **1977**, *24*, 337–342. [CrossRef]
59. Keshuov, S.; Tokmoldin, N.; Chuchvaga, N.; Tokmoldin, S.; Isova, A. An Algorithm for Optimization of Heterojunction Silicon Solar Cells by Ranking of Fabrication Parameters Influencing their Efficiency. *Ekoloji* **2019**, *28*, 2681–2692.
60. Chuchvaga, N.A.; Kislyakova, N.M.; Aimaganbetov, K.P.; Rakymetov, B.A.; Tokmoldin, N.S. Investigation of the effect of wet chemical treatment on the surface of single-crystal silicon wafers. *Recent Contrib. Phys.* **2018**, *67*, 108–114.
61. Mil'Shtein, S.; Zinaddinov, M.; Tokmoldin, N.; Tokmoldin, S. Design and fabrication steps of silicon heterostructured piin solar cell with corrugated surface. In Proceedings of the 2016 IEEE 43rd Photovoltaic Specialists Conference (PVSC) IEEE, Portland, OR, USA, 5–10 June 2016; pp. 0342–0345.
62. Bobyl, A.V.; Terukov, E.I. Development of cheap Si-based solar cells using plasma chemical technologies. *AgroEcoEngineering* **2016**, *88*, 35–45.
63. Chuchvaga, N.A.; Titov, A.S.; Tokmoldin, N.S.; Tokmoldin, S.Z.; Terukov, E.I. Investigation of Passivation of Surface States of Single Crystalline Silicon in Heterostructures with an Integrated Thin Amorphous Layer. *Proc. Natl. Acad. Sci. USA Repub. Kazakhstan Ser. Phys. Inf. Technol.* **2020**, *5*, 95–101.
64. García-Hernansanz, R.; Duarte-Cano, S.; Pérez-Zenteno, F.; Gutierrez, D.C.; Algaidy, S.; Garcia-Hemme, E.; Olea, J.; Pastor, D.; del Prado, A.; Andrés, E.S.; et al. Transport mechanisms in hyperdoped silicon solar cells. *Semicond. Sci. Technol.* **2022**, *38*, 124001. [CrossRef]
65. Brooks, W.; Wang, H.; Mil, S. Solar harvesting by a heterostructured cell with built-in variable width quantum wells. *AIP Conf. Proc.* **2018**, *1934*, 020003.
66. Buzaneva, E.V. Microstructures of integrated electronics. *M Radio Commun.* **1990**, *V1*, 203–241.
67. Rui, W.; Mujahid, M.; Duan, Y.; Wang, Z.-K.; Xue, J.; Yang, Y. A review of perovskites solar cell stability. *Adv. Funct. Mater.* **2019**, *29*, 1808843.
68. Tobias, F.; Kurpiers, J.; Roland, S.; Tokmoldin, N.; Shoaee, S.; Ferron, T.; Collins, B.A.; Janietz, S.; Vandewal, K.; Neher, D. On the Interplay between CT and Singlet Exciton Emission in Organic Solar Cells with Small Driving Force and Its Impact on Voltage Loss. *Adv. Energy Mater.* **2022**, *12*, 2200641.
69. Juan, B.; Juarez-Perez, E.J. The causes of degradation of perovskite solar cells. *J. Phys. Chem. Lett.* **2019**, *10*, 5889–5891.
70. Available online: https://www.nrel.gov/pv/cell-efficiency.html (accessed on 17 April 2023).
71. Li, Z.; Zhao, Y.; Wang, X.; Sun, Y.; Zhao, Z.; Li, Y.; Zhou, H.; Chen, Q. Cost analysis of perovskite tandem photovoltaics. *Joule* **2018**, *2*, 1559–1572. [CrossRef]
72. Niraj, N.L.; Dkhissi, Y.; Li, W.; Hou, Q.; Cheng, Y.-B.; Bach, U. Perovskite tandem solar cells. *Adv. Energy Mater.* **2017**, *7*, 1602761.
73. Available online: https://www.pv-magazine.com/2022/12/20/hzb-achieves-world-record-32-5-efficiency-for-perovskite-tandem-solar-cell/ (accessed on 17 April 2023).
74. Wang, Z.; Song, Z.; Yan, Y.; Liu, S.; Yang, D. Perovskite—A perfect top cell for tandem devices to break the S–Q limit. *Adv. Sci.* **2019**, *6*, 1801704. [CrossRef]
75. Ul, K.C.; Jung, E.D.; Noh, Y.W.; Seo, S.K.; Choi, Y.; Park, H.; Song, M.H.; Choi, K.J. Strategy for large-scale monolithic Perovskite/Silicon tandem solar cell: A review of recent progress. *EcoMat* **2021**, *3*, e12084.

76. Wang, H.-P.; Sun, K.; Noh, S.Y.; Kargar, A.; Tsai, M.-L.; Huang, M.-Y.; Wang, D.; He, J.-H. High-performance a-Si/c-Si heterojunction photoelectrodes for photoelectrochemical oxygen and hydrogen evolution. *Nano Lett.* **2015**, *15*, 2817–2824. [CrossRef]
77. Li, S.; Lin, H.; Yang, G.; Ren, X.; Luo, S.; Ye, J. One-step construction of buried a-Si/c-Si junction photocathodes for boosting photoelectrochemical hydrogen production. *Chem. Eng. J.* **2023**, *455*, 140898. [CrossRef]

MDPI
St. Alban-Anlage 66
4052 Basel
Switzerland
www.mdpi.com

Coatings Editorial Office
E-mail: coatings@mdpi.com
www.mdpi.com/journal/coatings

Academic Open
Access Publishing

mdpi.com

ISBN 978-3-7258-0996-7